Orazio Descalzi
Marcel Clerc
Stefania Residori
Gaetano Assanto *Editors*

Localized States in Physics: Solitons and Patterns

Springer

Localized States in Physics: Solitons and Patterns

Orazio Descalzi • Marcel Clerc • Stefania Residori
Gaetano Assanto
Editors

Localized States in Physics: Solitons and Patterns

Springer

Editors
Orazio Descalzi
Universidad de los Andes
Facultad de Ingeniería y Cs. Aplicadas
Av. San Carlos de Apoquindo 2200
Las Condes
Santiago
Chile
odescalzi@miuandes.cl

Marcel Clerc
Universidad de Chile
Fac. de Cs. Físicas y Mat.
Depto. de Física
Casilla 487 - 3
Santiago
Chile
marcel@dfi.uchile.cl

Stefania Residori
Institut Non-linéaire de Nice
route de Lucioles 1361
06560 Valbonne
France
stefania.residori@inln.cnrs.fr

Gaetano Assanto
University Roma Tre
Nonlinear Optics and OptoElectronics Lab
Via della Vasca Navale 84
00146 Roma
Italy
assanto@uniroma3.it

ISBN 978-3-642-16548-1 e-ISBN 978-3-642-16549-8
DOI 10.1007/978-3-642-16549-8
Springer Heidelberg Dordrecht London New York

Cover design: eStudio Calamar S.L.

Printed on acid-free paper

Springer is part of Springer Science+Business Media (www.springer.com)

Preface

Physical systems driven far from thermodynamic equilibrium can give rise to a variety of dissipative spatial structures through spontaneous breaking of symmetries. A fascinating feature of these pattern-forming systems is their tendency to originate spatially confined states. Such localized states can exist as wave packets or propagating entities through space and/or time. Observed in many different branches of science, localized states appear to be ubiquitous in nature and characterized by common macroscopic properties, independently of the specific physical laws governing the underlying field and/or matter interactions. Even though Localized States in Physics can be found in such different domains as hydrodynamics, optics, granular matter, reaction-diffusion systems, neural networks, plasmas, Bose-Einstein condensates etc., books on the topic are still very rare and often devoted to a particular type. This Book is based on a series of lectures given at a workshop on the subject: it reflects the spirit and the breadth of the meeting, held in 2008 at the University of los Andes, Santiago, Chile. Its main motivations stem from the need to bring together - coolate and compare - various approaches to the description of localized states in physics, offering a comprehensive panorama of confined states, from localized patterns to solitons, convectons, oscillons, pulses, etc., aimed at establishing a common - or at least shared - comprehension of these physical states. In fluids, for instance, convecting regions can coexist stably with non-convecting regions in uniformly heated cells. Localized hexagonal patterns have also been observed in a parametrically excited layer of fluid. In chemical systems, autocatalytic reactions on metallic surfaces can lead to solitary waves with partial and full annihilation after collision of pulses traveling in opposite directions. In granular matter, vertically driven layers of particles (sand, rice, stones, metal balls, etc.) reveal that, for peak acceleration exceeding a critical value, standing wave patterns spontaneously form and oscillate at half the excitation frequency. Square, stripe, hexagonal and spiral patterns can emerge, depending on the oscillation frequency and amplitude of the forcing, including coherent states such as localized standing waves or oscillons. Localized states are also relevant in neural systems, where action potentials propagate along axons or networks of thalamic neurons exhibit activity waves, just to mention two examples. In optics, the interplay between dispersion/diffraction

and the medium nonlinearity leads to light propagation in space/time self-confined beams, the so-called optical solitons. In the presence of feedback, optical localized structures such as cavity solitons have been identified as transverse solutions encompassing bistability; they have been observed in several media and controlled by suitable addressing protocols. Finally, coherence and interference properties of atomic clouds of Bose-Einstein condensates, as well as localized structures in population models, have been investigated. The book covers quite a few of the most active and interesting contemporary aspects of Localized States in Physics, providing both review elements and current information on the latest research in the field. It consists of thirteen chapters discussing localized objects in optics, fluids and neural networks. The first four chapters are mostly dedicated to fundamental research in light localization. Reports on the state-of-the-art in optical spatial solitons, self-confined light and optical turbulence are presented with particular emphasis on experimental observations. The related theoretical work is treated in a general way and recent nonlinear optical experiments are reported to support the various predictions. The next three chapters deal with localized structures as localized solutions of pattern-forming systems. Analogies are drawn between fluids and optics, with a chapter dedicated to confined convective states in fluids and another one to optical transverse structures in liquid crystal light-valves. The recent theoretical developments in pattern localization are treated in a dedicated chapter, where crystal-like hexagonal structures are shown to localize according to the symmetry of the underlying grid. In the second part of the book special attention is paid to the potentials of localized states towards applications. Four chapters are devoted to optical systems and their use for controllable light pixels. Finally, excitability and localized states are treated in the last two chapters, where pulse localization is illustrated with examples in a nonlinear optical cavity and in neural networks. The Book as a whole is intended for an audience of senior and junior researchers and graduate students working in the field of pattern formation, instabilities and spatio-temporal dynamics of macroscopic systems far from equilibrium. It provides an overview of the state-of-the-art in localized states to a readership of physicists, mathematicians, electrical/electronic engineers. We trust that a number of scientists from neighbouring areas, such as e.g. biology, sociology, environment science and meteorology, will find its contents stimulating and informative.

Santiago de Chile,
August 2010

Orazio Descalzi
Marcel G. Clerc
Stefania Residori
Gaetano Assanto

Acknowledgements

We wish to thank the following national and international institutions for the their financial support, that made possible **Localized states in Physics: a focused workshop 2008**:

- Facultad de Ingeniería y Cs. Aplicadas, Universidad de los Andes, Chile.
- Fondo de Ayuda a la Investigación, Universidad de los Andes, Chile.
- Departamento de Física, Facultad de Cs. Físicas y Matemáticas, Universidad de Chile, Chile.
- Nonlinear Optics and OptoElectronics Lab, CNISM, University of Rome "Roma Tre", Italy.
- Institut Non Linéaire de Nice, France.
- The Center for Advanced Interdisciplinary Research in Materials – CIMAT (Chile).
- The Consortium of the Americas for Interdisciplinary Science, University of New Mexico (USA).
- Programa Bicentenario de Ciencia y Tecnología, Anillo ACT 15, "Dynamics, Singularities and Geometry of Matter out of Equilibrium".

Contents

Part II Localized structures in pattern forming systems

Part III Localized structures for optical applications

List of Contributors

Miroslaw A. Karpierz
Faculty of Physics, Warsaw University of Technology, Koszykowa 75, 00662 Warsaw-Poland, e-mail: karpierz@if.pw.edu.pl

Gaetano Assanto
NooEL, Nonlinear Optics and OptoElectronics Lab, CNISM, University of Rome "Roma Tre", Via della Vasca Navale 84, 00146 Rome - Italy, e-mail: assanto@uniroma3.it

Mousa Ayoub
Institut für Angewandte Physik and Center for Nonlinear Science, Westfälische Wilhelms-Universität Münster, Corrensstr. 2/4, 48149 Münster, Germany, e-mail: Ayoubm@uni-muenster.de

Björn Gütlich
Institut für Angewandte Physik and Center for Nonlinear Science, Westfälische Wilhelms-Universität Münster, Corrensstr. 2/4, 48149 Münster, Germany

Cornelia Denz
Institut für Angewandte Physik and Center for Nonlinear Science, Westfälische Wilhelms-Universität Münster, Corrensstr. 2/4, 48149 Münster, Germany, e-mail: denz@uni-muenster.de

Francesco Papoff
SUPA, Department of Physics, University of Strathclyde, 107 Rottenrow, Glasgow, G4 0NG, Scotland, U.K. e-mail: papoff@phys.strath.ac.uk

Gian-Luca Oppo
SUPA, Department of Physics, University of Strathclyde, 107 Rottenrow, Glasgow, G4 0NG, Scotland, U.K. e-mail: gianluca@phys.strath.ac.uk

William Firth
SUPA, Department of Physics, University of Strathclyde, 107 Rottenrow, Glasgow, G4 0NG, Scotland, U.K. e-mail: willie@phys.strath.ac.uk

Umberto Bortolozzo
INLN, Université de Nice Sophia-Antipolis, CNRS, 1361 route des Lucioles 06560 Valbonne, France e-mail: Umberto.Bortolozzo@inln.cnrs.fr

Marcel G. Clerc
Departamento de Física, Facultad de Ciencias Físicas y Matemáticas, Universidad de Chile, Casilla 487-3, Santiago, Chile, e-mail: marcel@galileo.dfi.uchile.cl

René G. Rojas
Instituto de Física, Pontificia Universidad Católica de Valparaíso, Casilla 4059, Valparaíso, Chile e-mail: rene.rojas@ucv.cl

Florence Haudin
INLN, Université de Nice Sophia-Antipolis, CNRS, 1361 route des Lucioles 06560 Valbonne, France e-mail: Florence.Haudin@inln.cnrs.fr

Stefania Residori
INLN, Université de Nice Sophia-Antipolis, CNRS, 1361 route des Lucioles 06560 Valbonne, France, e-mail: Stefania.Residori@inln.cnrs.fr

Daniel Escaff Dixon
Complex Systems Group, Facultad de Ingeniería y Cs. Aplicadas, Universidad de los Andes, Av. San Carlos de Apoquindo 2200, Santiago, Chile e-mail: descaff@uandes.cl

Giovanna Tissoni
CNISM and INFM–CNR, Dipartimento di Fisica e Matematica, Università dell'Insubria, Como, Italy e-mail: giovanna.tissoni@uninsubria.it

Franco Prati
CNISM and INFM–CNR, Dipartimento di Fisica e Matematica, Università dell'Insubria, Como, Italy e-mail: franco.prati@uninsubria.it

Luigi A. Lugiato
CNISM and INFM–CNR, Dipartimento di Fisica e Matematica, Università dell'Insubria, Como, Italy e-mail: luigi.lugiato@uninsubria.it

Keivan M. Aghdami
Physics Department, Payame Noor University, Mini City, 19569 Tehran, Iran

Massino Brambilla
INFM–CNR, Dipartimento di Fisica Interateneo, Politecnico di Bari, Italy e-mail: m.brambilla@poliba.it

Arantxa Alonso
Departament de Física Aplicada, Universitat Politècnica de Catalunya, Barcelona, Spain e-mail: arantxa@fa.upc.edu

Oriol Batiste
Departament de Física Aplicada, Universitat Politècnica de Catalunya, Barcelona, Spain e-mail: oriol@fa.upc.edu

Isabel Mercader
Departament de Física Aplicada, Universitat Politècnica de Catalunya, Barcelona, Spain e-mail: isabel@fa.upc.edu

Edgar Knobloch
Department of Physics, University of California, Berkeley CA 94720, USA e-mail: knobloch@berkeley.edu

Damià Gomila
IFISC, Instituto de Física Interdisciplinar y Sistemas Complejos (CSIC-UIB), Campus Universitat Illes Balears, 07122 Palma de Mallorca, Spain, e-mail: damia@ifisc.uib-csic.es

Adrián Jacobo
IFISC, Instituto de Física Interdisciplinar y Sistemas Complejos (CSIC-UIB), Campus Universitat Illes Balears, 07122 Palma de Mallorca, Spain, e-mail: jacobo@ifisc.uib-csic.es

Manuel A. Matías
IFISC, Instituto de Física Interdisciplinar y Sistemas Complejos (CSIC-UIB), Campus Universitat Illes Balears, 07122 Palma de Mallorca, Spain, e-mail: manuel.matias@ifisc.uib-csic.es

Pere Colet
IFISC, Instituto de Física Interdisciplinar y Sistemas Complejos (CSIC-UIB), Campus Universitat Illes Balears, 07122 Palma de Mallorca, Spain, e-mail: pere@ifisc.uib-csic.es

Dmitry V. Dylov
Department of Electrical Engineering, Princeton University, Olden Street, Princeton, New Jersey 08544, USA e-mail: dvd@princeton.edu

Jason W. Fleischer
Department of Electrical Engineering, Princeton University, Olden Street, Princeton, New Jersey 08544, USA e-mail: jasonf@princeton.edu

Richard S. Tasgal
Departments of Chemistry and Electro-Optics, and the Ilse Katz Center for Nano-Science, Ben-Gurion University of the Negev, Beer-Sheva 84105, Israel e-mail: tasgal@gmail.com

Roman Shnaiderman
Departments of Chemistry and Electro-Optics, and the Ilse Katz Center for Nano-Science, Ben-Gurion University of the Negev, Beer-Sheva 84105, Israel e-mail: rshnaider@gmail.com

Yehuda B. Band
Departments of Chemistry and Electro-Optics, and the Ilse Katz Center for Nano-Science, Ben-Gurion University of the Negev, Beer-Sheva 84105, Israel e-mail: band@bgu.ac.il

Jason Laurie
Mathematics Institute, University of Warwick, Coventry CV4 7AL, United Kingdom e-mail: J.P.Laurie@warwick.ac.uk

Sergey Nazarenko
Mathematics Institute, University of Warwick, Coventry CV4 7AL, United Kingdom e-mail: S.V.Nazarenko@warwick.ac.uk

Massimo Giudici
Université de Nice Sophia Antipolis, Centre National de la Recherche Scientifique, Institut Non Linéaire de Nice, 1361 route des lucioles, Valbonne, France e-mail: Massimo.Giudici@inln.cnrs.fr

Francesco Pedaci
Université de Nice Sophia Antipolis, Centre National de la Recherche Scientifique, Institut Non Linéaire de Nice, 1361 route des lucioles, Valbonne, France

Emilie Caboche
Université de Nice Sophia Antipolis, Centre National de la Recherche Scientifique, Institut Non Linéaire de Nice, 1361 route des lucioles, Valbonne, France

Patrice Genevet
Université de Nice Sophia Antipolis, Centre National de la Recherche Scientifique, Institut Non Linéaire de Nice, 1361 route des lucioles, Valbonne, France e-mail: patrice.genevet@inln.cnrs.fr

Stephane Barland
Université de Nice Sophia Antipolis, Centre National de la Recherche Scientifique, Institut Non Linéaire de Nice, 1361 route des lucioles, Valbonne, France

Jorge Tredicce
Université de Nice Sophia Antipolis, Centre National de la Recherche Scientifique, Institut Non Linéaire de Nice, 1361 route des lucioles, Valbonne, France e-mail: Jorge.Tredicce@inln.cnrs.fr

Jaime E. Cisternas
Complex Systems Group, Facultad de Ingeniería y Ciencias Aplicadas, Universidad de los Andes, Santiago, Chile e-mail: jecisternas@miuandes.cl

Thomas M. Wasylenko
Department of Chemical Engineering, Princeton University, Princeton, U.S.A. Current address: Department of Chemical Engineering, Massachusetts Institute of Technology, Cambridge, U.S.A. e-mail: twasylen@mit.edu

Ioannis G. Kevrekidis
Department of Chemical Engineering and Program of Applied and Computational Mathematics, Princeton University, Princeton, U.S.A. e-mail: yannis@princeton.edu

Part I
Solitons, self-confined light and optical turbulence

Chapter 1
Light Self-trapping in Nematic Liquid Crystals

Miroslaw A. Karpierz and Gaetano Assanto

Abstract We review the most important achievements and recent progress in the area of light-beam self-localization into optical spatial solitons in reorientational molecular media, with specific focus on nematic liquid crystals in planarly aligned, twisted and chiral arrangements.

1.1 Introduction

Liquid crystals are widely used in displays for a large and ever growing number of applications, including high resolution television sets. It is less known to the general public that these molecular materials are employed and studied with a much larger set of scientific objectives, including electro-optic modulators and nonlinear photonics, particularly in devices for light switching and all-optical circuits towards novel generations of optical telecom systems. These molecular dielectrics are fluid, transparent, damage resistant, temperature and voltage tunable, etc. [1, 2, 3]. When the organic molecules, typically large and rod-shaped, are ordered in the so-called nematic phase, liquid crystals tend to exhibit a large (optical and radio-frequency) birefringence and their optical properties can also be modified by light through a nonlinear reorientational response, i.e. their constituent organic molecules can rotate and reorientate in space based on the optical excitation [1, 2, 3]. The latter nonlinear response is known as optical reorientation and has been exploited to investigate light-beam self-localization in non-diffracting filaments or spatial solitons, i.e. beams which do not spread upon propagation, maintain an invariant transverse

Miroslaw A. Karpierz
Faculty of Physics, Warsaw University of Technology, Koszykowa 75, 00662 Warsaw-Poland
e-mail: karpierz@if.pw.edu.pl

Gaetano Assanto
NooEL, Nonlinear Optics and OptoElectronics Lab, CNISM, University of Rome "Roma Tre"
Via della Vasca Navale 84, 00146 Rome - Italy, e-mail: assanto@uniroma3.it

O. Descalzi et al. (eds.), *Localized States in Physics: Solitons and Patterns*,
DOI 10.1007/978-3-642-16549-8_1,

profile via a power-driven increase in refractive index and are able to guide weaker signals [4, 5, 6, 7]. The molecular nonlinearity of nematic liquid crystals (NLC) is large (i.e. it requires low powers), depends on field polarization but is substantially independent on wavelength in the whole transparency range, typically from visible to mid-infrared; being associated to molecular motion in a fluid, it is rather slow in time, this latter drawback requiring a careful choice/selection of potential applications in reconfigurable circuits. The light-driven NLC reorientational response supports various phenomena [2, 3] and, as anticipated, the generation and propagation of stable and robust self-trapped spatial solitary waves, also named Nematicons [4]. The first solitons in NLC were observed in hollow capillaries filled with dye-doped materials [8, 9, 10]; they exploited the thermal response through absorption and, in some cases, a phase transition from nematic to isotropic states. Recently, the most studied geometries for optical solitons have been planar cells with non-absorbing NLC, various boundary conditions and applied voltage biases. In the next section we give a brief account of the basics of the reorientation response and the excitation of nematicons. In Section 11.3 we overview the main recent results on nematicons in undoped nematic liquid crystals in planar geometries. In Section 7.4 we discuss spatial optical solitons in twisted and chiral NLC.

1.2 Reorientational Self-focusing in Nematic Liquid Crystals

Optical reorientation in nematic liquid crystals relies on the structure of the medium, which consist of anisotropic elongated non-polar molecules in a fluid state [1]. In the isotropic phase these molecules are disordered in position and orientation, the latter usually defined by the angle of their major axis or director **n**, a unity vector corresponding to the optic axis. In the nematic phase, the NLC director exhibits an average angular orientation, typically mediated by molecular anchoring at the boundaries of a cell. The director distribution in an NLC cell can be modified by anchoring at the surfaces, applied electromagnetic fields, medium temperature, light beams. NLC, in fact, maintain their fluid state despite the anchoring, with changes in director orientation related to the free energy of density:

$$f_{\mathrm{F}} = \frac{1}{2}K_{11}\left(\nabla\cdot\mathbf{n}\right)^2 + \frac{1}{2}K_{22}\left(\mathbf{n}\cdot\nabla\times\mathbf{n}+G\right)^2 + \frac{1}{2}K_{33}\left(\mathbf{n}\times\nabla\times\mathbf{n}\right)^2, \qquad (1.1)$$

with K_{ii} the elastic (Frank) constants for the three basic spatial distortions of the molecules: splay (K_{11}), twist (K_{22}) and bend (K_{33}). In most common NLC $K_{33} > K_{11} > K_{22}$ and are of the order of a few pN units [1, 2, 3]. Expression (1) is often simplified by taking $K_{11} = K_{22} = K_{33} = K$. The parameter G in the second term on the RHS of (1) describes chirality with pitch p: $G = 0$ for standard NLC and $G = 2\pi/p$ for chiral nematic liquid crystals (ChNLC). Owing to the elongated shape of molecules in NLC, valence electrons have a larger mobility along the major axis; hence, the dielectric permittivity is higher for field vectors parallel to **n**. In the nematic phase, therefore, typical NLC are birefringent dielectrics with uni-

axial properties, i. e. $\Delta\varepsilon = \varepsilon_{\parallel} - \varepsilon_{\perp}$, $\varepsilon_{\parallel}$ and $\varepsilon_{\perp}$ being the components of the electric permittivity (at low and/or optical frequencies) for extraordinary and ordinary polarizations, respectively. An electric field $\mathbf{E}$, either externally applied (e.g. a voltage) or associated to a propagating light beam, can rotate the main molecular axis by a Coulombian torque, the latter trying to align $\mathbf{n}$ along the field vector despite anchoring at the boundaries and the free energy (1). This latter interaction energy has density

$$f_{\mathrm{el}} = -\frac{\varepsilon_0 \Delta\varepsilon}{2} \left\langle (\mathbf{n}\cdot\mathbf{E})^2 \right\rangle \tag{1.2}$$

Since energy (2) is minimized when $\mathbf{n}$ is parallel to the $\mathbf{E}$ field vector, the reorientational response is a saturable one: the maximum nonlinearity corresponds to a change from $\varepsilon_{\perp}$ to $\varepsilon_{\parallel}$ or from ordinary index $n_{\perp}$ to extraordinary index $n_{\parallel}$. An intense enough extraordinarily polarized beam, such that $\mathbf{E}$, propagation wavevector $\mathbf{k}$ and NLC optic axis $\mathbf{n}$ are coplanar, can alter the molecular orientation, increase the electric permittivity and the extraordinary index of refraction, give rise to self-focusing. Such effect can be modeled by deriving the Euler-Lagrange-Rayleigh equations from the minimization of the total free energy, which includes the deformation energy, the interaction energy with external fields, the interaction energy with the boundaries and the dissipation energy [7]. The latter has density f_{R}

$$f_{\mathrm{R}} = \frac{1}{2}\gamma \left(\frac{\partial \mathbf{n}}{\partial t} \right)^2 \tag{1.3}$$

with γ the orientational viscosity. The density f_{R} is required in time-dependent analyses.

When the director at the boundaries and the electric field $\mathbf{E}$ lie in the same plane, the angle θ defining the orientation of the director $\mathbf{n}$ with respect to the propagation coordinate z can describe the reorientation in two-dimensional problems, as sketched in Fig. 1.1. The refractive index for an extraordinarily polarized field varies with θ according to the usual

$$n_{\mathrm{e}}(\theta) = \frac{n_{\perp} n_{\parallel}}{\sqrt{n_{\perp}^2 \cos^2\theta + n_{\parallel}^2 \sin^2\theta}} \tag{1.4}$$

For the geometry sketched in Fig. 1.1 the director $\mathbf{n} = (\sin\theta, 0, \cos\theta)$. Assuming an initial orientation $\theta = \theta_0$, nonlinear beam propagation at wavelength λ (frequency ω) is ruled by the coupled system

$$4K\nabla_{\perp}^2\theta + \varepsilon_0 \Delta\varepsilon \sin(2\theta)|A|^2 = 0 \tag{1.5}$$

$$2ik\frac{\partial}{\partial z}A + \nabla_{\perp}^2 A + \frac{\omega^2}{c^2} n_{\mathrm{e}}^2(\theta) A - k^2 A = 0 \tag{1.6}$$

with A the slowly-varying beam envelope, $\nabla_{\perp}^2 = \partial^2/\partial x^2 + \partial^2/\partial y^2$ the Laplacian in the transverse plane, $k \approx (\omega/c)\sqrt{n_{\perp}^2 + \Delta\varepsilon \sin^2\theta_0}$, c the light speed in vacuum [11].

Eq. (6) is a saturable (θ cannot exceed $\pi/2$) nonlinear Schrödinger-like equation with an index increase limited by $\Delta n = n_{\parallel} - n_{\perp}$. In Eq. (5) and Eq. (6), the initial value θ_0 can represent the effect of a fixed pre-tilt or a tilt induced by a voltage V applied to the NLC thickness across x. A small initial tilt, such that **n** and **E** are not perpendicular to one another, prevents the threshold effect known as Fréedericksz transition. Eq. (6) holds valid with $\theta_0 = constant$ for narrow beams in thick cells, i. e., in NLC regions far from the anchoring boundaries. System (5)-(6) models a nonlocal nonlinear response, whereby the reorientational index change extends beyond the transverse size of the beam field envelope [12]. Nonlocality, as well as saturation, allow nematicons to be stable and robust in 2+1 dimensions [13, 14]. Fig. 1.1(b) displays the calculated distribution of $\theta(x)$ as compared to a bell-shaped electric field excitation for various intensities I_0. It is apparent that the boundary conditions affect the nonlocal response and its strength depending on the waist of the beam [5, 15, 16].

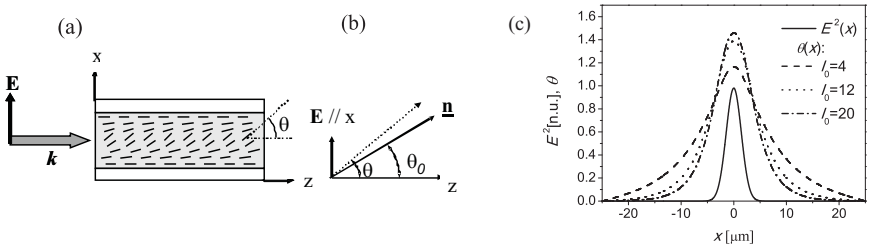

Fig. 1.1 (a) Geometry of a bounded NLC layer in a planar cell with voltage bias across the thickness. (b) The input **E** field belongs to the principal plane xz and is coplanar with **n** and $\mathbf{k} \parallel \mathbf{z}$. (c) Distribution of $\theta(x)$ for various electric field excitations. The field profile is the solid curve. In this 1D calculations we used an NLC layer thickness of 50 μm and boundary conditions $\theta(-d/2) = \theta(d/2) = 0.01$

The reorientational response of NLC, stemming from the shape of the constituent non polar molecules determines the properties of spatial optical solitons. The nonlinearity is polarization sensitive, self-focusing, saturable, non instantaneous and nonlocal; hence, it supports stable two-dimensional propagating solitons. Moreover, owing to the refractive index increase counterbalancing diffraction, co-polarized signals of different wavelengths can be guided within the soliton channels [11, 17]. By using the correct input beam polarization, applying suitable boundary conditions at the interfaces containing the layer of NLC, e.g. by mechanical rubbing, appropriate pre-tilt θ_0 can maximize the nonlinear response and allow mW power excitations to generate nematicons with propagation over several Rayleigh distances, i. e. to define reconfigurable signal interconnects. In the remaining of this chapter we will illustrate the main properties of low-power reorientational nematicons in threshold-less configurations.

Nematicons have been investigated in various cell geometries, from hollow capillaries to thick cells with fiber in/out connections, to thin planar waveguides. The main planar cells for 2D nematicons are sketched in Fig. 1.2 and consist of glass

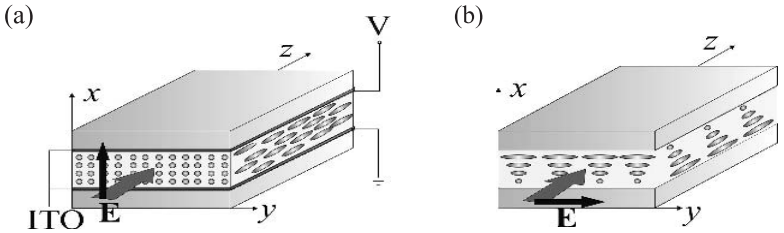

Fig. 1.2 Most common NLC planar cells for the study of optical spatial solitons: (a) planar anchoring with external voltage bias V applied by means of Indium Tin Oxide (ITO) thin film electrodes, (b) twisted or chiral NLC arrangement. The wide arrows along z indicate the excitation field wavevector of amplitude **E**, the thinner arrows refer to the input linear polarization

plates with proper rubbing at the internal interfaces [11]. The plates are held parallel and separated by spacers. Thin film transparent electrodes (e.g. Indium Tin Oxide) can be used to apply the desired low-frequency bias and tune the initial orientation θ_0. Input and output glass slabs can also be used to seal the cells and avoid meniscus formation and beam depolarization. When the NLC thickness is much larger than the waist of the input beam, the NLC layer can be treated as a bulk and the observation of (2+1) dimensional spatial solitons is possible [4, 7, 11, 13]. Conversely, if the thickness is comparable with the beam waist, then the structure is better modelled as a planar waveguide and can support (1+1) dimensional nematicons [5, 6].

1.3 Spatial Optical Solitons in Purely Nematic Liquid Crystals

The basic geometry adopted for demonstrating Nematicons in a planar glass cell containing undoped NLC (specifically, the Merck mixture known as E7) is sketched in Fig. 1.1(a) and Fig. 1.2(a) [7, 11]. The excitation was a linearly polarized Gaussian beam with the electric field parallel to x, i.e. extraordinarily-polarized. Surface anchoring and applied voltage across the $d = 75$ μm thickness guaranteed a threshold-less all-optical response in the uniaxial dielectric, as described by Eq. (4) and Eq. (5). In the presence of the external bias $V = dE_{\rm rf}$, neglecting walk-off in the plane xz and non-paraxial effects, the evolution of the slowly-varying beam amplitude A propagating along z in the mid-plane of the cell is modelled by [7, 11]:

$$2ik\frac{\partial}{\partial z}A + \nabla_\perp^2 A + \frac{\omega^2}{c^2}\left(n_\parallel^2 - n_\perp^2\right)\left(\sin^2\theta - \sin^2\theta_0\right)A = 0 \quad (1.7)$$

$$K\frac{\partial^2\theta}{\partial z^2} + K\nabla_\perp^2\theta + \frac{1}{2}\Delta\varepsilon_{\rm RF}E_{\rm rf}^2\sin(2\theta) + \frac{1}{4}\varepsilon_0\left(n_\parallel^2 - n_\perp^2\right)|A|^2\sin(2\theta) = 0 \quad (1.8)$$

with θ_0 the pre-tilt and θ the director orientation due to both light and voltage, $\Delta\varepsilon_{\rm RF}$ the dielectric anisotropy in the low frequency region.

System (7), for narrow nematicons with respect to the cell and small waist compared to the extent of the nonlocal response, reduces to a saturable nonlinear Schrödinger equation with nonlocal and stable 2D+1 self-localized solutions [12]. In this limit, nematicons exhibit the features attributed to "accessible" solitons by Snyder and Mitchell [14], with a breathing character resulting in the (quasi) periodic oscillation of their waist and peak intensity [12, 13, 14]. This breathing is excitation-dependent and can be reduced by exciting the solitons with power and waist close to their existence curve. In several experimental scenarios, nematicons often appear as transversely invariant beams with a slowly decaying intensity due to Rayleigh scattering in the medium. Self-localized solutions in the "local" regime can also be found for beams of waist comparable to the nonlocal range [18, 19]. Fig. 1.3(a) displays actual (colour-coded) images of individual 2mW Gaussian green (514.5nm) beams in the ordinary (top panel) and extraordinary (bottom) polarizations, resulting in linear (diffraction) and nonlinear (self-localized) propagation, respectively, as observed by collecting the out-of-plane scattered photons with a camera. The linear behaviour in the ordinary polarization corresponds to an **E**-field orthogonal to **n**; hence, to lack of reorientation below the Freedericks threshold. The nematicon (Fig. 1.3(a, lower panel) remains invariant over distances exceeding 20 diffraction lengths. Fig. 1.3(c) shows the corresponding evolution of a red (632.8 nm) probe (signal) co-polarized and co-launched with the pump: as a nematicon is generated, the weak signal is confined in the soliton waveguide despite its longer wavelength: another demonstration of the nonlocal nature of nematicons, inasmuch as the numerical aperture of the solitary channel exceeds that associated to the spatial extent of the self-localized solution.

Another effect of nonlocality is low-pass filtering. In the case of spatial incoherent excitations, e.g. a speckled beam produced by a diffuser, nonlocality can eliminate the high frequency wave-vector components and allow a spatial soliton to be formed, even if at the price of a larger power [20, 21, 23]. Fig. 1.3(b) and Fig. 1.3(d) display diffraction and self-localization of pump (Fig. 1.3(b)) and probe (Fig. 1.3(d)) in ordinary (top panels) and extraordinary (bottom) polarizations, respectively. It is apparent that an excitation of 2.7 mW (versus 2.0 mW in the coherent case) suffices to compensate the larger diffraction associated to the speckled input.

The incoherent character of nonlocal solitons also allows the formation of vector nematicons with two (or more) co-polarized wavelength components [24, 25], as well as the mutual attraction between nematicons, propagating either in plane [26, 27, 28] or out of plane [29, 30, 31, 32]. Fig. 1.4 illustrates a couple of simple in plane interactions between two solitons excited by equi-power beams propagating at a small angle. Since the initial separation does not exceed the nonlocal range, the nematicons tend to attract as the refractive perturbation links the two self-induced waveguides, until the in initially diverging beams become parallel (Fig. 1.4(b)). At higher input powers (Fig. 1.4(c)) the mutual attraction becomes strong enough to make the two solitons cross and interleave, exchanging their position along y. This power-dependent interaction can be exploited for all-optical switching and logic gates.

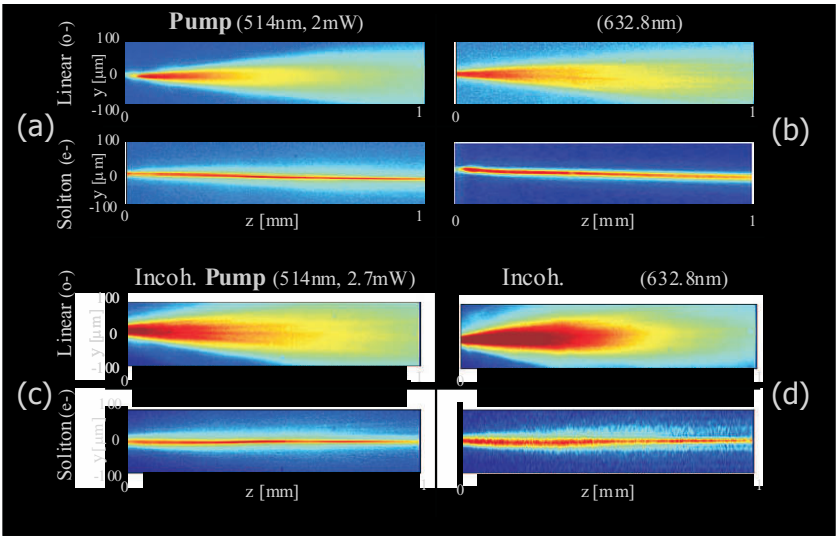

Fig. 1.3 Colour coded images of beam propagation from an Ar^+ laser (left) and a collinear co-polarized He-Ne laser (right) in a planar NLC cell with E7. (a) Top row: linear diffraction when injecting an ordinary polarization. Bottom: soliton propagation in the extraordinary polarization ($\| \mathbf{x}$); (b) corresponding linear (top) and nonlinear (bottom) evolution of the probe (100 μW). (c-d) Spatially incoherent beam propagation as in (a) and (b), respectively, but for a (c) 2.7 mW pump and (d) an equally incoherent probe

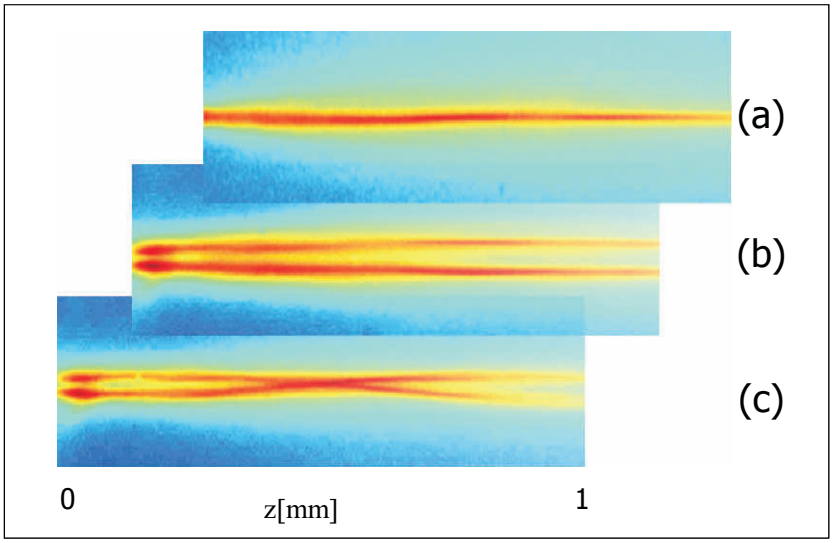

Fig. 1.4 Color coded images of (a) a single nematicon in a planar cell; (b) two identical nematicons launched by ≈2 mW beams forming a mutual angle of 1.7^o; (c) same as in (b) but with launch powers ≈4 mW

Figure 1.5 summarizes a few other cases of interactions between nematicons. If the initial separation and/or angle are large enough, the two spatial solitons cross each other (Fig. 1.5(a)) while maintaining straight trajectories, as for one-dimensional Kerr solitons [21]. Fig. 1.5(b) illustrates the formation of a few nematicons using a wide beam focused well inside the cell [33]: transverse modulational instability mediates the formation of a number of solitons depending on the size and power of the optical excitation [22, 34, 35]. Several nematicons can also be the by-product of a dispersive shock wave or undular bore [36]. Fig. 1.5(c) illustrates the interaction of two equi-power solitons lauched skew in the cell: mutual attraction gives rise to a cluster of nematicons with spiralling trajectories and angular momentum. Since the latter is proportional to the photon content of each soliton, as the excitation increases the cluster rotates faster, as displayed in Fig. 1.5(d) showing the output images of the two light spots versus input power [30, 31]. A similar behaviour has been also predicted with clusters of nematicons of different wavelengths and with more than two components.

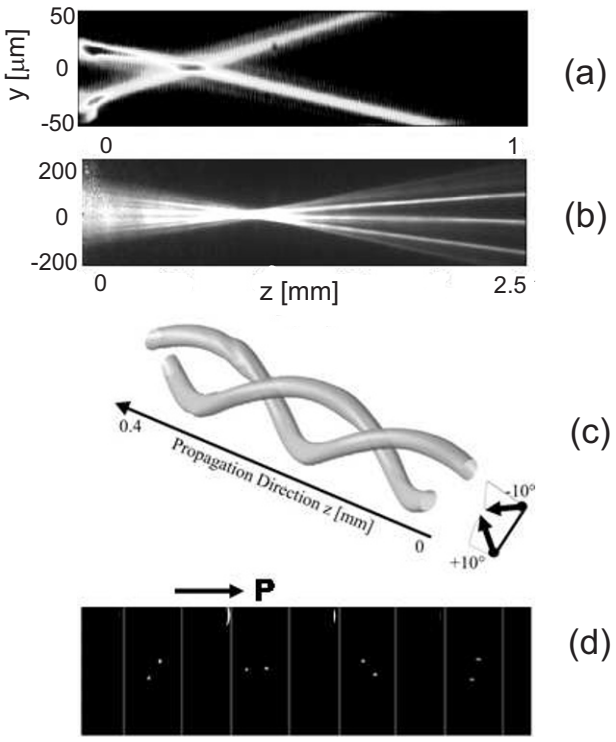

Fig. 1.5 (a) In plane crossing of two identical nematicons. (b) Multiple soliton generation by a focused light beam. (c) Out-of-plane attraction between two skew nematicons. (d) The photographs taken at the output of the cell show that, as the excitation increases, the cluster rotates faster in propagation, with a power-dependent angular change (π , in this set)

Nematicons are extraordinarily polarized wave-packets in uniaxials; hence, they undergo walk-off, i. e. their photon flux forms an angle

$$\delta(\theta) = \tan^{-1}\left(\frac{\left(n_{\parallel}^2 - n_{\perp}^2\right)\sin(2\theta)}{n_{\parallel}^2 + n_{\perp}^2 + \left(n_{\parallel}^2 - n_{\perp}^2\right)\cos(2\theta)}\right) \tag{1.9}$$

with the wave-vector. Such angle can be as large as $7-9^{o}$ in typical NLC, and suitable launch conditions need be adopted to prevent or reduce it not to make the soliton hit the cell boundaries [37]. Boundaries contribute to define the potential landscape for soliton propagation and can play an important role in the actual nematicon path within finite cells [38, 39, 40]. Since walk-off depends on the angle θ which, in turn, can be controlled by the external bias, the applied voltage can also be used to change nematicon trajectory by varying δ , either in the whole cell or in specific regions of it [41, 42, 43, 44]. In the latter case, graded interfaces can be formed and support soliton refraction or total internal reflection [43, 44]. Examples of refraction and total internal reflection in a cell with two electrodes defining regions of higher and lower optical densities are shown in Fig. 1.6 (a-b). Analogous effects can be obtained by illuminating NLC regions and inducing reorientation along the path of the nematicon. This has been demonstrated with lens-like perturbations in undoped NLC and Azo-NLC [45, 46], through dye-mediated absorption and surface anchoring [47], in liquid crystal light valves by means of a photoconductive layer altering the voltage drop across the NLC [48]. Finally, owing to the large walk-off, double refraction in uniaxial NLC can originate negative refraction at the input glass-NLC interface, with the soliton propagating in the same half-plane of the incident wave vector, as visible in Fig. 1.6(c) comparing ordinary and extraordinary (self-confined) beam propagation [49].

1.4 Spatial Optical Solitons in Chiral Nematic Liquid Crystals

In twisted and chiral nematic cells the molecular director is parallel to the glass plates (interfaces) and twisted within the film thickness (Fig. 1.2(b)) [50, 51]. Such an orientation is typically induced by the boundary conditions (in twisted nematics, TNLC) and by the chiral properties (in cholesteric liquid crystals, ChNLC). For light polarized along y the refractive index varies across the sample thickness from the ordinary value $n_{\perp}$ in planes where $\theta = 0$ to the extraordinary $n_{\parallel}$ in planes where $\theta = \pi/2$. A self-trapped light beam propagates in the thin layer where the refractive index is the largest (close to $n_{\parallel}$). In ChNLC several such layers occur throughout the liquid crystal and their number depends on the chirality pitch and the thickness of the film.

In the configurations investigated a light beam propagates in the z-direction parallel to the glass plates and is initially linearly polarized with the electric field vector $\mathbf{E} = \mathbf{y}E_{\mathrm{y}}$ also parallel to the interfaces. Because the birefringence axis rotates across

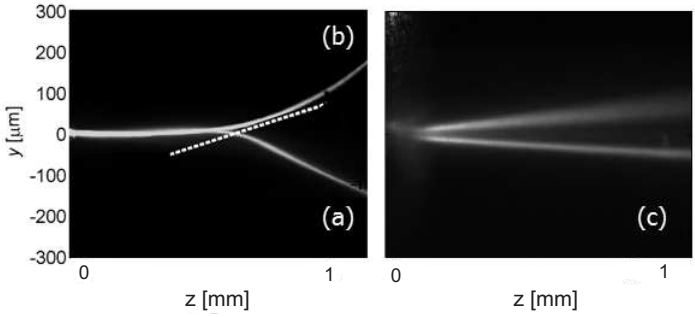

Fig. 1.6 (a-b) A planar cell with suitable director orientation in the plane *yz* and two sets of electrodes can be used to define two dielectric regions separated by a graded interface (dashed line). If the nematicon, injected from the left, reaches the interface from an optically rarer region, it can undergo refraction as in (a). If the input region is denser, the soliton can undergo total internal reflection, as in (b). The overall change in angle from refraction to reflection in this experiment is $18+22=40^{\circ}$. (c) Double refraction in NLC: the ordinary beam component (upper) undergoes positive refraction while diffracting; the extraordinary beam nematicon propagates with negative refraction (towards $y<0$) at the walk-off angle with respect to **k** (along the ordinary beam)

the layer, during propagation all components of electric and magnetic fields appear. However, only E_{y} and E_{z} are important for reorientation. Using the Euler-Lagrange equation for energy minimization, the following partial differential equation can be obtained:

$$K\frac{\partial^2\theta}{\partial x^2}+\frac{1}{4}\varepsilon_0\Delta\varepsilon\left[\left(|E_{\mathrm{z}}|^2-\left|E_{\mathrm{y}}\right|^2\right)\sin(2\theta)+\left(E_{\mathrm{y}}^*E_{\mathrm{z}}+E_{\mathrm{z}}^*E_{\mathrm{y}}\right)\cos(2\theta)\right]=0 \quad (1.10)$$

where $\theta(x)=\theta_0+2\pi x/p$ is the initial orientation (without electric field) and p is the chirality pitch. The description of light propagation in a twisted or a chiral NLC layer can be simplified by assuming that the beam profile along x is roughly constant, a hypothesis which is correct at some distance from the input, where the self-guided mode is formed. In this limit, taking $E_{\mathrm{z}}<<E_{\mathrm{y}}$, the slowly varying amplitude A is ruled by [50, 51]:

$$2\mathrm{i}\beta\frac{\partial}{\partial z}A-\frac{\partial^2}{\partial y^2}\gamma_1 A+2\mathrm{i}\beta\frac{\partial}{\partial y}\gamma_2 A-\beta^2\left(\gamma_1-\gamma_1^{(0)}\right)=0 \quad (1.11)$$

where β is the propagation constant of the planar waveguide mode and the coefficients γ_1 and γ_2 depend on the orientation angle ($\gamma_1^{(0)}$ is the value of γ_1 for the initial orientation). These coefficients have a saturable form and can be calculated for any specific liquid crystal layer. γ_2 is connected with the walk-off of the light beam when the latter is asymmetrically launched into the film. γ_1 relates to nonlinearity and is responsible for self-focusing and the creation of spatial solitons. The

simplified equation predicts that a beam gets self-trapped and the walk-off varies with intensity.

Experimentally, it was demonstrated that TNLC can support spatial solitons for light powers of a few tens of milliwatts. In the asymmetric case the results also show a change in direction of propagation with increased excitation. Most experiments were carried out in a cell of thickness $d = 50$ μm filled with 6CHBT (4-trans-4'-n-hexyl-cyclohexyl-isothiocyanatobenzene) [52, 53]. An Ar^+ laser beam ($\lambda = 514$ nm) with initial waist of a few micrometers formed nematicons at powers approximately 100 and 20 mW in the symmetric and asymmetric configurations, respectively [17, 54]. The solitary beam exhibited an invariant transverse distribution over a propagation distance > 50 times the Rayleigh length (a few millimeters).

The relatively large power required to form nematicons in TNLC can be reduced by decreasing the film thickness d. This can be obtained in ChNLC with a smaller pitch, where nematicons are substantially similar to those in TNLC [55, 56]. However, the former offer some new opportunities because the width of a guiding layer (in x) is not only determined by the sample thickness (as in TNLC) but also by the chirality pitch. As a result, in ChNLC it is easier to change the thickness of a layer and -as a consequence- the nonlinear strength. It is also possible to utilize multilayers for the propagation of independent or interacting nematicons, as schematically shown in Fig. 1.7(a).

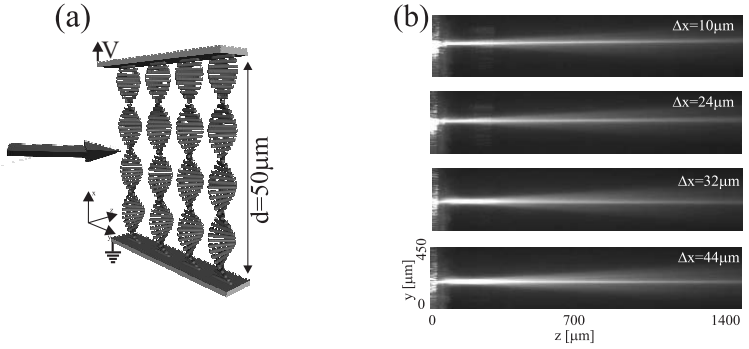

Fig. 1.7 (a) ChNLC cell geometry and (b) experimental results showing the formation of nematicons in different layers across the film, as obtained by launching the input beam in distinct vertical positions Δx.

Typical results in ChNLC are presented in Fig. 1.7(b) for a Ti:Sapphire ($\lambda = 790$ nm) laser beam with input waist of about 2 μm . Spatial solitons were excited in a cell with pitch $p = 25$ μm at powers $P \approx 30$ mW (66-67). Nematicons were size invariant for about 2 mm of propagation (> 80 Rayleigh lengths). Due to the finite thickness of each layer in ChNLC, self focusing could balance diffraction and give rise to self-trapped solitons only in a limited waist range. Moreover, by changing the vertical input position along x, it was possible to launch as many solitons as layers in the ChNLC structure, as reported in Fig. 1.7(b) corresponding to the four layers

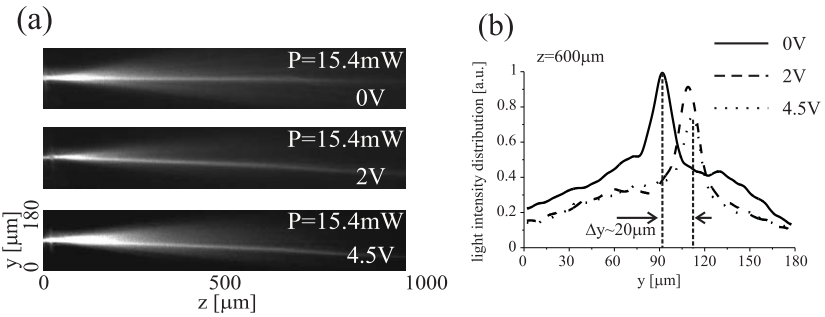

Fig. 1.8 Experimental results on spatial solitons in ChNLC: (a) light beam propagation for various external electric fields (marked on photos) and (b) corresponding intensity profiles at a distance $z = 0.6$ mm.

of a cell about 50 μm thick and with a 25 μm pitch. The four nematicons could be injected independently, separated by $10 - 12$ μm.

Using the smaller pitch $p = 10$ μm the power required to form soliton was reduced to $P < 10$ mW. Additionally, similar to the nematicons discussed in Sect. 11.3, even in TNLC and ChNLC we verified that the solitary waveguide was able to confine different wavelength signals, specifically a co-polarized low-power probe from a Helium-Neon laser ($\lambda = 633$ nm). When two nematicons were launched close to one another in the same layer, they attracted and eventually merges into a single self-trapped beam.

Small changes in input beam polarization caused nematicons to change direction of propagation. However, if the polarization is sufficiently rotated, then diffraction in a non-soliton polarization prevailed over self-focusing. Similar results were observed when the external electric field was applied perpendicularly to the layer. The direction of nematicon propagation could be controlled by a voltage V, as presented in Fig. 1.8. For larger values of the external electric field (in our example for V$>$ 6 V) the induced reorientation prevented an effective self-trapping of light.

1.5 Conclusions

Nematic liquid crystals, organic self-assembling molecular fluid dielectrics with anisotropic optical properties, are ideal material systems for studying self-localization of light into spatial solitons at milliwatt powers and over millimeter distances. Their reorientational response, saturable nonlocal and polarization sensitive, supports several types of self confinement and soliton all-optical effects, including signal trapping and routing, switching, processing. We predict that various other light localization phenomena, from dispersive shock waves to undular bores and soliton propagation in random potentials, will find experimental validation in these media.

Acknowledgements We are indebted with various collaborators, including U. Bortolozzo, M. Kaczmarek, I. C. Khoo, A. A. Minzoni, E. Nowinowski, S. Residori, M. Sierakowski, F. Simoni, N. F. Smyth, C. Umeton. We are grateful to our students and associates for the extensive contributions to this work: A. Alberucci, C. Conti, A. Fratalocchi, K. Jaworowicz, U. A. Laudyn, M. Kwasny, M. Peccianti, A. Piccardi and K. A. Rutkowska.

References

1. P. G. de Gennes, *The physics of liquid crystals*, (Clarendon Press, Oxford, 1974)
2. I. C. Khoo, N. T. Wu, *Optics and nonlinear optics of liquid crystals*, (World Scientific Publ., Singapore, 1993)
3. F. Simoni, *Nonlinear Optical Properties of Liquid Crystals*, (World Scientific Publ., London, 1997)
4. G. Assanto, M. Peccianti, C. Conti, Opt. Photon. News **14**, 44–48 (2003)
5. M. A. Karpierz, M. Sierakowski, M. Swillo, T. R. Wolinski, Mol. Cryst. Liq. Cryst. **320**, 157–164 (1998)
6. M. A. Karpierz, Phys Rev. E **66**, 036603 (2002)
7. G. Assanto, M. Peccianti, IEEE J. Quantum Electron. **39**, 13–21 (2003)
8. E. Braun, L. P. Faucheux, A. Libchaber, Phys. Rev. A **48**, 611–622 (1993)
9. M. Warenghem, J. F. Henninot, G. Abbate, Opt. Express **2**, 483–490 (1998)
10. F. Derrien, J. F. Henninot, M. Warenghem, G. Abbate, J. Opt. A - Pure Appl. Opt. **2**, 332-337 (2000)
11. M. Peccianti, G. Assanto, A. De Luca, C. Umeton, I. C. Khoo, Appl. Phys. Lett. **77**, 7–9 (2000)
12. C. Conti, M. Peccianti, G. Assanto, Phys. Rev. Lett. **91**, 073901 (2003)
13. C. Conti, M. Peccianti, G. Assanto, Phys. Rev. Lett. **92**, 113902 (2004)
14. A. W. Snyder, D. J. Mitchell, Science. **276**, 1538–1541 (1997)
15. M. Peccianti, C, Conti, G. Assanto, Phys. Rev. E **68**, 025602 (2003)
16. A. A. Minzoni, N. F. Smyth, A. L. Worthy, J. Opt. Soc. Am. B **24**, 1549–1556 (2007)
17. U. A. Laudyn, M. Kwany, K. Jaworowicz, K. A. Rutkowska, M. A. Karpierz, G. Assanto, Photon. Lett. Pol. **1**, 7–9 (2009)
18. C. Garcia-Reimbert, A. A. Minzoni, N. F. Smyth, A. L. Worthy, J. Opt. Soc. Am. B **23**, 2551–2558 (2006)
19. C. Garcia-Reimbert, A. A. Minzoni, N. F. Smyth, J. Opt. Soc. Am. B **23**, 294–301 (2006)
20. M. Peccianti, G. Assanto, Opt. Lett. **26**, 1791–1793 (2001)
21. M. Peccianti, G. Assanto, Phys. Rev. E **26**, 035603–035606R (2002)
22. M. Peccianti, C. Conti, E. Alberici, G. Assanto, Laser Phys. Lett. **2**, 25–29 (2005)
23. K. G. Makris, H. Sarkissian, D. N. Christodoulides, G. Assanto, J. Opt. Soc. Am. B **22**, 1371–1377 (2005)
24. A. Alberucci, M. Peccianti, G. Assanto, A. Dyadyusha, M. Kaczmarek, Phys. Rev. Lett. **97**, 153903 (2006)
25. G. Assanto, N. F. Smyth, A. L. Worthy, Phys. Rev. A **78**, 013832 (2008)
26. M. Peccianti, K. A. Brzdakiewicz, G. Assanto, Opt. Lett. **27**, 1460–1462 (2002)
27. M. Peccianti, C. Conti, G. Assanto, A. De Luca, C, Umeton, Appl. Phys. Lett. **81**, 3335–3337 (2002)
28. G. Assanto, M. Peccianti, K. A. Brzdakiewicz, A. De Luca, C. Umeton, J. Nonl. Opt. Phys. Mat. **12**, 123–134 (2003)
29. A. Fratalocchi, M. Peccianti, C. Conti, G. Assanto, Mol. Cryst. Liq. Cryst. **421**, 197–207 (2004)
30. A. Fratalocchi, A. Piccardi, M. Peccianti, G. Assanto, Opt. Lett. **32**, 1447–1449 (2007)
31. A. Fratalocchi, A. Piccardi, M. Peccianti, G. Assanto, Phys. Rev. A **75**, 063835 (2007)

32. G. Assanto, N. F. Smyth, A. L. Worthy, Phys. Rev. A **78**, 013832 (2008)
33. M. Peccianti, C. Conti, G. Assanto, Opt. Lett. **28**, 2231–2233 (2003)
34. G. Assanto, M. Peccianti, C. Conti, IEEE J. Sel. Top. Quantum Electron. **10**, 862–869 (2004)
35. M. Peccianti, G. Assanto, Opt. Lett. **30**, 2290–2292 (2005)
36. G. Assanto, T. Marchant, N. Smyth, Phys. Rev. A **78**, 063808 (2008)
37. M. Peccianti, A. Fratalocchi, G. Assanto, Opt. Express **12**, 6524–6529 (2004)
38. A. Alberucci, G. Assanto, J. Opt. Soc. Am. B **24**, 2314–2320 (2007)
39. A. Alberucci, M. Peccianti, G. Assanto, Opt. Lett. **32**, 2795–2797 (2007)
40. A. Alberucci, G. Assanto, D. Buccoliero, A. S. Desyatnikov, T. R. Marchant, N. F. Smyth, Phys. Rev. A **79**, 043816 (2009)
41. M. Peccianti, C. Conti, G. Assanto, A. De Luca, C. Umeton, Nature A **432**, 733–737 (2004)
42. G. Assanto, C. Umeton, M. Peccianti, A. Alberucci, J. Nonl. Opt. Phys. Mat. **15**, 33–42 (2006)
43. M. Peccianti, A. Dyadyusha, M. Kaczmarek, G. Assanto, Nat. Phys. **2**, 737–742 (2006)
44. M. Peccianti, G. Assanto, A. Dyadyusha, M. Kaczmarek, Opt. Lett. **32**, 271–273 (2007)
45. A. Pasquazi, A. Alberucci, M. Peccianti, G. Assanto, Appl. Phys. Lett. **87**, 261104 (2005)
46. S. V. Serak, N. V. Tabiryan, M. Peccianti, G. Assanto, IEEE Photon. Techn. Lett. **18**, 1287–1289 (2006)
47. A. Piccardi, G. Assanto, L. Lucchetti, F. Simoni Appl. Phys. Lett. **93**, 171104 (2008)
48. A. Piccardi, U. Bortolozzo, S. Residori, G. Assanto, Opt. Lett. **34**, 737–739 (2009)
49. M. Peccianti, G. Assanto, Opt. Express **15**, 8021-8028 (2007)
50. M.A. Karpierz, M. Sierakowski, T.R. Wolinski, Mol. Cryst. Liq. Cryst. **375**, 313-320 (2002)
51. M.A. Karpierz, K.A. Brzdakiewicz, Q.V. Nguyen, Acta Phys. Pol. A **103**, 169-175 (2003)
52. J. Baran, Z. Raszewski, R. Dabrowski, J. Kedzierski, J. Rutkowska, Mol. Cryst. Liq. Cryst. **123**, 237-242 (1985)
53. R. Dabrowski, J. Dziaduszek, T. Szczucinski, Mol. Cryst. Liq. Cryst. **124**, 241-246 (1985)
54. K. Jaworowicz, K.A. Brzdakiewicz, M.A. Karpierz, M. Sierakowski, Mol. Cryst. Liq. Cryst. **453**, 301-307 (2006)
55. U.A. Laudyn, K. Jaworowicz, M.A. Karpierz, Mol. Cryst. Liq. Cryst. **489**, 214-221 (2008)
56. U.A. Laudyn, M. Kwasny, M.A. Karpierz, Appl. Phys. Lett. **94**, 091110 (2009)

Chapter 2
Photonic Plasma Instabilities and Soliton Turbulence in Spatially Incoherent Light

Dmitry V. Dylov and Jason W. Fleischer

Abstract We develop a plasma theory of nonlinear statistical optics. In this model, partially spatially incoherent light is treated as an ensemble of speckles which can interact through the nonlinearity. A photonic plasma frequency is defined, as is a photonic Debye length. This approach unifies previous observations using partially coherent light and predicts a new class of optical phenomena. Examples include the two-scale energy transfer common to modulation instability and the continuous excitation of modes from the gradient-driven bump-on-tail instability. The latter example, well-known from plasma physics, represents a new regime for optical experiments. We observe it here by considering the nonlinear coupling of two partially coherent beams in a self-focusing photorefractive crystal. For weak wave coupling, determined by small modal density within a Debye sphere, we observe momentum exchange with no variation in intensity. For strong wave coupling, modulations in intensity appear, as does evidence for wave (Langmuir) collapse at large scales.

To achieve a broader range of wave coupling, we consider a double bump-on-tail geometry. This system can be modeled as a pair of coupled single-hump instabilities whose interaction involves general issues of nonlinear competition, synchronization, etc. For the case of strong wave coupling, the multiple humps merge into a single-peaked profile with an algebraic k^{-2} inertial range. This self-similar spectrum, representing an ensemble of dynamically-interacting solitons atop a sea of radiation modes, is a definitive observation of soliton (Langmuir) turbulence.

Dmitry V. Dylov
Department of Electrical Engineering, Princeton University, Olden Street, Princeton, New Jersey 08544, USA, e-mail: dvd@princeton.edu

Jason W. Fleischer
Department of Electrical Engineering, Princeton University, Olden Street, Princeton, New Jersey 08544, USA, e-mail: jasonf@princeton.edu

O. Descalzi et al. (eds.), *Localized States in Physics: Solitons and Patterns*,
DOI 10.1007/978-3-642-16549-8_2,

2.1 Introduction

Dynamical instabilities occur in every nonlinear wave system. Perhaps the simplest is modulation instability (MI), in which perturbations grow at the expense of a uniform background. For example, a plane wave propagating in a self-focusing medium will break up into stripes, with a characteristic period determined by a balance between diffraction/dispersion and nonlinearity. If the background is statistical, *e.g.* thermal, then attempts at growth are de-phased by the background, and there is a nonlinear threshold for instability [1, 2, 3, 4]. Put another way, mode coupling must be sufficiently strong to generate enough correlation for unstable growth. Once instability begins, the evolution is again characterized by a direct transfer between the background and a preferred scale (this time determined by the correlation length). The resulting array of solitons is then free to interact over longer evolution times/propagation distances.

A contrasting process of energy transfer is one that occurs over a continuum of scales. This type of dynamics involves a local coupling between adjacent modes in wavenumber space, resulting in a self-similar cascade. This process gives an algebraic power spectrum and is typical of homogeneous turbulence, such as that described by Kolmogorov theory [5, 6]. It is simpler, in some senses, as dimensional analysis and scaling arguments can be used to characterize the dynamics.

The two methods of energy transfer represent complementary limits. Two-scale coupling can cascade, with higher-order effects appearing. This includes the generation of higher-order modes [7], condensation processes [8, 9, 10], and soliton clustering [11]. Likewise, local coupling can generate localized structures which can evolve dynamically [5, 12, 13]. This convergence of dynamics should not be surprising, as they are nothing but different pathways to the same asymptotic state.

Until recently [14, 15, 16, 7, 17, 18], only two-scale dynamics had been demonstrated experimentally in optics, *viz.* the snake instability in self-defocusing media [19] and modulation instability in self-focusing media [3, 4]. Here, we outline our work on instabilities which cascade modes over a range of scales. As optical turbulence is our ultimate goal, we use light that is partially spatially incoherent. Such beams can be treated as an ensemble of speckles which, in a nonlinear medium, can be considered as quasi-particles that interact through large-scale modulation waves [14]. This description gives rise to a photonic plasma interpretation. It unifies all previous observation in nonlinear statistical optics and predicts a wide range of new dynamics.

As a particular example, we consider an all-optical bump-on-tail instability. This instability, well-known in plasma physics [8, 9], is a *gradient-driven* effect which couples modes across a range of scales. We show that instability occurs whenever higher-momentum modes are more populated than lower ones, regardless of nonlinear coupling strength, and derive analytic dispersion relations for the growth rates. Experimentally, we observe the dynamics by considering the nonlinear coupling of two partially-coherent beams in a self-focusing photorefractive medium. For weak nonlinear interactions, the result is momentum (k) transfer without any observable

variation in intensity (x). For strong interactions, both x-space modulations and k-space dynamics appear.

As the dynamics evolve, the growing perturbations start to back-react on their underlying source distribution. The source intensity becomes depleted and its spectral profile is modified. For this stage, linear theory is no longer adequate. To address this, we develop a quasi-linear theory and apply it to the bump-on-tail example, showing explicitly how modes grow until there is no more driving gradient. For even stronger wave growth, wave-wave interactions become dominant. That is, the perturbed modes interact with each other, independent of the background distribution. This is a highly nonlinear state, and it is difficult to achieve experimentally with limited nonlinearity and propagation distance. To facilitate the process, we consider a double bump-on-tail geometry, so that a broader range of unstable wavenumbers can grow and interact. We show that the dynamics can be treated as a coupled pair of individual bump-on-tail instabilities. It is thus a model system which can address a variety of general issues in nonlinear dynamics, including synchronization, competition, parametric pumping, and cascades of energy and momentum transfer [20]. In our case, we show analytically and experimentally that the momentum cascade leads to an algebraic k^{-2} power spectrum. The results highlight the difficulty of synchronized wave mixing inherent in noisy nonlinear systems and demonstrate a pathway towards all-optical studies of turbulence.

2.2 Basic Theory and Formalism

Our starting equation is the nonlinear Shrödinger equation (NLS) for the slowly varying, partially coherent field packet $\psi(\boldsymbol{r},z)$, which reads

$$i\frac{\partial\psi}{\partial z}+\frac{\beta}{2}\nabla_{\boldsymbol{r}}^2\psi+\kappa G(\langle\psi^*\psi\rangle)\psi=0. \tag{2.1}$$

Here, $\boldsymbol{r}$ is a diffraction\dispersion variable, the propagation is along z and coefficient $\beta=\lambda/2\pi n_0$ is the diffraction (or second-order dispersion) coefficient for light of wavelength λ in a medium with base index of refraction n_0, κ is the nonlinear coefficient, and $G(\langle\psi^*\psi\rangle)$ is the nonlinear response function of the medium. The bracket $\langle...\rangle$ denotes statistical ensemble average; it is valid when the medium's response time is much longer than the characteristic time of the intensity fluctuations of the statistical wave packet.

2.2.1 Wigner Formalism

There are many equivalent ways to treat such partially coherent light [21]; here, we use a full wave-kinetic approach via the Wigner formalism [22, 23]. In this

method Eq. (2.1) is transformed by the Wigner function (including the Klimontovich statistical average), defined as

$$f(\boldsymbol{r},\boldsymbol{k},z) = (2\pi)^{-3}\int_{-\infty}^{+\infty} d^3\boldsymbol{\xi}\cdot e^{i\boldsymbol{k}\cdot\boldsymbol{\xi}}\left\langle \psi^*\left(\boldsymbol{r}+\frac{\boldsymbol{\xi}}{2}\right)\psi\left(\boldsymbol{r}-\frac{\boldsymbol{\xi}}{2}\right)\right\rangle. \tag{2.2}$$

Equation (2.2) satisfies the intensity relation $\langle\psi^*(\boldsymbol{r},z)\psi(\boldsymbol{r},z)\rangle = \int_{-\infty}^{+\infty} d^3\boldsymbol{k} f(\boldsymbol{r},\boldsymbol{k},z)$. Eq. (2.1) transformed by (2.2) takes the following form [22, 23, 24, 25, 14]

$$\frac{\partial f}{\partial z} + \beta\boldsymbol{k}\cdot\nabla_{\boldsymbol{r}} f + 2\kappa G\left(\langle\mid\psi\mid^2\rangle\right)\left[\sin\left(\frac{1}{2}\frac{\overleftarrow{\partial}}{\partial\boldsymbol{r}}\cdot\frac{\overrightarrow{\partial}}{\partial\boldsymbol{k}}\right)\right] f = 0, \tag{2.3}$$

where the arrows in the sine operator indicate that the spatial derivative acts on the function G (to the left) and the momentum derivative acts on the distribution f (to the right) [24, 25].

In the geometrical optics approximation (the long-wavelength limit): $\Delta\boldsymbol{k}\cdot\Delta\boldsymbol{r} \gg 2\pi$), so that Eq. (2.3) reduces to

$$\frac{\partial f}{\partial z} + \beta\boldsymbol{k}\cdot\nabla_{\boldsymbol{r}} f - \kappa\mathscr{E}(\boldsymbol{r},z)\cdot\nabla_{\boldsymbol{k}} f = 0, \tag{2.4}$$

where the self-consistent driving field $\mathscr{E}(\boldsymbol{r},z)$ is introduced as

$$\mathscr{E}(\boldsymbol{r},z) = -\nabla_{\boldsymbol{r}} G\left(\langle\mid\psi\mid^2\rangle\right). \tag{2.5}$$

Equation (2.3) is known as a Wigner-Moyal equation for the evolution of the Wigner distribution function $f(\boldsymbol{r},\boldsymbol{k},z)$. Its simplification (2.4) has a form of the Vlasov transfer equation [8, 24] or, essentially, a radiation transfer equation [26, 27, 21]. It is valid for slow (long-wavelength) variations in the refractive index when the average speckle size (correlation length l_c) of the light is smaller than the beam envelope. Note that the usual form of this short-wave–long-wave dynamics is coupled but has been reduced to a single equation by implicitly absorbing intensity fluctuations in $G\left(\langle\mid\psi\mid^2\rangle\right)$. Equation (2.4) implies the conservation of the number of optical quasi-particles in $\{\boldsymbol{r},\boldsymbol{k}\}$-space. In this chapter we will treat these quasi-particles collectively and borrow language from plasma physics. Eqs. (2.4), (2.5) then become a starting point to account for spectral dynamics of localization, oscillations and instabilities in statistical, nonlinear optics.

In plasma physics the self-consistent driving field defined in (2.5) is responsible for ponderomotive self-focusing, corresponding to the drift of electrons down a gradient in the plasma density [8, 6, 28, 29]. The corresponding nonlinear index change can be viewed as a divergence (variation) of $\mathscr{E}(\boldsymbol{r},z)$ resulting from the local intensity inhomogeneity. Mathematically we can express it in terms of the generic condition for $G(\langle\psi^*\psi\rangle)$:

$$\nabla_{\boldsymbol{r}}\cdot\mathscr{E}(\boldsymbol{r},z) = \kappa\left(\langle I_0\rangle - \int_{-\infty}^{+\infty} d^3\boldsymbol{k} f(\boldsymbol{r},\boldsymbol{k},z)\right), \tag{2.6}$$

where $\langle I_0 \rangle$ is a uniform background intensity without any variations. Equation (2.6) is a Poisson equation [8] that implies that nonlinearity acts as a uniformly distributed volumetric "charge". It is valid if the following physically sensible conditions are met: the right-hand side has to be finite, the functions G and $\mathscr{E}$ have to be spatially continuous, and the medium has to have only smooth optical inhomogeneities (if any).

2.2.2 Initial Stages of Instability. Linear Perturbation Theory

Initial stages of instabilities in nonlinear media can be studied by standard perturbation analysis. To illustrate the main points, we consider perturbations around a spatially uniform distribution $f_0(\boldsymbol{k})$:

$$f(\boldsymbol{r},\boldsymbol{k},z) = f_0(\boldsymbol{k}) + \sum_{\boldsymbol{\alpha}} \rho_{\boldsymbol{\alpha}}(\boldsymbol{k},z) e^{i\boldsymbol{\alpha}\cdot\boldsymbol{r}}, \tag{2.7}$$

with $|\,\rho_{\boldsymbol{\alpha}}\,| \ll |\,f_0\,|$ for all wavenumbers $\boldsymbol{\alpha} \neq 0$. In the unperturbed state, the nonlinear driving field (2.5) is assumed to be zero, so that $\mathscr{E}(\boldsymbol{r},z)$ can be regarded as a small quantity (weak nonlinearity). In terms of the Fourier modes,

$$\mathscr{E}(\boldsymbol{r},z) = \sum_{\boldsymbol{\alpha}} \mathscr{E}_{\boldsymbol{\alpha}}(z) e^{i\boldsymbol{\alpha}\cdot\boldsymbol{r}}. \tag{2.8}$$

Substituting (10.1) and (2.8) in Eqs. (2.4) and (2.6), noting that $\int_{-\infty}^{+\infty} d^3\boldsymbol{k} f_0(\boldsymbol{k}) = \langle I_0 \rangle$, and linearizing in the perturbations yields

$$\frac{\partial \rho_{\boldsymbol{\alpha}}}{\partial z} + i\beta\,\boldsymbol{\alpha}\cdot\boldsymbol{k}\,\rho_{\boldsymbol{\alpha}} - \kappa \mathscr{E}_{\boldsymbol{\alpha}} \cdot \nabla_{\boldsymbol{k}} f_0 = 0, \tag{2.9}$$

$$\mathscr{E}_{\boldsymbol{\alpha}} = \frac{\kappa}{\alpha^2} i\boldsymbol{\alpha} \int_{-\infty}^{+\infty} d^3\boldsymbol{k}\,\rho_{\boldsymbol{\alpha}}. \tag{2.10}$$

One can solve these equations using the Laplace transformation along the propagation coordinate ($\sim e^{gz}$). The resulting dispersion function is

$$D_{\boldsymbol{\alpha}}(g) = 1 + \frac{\kappa^2}{\alpha^2\beta} \int_{-\infty}^{+\infty} d^3\boldsymbol{k} \frac{\boldsymbol{\alpha}\cdot\nabla_{\boldsymbol{k}} f_0}{ig - \boldsymbol{\alpha}\cdot\boldsymbol{k}}. \tag{2.11}$$

The stability of the partially coherent beam in a nonlinear medium is then determined by the zeros in g of the dispersion function (2.11).

2.2.3 Growth Rate and Conditions for Weak/Strong Turbulence

For simplicity, we reduce the problem to one transverse dimension. The dispersion relation (2.11) becomes [3, 24, 30, 25, 14]

$$D_\alpha(g) = 1 + \frac{\kappa^2}{\alpha\beta}\int_{-\infty}^{+\infty} dk \frac{\partial f_0/\partial k}{ig - \alpha k}. \tag{2.12}$$

Initially, the function $D_\alpha(g)$ is defined for Re $g > 0$ and then is analytically continued into the rest of the plane. If there is a complex root $g(\alpha) = g_R(\alpha) - ig_I(\alpha)$ of $D_\alpha(g) = 0$, and $g_R(\alpha) > 0$, then any intensity perturbation will grow exponentially (instability).

A Lorentzian distribution $f_0(k) = (I_0 \Delta k/\pi)/\left(k^2 + \Delta k^2\right)$ plugged into Eq. (2.12) allows an exact solution to the growth rate:

$$\frac{g}{\beta\alpha^2} = -\Delta k + \frac{\alpha}{2}\sqrt{\frac{4\kappa I_0}{\beta\alpha^2} - 1}, \tag{2.13}$$

where $\Delta k = 2\pi/l_c$ represents the spectral spread for a beam with correlation length l_c. This gain coefficient, similar to that originally derived in Ref. [3], separates the effects of nonlinearity and statistics and shows a clear threshold value for the development of perturbations. As in plasma physics [1, 2], modulations will not appear unless the nonlinearity Δn is greater than the angular spread (effective temperature) $(\Delta k/k_0)^2$. Below threshold, modulations are suppressed, a de-phasing which Fedele and Anderson *et al.* interpreted as a type of Landau damping due to the monotonically-decreasing distribution f_0 [30, 24, 25]. However, they did not identify plasma-like parameters or consider the potential for inverse Landau damping (wave growth) when the distribution is non-monotonic.

To treat the gradient-driven dynamics at initial stages of instability, we consider first weak growth ($|g_R| \ll |g_I|$) in the long-wavelength limit ($|ig| \gg \alpha k$). Expanding the denominator in Eq. (2.12) then gives

$$\frac{g^2}{\beta\alpha^2} \approx \kappa \int_{-\infty}^{+\infty} dk\, f_0(k) \left[1 + 3\left(\frac{\alpha\beta}{g}\right)^2 k^2\right]. \tag{2.14}$$

To be consistent with the quasi-thermal light used in the experiment [31], we consider a Gaussian beam profile (the detailed difference between this distribution and a Lorentzian will be addressed in Section 2.4 below):

$$f_0(k) = \frac{I_0}{\sqrt{2\pi}\,\Delta k}\exp\left(-\frac{k^2}{2\Delta k^2}\right). \tag{2.15}$$

Note that a Lorentzian distribution will give the same results below, though more care is needed to handle the divergence of $\langle k^2\rangle$ in Eq. (2.14). The form (2.15) of the intensity is more true to the plasma mapping [18], in which the underlying

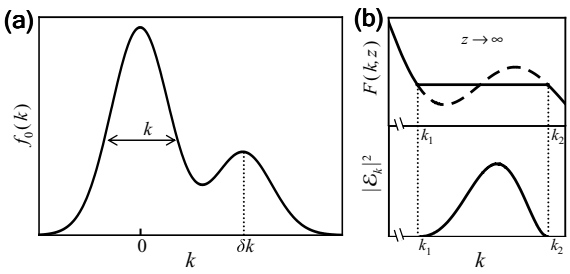

Fig. 2.1 Quasi-thermal unstable light. (a) Typical double-hump distribution in k-space for BOT instability. (b) Asymptotic quasi-linear plateau and corresponding spectral energy density in the unstable region $k_1 \le k \le k_2$.

distribution is Maxwell-Boltzmann. We note, however, that there is no true equilibrium distribution in the optical system, as there are no collisions available for relaxation [32]. Put another way, the dynamical system (2.4) conserves entropy, so that there are many possible steady-state profiles with which to start.

Explicitly accounting for the principal value and pole in Eq. (2.14) gives

$$g(\alpha) = ig_p\left(1+\frac{3}{2}\alpha^2\lambda_D^2\right) + \frac{\pi}{2}\kappa\alpha\sqrt{\frac{\kappa I_0}{\beta}}\left(\frac{\partial f_0}{\partial k}\right)\Bigg|_{k=g_p/\alpha\beta}, \tag{2.16}$$

where g_p is an effective plasma frequency and λ_D is an effective Debye length, with $\alpha\lambda_D \ll 1$. These parameters are

$$g_p = \sqrt{\frac{\kappa I_0}{\beta}}\,, \qquad \lambda_D = \frac{\beta\Delta k}{g_p}\,. \tag{2.17}$$

The first term in Eq. (2.17) is a Bohm-Gross dispersion relation [8] for nonlinear statistical light, showing that optical speckles can interact via Langmuir-type waves [14, 18]. Growth or damping of these waves is a resonant process that depends on the relative (spatial) phase velocity of the underlying quasi-particles (speckles). From the second term in Eq. (2.16), it is clear that there are no growing modes if $\partial f_0/\partial k < 0$, *e.g.*, for a quasi-thermal Gaussian distribution, since on average more quasi-particles travel slower than the interaction wave than faster. However, the weak limit used to derive (2.16) breaks down when $\alpha\lambda_D \approx 1$, or $\kappa I_0 \approx \beta\langle\Delta k^2\rangle$; in this case case, the growth rate exceeds the rate of statistical dephasing (spectral bandwidth) of the background, causing intensity modulations to appear [1, 9]. Interestingly, this strong-coupling condition becomes the instability threshold reported earlier in [3].

Not considered before, however, was the possibility for optical instability by inverse Landau damping when $\partial f_0/\partial k > 0$ (see Fig. 2.1(a) for a typical distribution). A prime example is the "bump-on-tail" (BOT) instability, well-known from plasma physics [8], in which a non-equilibrium hump is added to one side of an equilibrium distribution. To our knowledge, the BOT instability has never before been demonstrated outside of a plasma context. However, it should be clear from the above

derivation that BOT dynamics should occur in any wave-kinetic system, including hydrodynamics [33], optics, and (potentially) Bose-Einstein condensates.

The dynamics within this photonic plasma depend on the spectral density of perturbation modes within a Debye sphere. For the weak-coupling regime considered above, defined by $\alpha\lambda_D \ll 1$ [1, 9, 3], the BOT instability is mostly a momentum-space effect [14]. Above this threshold, intensity modulations appear [1, 34, 3, 4], wave-wave coupling (*vs.* wave-speckle coupling) becomes dominant [14, 10, 9], and the perturbation method ceases to apply. Adopting plasma language, we define these two limits as regimes of *weak* and *strong* optical Langmuir turbulence [15].

2.2.4 Debye Scaling

In all previous work, the statistics of the input beam and the nonlinearity of the medium have been considered separate parameters, as they are controlled separately in the experiments. However, Eq. (2.16) shows that they are joined in the composite parameter of the photonic Debye length λ_D. As in material plasma, λ_D signifies the amount of interaction wave inhibition (screening) due to the random de-phasing of waves [14].

The photonic Debye length provides a natural length scale for highly incoherent beams, *i.e.* beam for which the correlation length is significantly less than the beam width ($l_c \ll w_0$). For example, narrow (Gaussian) beams that linearly expand as $(w(z)/w_0)^2 = 1+\bar{z}^2$, where $\bar{z} = z/L_D$ is the propagation distance measured in terms of the linear diffraction length L_D, evolve nonlinearly as

$$\left(\frac{w(z)}{w_0}\right)^2 = 1+\bar{z}^2\left(1-\bar{\lambda}_D^2\right), \tag{2.18}$$

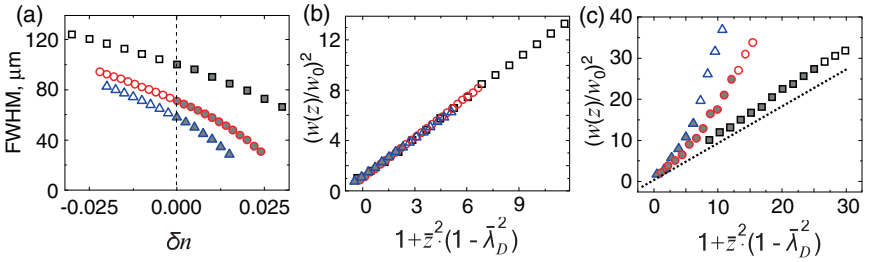

Fig. 2.2 Numerical and eperimental results for the nonlinear diffraction of a spatially incoherent beam. (a) Plot of full-width half-maximum versus δn at a fixed propagation distance $z = 1cm$. (b) Plot of simulation results in (a) using scaling from Eq. (2.18); (c) Experimental results measured after propagation in a photorefractive crystal. The dashed line represents the highly-incoherent limit of Eq. (2.18).

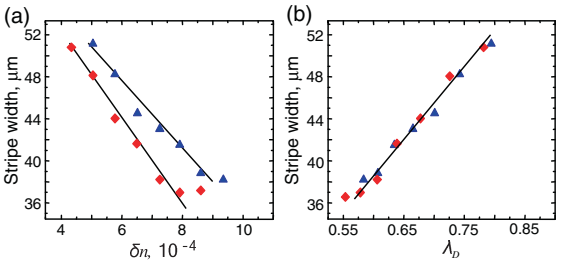

Fig. 2.3 Period of MI pattern ("stripe width") as a function of (a) nonlinearity and (b) Debye length. Data for two correlation lengths of $80\mu m$ (triangles) and $92\mu m$ (rhombus) are shown. Notice the collapse of data after Debye scaling.

where $\overline{\lambda}_D$ is the Debye length normalized to the nonlinear length that characterizes a coherent soliton [35]. Numerical and experimental verification of this formula, for nonlinearities below the soliton limit, are shown in Fig. 2.2.

Technically, the plasma formula (2.16) is only valid for weak perturbations, for which $|g_R| \ll |g_I|$. On the other hand, it is reasonable to use the Langmuir modes from this theory as a basis for further interactions when the nonlinearity is increased [12, 13]. This suggests that the Debye length remains a valid scaling parameter. As shown in Fig. 2.3 for the case of incoherent modulation instability, this is indeed the case.

Finally, these results can be generalized to more complex cases. For example, multiple-stream geometries in k-space can be represented in terms of Gaussian multi-hump distribution, with the "humps" positioned at different spatial frequencies (angular separations) δk_{01}, δk_{12}, δk_{23},...,$\delta k_{M-1\,M}$:

$$f_0(k) = \frac{1}{\sqrt{2\pi}\,\Delta k}\left[I_0 e^{-\frac{k^2}{2\Delta k^2}} + \sum_{j=1}^{M} I_j \mathrm{e}^{-\frac{(k-\delta k_{j-1\,j})^2}{2\Delta k^2}}\right], \tag{2.19}$$

then the system's dynamics would still be described simply by Eq. (2.16), but with the Debye length scaled as [15]

$$\tilde{\lambda}_D = \sqrt{\frac{\beta^3}{\kappa}\left(\frac{\Delta k^2}{I_{tot}} + \sum_{j=1}^{M}\frac{\delta k_{j-1\,j}^2}{I_j}\right)}. \tag{2.20}$$

Note that due to the redistribution and reshaping of the total intensity $I_{tot} = \sum_j I_j$, the threshold for the appearance of intensity modulations will shift as well.

2.3 Quasi-Linear Approximation

It was mentioned in the Section 2.2.4 that after the initial steps of instability, linear perturbation theory ceases to be valid [14, 36, 37]. The reason is that the shape of distribution function changes with time, due to energy depletion and back-reaction by the perturbations. In this section we will treat such dynamics as time-dependent

(or, more rigorously, z-dependent), which means that it is necessary to consider evolution of perturbations as well.

2.3.1 General Derivation

We proceed by returning to the one-dimensional case of Eq. (2.4). Using the Fourier decompositions (10.1) and (2.8), we rewrite (2.10) as

$$\frac{\partial \rho_\alpha(k,z)}{\partial z} + i\beta\alpha k\rho_\alpha(k,z) - \kappa\mathscr{E}_\alpha(z)\frac{\partial(f_0(k)+\rho_0(k,z))}{\partial k} = 0, \tag{2.21}$$

where we neglected the wave-wave interaction term $\sum_{\alpha'\neq 0}\mathscr{E}_{\alpha-\alpha'}\partial_k\rho_{\alpha'}$ and took only first term ρ_0 to account for z-dependence of Wigner distribution function. We assume that ρ_0 is a slowly varying function of z, while f_0 is a distribution giving rise to a weak instability (like in the double-hump case of Fig. 2.1(a)). The rate of change of ρ_0 is given by

$$\frac{\partial \rho_0}{\partial z} = \sum_\alpha \mathscr{E}_{-\alpha}\frac{\partial \rho_\alpha}{\partial k}. \tag{2.22}$$

Now assume that ρ_α and $\mathscr{E}_\alpha$ have the following form:

$$\begin{aligned}\rho_\alpha(k,z) &= \hat{\rho}_\alpha(k)\exp\left(\int^z d\zeta[g_R(\zeta) - ig_I(\zeta)]\right),\\ \mathscr{E}_\alpha(z) &= \hat{\mathscr{E}}_\alpha\exp\left(\int^z d\zeta[g_R(\zeta) - ig_I(\zeta)]\right).\end{aligned} \tag{2.23}$$

The solution to (2.21) is then

$$\rho_\alpha = \frac{i\kappa}{\beta}\mathscr{E}_\alpha\frac{\partial/\partial k(f_0+\rho_0)}{ig_R + g_I - \alpha k}, \tag{2.24}$$

This result can be plugged into Poisson's equation, and analogous calculations of the dispersion relation and growth rate yield:

$$D_\alpha(g) = 1 + \frac{\kappa^2}{\alpha\beta}\int_{-\infty}^{+\infty} dk\frac{\partial/\partial k(f_0+\rho_0)}{ig_R + g_I - \alpha k}, \tag{2.25}$$

$$g_R = \frac{\pi}{2}\kappa\alpha\sqrt{\frac{\kappa I_0}{\beta}}\left(\frac{\partial\,(f_0+\rho_0)}{\partial k}\right)\Bigg|_{k=g_p/\alpha\beta}. \tag{2.26}$$

Notice that g_R became a slowly varying function of z through ρ_0. The long-term processes can be studied now by examining the long-term behavior of ρ_0. For this we substitute Eq. (2.24) into Eq. (2.22), which gives

$$\frac{\partial \rho_0}{\partial z} = \frac{\kappa^2}{\beta^2} \sum_\alpha |\mathscr{E}_\alpha|^2 \frac{\partial}{\partial k} \left[\frac{g_R}{(g_I - \alpha k)^2 + g_R^2} \frac{\partial F}{\partial k} \right], \tag{2.27}$$

where we used $\mathscr{E}_\alpha = \mathscr{E}_{-\alpha}$, and $F(k,z) \equiv f_0(k) + \rho_0(k,z)$. Note that Eq. (2.27) has the form of a diffusion equation. Turning from sums to continuous integrals and using (2.23) we get

$$\frac{\partial F}{\partial z} = \frac{\partial}{\partial k} \left(D_k \frac{\partial F}{\partial k} \right), \tag{2.28}$$

$$\frac{\partial |\mathscr{E}_\alpha|^2}{\partial z} = 2 g_R |\mathscr{E}_\alpha|^2, \tag{2.29}$$

where the k-space diffusion function is defined as

$$D_k = \frac{\kappa^2}{\beta^2} \int_{-\infty}^{+\infty} d\alpha |\mathscr{E}_\alpha|^2 \frac{g_R}{(g_I - \alpha k)^2 + g_R^2}. \tag{2.30}$$

Eqs. (2.28) and (2.29) are the basic equations of quasi-linear theory for statistical light. They govern the rate of change of the distribution F and spectral energy density $|\mathscr{E}_\alpha|^2$ as the light propagates in a moderately nonlinear medium.

2.3.2 Bump-on-Tail Dynamics

We now apply the quasi-linear formalism to the bump-on-tail instability shown in Fig. 2.1. Previously thought to exist only in plasma, the bump-on-tail (BOT) instability is a gradient-driven effect in which a non-equilibrium bump on the tail of a thermal distribution acts as a source of free energy [8]. As such, it requires an inverted population of statistical modes and is often considered a type of classical lasing [38]. In plasma, the effect occurs when a gas of charged particles interact through electrostatic, or Langmuir, waves. Recently, we showed that the same phenomenon could occur in the nonlinear propagation of statistical light, in which an ensemble of speckles interact through large-scale modulation waves [14].

The initial distribution may be written as

$$f_0(k) = \frac{I_0}{\sqrt{2\pi}\,\Delta k} \exp\left(-\frac{k^2}{2\Delta k^2} \right) + \frac{I_1}{\sqrt{2\pi}\,\Delta k} \exp\left(-\frac{(k-\delta k)^2}{2\Delta k^2} \right), \tag{2.31}$$

with $I_1 < I_0$ and $\delta k \geq \Delta k$. Theoretically, initial stages of BOT instability can be fully described by (2.16), with

$$g_p = \sqrt{\frac{\kappa(I_0 + I_1)}{\beta}}\ ,\ \lambda_D = \sqrt{\frac{\beta^3}{\kappa} \left(\frac{\Delta k^2}{I_0 + I_1} + \frac{\delta k^2}{I_1} \right)}\ . \tag{2.32}$$

This linearized theory, however, says nothing about the progression of the distribution after some distance of propagation, such as saturation (stabilization) of continued instability; it merely provides wavenumbers of unstable modes between the beams. The deficiency of standard linearized theory is that it considers $f_0(k)$ z-independent, which is no longer valid as the dynamics evolve.

Recalling that $|g_R| \ll |g_I|$, the fraction in the diffusion function (2.30) can be approximated as $\sim \pi\delta(g_I - \alpha k)$, yielding

$$\frac{\partial F}{\partial z} = \frac{\kappa^2}{\beta^2}\frac{\partial}{\partial k}\left[\frac{1}{|k|}|\mathscr{E}_k|^2\frac{\partial F}{\partial k}\right]. \tag{2.33}$$

The asymptotic state of the instability can be found by considering the change of the corresponding power spectrum $W(z) = 1/2\int dkF^2(k,z)$. Using (2.33), we have

$$\frac{\partial W}{\partial z} = \int_{-\infty}^{+\infty} dkF\frac{\partial F}{\partial z} = -\frac{\kappa^2}{\beta^2}\int_{-\infty}^{+\infty} dk\frac{1}{|k|}|\mathscr{E}_k|^2\left(\frac{\partial F}{\partial k}\right)^2. \tag{2.34}$$

Each term in the last integrand is positive, which means that W will decrease until either $|\mathscr{E}_k|^2 = 0$, or $\partial F/\partial k = 0$ for each value of k. The initial growth of modes is described by (2.16) and (2.32), and since $|\mathscr{E}_k|^2$ grows in the region between the two beams, the distribution function should flatten out so that there is no driving gradient $\partial F/\partial k$ (Fig. 2.1(b)). This "quasi-linear plateau" has been observed in recent experiments [14, 15] (to be discussed in Section 2.5).

Lastly, using (2.16), (2.32), and (2.33) and neglecting $\partial|\mathscr{E}_k|^2/\partial k$ at $z = 0$, we can calculate the asymptotic values of $|\mathscr{E}_k|^2$ and F as

$$|\mathscr{E}_k|^2\Big|_{z=\infty} = \frac{\pi\beta}{g_p}k^3\int_{k_1}^{k} dk[F(k,\infty) - f_0(k)], \tag{2.35}$$

$$F(k,\infty) = \frac{1}{k_2 - k_1}\int_{k_1}^{k_2} dkf_0(k), \tag{2.36}$$

where k_1 and k_2 are the k-vectors of the unstable region, $k_1 \le k \le k_2$, in which the plateau is established (see Fig. 2.1(b)). Expressions (2.35) and (2.36) provide the the effective overall gain of the flattening and the hight of the resulting plateau.

2.4 Numerical Analysis

2.4.1 Numerical Results for BOT Instability

To check the validity of the Quasi-Linear Approximation and Eqs. (2.35), (2.36), we have carried out numerical simulations of Eq. (2.4) and (2.5) for the case of a Kerr medium (Fig. 2.4). The bump-on-tail configuration was created by launching two partially incoherent beams of fixed spectral width $\Delta k/k_0 = 1.7 \times 10^{-3}$ at a

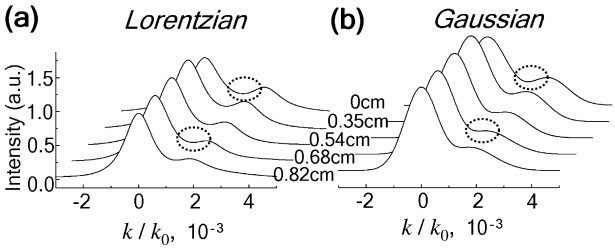

Fig. 2.4 Simulation of bump-on-tail propagation in a nonlinear Kerr-like medium. Shown are double-hump spectra for (a) Lorentzian and (b) Gaussian distributions. The total intensity and nonlinearity are kept constant ($\Delta n/n_0 = 1.74 \times 10^{-4}$) and only the shape of the statistics differs. Dashed circles highlight the initial driving gradient and formation of the quasilinear plateau, which occurs quicker in the Gaussian case.

relative angles $\delta k/k_0 = 2.0 \times 10^{-3}$. Comparisons between Lorentzian and Gaussian profiles for the distribution $f_0(k)$, at fixed total intensity $\langle I_0 \rangle$, show that the Gaussian distribution triggers the unstable dynamics faster. More details of this momentum transfer will be discussed in Section 2.5.

2.4.2 Numerical Results for Multiple BOT Instability

Figure 2.5 shows numerical simulation of the dynamics and the corresponding gain curves calculated from Eqs. (2.16) and (2.20) when three beams are launched into the medium (multiple bump-on-tail instability). As expected, modes grow in the regions of positive spectral slope until there is no more driving gradient. We find that the system is described effectively as a pair of coupled BOT instabilities: one

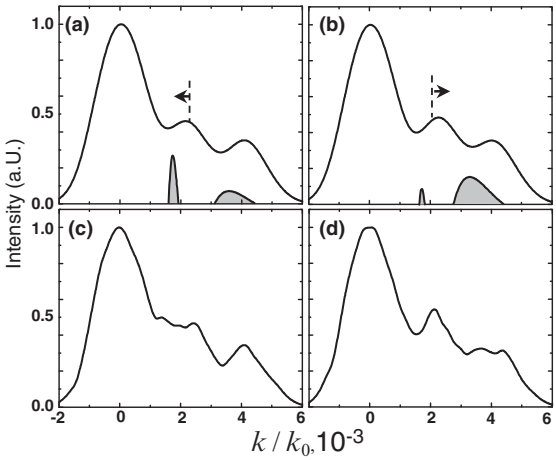

Fig. 2.5 Numerical simulation of multiple bump-on-tail instability. (a,b) Input profiles, with corresponding gain curves (shaded graphs at baseline), with the middle hump shifted (a) to the left of the equal gain value and (b) to the right. (c,d) Output pictures after $1cm$ of propagation ($\Delta n/n_0 = 1.74 \times 10^{-4}$).

on the left and one on the right, with negligible coupling between the leftmost and rightmost Gaussians due to their separation distance [15]. In this case, competition between the gain curves implies that plateau formation happens sequentially, even though the initial slopes and nonlinearity in the two regions are identical. If the middle hump is closer to the left (main) distribution, then the left region goes unstable first, and vice versa with a right bias (Figs. 2.5(c,d)). The balanced situation, with the central hump equidistant from either side, has gain curves of the same peak value and is unstable. In simulations, this initial condition always degenerated into one of the two asymmetric scenarios, a result supported by analytic perturbations of δk_{01} in Eq. (2.16).

2.5 Experimental Observation

2.5.1 Experimental Setup

Experimentally, we explore the bump-on-tail dynamics by considering the nonlinear interaction of two partially-coherent spatial beams. The setup is shown in Fig. 2.6. A statistical light input is created by focusing light from a 532*nm* CW laser onto a ground-glass diffuser and then imaging into a photorefractive SBN:60 ($Sr_{0.6}Ba_{0.4}Nb_2O_6$) crystal [31]. The correlation length, and correspondingly the spectral bandwidth, can be changed by varying the magnification properties of the imaging lens. To create a bump-on-tail or a double bump-on-tail distribution (Fig. 2.6, inset), the spatially-incoherent beam is split (one or more times) using a Mach-Zehnder interferometer, attenuated in the bump arm(s), and then recombined on the input face of the crystal.

For SBN, the nonlinear index change $\Delta n = \gamma E_{app}\langle I\rangle/(1+\langle I\rangle)$, where E_{app} is an electric field applied across the crystalline c-axis and $\gamma = n_0 r_{33}(1+\langle I_0\rangle)$ is a constant depending on the base index of refraction n_0, the electro-optic coefficient r_{33},

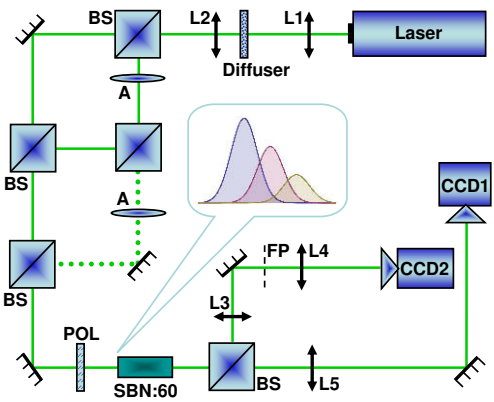

Fig. 2.6 Experimental Setup. 532*nm* laser light is made partially spatially incoherent by a ground-glass diffuser and separated into a superposition of two or three beams (for three, a dot-lined interferometer arm is added). A, attenuator; M, mirror; L, lens; BS, beam-splitter; POL, linear polarizer; SBN:60, nonlinear photorefractive crystal; FP, focal Fourier plane of the lens L3; CCD, digital detector.

and the spatially-homogeneous incident light intensity $\langle I_0 \rangle$ [27]. In the experiments, the beams have a relative angle of 0.3° (between any adjacent two beams), the intensity ratio is fixed at 3:2, and the strength of the nonlinearity (wave coupling) is controlled by varying the applied voltage (similar results occur at other angles and intensities). To observe the interaction, light exiting the crystal is directly imaged in both position (x) space and momentum (k) space, the latter by performing an optical Fourier transform.

For comparison and calibration, we performed a single-beam MI experiment with the main $\langle k \rangle = 0$ hump (not shown). In this case, the background distribution is Gaussian with a correlation length $l_c = 176\mu m$, and no intensity modulations appeared until the voltage reached $0.9kV$. Using $n_0 = 2.3$ and $r_{33} = 255pm/V$, this corresponds to a nonlinear index change of $\Delta n = 8 \times 10^{-4}$. Above this threshold, two symmetric momentum peaks appear at $k/k_0 = \pm 5.6 \times 10^{-3}$. This is the same behavior as in [4] but quantitatively calibrated to our initial input conditions and particular crystal.

2.5.2 Single Bump-on-Tail Instability

All-optical examples of a wave-kinetic bump-on-tail instability are shown in Figs. 2.7, 2.8 and 2.9. Figs. 2.7(a-f) show the behavior for weak interaction. In this case, the photorefractive nonlinearity is turned on by applying a $0.7kV$ voltage bias across the crystal, below the $0.9kV$ bias necessary to trigger single-beam MI. As shown in Figs. 2.7(c,f), nonlinear modes are excited precisely in the expected region of positive slope, growing until there is no more driving gradient (a process known as quasilinear flattening, see Section 2.3). Remarkably, the momentum-space distribution is changed [Figs. 2.7(e,f)] while the position-space intensity shows no observable variations [Fig. 2.7(d)].

The nature of the instability depends on the spectral geometry of the system. For a single-humped distribution [3], or one with widely-separated peaks [39], strong nonlinearity is required to see any significant dynamics. Here, the spectral peaks overlap, giving an unstable condition with $|g_R| \ll |g_I|$. The resulting momentum exchange, along with the resonance from Eq. (2.11), suggests that there is an underlying phase matching among the modes. Indeed, recent work with incoherent light in a medium with instantaneous (vs. inertial) nonlinearity shows an analogous velocity locking [40]. This demonstration, combined with similar momentum exchange observed in collisions of coherent vector solitons [41, 42], implies that the BOT dynamics should occur for true Kerr media as well. In the incoherent case considered here, the dynamics depends on the statistics of the interacting beams (Fig. 2.8). Local correlation measurements can reveal details of the speckle-wave coupling, but a simpler measure can be obtained from the visibility

$$\nu = (f(k_1) - f(k_{01}))/(f(k_1) + f(k_{01}))$$

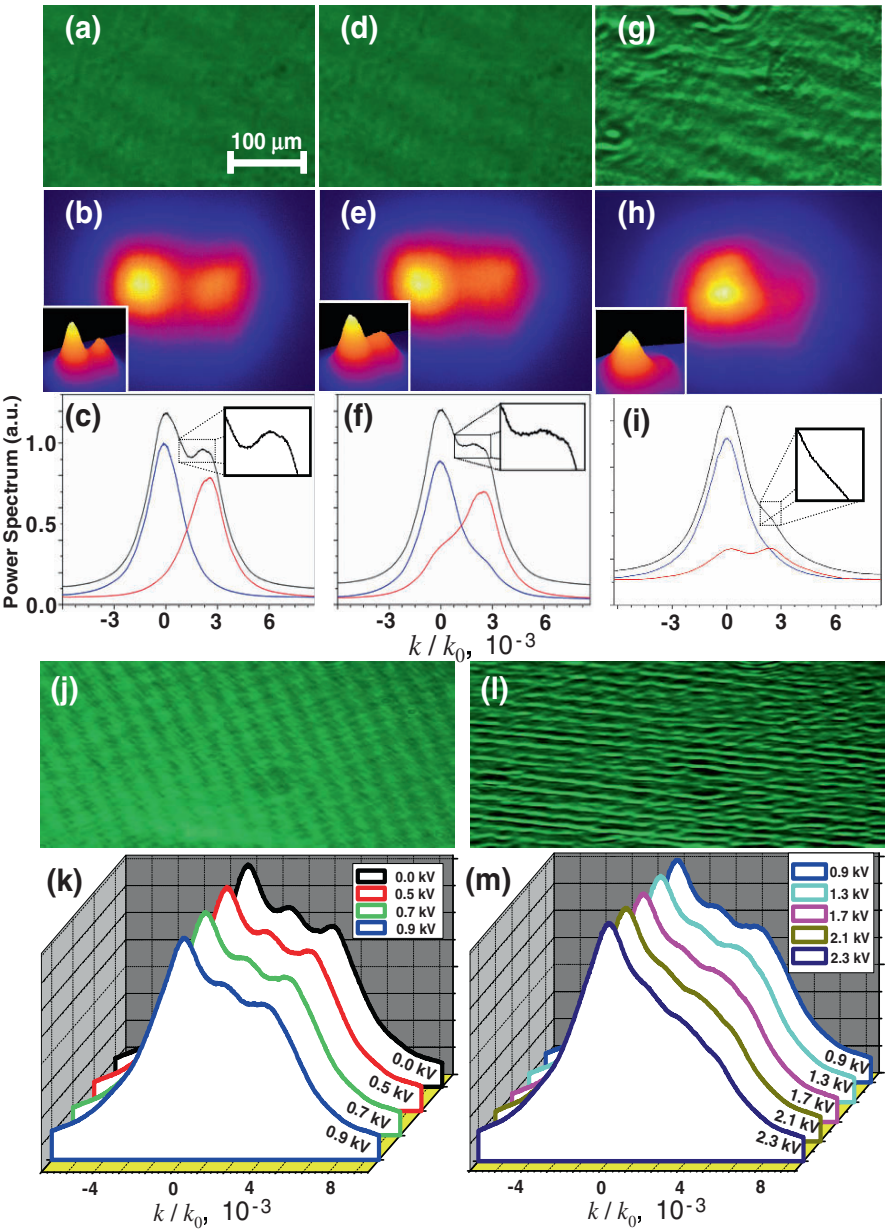

Fig. 2.7 Experimental output pictures of bump-on-tail and double bump-on-tail instability. (a,d,g,j,l) Intensity in position (x) space; (b,c,e,f,h,i,k,m) power spectrum in momentum (k) space. (a,b,c): crystals exit face after linear propagation of double-hump distribution (no applied voltage); (d,e,f): same, but nonlinear propagation (applied voltage of $0.7kV$, in the weak-coupling regime); (g,h,i) same, but in the strong-coupling regime ($1.6kV$). The blue and red curves in (c,f,i) show holographic readouts of single-beam propagation for the straight (blue) and angled (red) distributions, respectively. (j,k) Weak-coupling regime when the distribution is triple-humped. (l,m) Same, but in strong-coupling regime.

of the angled hump, as shown in Fig. 2.8(d). The efficiency of the flattening depends on the relative gain $|g_R|$ of the unstable modes. Using

$$\eta = (f_{NL}(k_{01}) - f_{Lin}(k_{01}))/(f_{NL}(k_0)) + f_{Lin}(k_0))$$

as a measure of efficiency, Fig. 2.8(e) shows interaction behavior that is relatively insensitive to nonlinear coupling strength but highly sensitive to beam statistics [14]. If the beam is too incoherent, then attempts at spectral energy transfer are de-phased. If the beam is too coherent, then the system loses its statistical nature (and thus its wave-kinetic properties). More rigorously, the first condition states that the angular separation between the beams must be greater than the spectral width of the distribution, while the second condition states that if the relative bandwidth is too small, then there are too few quasi-particles (speckles) in resonance with the growing waves [8, 9]. As a result, there is an optimal correlation length, for a given intensity ratio and angle given by $\partial g_R/\partial k = 0$, for efficient dynamical coupling.

For stronger nonlinearity, the system enters a regime of strong wave coupling, significantly distorting the original distribution in k-space and creating modulations in x-space (Figs. 2.7(g-i)). These modulations are different from those arising from MI, however, as the spectrum in Figs. 2.7(h,i) shows a range of modal excitation (between the original humps), rather than the symmetric high-k side lobes charac-

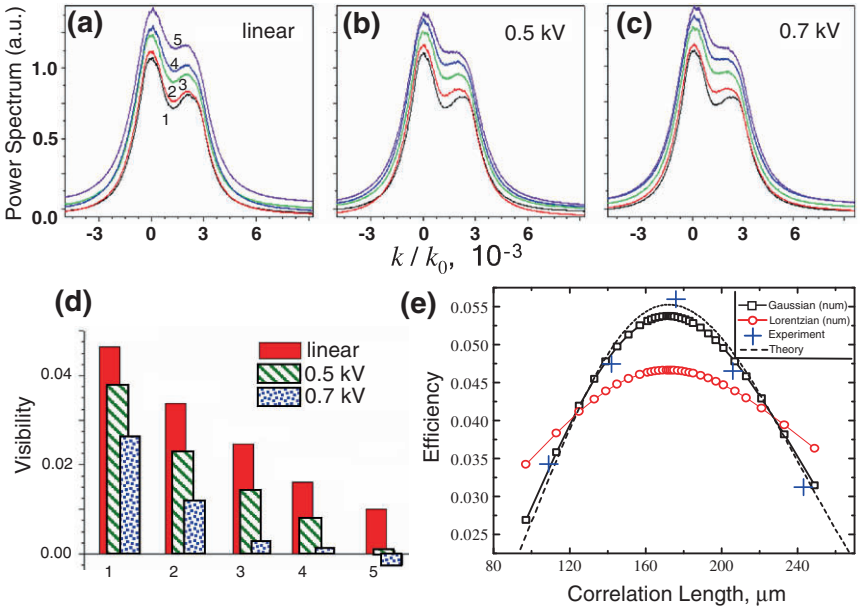

Fig. 2.8 Dynamical coupling as a function of correlation length and nonlinearity. (a-c) Power spectra at $0kV$ (linear), $0.5kV$ and $0.7kV$, respectively. (d) Visibility of the angled hump. (e) "Efficiency" of nonlinear flattening. Curves and bars in (a-d) are numbered for correlation lengths of $243\mu m$ (1), $206\mu m$ (2), $176\mu m$ (3), $142\mu m$ (4), and $109\mu m$ (5). Note the dependence of efficiency on the underlying distribution.

teristic of MI (*e.g.* [3, 43]). Using our reference correlation length $l_c = 176\mu m$, as in Fig. 2.7(a-f), we observe that the required nonlinearity for modulations is $1.1kV$, stronger than the one needed for single-beam MI. That is, the presence of a second statistical beam further suppresses the growth of modulations. Moreover, the appearance of modulations coincides with a breakdown of the quasilinear plateau and a resumption of wave growth in the unstable, non-equilibrium region [Fig. 2.7(i)].

The higher threshold can be understood by returning to the strong-coupling condition $\kappa I_0 \approx \beta\langle\Delta k^2\rangle$ obtained in Section 2.2. It is clear that for a given spectral width, additional intensity lowers the required value of κ for instability [3, 44]. However, the presence of a second beam increases the effective bandwidth due to cross-beam interaction, potentially requiring a higher value of κ. A simple estimate can be obtained by considering the variance of two Gaussian beams $\exp\left(-k^2/\Delta k^2\right) + A\exp\left(-(k-\delta k)^2/\Delta k^2\right)$, which is $\Delta k^2 + \delta k^2 A/(1+A)^2$. For $A = 2/3$ and $\delta k \sim \Delta k$, as in the experiments, there is an *increase* in threshold nonlinearity from κ to $(31/25)\kappa$. Given the measured single-beam MI threshold of $0.9kV$, the predicted double-beam threshold of $1.12kV$ matches the observed value.

2.5.3 Holographic Readout of Dynamics

The different behaviors above and below the modulation threshold are the result of different nonlinear dynamics within the initial distribution. Experimentally, we can observe this by taking advantage of the slow photorefractive response time of SBN and recording a volume hologram of the interactions. Subsequently, we can block one of the beams and use the other as a probe of the coupling, observing the energy transfer that would have happened if the other beam were present [41]. These holographic reconstructions are shown in Figs. 2.7(c,f,i). For linear propagation [Fig. 2.7(c)], each beam maintains its Gaussian form, as there is no nonlinear intensity interaction to induce an index change. By contrast, there are significant changes in the nonlinear cases. For weak coupling [Fig. 2.7(f)], light originally in the perturbative bump (shown in red) is seen to flow towards lower momentum states, while light from the equilibrium distribution (shown in blue) scatters in the opposite direction. For strong coupling [Fig. 2.7(i)], the momentum transfer is *asymmetric*. The thermal light is unchanged, while the non-thermal distribution looks *bimodal*, with half the intensity in the original angled hump and half centered at $\langle k\rangle = 0$, beyond the initial instability range of positive slope.

At this point, it is useful to revisit the plasma correspondence and interpret the scattering dynamics from a quasi-particle (speckle) perspective. From this viewpoint, the instability mechanism is essentially a resonant process, in which small-scale wavepackets generate and interact with large-scale modulations [41, 14]. The coupling threshold $\alpha\lambda_D \approx 1$ then separates the dynamics between regimes of weak and strong spatial turbulence. Indeed, weak (quasilinear) turbulence theory in plasma is characterized by the formation of a k-space plateau and the bidirectional transfer of momentum between the thermal and non-thermal distributions

[8, 45]. In the theory of strong turbulence, the thermal, non-resonant distribution is unchanged but the resonant distribution is greatly affected by wave-wave interactions [9]. In this case, there should be a direct transfer of momentum towards large scales ($\langle k \rangle = 0$), a stimulated scattering process known as Langmuir condensation in plasma physics [9, 10]. All of this is consistent with the observations in Figs. 2.7 (f) and (i). To the authors' knowledge, these internal dynamics have not been observed in material plasma.

2.5.4 Multiple Bump-on-Tail Instability and Long-Range Turbulence Spectra

Above the threshold $\alpha\lambda_D \sim 1$, the dynamics of the single BOT instability suggested that there is a turbulent breakdown of the quasi-linear plateau over the resonant range of k-vectors. However, the wavenumber region is too small to conclude that there is a self-similar spectrum between the humps. To extend the range, we add a third hump to the system, as described in Fig. 2.6.

Experimental results for the weak-coupling case are shown in Figs. 2.7(j) and 2.7(k). The output intensity remained uniform, up to unavoidable striations in the crystal, while the energy spectrum underwent significant redistribution due mode coupling. As the nonlinear interaction strength (applied voltage) was increased, the spectral bumps were observed to flatten. In all cases, the profile flattening was sequential, with lower momenta reaching a plateau first. This observation agrees with the simulations in Fig. 2.5 and supports the general conclusion that the final state of the system depends on the temporal sequence of wave diffusion [46, 6]. To our knowledge, this is the first demonstration of a multiple bump-on-tail instability and its associated competition of growth rates. Similar behavior should occur in any wave-kinetic system obeying Eq. (2.4), such as material plasma and cold atoms at finite temperature.

More complex behavior occurs for higher nonlinearity (Figs. 2.7(l) and 2.7(m)). In the strong coupling regime [14, 15, 1, 2, 3], modulations start to appear in intensity and momentum transfer continues beyond the plateau (zero-gradient) limit (though the inertial approximation is still valid [14, 4]). As before, wave-wave coupling is the dominant process of energy/momentum exchange [10, 9, 6]. A closer examination of this spectrum, shown in Fig. 2.9, reveals a self-similar profile with a k^{-2} fall-off. This algebraic spectrum holds for the entire wavenumber range between the first and last peaks, despite the fact that the central hump provided an initial region of stability ($\partial f_0/\partial k < 0$).

The intensity waves present in the strong-coupling regime (Fig. 2.7(l)) are suggestive of solitons and, indeed, an ensemble of solitons can give the observed power spectrum [47]. For N solitons occupying a space of length L in 1D, having random phases and positions and maintaining total energy E_S, the Wigner spectrum:

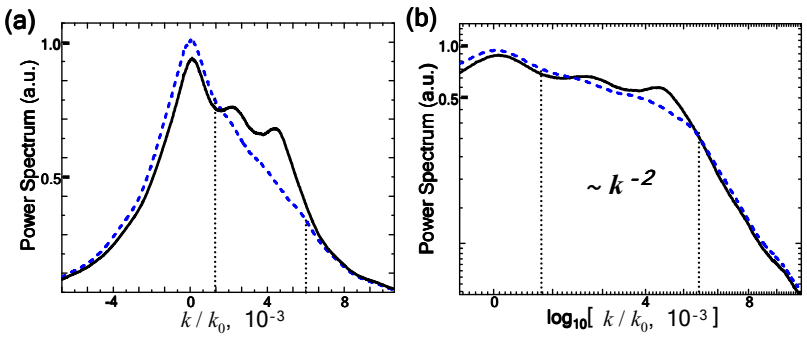

Fig. 2.9 Detailed look at the asymptotic spectral profile of the turbulent state during multiple BOT instability. (a) Comparison of input (solid) and output (dashed) profiles. (b) Comparison in log space, showing algebraic spectrum in interaction region.

$$\langle f_k \rangle \propto \frac{1}{L} \int_{N_{min}}^{N_{max}} dN\, N \wp(N) \left[\cosh(kN/E_S) \right]^{-2}, \tag{2.37}$$

where $\wp(N)$ is the probability for the system to be in the N-soliton state and $N_{min} \leq N \leq N_{max}$ due to soliton merging and turbulent redistribution. Choosing $N_{max} \sim E_S/k$ (using the condition of close packing) and replacing the $\cosh^{-2}$ term in (2.37) by a step function yields $\langle f_k \rangle \propto \frac{1}{L} \int_{N_{min}}^{E_S/k} dN\, N \wp(N)$. For the case when all states are occupied uniformly [$\wp(N)$ =const], $\langle f_k \rangle \propto k^{-2}$.

Interestingly, the equipartition spectrum k^{-2} observed experimentally in Section 2.5.4, is robust and appears in several different contexts of strong wave coupling. For example, dynamics with phase-dependent coupling — *e.g.*, four-wave mixing — can give an effective wave collision term that leads asymptotically to a k^{-2} spectrum [48, 49, 50]. For the phase-independent coupling here, the intensity-induced interactions are enough to drive the dynamics. Indeed, similar conservation arguments on the photonic plasmons (speckles), rather than number of solitons, also leads to a Rayleigh-Jeans distribution [48, 49, 50] $f_k = T/\left(k^2 - \mu\right)$, where the effective temperature $T \propto l_c^{-2}$ and the effective chemical potential μ is given by the average propagation constant (energy eigenvalue) of the waves. Note, however, that there must be a sufficient density of modes to achieve the equipartition. For example, the presence of (incoherent) solitons — *e.g.* from modulation instability — is not enough to guarantee equipartition. There must be enough interaction and propagation distance (evolution time) to go beyond soliton clustering [11] and cascade the interactions [12, 13]. Here, we encourage the wave-mixing cascade by seeding a quasi-thermal background distribution with additional non-equilibrium humps.

2.6 Discussion and Conclusions

In conclusion, we have treated the nonlinear propagation of statistical light as a photonic plasma of interacting speckles. A general Bohm-Gross dispersion relation was derived, allowing the identification of both a plasma frequency and a Debye length. These determined the nonlinear propagation constant and scale of wave dephasing, respectively. This approach unified previous observations using partially coherent light, such as nonlinear diffraction and incoherent modulation instability, and predicted a new class of optical phenomena. As representative examples, we considered single and multiple bump-on-tail instabilities. Optical methods of measurement, such as holography, allowed observation of dynamical behavior that had been predicted, but not observed, in material plasma. This included equal and opposite momentum exchange for weak nonlinear coupling and evidence for wave condensation for strong coupling. In the latter regime, wave-wave interactions caused the humped power spectrum to merge into a single-peaked profile, with an algebraic k^{-2} spectrum in the inertial range. This profile, and its associated intensity modulations, is the hallmark signature of optical Langmuir turbulence. The results extend plasma dynamics beyond their fluid context and show clearly that there is much potential for controlling correlation dynamics and optical energy distributions using plasma-type wave phenomena.

Acknowledgements We thank P.H. Diamond, C. Sun, and L.I. Dylova for very valuable discussions. This work was supported by the NSF, DOE and AFOSR.

References

1. A.A. Vedenov, L.I. Rudakov, Dokl. Akad. Nauk SSSR **159**, 767 (1964). DOI OSTI-ID-4648594
2. A.A. Vedenov, A.V. Gordeev, L.I. Rudakov, Plasma Physics **9**(6), 719 (1967). URL http://stacks.iop.org/0032-1028/9/719
3. M. Soljacic, M. Segev, T. Coskun, D.N. Christodoulides, A. Vishwanath, Phys. Rev. Lett. **84**(3), 467 (2000). DOI 10.1103/PhysRevLett.84.467
4. D. Kip, M. Soljacic, M. Segev, E. Eugenieva, D.N. Christodoulides, Science **290**(5491), 495 (2000). DOI 10.1126/science.290.5491.495. URL http://www.sciencemag.org/cgi/content/abstract/290/5491/495
5. U. Frisch, *Turbulence: The Legacy of A.N. Kolmogorov* (Cambridge University Press, Cambridge, 1995)
6. B.B. Kadomtsev, *Plasma Turbulence*, vol. 1 (Academic Press, London, New York, 1965)
7. S. Jia, W. Wan, J.W. Fleischer, Opt. Lett. **32**(12), 1668 (2007). URL http://ol.osa.org/abstract.cfm?URI=ol-32-12-1668
8. N.A. Krall, A.W. Trivelpiece, *Principles of Plasma Physics* (McGraw-Hill, New York, 1973, 1973)
9. M.V. Goldman, Rev. Mod. Phys. **56**(4), 709 (1984). DOI 10.1103/RevModPhys.56.709
10. P.A. Robinson, Rev. Mod. Phys. **69**(2), 507 (1997). DOI 10.1103/RevModPhys.69.507
11. Z. Chen, S.M. Sears, H. Martin, D.N. Christodoulides, M. Segev, Proceedings of the National Academy of Sciences of the United States of America **99**(8), 5223 (2002). DOI 10.1073/pnas.072287299. URL http://www.pnas.org/content/99/8/5223.abstract

12. V.N. Tsytovich, preprint, Academy of Sciences, USSR, [SOV PHYS USPEKHI, 1973, 15 (5), 632650] (150) (1969)
13. S.I. Popel, V.N. Tsytovich, S.V. Vladimirov, Physics of Plasmas **1**(7), 2176 (1994). DOI 10.1063/1.870617. URL http://link.aip.org/link/?PHP/1/2176/1
14. D.V. Dylov, J.W. Fleischer, Phys. Rev. Lett. **100**(10), 103903 (2008). DOI 10.1103/PhysRevLett.100.103903. URL http://link.aps.org/abstract/PRL/v100/e103903
15. D.V. Dylov, J.W. Fleischer, Phys. Rev. A (Atomic, Molecular, and Optical Physics) **78**(6), 061804 (2008). DOI 10.1103/PhysRevA.78.061804. URL http://link.aps.org/abstract/PRA/v78/e061804
16. W. Wan, S. Jia, J.W. Fleischer, Nat Phys **3**, 2007/01//print (2007). DOI 10.1038/nphys486. URL http://dx.doi.org/10.1038/nphys486
17. R. Dong, C.E. Rüter, D. Kip, O. Manela, M. Segev, C. Yang, J. Xu, Phys. Rev. Lett. **101**(18), 183903 (2008). DOI 10.1103/PhysRevLett.101.183903. URL http://link.aps.org/abstract/PRL/v101/e183903
18. D.V. Dylov, J.W. Fleischer, Opt. Lett. **34**(17), 2673 (2009). URL http://ol.osa.org/abstract.cfm?URI=ol-34-17-2673
19. A.V. Mamaev, M. Saffman, A.A. Zozulya, Phys. Rev. Lett. **76**(13), 2262 (1996). DOI 10.1103/PhysRevLett.76.2262
20. T. Bohr, M.H. Jensen, G. Paladin, A. Vulpiani, *Dynamical Systems Approach to Turbulence*, *Cambridge Nonlinear Science Series*, vol. 8 (Cambridge University Press, Cambridge, England, 1998, 1998)
21. D.N. Christodoulides, E.D. Eugenieva, T.H. Coskun, M. Segev, M. Mitchell, Phys. Rev. E **63**(3), 035601 (2001). DOI 10.1103/PhysRevE.63.035601
22. E. Wigner, Phys. Rev. **40**(5), 749 (1932). DOI 10.1103/PhysRev.40.749
23. J.E. Moyal, Mathematical Proceedings of the Cambridge Philosophical Society **45**(01), 99 (1949). DOI 10.1017/S0305004100000487
24. B. Hall, M. Lisak, D. Anderson, R. Fedele, V.E. Semenov, Phys. Rev. E **65**(3), 035602 (2002). DOI 10.1103/PhysRevE.65.035602
25. L. Helczynski, D. Anderson, R. Fedele, B. Hall, M. Lisak, IEEE J. Sel. Top. Quantum Electron. **8**(3), 408 (2002). DOI 10.1109/JSTQE.2002.1016342
26. V.V. Shkunov, D.Z. Anderson, Phys. Rev. Lett. **81**(13), 2683 (1998). DOI 10.1103/PhysRevLett.81.2683
27. D.N. Christodoulides, T.H. Coskun, M. Mitchell, M. Segev, Phys. Rev. Lett. **78**(4), 646 (1997). DOI 10.1103/PhysRevLett.78.646
28. S.V. Bulanov, M. Yamagiwa, T.Z. Esirkepov, D.V. Dylov, F.F. Kamenets, et al., Plasma Physics Reports **32**(4), 263 (2006)
29. S.V. Bulanov, D.V. Dylov, T.Z. Esirkepov, F.F. Kamenets, D.V. Sokolov, Plasma Physics Reports **31**(5), 369 (2005)
30. R. Fedele, D. Anderson, Journal of Optics B: Quantum and Semiclassical Optics **2**(2), 207 (2000). URL http://stacks.iop.org/1464-4266/2/207
31. W. Martienssen, E. Spiller, American Journal of Physics **32**(12), 919 (1964). DOI 10.1119/1.1970023. URL http://link.aip.org/link/?AJP/32/919/1
32. A. Picozzi, Opt. Express **15**(14), 9063 (2007). URL http://www.opticsexpress.org/abstract.cfm?URI=oe-15-14-9063
33. G.E. Vekstein, American Journal of Physics **66**(10), 886 (1998). DOI 10.1119/1.18978. URL http://link.aip.org/link/?AJP/66/886/1
34. S.L. Musher, A.M. Rubenchik, V.E. Zakharov, Physics Reports **252**(4), 177 (1995). DOI 10.1016/0370-1573(94)00071-A
35. C. Sun, D.V. Dylov, J.W. Fleischer, Opt. Lett. **34**(19), accepted (2009)
36. M. Lisak, D. Anderson, L. Helczynski-Wolf, P. Berczynski, R. Fedele, V. Semenov, Physica Scripta **T113**, 56 (2004). URL http://stacks.iop.org/1402-4896/T113/56
37. D. Anderson, B. Hall, M. Lisak, M. Marklund, Phys. Rev. E **65**(4), 046417 (2002). DOI 10.1103/PhysRevE.65.046417
38. V. Arunasalam, American Journal of Physics **36**(7), 601 (1968). DOI 10.1119/1.1975025. URL http://link.aip.org/link/?AJP/36/601/1

39. D. Anderson, L. Helczynski-Wolf, M. Lisak, V. Semenov, Phys. Rev. E **69**(2), 025601 (2004). DOI 10.1103/PhysRevE.69.025601
40. S. Pitois, S. Lagrange, H.R. Jauslin, A. Picozzi, Phys. Rev. Lett. **97**(3), 033902 (2006). DOI 10.1103/PhysRevLett.97.033902. URL http://link.aps.org/abstract/PRL/v97/e033902
41. C. Anastassiou, M. Segev, K. Steiglitz, J.A. Giordmaine, M. Mitchell, M. feng Shih, S. Lan, J. Martin, Phys. Rev. Lett. **83**(12), 2332 (1999). DOI 10.1103/PhysRevLett.83.2332
42. C. Anastassiou, J.W. Fleischer, T. Carmon, M. Segev, K. Steiglitz, Opt. Lett. **26**(19), 1498 (2001). URL http://ol.osa.org/abstract.cfm?URI=ol-26-19-1498
43. D.N. Christodoulides, M.I. Carvalho, J. Opt. Soc. Am. B **12**(9), 1628 (1995). URL http://josab.osa.org/abstract.cfm?URI=josab-12-9-1628
44. Z. Chen, J. Klinger, D.N. Christodoulides, Phys. Rev. E **66**(6), 066601 (2002). DOI 10.1103/PhysRevE.66.066601
45. A.N. Kaufman, Journal of Plasma Physics **8**(01), 1 (1972). DOI 10.1017/S0022377800006887
46. N.J. Fisch, J.M. Rax, Physics of Fluids B: Plasma Physics **5**(6), 1754 (1993). DOI 10.1063/1.860809. URL http://link.aip.org/link/?PFB/5/1754/1
47. A.S. Kingsep, L.I. Rudakov, R.N. Sudan, Phys. Rev. Lett. **31**(25), 1482 (1973). DOI 10.1103/PhysRevLett.31.1482
48. S. Dyachenko, A.C. Newell, A. Pushkarev, V.E. Zakharov, Physica D **57**(1–2), 96 (1992). DOI 10.1016/0167-2789(92)90090-A
49. V.M. Malkin, Phys. Rev. Lett. **76**(24), 4524 (1996). DOI 10.1103/PhysRevLett.76.4524
50. A. Picozzi, Opt. Express **15**(14), 9063 (2007). DOI 10.1364/OE.15.009063. URL http://www.opticsexpress.org/abstract.cfm?URI=oe-15-14-9063

Chapter 3
Gap-Acoustic Solitons: Slowing and Stopping of Light

Richard S. Tasgal, Roman Shnaiderman, and Yehuda B. Band

Abstract Solitons are paradigm localized states in physics. We consider here gap-acoustic solitons (GASs), which are stable pulses that exist in Bragg waveguides, and which offer promising new avenues for slowing light. A Bragg grating can be produced by doping the waveguide with ions, and imprinting a periodic variation in the index of refraction with ultraviolet light. The Bragg grating in an optical waveguide reflects rightward-moving light to the left, and vice versa, and creates a gap in the allowed frequency spectrum of light. Nonlinearities, though, add complications to this simple picture. While low intensity light cannot propagate at frequencies inside the band gap, more intense fields can exist where low-intensity fields cannot. An optical gap soliton is an intense optical pulse which can exist in a Bragg waveguide because the intensity and nonlinearity let it dig a hole for itself inside the band gap, in which it can then reside. Far from the center of the pulse, the intensity is weak, and drops off exponentially with distance from the center. The optical gap soliton structure can be stable, and can have velocities from zero (i.e., stopped light) up to the group-velocity of light in the medium. When one also considers the system's electrostrictive effects, i.e., the dependence of the index of refraction on the density of the material, which is a universal light-sound interaction in condensed matter, one obtains GASs. These solitons share many of the properties of standard gap solitons, but they show many fascinating new characteristics. GASs have especially interesting dynamics when their velocities are close to the speed of sound, in which range they interact strongly with the acoustic field. GASs which are moving

Richard S. Tasgal
Departments of Chemistry and Electro-Optics, and the Ilse Katz Center for Nano-Science, Ben-Gurion University of the Negev, Beer-Sheva 84105, Israel e-mail: tasgal@gmail.com

Roman Shnaiderman
Departments of Chemistry and Electro-Optics, and the Ilse Katz Center for Nano-Science, Ben-Gurion University of the Negev, Beer-Sheva 84105, Israel e-mail: rshnaider@gmail.com

Yehuda B. Band
Departments of Chemistry and Electro-Optics, and the Ilse Katz Center for Nano-Science, Ben-Gurion University of the Negev, Beer-Sheva 84105, Israel e-mail: band@bgu.ac.il

O. Descalzi et al. (eds.), *Localized States in Physics: Solitons and Patterns*,
DOI 10.1007/978-3-642-16549-8_3,

at supersonic velocities may experience instabilities which leave the GAS whole, but bring the velocity abruptly to almost zero. Furthermore, GASs may be made to change velocity by collision with acoustic pulses. Moving GASs may be retarded by the phonon viscosity, as well as by interaction with high wave number (Brillouin) acoustic waves. Thus, the opto-acoustic interactions provide the basis for a set of tools with which light in the form of a GAS can be slowed down and controlled. In contrast with other forms of slow or stopped light, GASs can exist at room temperature, in relatively unexotic materials. This makes the GAS an attractive form in which to create and work with slow and stopped light.

3.1 Introduction

One of the paradigm examples of localized states in physics is the soliton, a pulse that gets its stability from a balance of dispersion and nonlinearity. The gap-acoustic soliton (GAS) is an optical and acoustic structure that can exist in an optical waveguide with a Bragg grating. Figure 3.1 is a schematic illustration of a fiber waveguide with a periodically varying refractive index with light and sound waves propagating within it. A Bragg grating can be produced by doping the waveguide with ions (e.g., germanium), and imprinting a periodic variation in the index of refraction with ultraviolet light [1]. As we shall see, GASs are good systems in which to realize slow light. GASs can be viewed from three perspectives: (1) as an extension of optical gap solitons to a regime where their interaction with sound waves is important, (2) as a new application of electrostriction and Brillouin scattering, or (3) as a means to produce slow light.

The study of solitons has a long history. There is a narrow definition, which applies only to completely integrable systems. In this strict sense, solitons are connected to the inverse scattering method [2]. A broader definition of a soliton is a pulse that is stable due to a balance of dispersion and nonlinearity [1, 2]. The first solitons to be discovered were localized shallow-water waves, by John Scott Russell in 1834 [3], known as Korteweg–de Vries (KdV) solitons [4]. The KdV equation was shown to be completely integrable by the inverse scattering method, and that the pulses are solitons in the stricter sense was demonstrated much later [2, 5]. The first optical soliton discovered was in the nonlinear Schrödinger (NLS) equation. The NLS equation was found to be completely integrable and to support solitons, in the strict sense, in Ref. [6]. Independently, Ref. [7] showed that there are solitons in the broad sense which can be realized in optical fibers. In the NLS equation, linear (small amplitude) continuous wave (cw) solutions exist along a parabolic curve in the space (k, ω) of wave number and frequency that is concave upwards (there is a maximum wave number). The soliton solutions exist in the space above the cw dispersion curve.

The first gap soliton article did not use the phrase “gap soliton,” but rather referred to the equations as the massive Thirring model (MTM) [8], with particle physics in mind rather than optics. The solutions discovered were solitons even in

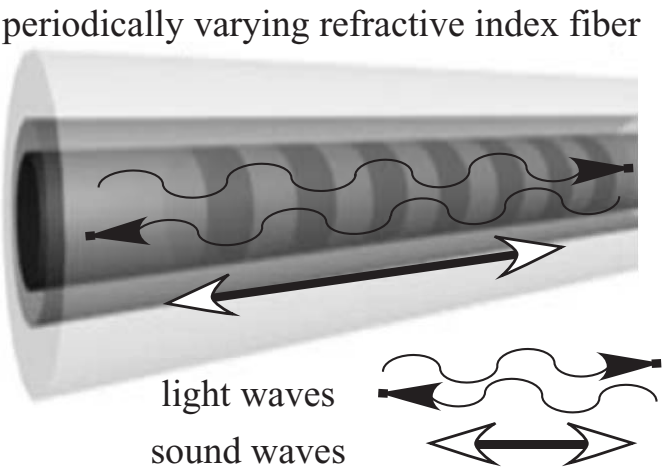

Fig. 3.1 Schematic illustration of a fiber with a periodically-varying refractive index. Light and sound waves propagate in the fiber. Photons are shown as wavy lines with arrows indicating the direction of motion and phonons are shown as a solid line with double-sided arrows.

the strictest sense—the system was shown to be integrable by the inverse scattering method, and the pulse solutions (solitons) were shown to correspond to poles of the transmission coefficient [9]. The frequencies of the solitons are inside the gap between the continuous wave solutions of the linear system appropriate for low-intensity waves. However, the soliton frequencies *are not all* between the maximum of the lower cw band and the minimum of the upper cw band; for this reason, interpreting the band gap more narrowly, some authors prefer the term "Bragg soliton" for solitons with frequencies that are either above the minimum of the upper cw band or below the maximum of the lower cw band—see, e.g., Ref. [10]. Independently of the mathematical discovery of the gap solitons, a qualitative description and prediction of the still theoretical optical gap solitons was made in Ref. [11]. Exact analytic forms for optical gap solitons were found for a nonlinearity with self-phase modulation in addition to cross-phase modulation: Ref. [12] found the solutions in the exact middle of the band gap, and Ref. [13] found the full family of gap soliton solutions. This is not a completely integrable system, and the pulses are solitons in the broader sense but not the narrower sense. As a result, the pulses are not guaranteed to have the stability of the MTM solitons.

The stability of gap solitons beyond the completely integrable MTM limit (optical gap solitons have self-phase modulation, so are not MTM), was not immediately clear. Ref. [12] showed one direct numerical simulation of a gap soliton collision, in which the individual gap solitons were stable, and the solitons emerged from a collision intact but perturbed. Ref. [14] performed variational model calculations of optical gap solitons, which showed some regions where excited modes exist, and other regions with instabilities. References [15, 16, 17] showed rigorously that op-

tical gap solitons are stable in the top half of the frequency band gap, and unstable in most of the bottom half of the band gap.

Reference [18] generalized the optical gap soliton equations to include dependence of the index of refraction on the density of the material, and acoustic waves. In other words, acoustic waves and their interaction with light through electrostriction were included in the model. New generalized "gap-acoustic soliton" (GAS) solutions were also found. The GASs are similar to optical gap solitons, but they exhibit many intriguing novel dynamical properties, especially when the soliton velocities are small. Reference [19] looked in detail at the system in the case that the physical parameters of bulk fused silica, and found that electrostriction will have much large, not merely perturbative, influences on the GASs when velocities are as slow as two orders of magnitude less than the group velocity of light; solitons need not be, as is the speed of sound, five orders of magnitude slower than the speed of light, for acoustic effects to be strongly felt.

Dependence of the index of refraction on the density of the material is a universal property of materials [20], and interaction of light with sound waves is ubiquitous. Interaction between light and high wavenumber acoustic waves—approximately twice the wave numbers of the light—is called Brillouin scattering [21], and interaction between light and low wavenumber acoustic waves is generally referred to as electrostriction [22]. Distinctions in nomenclature notwithstanding, the two effects have the same physical source. Reference [19] derived the Brillouin scattering (short acoustic wavelength) interaction together with the electrostrictive (long acoustic wavelength) interactions in a unified manner.

There have been significant research efforts in recent decades towards the achievement of slow light (see, e.g., Ref. [23]). One way to achieve slow light is to use electromagnetically-induced transparency to reduce group-velocities without large absorption [23]. Another form of slow light—which we concentrate on here—is the optical gap soliton, which moves slower than the group velocity or even at velocity zero [8, 9, 11, 12, 13, 15, 16, 17, 24, 25, 26, 27, 28, 29]. Optical gap solitons may exist in a nonlinear waveguide with a Bragg grating. The Bragg grating creates a band gap for light that is in-phase with the grating. The nonlinearity allows a pulse of light in the waveguide to dig a hole for itself in the forbidden region. This structure may be stable, balancing the nonlinearity against the Bragg-grating-induced dispersion, i.e., it will be a soliton. This optical soliton may have a velocity which is slow or even zero. It is slow or stopped light. To date, the slowest experimentally realized optical gap solitons had velocity $c/6$ [29]. When the soliton velocity is comparable to the sound velocity, the interaction between the light and sound can be strong because they can propagate together.

The outline of this paper is as follows. Section 3.2 gives a derivation of the equations for the dynamics of the optical gap soliton system, along with all the acoustic interactions that the system supports. Section 3.3 details the general properties of this system, and Sec. 3.4 gives the soliton solutions. Section 3.5 goes over the stability properties of the solitons, and retardation effects to obtain slow light. Finally, Sec. 3.6 contains a summary and conclusion.

3.2 Derivation of the Equations

We begin with general equations for two fields, light and sound. Light is governed by Maxwell's equations. Sound can be described by a wave equation for the density change in the medium. In addition, light and sound interact via electrostriction. For optical gap solitons in a fiber, the light is of approximately one color, but the direction can be either forward or backward. The electromagnetic field can thus be broken down into two separate slowly-varying envelopes about fast-varying carrier waves, one for forward-moving light and one for backward-moving light. The acoustic fields that interact with this light can be of high wave number or low wave number. The high wave number acoustic fields can be either forward- or backward-moving. The low wave number acoustic field is centered at wave number zero, with some spread to both positive and negative values. The acoustic field for this system can then be broken down into three slowly-varying envelopes, two for the high wave number waves, and one for low wave number.

3.2.1 Electromagnetic Field Equations with Phonon Perturbations

The starting point of the derivation is Maxwell's equations. We begin considering an isotropic medium without free charges, currents, or magnetic polarization. Bragg and Brillouin scattering will be covered as extensions of this, by dropping the assumption of isotropy. The electromagnetic field, and the linear and nonlinear polarization of the medium satisfy the equations,

$$\nabla \cdot (\mathbf{E} + 4\pi \mathbf{P}_{\text{linear}} + 4\pi \mathbf{P}_{\text{NL}}) = 0 \tag{3.1a}$$

$$\nabla \cdot \mathbf{B} = 0 \tag{3.1b}$$

$$\nabla \times \mathbf{E} = -\frac{1}{c}\frac{\partial}{\partial t}\mathbf{B} \tag{3.1c}$$

$$\nabla \times \mathbf{B} = -\frac{1}{c}\frac{\partial}{\partial t}(\mathbf{E} + 4\pi \mathbf{P}_{\text{linear}} + 4\pi \mathbf{P}_{\text{NL}}), \tag{3.1d}$$

The dependence of polarization $\mathbf{P} = \mathbf{P}_{\text{linear}} + \mathbf{P}_{\text{NL}}$ on the electromagnetic field $\mathbf{E}, \mathbf{B}$, has a part which is linear in the electromagnetic field, with an additional dependence on the density of the material,

$$\mathbf{E} + 4\pi \mathbf{P}_{\text{linear}} \equiv \mathbf{D} = n^2(\omega, w)\,\mathbf{E}, \tag{3.2a}$$

where the expression on the right hand side, relating electric displacement to electric field via a frequency-dependent index of refraction, holds in frequency space and in real space for monochromatic fields. We have indicated a dependence of the index of refraction on the density of the material w. There is also a contribution to the polarization due to a third-order Kerr nonlinearity:

$$\mathbf{P}_{\mathrm{NL}} = \frac{\chi_s}{3}(\mathbf{E}\cdot\mathbf{E})\mathbf{E}. \tag{3.2b}$$

Fourier transform over the time dimension to get the equation in frequency-space. In an isotropic medium, Coulomb's law (3.1a) and Ampere's law (3.1d) take the form

$$0 = n(\omega)^2\,\boldsymbol{\nabla}\cdot\mathbf{E}(\mathbf{x},\omega) + 4\pi\,\boldsymbol{\nabla}\cdot\mathbf{P}_{\mathrm{NL}}(\mathbf{x},\omega)\,, \tag{3.3a}$$

$$0 = \boldsymbol{\nabla}\times\mathbf{B}(\mathbf{x},\omega) + i\frac{\omega}{c}\left[n(\omega)^2\mathbf{E}(\mathbf{x},\omega) + 4\pi\mathbf{P}_{\mathrm{NL}}(\mathbf{x},\omega)\right]. \tag{3.3b}$$

Inserting these into the curl of Faraday's law (3.1c) gives the wave equation,

$$\begin{aligned} 0 = &\left[\nabla^2 + \frac{n(\omega)^2\omega^2}{c^2}\right]\mathbf{E}(\mathbf{x},\omega) \\ &+\frac{4\pi\,\omega^2}{c^2}\mathbf{P}_{\mathrm{NL}}(\mathbf{x},\omega) + \frac{4\pi}{n(\omega)^2}\boldsymbol{\nabla}\left[\boldsymbol{\nabla}\cdot\mathbf{P}_{\mathrm{NL}}(\mathbf{x},\omega)\right]. \end{aligned} \tag{3.4a}$$

A Fourier transform in the spatial dimensions gives the wave equation in momentum space,

$$\begin{aligned} 0 = &\left[k^2 - \frac{n(\omega)^2\,\omega^2}{c^2}\right]\mathbf{E}(\mathbf{k},\omega) \\ &-\frac{4\pi\,\omega^2}{c^2}\left\{\mathbf{P}_{\mathrm{NL}}(\mathbf{k},\omega) - \frac{c^2}{n(\omega)^2\,\omega^2}\mathbf{k}\left[\mathbf{k}\cdot\mathbf{P}_{\mathrm{NL}}(\mathbf{k},\omega)\right]\right\}. \end{aligned} \tag{3.4b}$$

If the nonlinear polarization is transverse, which will be the case with the Kerr nonlinearity (3.2b), and transverse electric field, the last terms on the right-hand sides of Eqs. (3.4) vanish. The basic optical gap soliton has one (nontrivial) spatial dimension, and takes the system to have light of one polarization, so we reduce the generality of the mathematical model and obtain,

$$0 = \left[\frac{\partial^2}{\partial z^2} + \frac{n(\omega)^2\omega^2}{c^2}\right]E(z,\omega) + \frac{4\pi\,\omega^2}{c^2}P_{\mathrm{NL}}(z,\omega)\,. \tag{3.5a}$$

$$0 = \left[k^2 - \frac{n(\omega)^2\,\omega^2}{c^2}\right]E(k,\omega) - \frac{4\pi\,\omega^2}{c^2}P_{\mathrm{NL}}(k,\omega)\,. \tag{3.5b}$$

If we consider the wave equation (3.5) in the vicinity of frequency ω_0 and wave number $k_0 = n(\omega_0)\omega_0/c$, complete the square for the quadratic equation, Taylor expand in the small terms, and truncate, we obtain,

$$0 = \left[(k_0+\delta k)^2 - \frac{n(\omega_0+\delta\omega)^2\,(\omega_0+\delta\omega)^2}{c^2} - \frac{4\pi\,(\omega_0+\delta\omega)^2}{c^2}\frac{P_{\rm NL}(k_0+\delta k,\omega_0+\delta\omega)}{E(k_0+\delta k,\omega_0+\delta\omega)}\right] E(k_0+\delta k,\omega_0+\delta\omega)\,, \tag{3.6a}$$

$$0 = \left[\mp(k_0+\delta k) + \frac{n(\omega_0+\omega)\,(\omega_0+\omega)}{c}\sqrt{1+\frac{4\pi}{[n(\omega_0+\omega)]^2}\frac{P_{\rm NL}}{E}}\right] E(k_0+\delta k,\omega_0+\delta\omega)\,, \tag{3.6b}$$

$$= \mp(k_0+\delta k)E(k_0+\delta k,\omega_0+\delta\omega) + \frac{n(\omega_0+\omega)\,(\omega_0+\omega)}{c}E + \frac{2\pi(\omega_0+\omega)}{n(\omega_0+\omega)c}P_{\rm NL}(k_0+\delta k,\omega_0+\delta\omega)+\ldots \tag{3.6c}$$

$$= \mp\delta kE(k_0+\delta k,\omega_0+\delta\omega) + \left(\frac{n(\omega_0)\,\omega_0}{c}\mp k_0\right)E + \frac{d}{d\omega}\left(\frac{n(\omega)\,\omega}{c}\right)_{\omega_0}\omega E + \frac{2\pi\omega_0/c}{n(\omega_0)}P_{\rm NL}(k_0+\delta k,\omega_0+\delta\omega)+\ldots \tag{3.6d}$$

Let us now Fourier transform back to real space, and include a nonuniformity in the index of refraction, which is also a function of the material density,

$$0 = ik_0'\frac{\partial}{\partial t}E(z,t) \pm i\frac{\partial}{\partial z}E + \left(\frac{n(\omega_0,z,W)\,\omega_0}{c}\mp k_0\right)E + \frac{2\pi}{k_0}\left(\frac{\omega_0}{c}\right)^2 P_{\rm NL}(z,t)+ \tag{3.7a}$$

$$= ik_0'\frac{\partial}{\partial t}E(z,t) \pm i\frac{\partial}{\partial z}E + \left(\frac{\omega_0}{c}\Delta n(z) + \frac{\omega_0}{c}\frac{dn}{dW}W\right)E + \frac{2\pi}{k_0}\left(\frac{\omega_0}{c}\right)^2 P_{\rm NL}(z,t) \tag{3.7b}$$

Here $k_0 = \pm n(\omega_0)\omega_0/c$ is the phase velocity, and $k_0' = (d/d\omega)[n(\omega)\omega/c]_{\omega=\omega_0}$ is the reciprocal of the group velocity. When arguments of the index of refraction are implicit, they are based on an average value at a baseline material density W. $\Delta n(z)$ is the spatially-varying part of the refractive index. The result is an equation for a slowly-varying envelopes about a carrier wave with wave vector (k_0,ω_0).

Equation (3.7) applies generally to any quasi-monochromatic electromagnetic field with any nonlinearity. For the optical gap soliton, there is one frequency of light in the system, and the light may be traveling forward or backward. The electric field E may then be written as two slowly-varying envelopes (SVEs) about carrier waves with frequencies $\omega = \omega_0$ and wave numbers $k = \pm k_0 = \pm n(\omega_0)\omega_0/c$. The acoustic fields that can interact with these light fields are those centered at wave numbers $k = 0$ and $\pm 2k_0$. If the speed of sound (which we can refer to as $\beta_{\rm sound}$) is constant—which to a good approximation it is—then for the carrier waves of the acoustic waves, the frequencies of the acoustic waves are simply the speed of sound ($\beta_{\rm sound}$) times the wave numbers. We also allow the index of refraction to have a small component at half the wavelength of the light, which will yield Bragg scattering from the periodic grating set up in the material,

$$E(z,t) = U(z,t)\exp[i(k_0 z - \omega_0 t)] + V(z,t)\exp[-i(k_0 z + \omega_0 t)] + U^*(z,t)\exp[-i(k_0 z - \omega_0 t)] + V^*(z,t)\exp[i(k_0 z + \omega_0 t)], \tag{3.8a}$$

$$W(z,t) = W_u(z,t)\exp[2ik_0(z - \beta_{\text{sound}} t)] + W_v(z,t)\exp[-2ik_0(z + \beta_{\text{sound}} t)] + W_u^*(z,t)\exp[-2ik_0(z - \beta_{\text{sound}} t)] + W_v^*(z,t)\exp[2ik_0(z + \beta_{\text{sound}} t)] + W_0(z,t), \tag{3.8b}$$

$$\Delta n(z) = \Delta n \cos(2k_0 z). \tag{3.8c}$$

Substituting the fields in terms of SVEs [Eqs. (3.8)] into the general dynamical equations for light [Eq. (3.7b)], while taking the nonlinearity to be Kerr [Eq. (3.2b)], and separating the different frequency and wave number components, gives

$$0 = ik_0' U_t + iU_z + \kappa V + \frac{2\pi(\omega_0/c)^2}{k_0}(\chi_s|U|^2 + \chi_x|V|^2)u + \chi_{es}\left[W_0 U + \exp(-2ik_0\beta_{\text{sound}} t)\, W_u V + \exp(2ik_0\beta_{\text{sound}} t)\, W_v^* V\right], \tag{3.9a}$$

$$0 = ik_0' V_t - iV_z + \kappa^* U + \frac{2\pi(\omega_0/c)^2}{k_0}(\chi_x|U|^2 + \chi_s|V|^2)v + \chi_{\text{es}}\left[W_0 V + \exp(2ik_0\beta_{\text{sound}} t)\, W_u^* U + \exp(-2ik_0\beta_{\text{sound}} t)\, W_v U\right], \tag{3.9b}$$

where

$$\kappa = \frac{\omega_0}{c}\frac{\Delta n}{2}, \tag{3.10a}$$

$$\chi_{\text{es}} = \frac{\omega_0}{c}\frac{dn}{dW}. \tag{3.10b}$$

This assumes that the speed of sound β_{sound} is small enough so that the frequencies $2k_0\beta_{\text{sound}}$ are within the frequency spread of the SVEs, U and V. These are the equations for the dynamics of the SVEs of light.

3.2.2 Acoustic Wave Equations with Electrostrictive Perturbations

To complete the dynamical system, we need equations for the density of the material—that is, acoustic waves. In silica glass, the speed of sound has a very weak dependence on frequency, and acoustic waves are also subject to viscosity [30]. Dependence of the index of refraction on the density of the material creates electrostriction, a force (pressure gradient) attracting the material to regions of higher light intensity. The equation for evolution of the density of a material of this system is [22, 31]

$$0 = \frac{\partial^2}{\partial t^2} W(x,y,z,t) - \beta_{\text{sound}}^2 \nabla^2 W - \Gamma_s \frac{\partial}{\partial t}\nabla^2 W + \frac{\Lambda}{2}\nabla^2 \langle E(x,y,z,t)^2 \rangle, \tag{3.11}$$

where $W(x,y,z,t)$ is the density of the material, $E(x,y,z,t)$ is the amplitude of the electric field, $\nabla^2 = \partial^2/\partial x^2 + \partial^2/\partial y^2 + \partial^2/\partial z^2$ is the Laplacian, β_{sound} is the speed of sound, Γ_s is a phonon viscosity coefficient, and Λ is an electrostrictive coefficient. We will focus on single-mode waveguides, in which any transverse dynamics are trivial, in the sense that that the transverse confinement affects only the values of the coefficients, but qualitative terms will be the same as one-dimensional infinite plane waves [32].) This reduces the system to 1+1-dimensions,

$$0 = \frac{\partial^2}{\partial t^2} W(z,t) - \beta_{\text{sound}}^2 \frac{\partial^2}{\partial z^2} W - \Gamma_s \frac{\partial^3}{\partial t \partial z^2} W + \frac{\Lambda}{2} \frac{\partial^2}{\partial z^2} \langle E(z,t)^2 \rangle . \tag{3.12}$$

Since we will be dealing with optical gap solitons, the light in the system is approximately monochromatic and may be moving forward or backward, as expressed by Eq. (3.8a). Electrostrictive response times are on the order of 10^{-9} s [22]. This is several (~ 6) orders of magnitude slower than the temporally fast-varying terms ($\propto U^2, V^2, U^{*2}, V^{*2}$) for visible or near infra-red light, so these may be dropped from the averaged square field in the phonon equation (3.12),

$$\begin{aligned} 0 = {} & W_{tt} - \beta_{\text{sound}}^2 W_{zz} - \Gamma_s W_{tzz} \\ & + \Lambda \left[|U|^2 + |V|^2 + UV^* \exp(2ik_0 z) + U^* V \exp(-2ik_0 z) \right]_{zz} . \end{aligned} \tag{3.13}$$

where we have denoted partial derivatives by subscripts. Since $U(z,t)$ and $V(z,t)$ are SVEs, the phonons' source terms will be centered around wavenumbers $k = 0$, $2k_0$, and $-2k_0$. Thus light in the optical gap solitons will interact by electrostriction only with phonons around those same wave numbers, which is consistent with Eq. (3.8b). Fourier transform the phonon equation (3.13) to momentum space,

$$\begin{aligned} 0 = {} & -\omega^2 W(k,\omega) - i\omega k^2 \Gamma_s W + k^2 \beta_{\text{sound}}^2 W - k^2 \Lambda \mathscr{F}\{|U|^2 + |V|^2\}(k,\omega) \\ & - k^2 \Lambda \mathscr{F}\{UV^*\}(k - 2k_0, \omega) - k^2 \Lambda \mathscr{F}\{U^* V\}(k + 2k_0, \omega) . \end{aligned} \tag{3.14}$$

Since U and V are SVEs, $\mathscr{F}\{|U|^2 + |V|^2\}(k,\omega)$ will only be significant in the vicinity of $k \approx 0$, $\mathscr{F}\{UV^*\}(k - 2k_0, \omega)$ will only be significant at $k \approx 2k_0$, and $\mathscr{F}\{U^* V\}(k + 2k_0, \omega)$ will only be significant at $k \approx -2k_0$. We substitute the expression for W in Eq. (3.8b) into the general phonon equation (3.14), and separate into the different (and, in k-space, non-overlapping) regions:

$$0 = -\omega^2 W_0(k,\omega) - i\omega k^2 \Gamma_s W_0 + k^2 \beta_{\text{sound}}^2 W_0 - k^2 \Lambda \mathscr{F}\{|U|^2 + |V|^2\}(k,\omega) \tag{3.15a}$$

$$\begin{aligned} 0 = {} & (\omega - \omega_0)^2 W_u(k,\omega) + i(\omega - \omega_0)(k - 2k_0)^2 \Gamma_s W_u - (k - 2k_0)^2 \beta_{\text{sound}}^2 W_u \\ & + (k - 2k_0)^2 \Lambda \mathscr{F}\{UV^*\}(k - 2k_0, \omega - \omega_0) , \end{aligned} \tag{3.15b}$$

$$\begin{aligned} 0 = {} & (\omega - \omega_0)^2 W_v(k,\omega) + i(\omega - \omega_0)(k + 2k_0)^2 \Gamma_s W_v - (k + 2k_0)^2 \beta_{\text{sound}}^2 W_v \\ & + (k + 2k_0)^2 \Lambda \mathscr{F}\{U^* V\}(k + 2k_0, \omega) . \end{aligned} \tag{3.15c}$$

Here $W_u(k,\omega) = W(k - 2k_0, \omega - \omega_0)$, $W_v(k,\omega) = W(k + 2k_0, \omega - \omega_0)$, and $W_0(k,\omega) = W(k,\omega)$ are SVEs of the density W.

3.2.2.1 Slowly-Varying Phonon Field

We take the phonon equation (3.15a), which is for the region near the origin in (k,ω)-space, or the slowly-varying part of the phonon field, and inverse Fourier transform it to real space,

$$0 = W_{0,tt} - \beta_{\text{sound}}^2 W_{0,zz} - \Gamma_s W_{0,tzz} + \Lambda(|U|^2 + |V|^2)_{zz}\,. \tag{3.16}$$

This is the most useful form of the governing equations for low wave number (long wavelength) acoustic waves.

3.2.2.2 Brillouin Scattering—Phonon Fields at $k \approx 2k_0$

Consider Eq. (3.15b) for the part of the phonon field with wave numbers close to $k = 2k_0$. We complete the square, expand the root into a Taylor series, and drop higher-order terms:

$$\begin{aligned} 0 = {} & [\omega + 2i(k_0 + k/2)^2\Gamma_s + \omega_u \\ & \pm 2(k_0 + k/2)\beta_{\text{sound}}\{1 - (1/2)[(k_0 + k/2)\Gamma_s/\beta_{\text{sound}}]^2\}]\,W_u(k,\omega) \\ & \mp (k_0 + k/2)\Lambda\beta_{\text{sound}}^{-1}\mathscr{F}\{UV^*\}(k,\omega+\omega_0) + \ldots \end{aligned} \tag{3.17}$$

Dropping wavenumber dependence of the damping, higher-order dispersion, a self-steepening-like term (in the sense that it comes from going from a second- to a first-order differential equation), and the quadratic or higher terms in the phonon viscosity, since phonon viscosity is generally a small perturbation, we obtain

$$0 = \left[\omega + 2ik_0^2\Gamma_s \pm k\beta_{\text{sound}}\right] W_u(k,\omega) \mp k_0\Lambda\beta_{\text{sound}}^{-1}\mathscr{F}\{UV^*\}(k,\omega \mp 2k_0\beta_{\text{sound}}) + \ldots \tag{3.18}$$

where $\omega_0 = 2k_0\beta_{\text{sound}}$. We now inverse Fourier transform this to real space,

$$0 = iW_{u,t} + i(2k_0^2\Gamma_s)W_u \mp i\beta_{\text{sound}}W_{u,z} \mp \frac{k_0\Lambda}{\beta_{\text{sound}}}\exp[\mp 2ik_0\beta_{\text{sound}}t](UV^*) + \ldots \tag{3.19}$$

The positive sign is the relevant solution for the field W_u,

$$0 = iW_{u,t} + i\beta_{\text{sound}}W_{u,z} + i(2k_0^2\Gamma_s)W_u + \frac{k_0\Lambda}{\beta_{\text{sound}}}\exp(2ik_0\beta_{\text{sound}}t)\,UV^*\,. \tag{3.20a}$$

The corresponding equation for the Brillouin field moving in the opposite direction $(k = -2k_0)$ is

$$0 = iW_{v,t} - i\beta_{\text{sound}}W_{v,z} + i(2k_0^2\Gamma_s)W_v + \frac{k_0\Lambda}{\beta_{\text{sound}}}\exp(2ik_0\beta_{\text{sound}}t)\,UV^*\,. \tag{3.20b}$$

3.2.3 The Bragg-Brillouin-Kerr System

Let us collect the definitions of the SVEs of the electromagnetic and phonon fields,

$$\begin{aligned} E(z,t) &= U(z,t)\exp[i(k_0 z-\omega_0 t)]+V(z,t)\exp[i(-k_0 z-\omega_0 t)] \\ &\quad + U^*(z,t)\exp[-i(k_0 z-\omega_0 t)]+V^*(z,t)\exp[i(k_0 z+\omega_0 t)]\,, \qquad (3.21a) \\ W(z,t) &= W_0(z,t)+W_u(z,t)\exp[2ik_0(z-\beta_{\rm sound}t)]+W_v(z,t)\exp[-2ik_0(z+\beta_{\rm sound}t)] \\ &\quad + W_u^*(z,t)\exp[-2ik_0(z-\beta_{\rm sound}t)]+W_v^*(z,t)\exp[2ik_0(z+\beta_{\rm sound}t)]\,, \qquad (3.21b) \end{aligned}$$

and their dynamical equations,

$$\begin{aligned} 0 &= ik_0'U_t+iU_z+\kappa V+\frac{2\pi(\omega_0/c)^2}{k_0}(\chi_s|U|^2+\chi_x|V|^2)U \\ &\quad +\chi_{es}\left[W_0U+\exp(-2ik_0\beta_{\rm sound}t)\,W_uV+\exp(2ik_0\beta_{\rm sound}t)\,W_v^*V\right], \qquad (3.22a) \\ 0 &= ik_0'V_t-iV_z+\kappa U+\frac{2\pi(\omega_0/c)^2}{k_0}(\chi_x|U|^2+\chi_s|V|^2)V \\ &\quad +\chi_{es}\left[W_0V+\exp(2ik_0\beta_{\rm sound}t)\,W_u^*U+\exp(-2ik_0\beta_{\rm sound}t)\,W_vU\right], \qquad (3.22b) \\ 0 &= W_{0,tt}-\beta_{\rm sound}^2W_{0,zz}-\Gamma_sW_{0,tzz}+\Lambda(|U|^2+|V|^2)_{zz}\,. \qquad (3.22c) \\ 0 &= iW_{u,t}+i\beta_{\rm sound}W_{u,z}+i(2k_0^2\Gamma_s)W_u+\frac{k_0\Lambda}{\beta_{\rm sound}}\exp(2ik_0\beta_{\rm sound}t)\,UV^*, \qquad (3.22d) \\ 0 &= iW_{v,t}-i\beta_{\rm sound}W_{v,z}+i(2k_0^2\Gamma_s)W_v+\frac{k_0\Lambda}{\beta_{\rm sound}}\exp(2ik_0\beta_{\rm sound}t)U^*V\,. \qquad (3.22e) \end{aligned}$$

3.3 Lagrangian, Hamiltonian, and Conserved Quantities

The Bragg-Brillouin-Kerr system (3.22) can be derived from a Lagrangian density in the limit in which phonon viscosity is nil ($\Gamma_s=0$),

$$\begin{aligned} \mathscr{L} &= \frac{i}{2}k_0'(U^*U_t-UU_t^*)+\frac{i}{2}k_0'(V^*V_t-VV_t^*)+\frac{i}{2}(U^*U_z-UU_z^*)-\frac{i}{2}(V^*V_z-VV_z^*) \\ &\quad +\kappa U^*V+\kappa^*UV^*+\frac{2\pi(\omega_0/c)^2}{k_0}\left[\frac{\chi_s}{2}(|U|^4+|V|^4)+\chi_x|U|^2|V|^2\right] \\ &\quad +\frac{\chi_{es}}{2\Lambda}(r_t^2-\beta_{\rm sound}^2r_z^2)+\chi_{es}(|U|^2+|V|^2)r_z \\ &\quad +\frac{\chi_{es}\beta_{\rm sound}}{k_0\Lambda}\frac{i}{2}[(W_u^*W_{u,t}-W_uW_{u,t}^*)+(W_v^*W_{v,t}-W_vW_{v,t}^*)] \\ &\quad +\frac{\chi_{es}\beta_{\rm sound}^2}{k_0\Lambda}\frac{i}{2}[(W_u^*W_{u,z}-W_uW_{u,z}^*)-(W_v^*W_{v,z}-W_vW_{v,z}^*)] \\ &\quad +\chi_{es}\exp(2ik_0\beta_{\rm sound}t)\,(UV^*W_u^*+U^*VW_v^*) \\ &\quad +\chi_{es}\exp(-2ik_0\beta_{\rm sound}t)\,(U^*VW_u+UV^*W_v)\,, \qquad (3.23a) \end{aligned}$$

for which we have introduced a potential for the slowly-varying phonon field

$$r(z,t) \equiv \int_{z_0}^{z} W_0(z',t)dz', \tag{3.23b}$$

where z_0 is an arbitrary constant.

The system has a Hamiltonian and three conserved quantities, corresponding to conservation of momentum P, conservation of the number of photons N (also sometimes called energy), and conservation of mass M (slightly abstracted, such that divergences on an infinite domain are avoided),

$$\begin{aligned} H = \int_{-\infty}^{\infty} dz \Big\{ & -\frac{i}{2}(U^*U_z - UU_z^*) + \frac{i}{2}(V^*V_z - VV_z^*) - \kappa U^*V - \kappa^* UV^* \\ & - \frac{2\pi(\omega_0/c)^2}{k_0 A}\left[\frac{\chi_s}{2}(|U|^4+|V|^4) + \chi_x |U|^2|V|^2\right] \\ & + \frac{\chi_{es}}{2\Lambda}(r_t^2 + \beta_{\text{sound}}^2 r_z^2) - \chi_{es}(|U|^2+|V|^2)r_z \\ & - \frac{\chi_{es}\beta_{\text{sound}}^2}{k_0\Lambda}\left[\frac{i}{2}(W_u^*W_{u,z} - W_uW_{u,z}^*) - \frac{i}{2}(W_v^*W_{v,z} - W_vW_{v,z}^*)\right] \\ & - \chi_{es}\exp(-2ik_0\beta_{\text{sound}}t)\,(U^*VW_u + UV^*W_v) \\ & - \chi_{es}\exp(2ik_0\beta_{\text{sound}}t)\,(UV^*W_u^* + U^*VW_v^*)\Big\}\,, \end{aligned} \tag{3.24a}$$

$$\begin{aligned} P = \int_{-\infty}^{\infty} \Bigg\{ & \frac{i}{2}(U^*U_z - UU_z^*) + \frac{i}{2}(V^*V_z - VV_z^*) \\ & + \frac{\chi_{es}}{\Lambda k_0'}\left[r_z r_t + \frac{\beta_{\text{sound}}}{k_0}\frac{i}{2}(W_u^*W_{u,z} - W_uW_{u,z}^* + W_v^*W_{v,z} - W_vW_{v,z}^*)\right]\Bigg\} dz \end{aligned} \tag{3.24b}$$

$$N = \int_{-\infty}^{\infty} (|U|^2 + |V|^2)dz, \tag{3.24c}$$

$$M = \int_{-\infty}^{\infty} r_t dz. \tag{3.24d}$$

If phonon viscosity is included, then the number of photons N and the material mass M are still constant, but the momentum P and the energy H decay according to the formulas

$$\frac{d}{dt}H = \frac{\Gamma\chi_{es}}{\Lambda}\int_{-\infty}^{\infty} W_{0,t}W_{0,z}dz, \tag{3.25a}$$

$$\frac{d}{dt}P = -\frac{\Gamma\chi_{es}}{\Lambda k_0'}\int_{-\infty}^{\infty} (W_{0,t})^2 dz. \tag{3.25b}$$

3.3.1 Dimensionless Variables

To give a clearer and more systematic picture of the dynamics, we rewrite the equations in terms of dimensionless variables,

$$u \equiv \sqrt{\frac{2\pi(\omega_0/c)^2}{\kappa k_0}}\,U\,, \tag{3.26a}$$

$$v \equiv \sqrt{\frac{2\pi(\omega_0/c)^2}{\kappa k_0}}\,V\,, \tag{3.26b}$$

$$w_0 \equiv \frac{1}{\kappa}\,W_0\,, \tag{3.26c}$$

$$w_u \equiv \frac{1}{\kappa}\,W_u\,, \tag{3.26d}$$

$$w_v \equiv \frac{1}{\kappa}\,W_v\,, \tag{3.26e}$$

$$\tau \equiv \frac{\kappa}{k_0'}\,t\,, \tag{3.26f}$$

$$\zeta \equiv \kappa z\,. \tag{3.26g}$$

The governing Eqs. (3.22) take the form

$$0 = iu_\tau + iu_\zeta + (1+\kappa_{\rm Brill})v + (\chi_s|u|^2 + \chi_x|v|^2 + \chi_{es}w)u\,, \tag{3.27a}$$

$$0 = iv_\tau - iv_\zeta + (1+\kappa^*_{\rm Brill})u + (\chi_x|u|^2 + \chi_s|v|^2 + \chi_{es}w)v\,, \tag{3.27b}$$

$$0 = w_{0,\tau\tau} - \Gamma\, w_{0,\tau\zeta\zeta} - \beta_s^2\, w_{0,\zeta\zeta} + \lambda\,(|u|^2+|v|^2)_{\zeta\zeta}\,, \tag{3.27c}$$

$$0 = iw_{u,t} + i\beta_s w_{u,z} + i[2(k_0/\kappa)^2\Gamma]w_u + \frac{\lambda k_0/\kappa}{\beta_s}\exp[2i(k_0/\kappa)\beta_s\tau]\,uv^*\,, \tag{3.27d}$$

$$0 = iw_{v,t} - i\beta_s w_{v,z} + i[2(k_0/\kappa)^2\Gamma]w_v + \frac{\lambda k_0/\kappa}{\beta_s}\exp[2i(k_0/\kappa)\beta_s\tau]\,u^*v\,, \tag{3.27e}$$

with

$$\kappa_{\rm Brill}(\zeta,\tau) = \exp[2i(k_0/\kappa)\beta_s\tau]w_u + \exp[-2i(k_0/\kappa)\beta_s\tau]w_v^*\,, \tag{3.28}$$

and normalized coefficients

$$\beta_s = \beta_{\rm sound}\,k_0'\,, \tag{3.29a}$$

$$\Gamma = \Gamma_s\,\kappa\,k_0'\,, \tag{3.29b}$$

$$\lambda = \Lambda\,\chi_{\rm es}\frac{k_0(k_0')^2}{2\pi(\omega_0/c)^2}\,. \tag{3.29c}$$

In ordinary optical materials, $\chi_x = 2\chi_s$. We have elected to eliminate one fewer variable than is possible, keeping χ_x, to make clearer the effects of large electrostriction compared to instantaneous Kerr effect.

3.4 Gap-Acoustic Solitons

Let us begin by looking at Eqs. (3.27) without the Brillouin fields w_u, w_v,

$$0 = iu_\tau + iu_\zeta + v + (\chi_s|u|^2 + \chi_x|v|^2)u + \chi_{es} w u\,, \tag{3.30a}$$
$$0 = iv_\tau - iv_\zeta + u + (\chi_x|u|^2 + \chi_s|v|^2)v + \chi_{es} w v\,, \tag{3.30b}$$
$$0 = w_{0,\tau\tau} - \Gamma w_{0,\tau\zeta\zeta} - \beta_s^2 w_{0,\zeta\zeta} + \lambda(|u|^2 + |v|^2)_{\zeta\zeta}\,, \tag{3.30c}$$

We found a family of solutions for gap-acoustic solitons for Eqs. (3.30) with zero phonon viscosity ($\Gamma = 0$),

$$u(\zeta,\tau) = \sqrt{\gamma(1+\beta)}\,\alpha \sin Q \,\mathrm{sech}(\tilde{\zeta}\sin Q - \frac{i}{2}Q)\exp[i\theta(\tilde{\zeta}) - i\tilde{\tau}\cos Q]\,, \tag{3.31a}$$
$$v(\zeta,\tau) = -\sqrt{\gamma(1-\beta)}\,\alpha \sin Q \,\mathrm{sech}(\tilde{\zeta}\sin Q + \frac{i}{2}Q)\exp[i\theta(\tilde{\zeta}) - i\tilde{\tau}\cos Q]\,, \tag{3.31b}$$
$$w(\zeta,\tau) = \frac{\lambda}{\beta_s^2 - \beta^2}\frac{4|\alpha|^2\gamma\sin^2 Q}{\cosh(2\tilde{\zeta}\sin Q) + \cos Q}\,, \tag{3.31c}$$

where

$$\theta(\tilde{\zeta}) = 4|\alpha|^2\gamma^2\beta[\chi_s + \lambda\chi_{es}/(\beta_s^2 - \beta^2)]\tan^{-1}\{\tanh[\tilde{\zeta}\sin Q]\tan(Q/2)\}\,, \tag{3.32a}$$
$$\alpha = \{\chi_x + \chi_s\gamma^2(1+\beta^2) + 2\lambda\gamma^2/(\beta_s^2 - \beta^2)\}^{-1/2}\,, \tag{3.32b}$$
$$\tilde{\tau} \equiv \gamma(\tau - \beta\zeta)\,, \tag{3.32c}$$
$$\tilde{\zeta} \equiv \gamma(\zeta - \beta\tau)\,, \tag{3.32d}$$
$$\gamma \equiv (1-\beta^2)^{-1/2}\,, \tag{3.32e}$$

and α must be real-valued. In the quiescent limit ($\beta \to 0$), these are also solutions for non-zero phonon viscosity ($\Gamma > 0$). The solitons Eqs. (3.31)-(3.32) have two essential intrinsic parameters, β, the velocity, and Q, which takes values $0 < Q < \pi$.

The soliton parameter Q resembles a similar parameter in the family of the ordinary gap solitons. The soliton's full width at half maximum intensity is $[\cosh^{-1}(2+\cos Q)/(\gamma\sin Q)]$. Frequency in the rest frame is $\gamma\cos Q$. Frequency in the frame moving with the soliton *is not* generally equal to $\cos Q$ because group velocity in a medium is normally less than the speed of light in vacuum. The soliton velocity (β) may have any value up to the group velocity of light in the medium ($|\beta| < 1$), except for a range of slightly supersonic gap solitons, $|\beta| \notin [\beta_s, \beta_{\mathrm{cr}}]$, where

$$\beta_{\rm cr}^2 = \frac{1}{2}\left[\beta_s^2 + \frac{\chi_x+\chi_s}{\chi_x-\chi_s} + \sqrt{\left(\beta_s^2 - \frac{\chi_x+\chi_s}{\chi_x-\chi_s}\right)^2 - \frac{8\lambda\chi_{es}}{\chi_x+\chi_s}}\right] . \tag{3.33}$$

In fused silica, the critical velocity is 10% greater than the speed of sound, $\beta_{\rm cr} = 1.10\beta_s$ [19]. Bright supersonic as well as subsonic solitons exist if the critical velocity $\beta_{\rm cr}$ is less than the speed of light in the medium. (The equations suggest existence of a dark soliton [33] in the supersonic region $\beta_s < \beta < \beta_{\rm cr}$, but we choose to limit this paper to bright solitons.) The closer the soliton velocity is to the speed of sound, the larger is the percentage of energy in the phonon field. Figure 3.2 shows a moderately supersonic soliton.

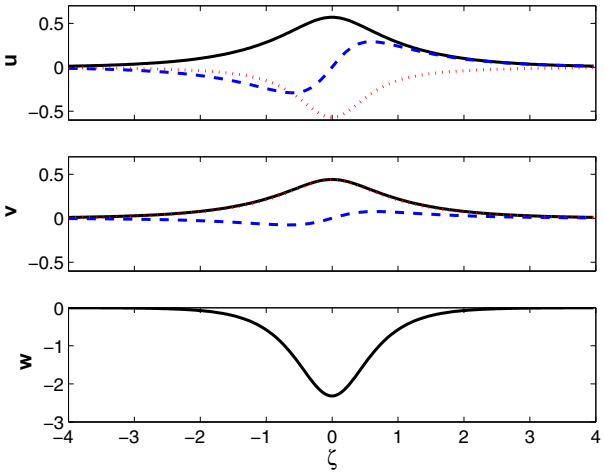

Fig. 3.2 Supersonic gap-acoustic soliton. The solitons's frequency is in the middle of the band gap (soliton parameter $Q = \pi/2$), and it's velocity is $\beta_s = 0.25$, which is 125% of the speed of sound, $\beta_s = 0.2$. The self- and cross-phase modulation coefficients are $\chi_s = 1$, $\chi_x = 2$, and the electrostrictive coefficients are $\chi_{es} = 1$, $\lambda = 0.1$. The first part of the figure shows the amplitude of the envelope u of the forward-moving electromagnetic wave, the second the envelope v of the backward-moving wave, and the third part the acoustic field (material density). Solid lines are for the magnitudes of the amplitudes, dashed lines for the real parts, and dotted lines are for the imaginary parts.

The gap-acoustic solitons (3.31)-(3.32) reduce to standard gap solitons [13] in the limit of zero electrostriction ($\lambda = 0$). There are resemblances to solitons in the Zakharov system [34, 35, 36], in that both contain dispersive equations coupled to a nondispersive equation, interaction with the non-dispersive field changes the amplitude of the soliton, and the dispersive field takes a profile the same shape as the soliton intensity. Below the speed of sound, the accompanying phonon pulse is a positive density variation, and above the speed of sound, the phonon pulse is a depression.

Note that Eqs. (3.30) do not admit optical solitons without an acoustic component; purely acoustic pulses are possible. In the case of zero phonon viscosity $\Gamma = 0$, these have the form $u = v = 0$, while the phonon field w is a combination of two arbitrary functions, $w(\zeta,\tau) = w_+(\zeta-\tau)$ and $w_-(\zeta+\tau)$, which represent forward- and backward-moving acoustic waves.

The soliton's (quasi-)conserved quantities, number of photons, phonons, momentum, and Hamiltonian, are obtained by substituting the soliton formulas (3.31)-(3.32) into Eqs. (3.24) to obtain

$$M_{\mathrm{GAS}} = \frac{\lambda}{\beta_s^2-\beta^2} 4|\alpha|^2 Q, \tag{3.34a}$$

$$N_{\mathrm{GAS}} = 4|\alpha|^2 Q, \tag{3.34b}$$

$$\begin{aligned} P_{\mathrm{GAS}} &= \beta\gamma(4|\alpha|^2)\sin Q \\ &\quad + \beta\gamma^3(4|\alpha|^2)^2\left(\chi_s + \frac{\lambda\chi_{es}}{\beta_s^2-\beta^2}\right)(\sin Q - Q\cos Q) \\ &\quad + \beta\gamma(4|\alpha|^2)^2\frac{\lambda\chi_{es}}{(\beta_s^2-\beta^2)^2}(\sin Q - Q\cos Q), \end{aligned} \tag{3.34c}$$

$$\begin{aligned} H_{\mathrm{GAS}} &= 4\gamma|\alpha|^2\{\sin Q + \gamma^{-2}(\sin Q - Q\cos Q) \\ &\quad -[\chi_s(1+\beta^2-4\gamma^2\beta^2)+\chi_x\gamma^{-2}](\sin Q - Q\cos Q) \\ &\quad +4|\alpha|^2\frac{\lambda\chi_{es}}{(\beta_s^2-\beta^2)^2}(\sin Q - Q\cos Q). \end{aligned} \tag{3.34d}$$

If a GAS is the only field present in the system (i.e., dispersive radiation can be neglected), then the decay of a GAS's quasi-conserved quantities can be calculated by inserting the GAS formulas (3.31)-(3.32) into Eqs. (3.25) [37],

$$\begin{aligned} \frac{d}{d\tau}P_{\mathrm{GAS}} &= -\frac{\Gamma\chi_{es}}{\lambda}\gamma\beta\int_{-\infty}^{\infty}(w_{0,\zeta})^2 d\zeta \\ &= -2\Gamma\lambda\chi_{es}\beta\gamma^3\left(\frac{4\gamma|\alpha|^2}{\beta_s^2-\beta^2}\right)^2\left(\sin Q - \frac{1}{3}\sin^3 Q - Q\cos Q\right), \end{aligned} \tag{3.35a}$$

$$\begin{aligned} \frac{d}{d\tau}H_{\mathrm{GAS}} &= -\frac{\Gamma\chi_{es}}{\lambda}\gamma\int_{-\infty}^{\infty}(w_{0,\zeta})^2 d\zeta \\ &= -2\Gamma\lambda\chi_{es}\gamma^3\left(\frac{4\gamma|\alpha|^2}{\beta_s^2-\beta^2}\right)^2\left(\sin Q - \frac{1}{3}\sin^3 Q - Q\cos Q\right), \end{aligned} \tag{3.35b}$$

It is in fact impossible for both N_{GAS} and M_{GAS} to remain constant while P_{GAS} and H_{GAS} decay according to Eqs. (3.35). This prooves that phonon viscosity causes a moving GAS to emit dispersive radiation. That phonon viscosity retards the soliton and that it causes emission of phonons from the slowing soliton is confirmed by direct numerical simulation, as illustrated by Fig. 3.3. Slowing of a GAS might also be achieved in a fiber loop with a mechanism for damping out emitted sound waves.

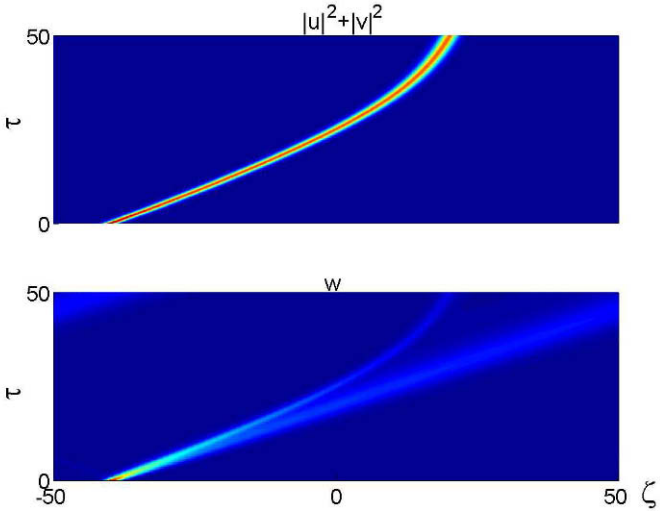

Fig. 3.3 Gap-acoustic soliton decelerating due to phonon viscosity. The top shows evolution of the light intensity, and the bottom shows the material density. The soliton begins with dimensionless velocity $\beta = 0.19$, compared to sound velocity $\beta_s = 0.2$. The soliton parameter is $Q = \pi/2$, frequency in the middle of the band gap. The electrostrictive coefficients are $\chi_{es} = 1$, $\lambda = 0.001$, the phonon viscosity is $\Gamma = 0.04$, and the self- and cross-phase modulation coefficients are $\chi_s = 1$, $\chi_x = 2$.

Brillouin scattering—interaction of the light fields u, v with the high wave number acoustic fields w_u, w_v—can be calculated explicitly in the approximation that the Brillouin fields are small perturbations to the GAS. This is the same as neglecting the effect of the Brillouin fields on the GAS. We can show that a moving GAS will emit acoustic waves preferentially backwards, carrying off some of the GAS's momentum, thus retarding it. The effect is relatively small, except when the soliton velocities are close to the group velocity of light in the medium. This retardation can add to the retardation effect on the GAS by phonon viscosity.

3.5 Soliton Stability and Instability

To analyze stability of gap-acoustic solitons, we carried out full numerical simulations of the partial differential equations (3.30) using a split-step fast Fourier transform scheme, which treats the linear part of the equations in momentum space, and the nonlinear part in real space [1]. The simulations were carried out systematically for three values of the soliton coefficient Q: $Q = \pi/3$ (in the middle of the top half of the band gap), which, for gap solitons without electrostriction ($\lambda = 0$) [11, 12, 13], is well inside the stable region; $Q = \pi/2$ (in the middle of the band gap), which is stable but close to the instability border; and $Q = 2\pi/3$ (in the middle of the bottom

half of the band gap), which has an oscillatory instability [15, 16, 17]. We calculated using ten different values of the electrostrictive coefficient, ranging over four orders of magnitude, $\lambda = 0.0001$ to 1, and the limit $\lambda \to \infty$. The speed of sound was held at $\beta_s = 0.2$. This is much faster than physically realistic (unless one were to consider light that is slow in the sense of the group velocity being much less than the phase velocity [23]). Choosing here to take the speed of sound relatively fast and studying a range of electrostrictive coefficients allows us to illustrate qualitative properties of the system that would be not easily demonstrated if simulations were limited to physically realizable cases. (A detailed analysis of the dynamics in a waveguide made of bulk fused silica can be found in Ref. [19]. In this case, the large disparity—five orders of magnitude—between the group velocity of light and the speed of sound makes a thorough study of the system computationally extremely expensive, rendering some effects practically indetectable and other effects huge.) The initial gap soliton velocity was taken at ten distinct values, from zero to twice the speed of sound $\beta = 2\beta_s = 0.4$, with special emphasis close to the speed of sound. For consistency in the stability analyses, all the direct numerical simulations had initial light amplitudes 1% greater than those of the exact soliton solutions. In addition to this systematic coverage of part of the parameter space, we ran many simulations at scattered values of all the free parameters.

Like gap solitons without electrostriction [15, 16, 17], gap-acoustic solitons are subject to oscillatory instabilities, which can grow until the soliton is destroyed, as illustrated in Fig. 3.4. In this case, when the oscillations grow too large, they destroy the soliton, which then goes into dispersive radiation moving to the left and to the right. Electrostriction, however, decreases the rate of growth of the oscillatory instability. The larger is the electrostrictive coefficient, the slower is the instability, as is visible in Fig. 3.5, which, over a series of runs with a range of electrostrictive coefficients, shows the growth rate of the instability to be smaller for larger electroctrictive coefficients λ.

Additionally, the closer the velocity is to the speed of sound, the greater is the damping of the oscillatory instability. Figure 3.6 shows evolution of the peak light intensity for four different soliton velocities (all subsonic, so as not to introduce the supersonic instability, which is detailed below). The growth rate of gap-acoustic solitons' instability is smaller the closer is the soliton velocity to the speed of sound. Common to both trends is that a larger phonon field has a stronger damping effect on the oscillatory instability. In contrast, without electrostriction, the dependence of the instability on soliton velocity is quite weak, and with no special importance to the speed of sound.

Next, we consider solitons which are known to be stable in the absence of electrostriction. Among our simulations, that is the runs with soliton parameters $Q = \pi/3$ and $Q = \pi/2$. All solitons that are stable with zero electrostriction were found to be stable with electrostriction and velocities up to the speed of sound. Above the speed of sound, a new and distinct ("supersonic") instability appears. It is associated with the downward slope of the soliton momentum with respect to velocity, which is due to the decreasing importance in the supersonic region of the acoustic contribution to the momentum as a function of soliton velocities. The su-

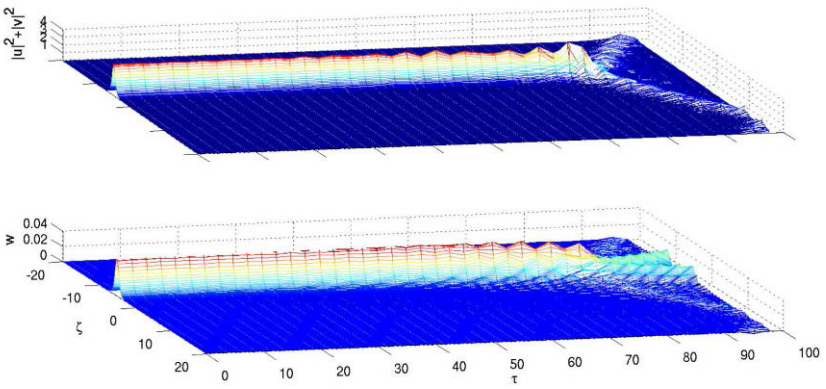

Fig. 3.4 Destruction of a gap-acoustic soliton by the oscillatory instability. The graph shows light intensity ($|u|^2+|v|^2$) and phonon fields (w). The soliton is described by parameter $Q=2\pi/3$, the velocity is zero ($\beta=0$), the electrostrictive coefficients are $\chi_{es}=1$, $\lambda=0.0005$, the speed of sound is $\beta_s=0.2$, and self- and cross-phase modulation are $\chi_s=1$, $\chi_x=2$.

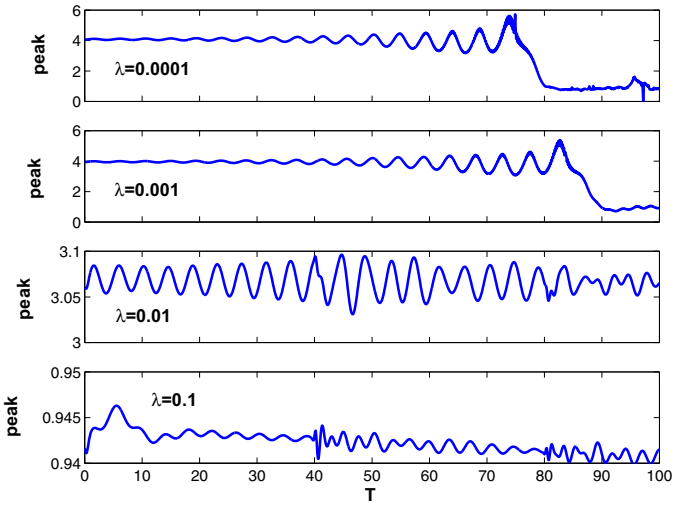

Fig. 3.5 Evolution of the peak powers $\{\max_\zeta(|u(\zeta,\tau)|^2+|v(\zeta,\tau)|^2)\}$ with time, for gap-acoustic solitons with four different electrostrictive coefficients, $\lambda=0.0001$, 0.001, 0.01, and 0.1, and $\chi_{es}=1$. The solitons are unstable, $Q=2\pi/3$, $\beta=0$, with self- and cross-phase modulation $\chi_s=1$, $\chi_x=2$, and speed of sound $\beta_s=0.2$.

personic instability goes away when the soliton velocity is high enough for the momentum in the electromagnetic part of the GAS to outweigh the momentum in the acoustic part of the GAS [19]. This supersonic instability is qualitatively different than the oscillatory instability, and is unknown for gap solitons without electrostriction. (A non-oscillatory and strongly velocity-dependent instability was found in Ref. [15]. This instability exists in a region that is already unstable because of two

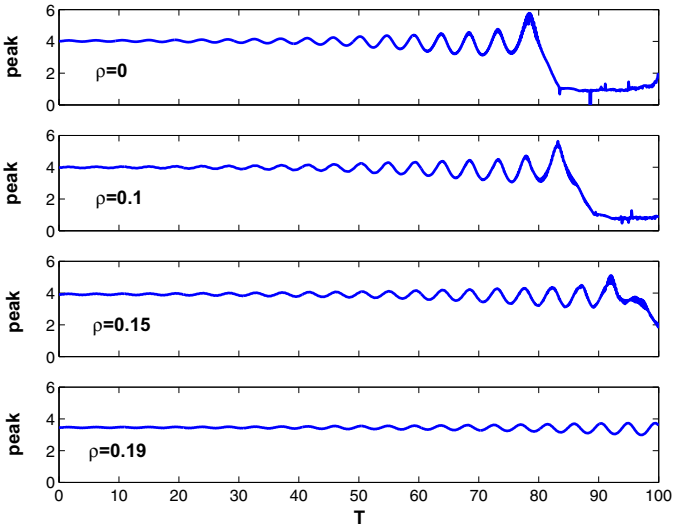

Fig. 3.6 Evolution of the peak powers $[\max_\zeta(|u(\zeta,\tau)|^2+|v(\zeta,\tau)|^2)]$ with time, for unstable gap-acoustic solitons at by four different subsonic velocities, $\beta = 0$, 0.1, 0.15, and 0.19, where the dimensionless speed of sound is $\beta = 0.2$. The solitons have electrostrictive coefficients, $\chi_{es} = 1$, $\lambda = 0.0005$, soliton parameter $Q = 2\pi/3$, and self- and cross-phase modulation $\chi_s = 1$, $\chi_x = 2$.

oscillatory instabilities, so may not be clearly realizable experimentally. It is not related to acoustic waves and the speed of sound plays no role in these dynamics.) Figures 3.7-3.8 show supersonic gap-acoustic soliton simulations, with the same parameters except for the initial soliton velocity. In almost all cases—displayed and not—the gap-acoustic solitons retained their integrity throughout the instability. The closer was the supersonic soliton's velocity to the speed of sound, the sooner the supersonic instability took effect. The changes in velocity were abrupt, and were accompanied by emission of phonons. The solitons sometimes changed speed and direction a few times before eventually settling to a stable subsonic GAS.

Figures 3.9-3.11 have the same parameters as Figs. 3.7-3.8, but with an order of magnitude larger electrostrictive coefficient. When the electrostrictive coefficient was larger (and the phonon field larger), the supersonic instabilities tended to be stronger in the sense that they happened sooner, and in that the soliton was more often destroyed. In some instances, as in Fig. 3.7, a soliton that was close to the speed of sound made a smooth transition to subsonic (necessarily passing through a non-solitonic configuration).

The GASs tend to end with velocities much slower than the speed of sound may because the momentum of the soliton is *larger* at slightly subsonic velocities than at many supersonic velocities. Figure 3.12 shows the momentum and energy in a soliton at fixed Q-parameter over a range of velocities. After onset of the supersonic instability, there is generally only enough momentum (and energy) for the resulting subsonic GAS to have a velocity up to a small percentage of the speed of sound.

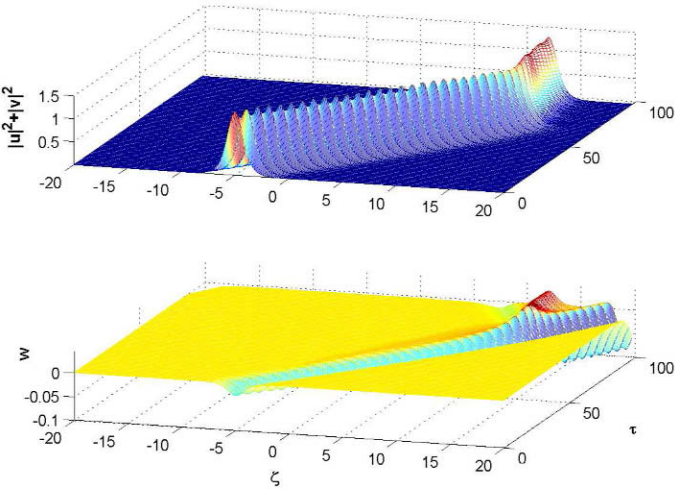

Fig. 3.7 Gap-acoustic soliton subject to the supersonic instability. The graph shows light intensity ($|u|^2 + |v|^2$) and phonon fields (W). The soliton parameter is ($Q = \pi/3$), with initially supersonic velocity ($\beta = 0.3$, compared to a speed of sound $\beta_s = 0.2$). The electrostrictive coefficients are $\chi_{es} = 1$, $\lambda = 0.001$, and self- and cross-phase modulation are $\chi_s = 1$, $\chi_x = 2$.

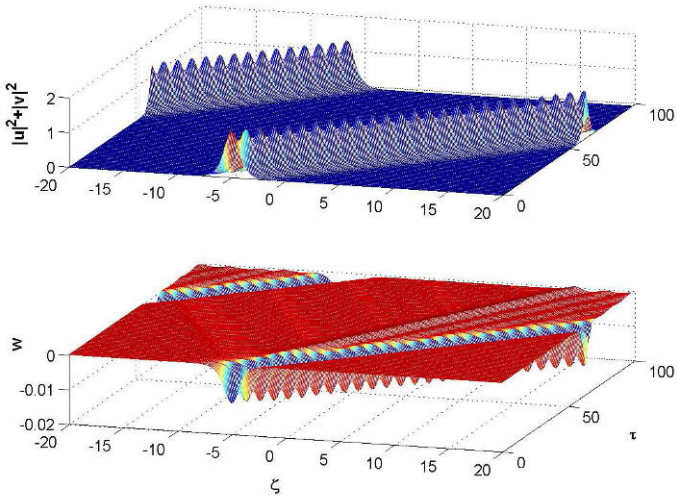

Fig. 3.8 Gap-acoustic soliton subject to the supersonic instability. The graph shows light intensity ($|u|^2 + |v|^2$) and phonon fields (W). The soliton parameter is ($Q = \pi/3$), with initially hypersonic velocity ($\beta = 0.4$, compared to a speed of sound $\beta_s = 0.2$). The electrostrictive coefficients are $\chi_{es} = 1$, $\lambda = 0.001$, and self- and cross-phase modulation are $\chi_s = 1$, $\chi_x = 2$.

The oscillatory instability and the supersonic instability can compete. For example, Fig. 3.13 shows a gap-acoustic soliton which first slows down sharply, going

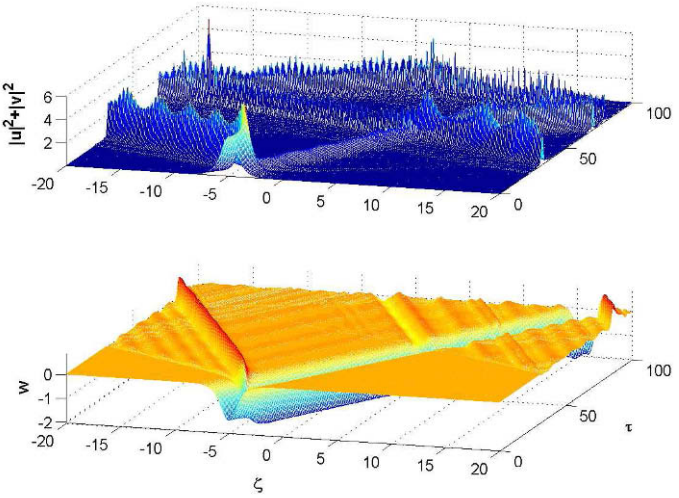

Fig. 3.9 Gap-acoustic soliton subject to the supersonic instability. The graph shows light intensity ($|u|^2 + |v|^2$) and phonon fields (W). The soliton parameter is ($Q = \pi/3$), with initially supersonic velocity ($\beta = 0.25$, compared to a speed of sound $\beta_s = 0.2$). The electrostrictive coefficients are $\chi_{es} = 1$, $\lambda = 0.01$, and self- and cross-phase modulation are $\chi_s = 1$, $\chi_x = 2$.

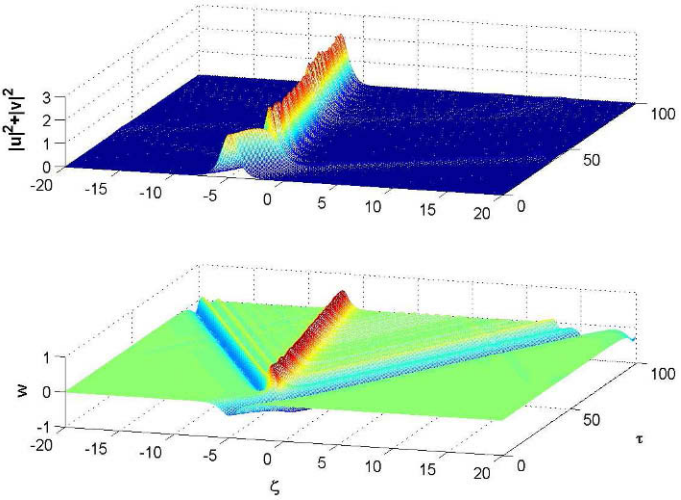

Fig. 3.10 Gap-acoustic soliton subject to the supersonic instability. The graph shows light intensity ($|u|^2 + |v|^2$) and phonon fields (W). The soliton parameter is ($Q = \pi/3$), with initially supersonic velocity ($\beta = 0.3$, compared to a speed of sound $\beta_s = 0.2$). The electrostrictive coefficients are $\chi_{es} = 1$, $\lambda = 0.01$, and self- and cross-phase modulation are $\chi_s = 1$, $\chi_x = 2$.

from supersonic to zero velocity, and after which the oscillatory instability grows until it destroys the soliton.

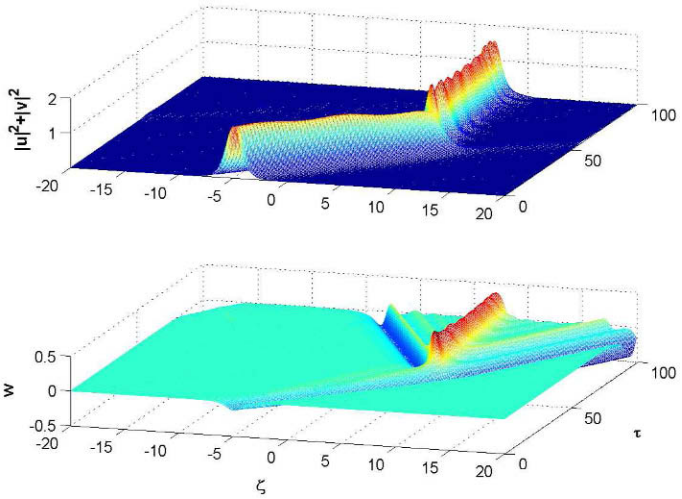

Fig. 3.11 Gap-acoustic soliton subject to the supersonic instability. The graph shows light intensity ($|u|^2 + |v|^2$) and phonon fields (W). The soliton parameter is ($Q = \pi/3$), with initially hypersonic velocity ($\beta = 0.4$, compared to a speed of sound $\beta_s = 0.2$). The electrostrictive coefficients are $\chi_{es} = 1$, $\lambda = 0.01$, and self- and cross-phase modulation are $\chi_s = 1$, $\chi_x = 2$.

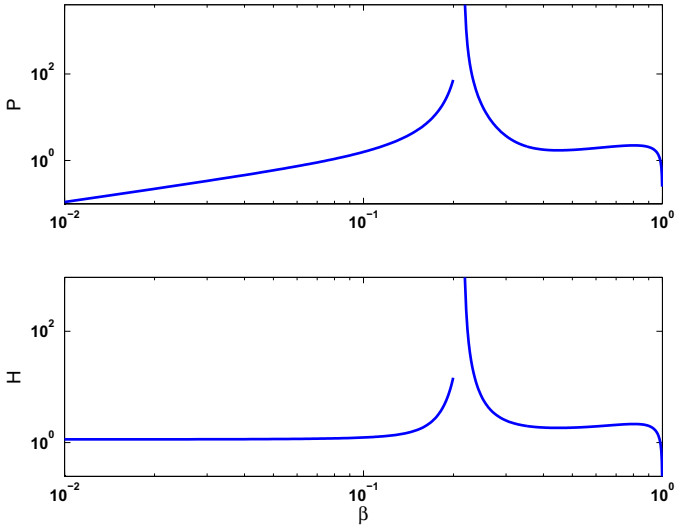

Fig. 3.12 Plots of the GAS momentum and energy over a range of soliton velocities, holding other parameters constant—$Q = \pi/2$, $\beta_s = 0.2$, $\chi_{es} = 1$, $\lambda = 0.01$, $\chi_s = 1$ and $\chi_x = 2$.

Larger electrostrictive coefficients damp the oscillatory instability and increase the supersonic instability, so changing the electrostriction can change the dominant type of instability. The dimensionality of the parameter space $(\chi_s/\chi_x, \lambda, \Gamma, \beta_s, \beta, Q)$ is too large, the behavior too varied, the sensitivity to initial conditions to strong,

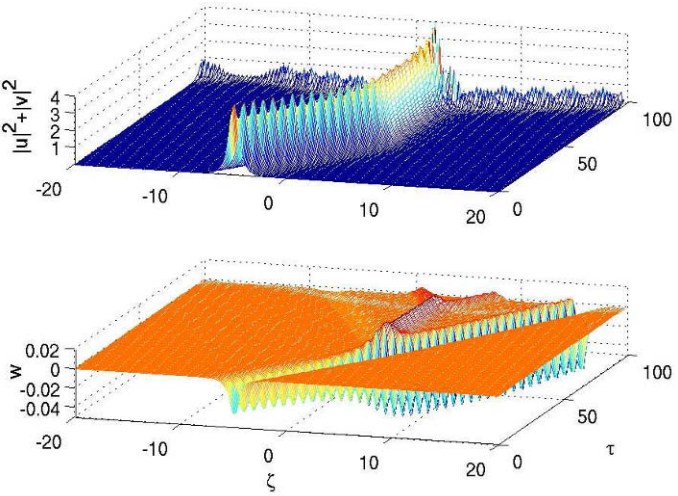

Fig. 3.13 Gap-acoustic soliton experiencing two instabilities, supersonic and oscillatory. The top and bottom parts of the figure show the light intensity and the material density, respectively. The soliton begins with dimensionless velocity $\beta = 0.25$, compared to sound velocity $\beta_s = 0.2$. The soliton parameter is $Q = 2\pi/3$, the electrostrictive coefficients are $\chi_{es} = 1$, $\lambda = 0.0002$, and self- and cross-phase modulation coefficients are $\chi_s = 1$, $\chi_x = 2$.

and the computational cost of numerical simulations too high to obtain a complete simple picture of the ultimate results following a GAS instability.

There are no breathers or localized excited states as a small perturbation about (i.e., on top of) the gap-acoustic solitons. Any oscillation of a localized mode generates waves in the acoustic field which move at velocity plus or minus the speed of sound. The acoustic field will carry away energy, dissipating the oscillations. Small oscillations have energy proportional to the amplitude of the oscillation, and the energy radiated away is also proportional to the square of the amplitude of the oscillation. Therefore, small oscillations about a stable GAS decay exponentially.

3.6 Summary and Conclusions

In this work, we formulated a set of equations to describe propagation of light in a nonlinear waveguide with a Bragg grating, with the light coupled to sound waves by electrostriction. Light waves' dispersion curve has a band gap in the vicinity of the resonance of the Bragg grating. Forward- and backward-moving light in the vicinity of the band gap can interact with acoustic waves of low wave numbers (in which case the interaction is generally referred to as electrostriction) or high wave numbers, twice the wave numbers of the light (in which case the interaction is called Brillouin scattering).

There is a localized structure in this system—a "gap-acoustic soliton", for the case when Brillouin scattering may be neglected; there is an exact analytic form of the solitons for the case of vanishing phonon viscosity, as well as for zero velocity solitons. Gap-acoustic solitons have frequencies in the band gap, as do standard gap solitons (without electrostriction). They exist at all velocities up to the speed of light in the medium, except for exactly the speed of sound (near which the phonon component of the soliton is large, and at which there is a singularity). Coupling of the light to the acoustic field via electrostriction changes the stability properties of the soliton. Solitons which would experience an oscillatory instability without electrostriction experience a damping of the instability, the larger the electrostrictive coefficient and/or the closer the velocity is to the speed of sound, the larger is the damping of the oscillatory instability. Electrostriction introduces a new "supersonic" instability for gap-acoustic solitons moving faster than the speed of sound. The closer the soliton is to the speed of sound, the faster the supersonic instability takes effect. The supersonic instability may cause an abrupt change in the velocity, or sometimes destruction of the soliton. The soliton may experience several changes in direction or some complex dynamics before going to a stable subsonic soliton or being destroyed. Phonon viscosity slows the gap-acoustic soliton and causes emission of significant phonon radiation. If the soliton is subsonic, the soliton velocity will decrease exponentially, and if the soliton is supersonic, phonon viscosity will slow the soliton to the speed of sound in finite time. Solitons cannot exist with speeds between the critical velocity and the speed of sound. But if the phonon viscosity makes the soliton pass through the velocity gap quickly, a soliton will emerge as a similar but subsonic gap-acoustic soliton. At velocities close to the group-velocity of light in the waveguide, Brillouin scattering can make the soliton emit acoustic radiation, which carries away momentum, and acts as an additional retardation mechanism for the moving soliton.

Since electrostriction, like the Kerr effect, is present to some extent in virtually all materials, any understanding of physically realistic optical gap solitons should entail a grasp of the effects of electrostriction. The results herein suggest that an initially fast-moving gap-acoustic soliton can be retarded by the effects of the nonzero phonon viscosity. A practical means of doing this would be in a recirculating loop. Either alternatively or complementarily, once a gap-acoustic soliton is slowed to on the order of the speed of sound, the gap-acoustic solitons supersonic instability will do the work of slowing the soliton to soliton to significantly below the speed of sound. In addition, the dynamics of gap-acoustic solitons open the door to new means of controlling light by sound.

References

1. G. P. Agrawal, *Nonlinear Fiber Optics* (Academic, San Diego, 2006).
2. M. J. Ablowitz and H. Segur, *Solitons and the Inverse Scattering Transform* (Society for Industrial and Applied Mathematics, 1981).
3. J. S. Russell, Report of the Eighteen Meeting of the British Association for the Advancement of Science (John Murray, London, 1849) **18**, 37.
4. D. J. Korteweg and G. de Vries, Philos. Mag. Ser. **5**, 422 (1895).
5. C. S. Gardner, J. M. Greene, M.D. Kruskal and R. M. Miura, Phys. Rev. Lett. **19** 1095, (1967).
6. V. E. Zakharov and A. B. Shabat Sov. Phys. JETP **34**, 62 (1972).
7. A. Hasegawa and F. Tappert, Appl. Phys. Lett. **23**, 171 (1973).
8. W. E. Thirring, Annals Phys. **3**, 91 (1958).
9. E. A. Kuznetsov and A. V. Mikhailov, Teor. Mat. Fiz. **30**, 193 (1977); D. J. Kaup and A. C. Newell, Lett. Nuovo Cimento **20**, 325 (1977).
10. B. J. Eggleton, C. Martijn de Sterke, and R. E. Slusher, J. Opt. Soc. Am. B **16**, 587 (1999).
11. W. Chen and D. L. Mills, Phys. Rev. Lett. **58**, 160 (1987).
12. D. N. Christodoulides and R. I. Joseph, Phys. Rev. Lett. **62**, 1746 (1989).
13. A. B. Aceves and S. Wabnitz, Phys. Lett. A **141**, 37 (1989).
14. B. A. Malomed and R. S. Tasgal, Phys. Rev. E **49**, 5787 (1994).
15. I. V. Barashenkov, D. E. Pelinovsky, and E. V. Zemlyanaya, Phys. Rev. Lett. **80**, 5117 (1998);
16. I. V. Barashenkov and E. V. Zemlyanaya, Comp. Phys. Comm. **126**, 22 (2000);
17. A. De Rossi, C. Conti, and S. Trillo, Phys. Rev. Lett. **81**, 85 (1998).
18. R. S. Tasgal, Y. B. Band, and B. A. Malomed, Phys. Rev. Lett. **98**, 243902 (2007).
19. R. S. Tasgal, R. Shnaiderman, and Y. B. Band, J. Opt. Soc. Am. B, in press.
20. J. D. Jackson, *Classical Electrodynamics* (Wiley, NY, 1975)
21. M. Born and E. Wolf, *Principles of Optics* (Pergamon, NY, 1980).
22. R. W. Boyd, *Nonlinear Optics* (Academic, NY, 2003).
23. M. D. Lukin and A. Imamoglu, Nature **413**, 273 (2001); R. W. Boyd and D. J. Gauthier, Progress in Optics **43**, 497 (2002).
24. A. B. Aceves, Chaos **10**, 584 (2002).
25. C. M. de Sterke, and J. E. Sipe, Progr. Opt. **33**, 203 (1994).
26. "Focus Issue: Bragg Solitons and Nonlinear Optics of Periodic Structures," Opt. Exp. **3**, 384 (1998).
27. W. C. K. Mak, B. A. Malomed, and P. L. Chu, J. Mod. Opt. **51**, 2141 (2004).
28. W. C. K. Mak, B. A. Malomed, and P. L. Chu, Phys. Rev. E **68**, 026609 (2003).
29. J. T. Mok, C. M. de Sterke, I. C. M. Littler, and B. J. Eggleton, Nature Phys. **2**, 775 (2006).
30. E. Rat, M. Foret, G. Massiera, R. Vialla, M. Arai, R. Vacher, and E. Courtens, Phys. Rev. B **72**, 214204 (2005); R. Vacher, E. Courtens, and M. Foret, Phys. Rev. B **72**, 214205 (2005). A. Devos, M. Foret, S. Ayrinhac, P. Emery, and B. Ruffl, Phys. Rev. B **77**, 100201 (2008).
31. I. L. Fabelinskii, *Molecular Scattering of Light* (Plenum, NY, 1968).
32. P. J. Thomas, N. L. Rowell, H. M. van Driel, and G. I. Stegeman, Phys. Rev. B **19**, 4986 (1979); D. T. Hon, Opt. Lett. **5**, 516 (1980); R. M. Shelby, M. D. Levenson, and P. W. Bayer, Phys. Rev. B **31**, 5244 (1985); K. Smith and L. F. Mollenauer, Opt. Lett. **14**, 1284 (1989); E. L. Buckland and R. W. Boyd, Opt. Lett. **21**, 1117 (1996); E. L. Buckland and R. W. Boyd, Opt. Lett. **22**, 676 (1997); A. Fellegara, A. Melloni, and M. Martinelli, Opt. Lett. **22**, 1615 (1997); P. J. Hardman, P. D. Townsend, A. J. Poustie, and K. J. Blow, Opt. Lett. **21**, 393 (1996); E. M. Dianov, A. V. Luchnikov, A. N. Pilipetskii, and A. N. Starodumov, Opt. Lett. **15**, 314 (1990).
33. J. Feng and F. K. Kneubuhl, IEEE J. Quantum Electron **29**, 590 (1992).
34. V. E. Zakharov, Zh. Eksp. Teor. Fiz. **62**, 1745 (1972) [Sov. Phys. JETP **35**, 908 (1972)].
35. A. S. Davidov, Phys. Scr. **20**, 387 (1979); L. Stenflo, Phys. Scr. **33**, 156 (1986).
36. H. Hadouaj, B. A. Malomed, and G. A. Maugin, Phys. Rev. A **44**, 3925–3931 (1991); H. Hadouaj, B. A. Malomed, and G. A. Maugin, Phys. Rev. A **44** 3932–3940 (1991); G. A. Maugin, H. Hadouaj, and B. A. Malomed, Phys. Rev. B **45**, 9688–9694 (1992).
37. V. I. Karpman, Phys. Scripta **20**, 462 (1979); V. I. Karpman and V. V. Solovev, Physica D **3**, 487 (1981).

Chapter 4
Optical Wave Turbulence and Wave Condensation in a Nonlinear Optical Experiment

Jason Laurie, Umberto Bortolozzo, Sergey Nazarenko and Stefania Residori

Abstract We present theory, numerical simulations and experimental observations of a 1D optical wave system. We show that this system is of a dual cascade type, namely, the energy cascading directly to small scales, and the photons or wave action cascading to large scales. In the optical context the inverse cascade is particularly interesting because it means the condensation of photons. We show that the cascades are induced by a six-wave resonant interaction process described by weak turbulence theory. We show that by starting with weakly nonlinear randomized waves as an initial condition, there exists an inverse cascade of photons towards the lowest wavenumbers. During the cascade nonlinearity becomes strong at low wavenumbers and, due to the focusing nature of the nonlinearity, it leads to modulational instability resulting in the formation of solitons. Further interaction of the solitons among themselves and with incoherent waves leads to the final condensate state dominated by a single strong soliton. In addition, we show the existence of the direct energy cascade numerically and that it agrees with the wave turbulence prediction.

Jason Laurie
Mathematics Institute, University of Warwick, Coventry CV4 7AL, United Kingdom e-mail: J.P.Laurie@warwick.ac.uk

Umberto Bortolozzo
INLN, Université de Nice Sophia-Antipolis, CNRS, 1361 route des Lucioles 06560 Valbonne, France, e-mail: Umberto.Bortolozzo@inln.cnrs.fr

Sergey Nazarenko
Mathematics Institute, University of Warwick, Coventry CV4 7AL, United Kingdom e-mail: S.V.Nazarenko@warwick.ac.uk

Stefania Residori
INLN, Université de Nice Sophia-Antipolis, CNRS, 1361 route des Lucioles 06560 Valbonne, France, e-mail: Stefania.Residori@inln.cnrs.fr

O. Descalzi et al. (eds.), *Localized States in Physics: Solitons and Patterns*,
DOI 10.1007/978-3-642-16549-8_4,

4.1 Introduction

The idea to create a state of optical wave turbulence (OWT) has been the subject of a large number of theoretical papers over the last thirty years [1, 2, 3, 4, 5]. Indeed there are some far-reaching fluid analogies in the dynamics of nonlinear light, for example vortex-like solutions [15, 7] and shock waves [8]. In the case of weakly interacting random waves, the dynamics and statistics of the optical field are predicted to share strong similarities with the system of random waves on water surface [9]. Indeed, OWT was theoretically predicted to exhibit dual cascade properties similar to 2D fluid turbulence, namely the energy cascading directly, from low to high frequencies, and the photons cascading inversely, toward the low energy states.

The mechanism for optical interactions is provided by the Kerr effect, which is routinely used in nonlinear optics and permits photon wave-mixing. When the nonlinearity is small, OWT can be described by *wave turbulence theory* (WTT) [9] which possesses classical attributes of general turbulence theory, particularly predictions of the Kolmogorov-like cascade states, which in the WTT context are called Kolmogorov-Zakharov (KZ) spectra. It appears that OWT has two KZ states: one describing the direct energy cascade from large to small scales, and the second one - an inverse cascade of wave action toward larger scales. It is the inverse cascade that can provide the mechanism for condensation of light, i.e. formation of a coherent phase out of initially incoherent wave field. Furthermore, it was theoretically predicted that in the course of the inverse cascade the nonlinearity will grow, which will eventually lead to the breakdown of WTT at a some low wavenumber k and the formation of coherent structures, i.e. solitons/collapses for the focusing nonlinearity or a quasi-uniform condensate and vortices [5] for the de-focusing case.

Experimentally, the problem of realizing the OWT state is that the nonlinearity is usually very weak and it is a challenge to make it overpower the dissipation. Here we show that the OWT regime can be implemented in a liquid crystal system [10], where optical solitons have been previously reported [11]. Our experiment is based on the propagation of an enlarged light beam inside a liquid crystal layer acting as the nonlinear medium. The principal direction of the light propagation plays the role of time and the 2D field evolution is described by a nonlinear Schrödinger equation (NLSE). Starting with weakly nonlinear waves with randomized phases, we observe the formation of an inverse cascade of photons towards the lowest wavenumbers. We show that the cascade is induced by a six-wave resonant interaction process, and it is characterized by increasing nonlinearity along the cascade. At low wavenumbers the nonlinearity becomes strong and, due to the focusing nature of the nonlinearity, it leads to modulational instability developing into solitons. Further interaction of the solitons among themselves and with incoherent waves leads to the final condensate state dominated by a single strong soliton.

Furthermore, it was theoretically predicted, and numerically observed in some WT systems, that in the course of the inverse cascade the nonlinearity will grow, which will eventually lead to the breakdown of the WTT description at low wavenumbers and to the formation of coherent structures [1, 3, 5, 12, 13, 2]. In optics, these can be solitons or collapses for focusing nonlinearity or a quasi-uniform condensate

and vortices for the defocusing case. The final thermalized state was studied extensively theoretically in various settings for non-integrable Hamiltonian systems starting with the pioneering paper by Zakharov *et al* [14], see also [15, 16, 17, 18, 19, 20, 21, 22, 23, 24]. The final state with a single soliton and small-scale noise was interpreted as a statistical attractor, and an analogy was pointed out to the over-saturated vapor system, where the solitons are similar to droplets and the random waves are like molecules [24]. There, small droplets evaporate while the big ones gain size from the free molecules, resulting in the decrease in the number of droplets. In our work we put emphasis on turbulence, i.e. on a transient non-equilibrium process leading to thermalization rather than the thermal equilibrium itself.

4.2 Experimental setup

The experimental apparatus is shown in Fig.4.1a. It consists of a liquid crystal cell, inside which a laminar shaped beam propagates, and with the input beam prepared in such a way, as to have an initial condition of weak and random waves. The liquid crystal (LC) cell is made by sandwiching a nematic layer (E48) of thickness $d = 50\ \mu m$ between two $20 \times 30\ mm^2$ glass windows and is schematically depicted in Fig.4.1b. On the interior, the glass walls are coated with Indium-Tin-Oxide (ITO) transparent electrodes. We have pre-treated the ITO surfaces with polyvinyl-alcohol, polymerized and then rubbed, in order to align all the molecules parallel to the confining walls. When a voltage is applied across the cell, liquid crystal molecules tend to reorient in such a way as to become parallel to the direction of the electric field. By applying a $1kHz$ electric field with rms voltage $V_0 = 2.5\ V$ we preset the molecular director to an average tilt angle Θ.

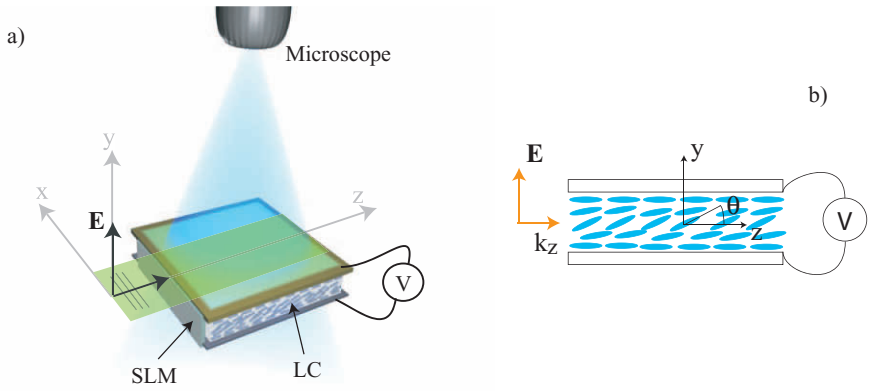

Fig. 4.1 Schematic representation of a) the experimental setup, b) the liquid crystal cell. A laminar shaped input beam propagates inside the liquid crystal (LC) layer; random space modulations are imposed at the entrance of the cell by means of a spatial light modulator (SLM). A voltage V is applied to the LC in order to favor the molecular reorientation towards the optical field **E**.

The LC layer behaves as a positive uniaxial medium, with $n_{\parallel} = n_z = 1.7$ the extraordinary and $n_{\perp} = 1.5$, the ordinary refractive indices [25]. LC molecules tend to turn more along the applied field and the refractive index $n(\Theta)$ follows the distribution of the tilt angle θ. When a linearly polarized beam is injected into the cell, the LC molecules reorient following the direction of the incoming beam polarization. The input light comes from a diode pumped solid state laser, $\lambda = 473\ nm$, polarized along y and shaped as a thin laminar Gaussian beam of 30 μm thickness. The beam evolution inside the cell is monitored with an optical microscope and a CCD camera. The light intensity is kept very low, $I_{in} = 30\ \mu W/cm^2$ to ensure the weakly nonlinear regime. A SLM at the entrance plane of the cell is used to produce suitable intensity masks for injecting random phased fields with large wavenumbers.

4.3 Theoretical Background

Theoretically, the evolution is described by a propagation equation for the input beam coupled to a relaxation equation for the LC dynamics

$$2iq\frac{\partial \psi}{\partial z} + \frac{\partial^2 \psi}{\partial x^2} + k_0^2 n_a^2 a\psi = 0, \tag{4.1}$$

$$\frac{\partial^2 a}{\partial x^2} - \frac{1}{l_\xi^2}a + \frac{\varepsilon_0 n_a^2}{4K}|\psi|^2 = 0, \tag{4.2}$$

where $\psi(x,z)$ is the complex amplitude of the input beam propagating along "time axis" $\hat{z}$, x the coordinate across the beam, a the liquid crystal reorientation angle, $n_a = n_e - n_o$ the birefringence of the LC, k_0 the optical wavenumber, ε_0 the vacuum permittivity and $l_\xi = \sqrt{\pi K/2\Delta\varepsilon}(d/V_0)$ the electrical coherence length of the LC [42], with K the elastic constant, $q^2 = k_0^2\left(n_o^2 + n_a^2/2\right)$ and $\Delta\varepsilon$ the dielectric anisotropy. Note that l_ξ fixes the typical dissipation scale, limiting the extent of the inertial range in which the OWT cascade develops. In other contexts, see e.g. [11, 27, 28], such a spatial diffusion of the molecular deformation has been denoted as a nonlocal effect. In our experiment, for $V_0 = 2.5\ V$ we have $l_\xi = 9\ \mu m$. By considering that a typical value of K is of the order of $\sim 10\ pN$, we can derive a typical dissipation length scale of the order of $\sim 10\ \mu m$.

4.3.1 Evolution Equation

Our system is modeled by two coupled equations, one describing the evolution of the complex amplitude of the input beam $\psi(x,z)$, equation (4.1) and the second for the liquid crystal reorientation angle $a(x,z)$, equation (4.2). However, it is convenient for us to construct a single evolutionary equation for the complex wave amplitude

$\psi(x,z)$. The system of equations (4.1) and (4.2) can be formally re-written, so that one eliminates the variable $a(x,z)$. In order to achieve this, one must invert the operator applied to $a(x,z)$ in equation (4.2). Subsequently, this procedure yields a single equation for the complex amplitude of the beam $\psi(x,z)$,

$$2iq\frac{\partial\psi}{\partial z}+\frac{\partial^2\psi}{\partial x^2}+\frac{k_0^2n_a^4\varepsilon_0}{4K}\psi\left(\frac{1}{l_\xi^2}-\frac{\partial^2}{\partial x^2}\right)^{-1}|\psi|^2=0. \tag{4.3}$$

Equation (4.3) models the full dynamics of the complex wave function $\psi(x,z)$, to the same extent as the system described by equations (4.1) and (4.2). On inspection of equation (4.3) we find that the operator applied to the nonlinear term is rather complicated and would not yield a scale invariant nonlinear interaction coefficient convenient for the application of WTT. The experimental setup is located in the long-wave limit, $kl_\xi \ll 1$ due to the nature of the LC. Therefore, we can overcome the problem of the nonlinear operator by expanding in terms of the small parameter kl_ξ.

4.3.2 Long-Wave Model

We derive this long-wave model by Taylor expanding the nonlinear operator in equation (4.3) in the limit $kl_\xi \ll 1$. Taking the expansion up to the order of $\mathcal{O}((kl_\xi)^4)$, one can derive an evolutionary equation for the wave function $\psi(x,z)$ that is of the form of a modified 1D NLSE. Note, that we took the expansion of the nonlinear operator up to the second order, this is because if we take the leading order, we would have identically the 1D NLSE, which is a completely integrable system. So the resultant non-integrable model for the evolution of $\psi(x,z)$ in the long-wave limit is,

$$2iq\frac{\partial\psi}{\partial z}=-\frac{\partial^2\psi}{\partial x^2}-\frac{\varepsilon_0n_a^4l_\xi^2k_0^2}{4K}\left(\psi|\psi|^2+l_\xi^2\psi\frac{\partial^2|\psi|^2}{\partial x^2}\right). \tag{4.4}$$

Equation (4.4) hold the property that it conserves the energy,

$$H=\int\left|\frac{\partial\psi}{\partial x}\right|^2-\frac{\varepsilon_0n_a^4l_\xi^2k_0^2}{8K}\left[|\psi|^4-l_\xi^2\left(\frac{\partial|\psi|^2}{\partial x}\right)^2\right]dx, \tag{4.5}$$

where H is defined as the Hamiltonian of the system and satisfies $2iq\partial\psi/\partial z=\delta H/\delta\psi^*$. Also equation (4.4) conserves the total number of photons, or wave action,

$$N=\int|\psi|^2dx. \tag{4.6}$$

4.3.3 The Fjørtoft Argument

As already mentioned, our system possesses two conserved quantities (energy H, and total wave action N), and as such will support a dual cascade regime [1]. This is analogous to 2D turbulence, where entrophy cascades towards high wavenumbers and energy towards low wavenumbers. It is worth to point out that, as opposed to 2D turbulence, WTT assumes weak nonlinearity of the system, and as such implies smallness of wave amplitudes. This weak nonlinearity assumption also implies that the linear energy is dominant over the nonlinear energy. In the case of weak nonlinearity, one can determine the direction of each cascade, by applying a Fjørtoft style argument [29].

Suppose that the forcing and damping occur over certain intervals of wavenumber space, damping near $k = 0$ to absorb the inverse cascade of particles, excitation in a small interval at intermediate wavenumber around $k = k_0$, and finally high frequency dissipation for $k > k_D$. Then, transfer of wave action an energy takes places and fluxes can be defined as

$$Q_k = \int_0^k \frac{\partial n_{k'}}{\partial t} dk' \tag{4.7}$$

$$P_k = \int_0^k \omega_{k'} \frac{\partial n_{k'}}{\partial t} dk', \tag{4.8}$$

representing, respectively, the flux of particle towards low wavenumbers and the flux of energy towards high wavenumbers. The Fjørtoft reasoning goes as follows: Assume that the system has reached a steady state, therefore the total amount of energy flux P_k, and wave action flux Q_k, contained within the system must be zero, i.e. $\int P_k dk = 0$, and $\int Q_k dk = 0$ respectively. Then, let the system be forced at a specific intermediate scale k_f, with both energy and wave action fluxes being generated into the system at rates P_f and Q_f. Moreover, let there exist two sinks, one at the high wavenumber limit $k_+ \gg k_f$, with energy and wave action being dissipated at rates P_+ and Q_+, and one at the low wavenumber limit $k_- \ll k_f$, dissipated at rates P_- and Q_-. Therefore, in between forcing and dissipation there exist two distinct inertial ranges where neither forcing or dissipation has an effect. In the weakly nonlinear regime, the energy flux is related to the wave action flux by $P_k \approx \omega_k Q_k = k^2 Q_k$. Therefore, in a steady state system, the energy and wave action balance implies that

$$P_f = P_- + P_+, \tag{4.9}$$

$$Q_f = Q_- + Q_+, \tag{4.10}$$

and roughly speaking, from weak nonlinearity we have

$$P_f \approx k_f^2 Q_f, \tag{4.11}$$

$$P_- \approx k_-^2 Q_-, \tag{4.12}$$

$$P_+ \approx k_+^2 Q_., \tag{4.13}$$

Subsequently, the balance equations (4.9) and (4.10) can be written as

$$k_f^2 Q_f \approx k_-^2 Q_- + k_+^2 Q_+, \tag{4.14}$$

$$Q_f = Q_- + Q_+, \tag{4.15}$$

respectively. One can then rearrange equations (4.14) and (4.15), so that we can predict at what rates the wave action and energy fluxes are dissipated at the two sinks at dissipative scales k_- and k_+. From equations (4.14) and (4.15) we find that,

$$Q_+ = \frac{k_f^2 - k_-^2}{k_+^2 - k_-^2} Q_f, \tag{4.16}$$

$$Q_- = \frac{k_f^2 - k_+^2}{k_-^2 - k_+^2} Q_f. \tag{4.17}$$

If we consider the region around large scales, $k_- \ll k_f < k_+$, then we have from equation (4.16): $k_f^2 Q_f \approx k_+^2 Q_+$ i.e. that energy is mostly absorbed at the region around k_+. Moreover, considering the region around small scales $k_- < k_f \ll k_+$, we have from (4.17) that $Q_f \approx Q_-$ i.e. that wave action is mostly absorbed at regions around k_-, this is illustrated in Fig. 4.2. Therefore, if we force at an intermediate scale, we should have the majority of the energy flowing towards high wavenumbers and the majority of the wave action flowing towards small wavenumbers. This determines the dual cascade picture of 1D OWT.

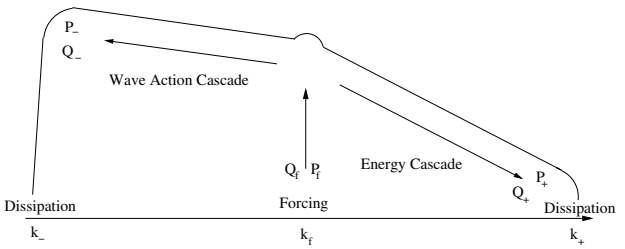

Fig. 4.2 The dual cascade regime in 1D OWT.

4.3.4 Hamiltonian Formulation

The Hamiltonian formulation provides a very convenient way of describing systems with waves. It enables us separate the linear and nonlinear wave dynamics and to mathematically describe their wave interactions. The most desirable way of describing the wave dynamics is to represent the Hamiltonian system in terms of the wave action variable $a(k,z)$. The wave action variable $a(k,z)$ is the Fourier coefficient in the Fourier representation of the complex beam amplitude variable $\psi(x,z)$, defined by its Fourier transform. Hamiltonian (4.5) can be written in terms of the wave action variable and can be expressed in the form,

$$H = H_2 + H_4 = \int \omega_k a_k a_k^* dk + \int W_{1234}\delta_{34}^{12} a_1 a_2 a_3^* a_4^* dk_{1234}, \tag{4.18}$$

we use the notation that $a(k_1,z)=a_1$, $\delta_{34}^{12}=\delta(k_1+k_2-k_3-k_4)$, $dk_{1234}=dk_1dk_2dk_3dk_4$ and * to denote the complex conjugate. The linear wave frequency is $\omega_k = k^2$, and the four-wave interaction coefficient W_{1234} for the nonlinear interaction of waves is

$$W_{1234} = \frac{\varepsilon_0 n_a^4 l_\xi^4 k_0^2}{16K}\left(k_1k_4 + k_2k_3 + k_2k_4 + k_1k_3 - 2k_3k_4 - 2k_1k_2\right) - \frac{\varepsilon_0 n_a^4 l_\xi^2 k_0^2}{8K}. \tag{4.19}$$

Hamiltonian (4.18) can be easily split into terms of differing orders of interaction (or nonlinearity) with respect to the wave action variable a_k. Hamiltonian (4.18), can be split into a quadratic term, H_2 - this corresponds to the linear wave dynamics of the propagation of a wave with linear frequency ω_k. But in addition, we have a quadric term H_4, which corresponds to the nonlinear wave dynamics.

In the limit $\varepsilon_0 n_a^4 l_\xi^2 k_0^2/2K \to 0$, equation (4.4) becomes the linear Schrödinger equation which has linear wave solutions $\psi(x,z) \sim b_k \exp(-i\omega_k z + ikx)$ with "frequencies" $\omega = k^2$ and constant complex amplitudes b_k. For weak nonlinearity the amplitude b_k become weakly dependent on "time" z.

Applicability of WTT needs to be checked, this is achieved by verify that the linear dynamics do indeed dominate in the system. The ratio of the linear term and the leading nonlinear term in the long-wave model is

$$J = \frac{4Kk^2}{\varepsilon_0 n_a^4 k_0^2 l_\xi^2 I}, \tag{4.20}$$

where $I = |\psi|^2$ is the input intensity. For the weak nonlinear regime to be reached, we require that the nonlinearity parameter $1 \ll J$. For nonlinear wave mixing to occur, waves must be in a state of resonance, this means that they must satisfy a resonance condition on the conservation of wavenumbers and frequencies. These conditions together are known as the resonant manifold condition, where both

$$k + k_1 - k_2 - k_3 = 0, \quad \omega_k + \omega_1 - \omega_2 - \omega_3 = 0, \tag{4.21}$$

are satisfied (for four-wave interactions). For a one-dimensional system with dispersion $\sim k^2$ there exists no non-trivial solution to the resonance condition (4.21). However, WTT provides a near-identity transformation that allows one to eliminate unnecessary lower orders of nonlinearity in the system if the corresponding order of wave interactions are absent.

4.3.5 Canonical Transformation

The near-identity transformation allows one to eliminate "unnecessary" lower orders of nonlinearity in the system if corresponding order of the wave interaction process is zero, i.e. there exist no non-trivial solutions to the resonant manifold condition of that order [9].

In our case, there can be no four-wave resonances (there are no non-trivial solution for the resonance conditions in for $\omega \sim k^x$ if $x > 1$). There are also no five-wave resonances because the original terms in the Hamiltonian are of the even orders. However, there are non-trivial solutions of the six-wave resonant conditions. Thus, one can use the near-identity transformation to convert our system into one with the lowest order interaction Hamiltonian to be of degree six.

A trick for finding a shortcut derivation of such a transformation is found in [9]. It relies on the fact that the time evolution operator is a canonical transformation. Taking the Taylor expansion of $a(k,z)$ around $a(k,0) = c(k,0)$ we get a desired transformation, that is by its derivation, canonical. The coefficients of each term can be calculated from an auxiliary Hamiltonian H_{aux} - this is a generic Hamiltonian with arbitrary interaction coefficients that once found, determines the canonical variable c_k.

A similar procedure was done in Appendix A3 of [9] to eliminate the cubic Hamiltonian in cases when the three-wave interaction is nil, and here we apply a similar approach to eliminate the quadric Hamiltonian. The transformation is represented as

$$a_k = c(k,0) + z\left(\frac{\partial c(k,z)}{\partial z}\right)_{z=0} + \frac{z^2}{2}\left(\frac{\partial^2 c(k,z)}{\partial z^2}\right)_{z=0} + \cdots \tag{4.22}$$

The transformation is canonical for all z, so for simplicity we set $z = 1$. Subsequently, Hamiltonian (4.18) can be transformed into,

$$H = H_2 + H_6 = \int \omega_k c_k c_k^* dk + \int T_{123456}\delta_{456}^{123} c_1^* c_2^* c_3^* c_4 c_5 c_6 dk_{123456}. \tag{4.23}$$

The explicit formula for T_{123456} stemming from the transformation is

$$T_{123456} = -\frac{1}{18}\sum_{i,j,k=1,i\neq j\neq k\neq i}^{3}\ \sum_{p,q,r=4,p\neq q\neq r\neq p}^{6}\left(\frac{W_{p+q-iipq}W_{j+k-rrjk}}{(\omega_{j+k-r}+\omega_r-\omega_j-\omega_k)}+\right.$$
$$\left.+\frac{W_{i+j-ppij}W_{q+r-kkqr}}{(\omega_{q+r-k}+\omega_k-\omega_q-\omega_r)}\right). \tag{4.24}$$

The six-wave interaction coefficient T_{123456} is formed from a coupling of two four-wave interactions W_{1234}, i.e. the six-wave interaction is produced from two coupled four-wave interactions that occur simultaneously, a simple graphic showing this is depicted in Fig. 4.3.

We find that the six-wave interaction coefficient T_{123456} is the sum of two terms of different scalings. However, in the long-wave limit, $kl_\xi \ll 1$, T_{123456} tends towards a k-independent constant

$$T_{123456} = \frac{\varepsilon_0^2 n_a^8 l_\xi^6 k_0^4}{64K^2}. \tag{4.25}$$

This implies that the six-wave interaction coefficient goes to zero in the long-wave limit.

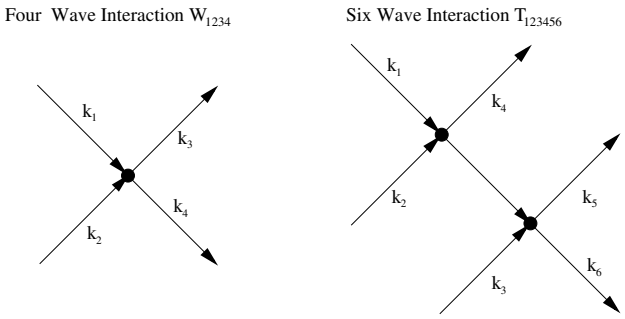

Fig. 4.3 Graphic to show how the six wave interactions arises from the coupling of two four wave interactions

4.3.6 The Kinetic Wave Equation

The kinetic wave equation (KE) describes the evolution of the wave action density $n_k = \langle c_k c_k^* \rangle$ (the averaging is over the random phases) of wave packets in Fourier space. In order to derive the kinetic equation, we must express the wave action Hamiltonian (4.23) into an equation for the wave action density n_k, by applying a random phase approximation (RPA). The dynamical equation for the variable c_k can be determined from Hamiltonian (4.23) by the relation $i\partial c_k/\partial z = \delta H/\delta c_k^*$,

$$i\frac{\partial c_k}{\partial z} - \omega_k c_k = \int T_{k12345} c_1^* c_2^* c_3 c_4 c_5 \delta_{345}^{k12} dk_{12345}. \tag{4.26}$$

By multiplying equation (4.26) by c_k^*, subtracting the complex conjugate, and averaging we arrive at

$$\frac{\partial n_k}{\partial z} = \frac{\partial \langle c_k c_k^* \rangle}{\partial z} = 6Im\left(\int T_{k12345} J_{k12345} \delta_{345}^{k12} dk_{12345} \right), \tag{4.27}$$

where $J_{k12345}\delta_{345}^{k12} = \langle c_k^* c_1^* c_2^* c_3 c_4 c_5 \rangle$.

To compute the average applied to J_{k12345}, one must use a RPA. Taking J_{k12345} to the zeroth order $J_{k12345}^{(0)}$ by assuming a Gaussian wave field, implies $J_{k12345}^{(0)}$ can be written as a product of three pair correlators,

$$\begin{aligned} J_{k12345}^{(0)} = n_1 n_2 n_3 \big[& \delta_3^k \left(\delta_4^1 \delta_5^2 + \delta_5^1 \delta_4^2 \right) \\ & + \delta_4^k \left(\delta_3^1 \delta_5^2 + \delta_5^1 \delta_3^2 \right) + \delta_5^k \left(\delta_3^1 \delta_4^2 + \delta_4^1 \delta_3^2 \right) \big]. \end{aligned} \tag{4.28}$$

However, due to the symmetry of T_{k12345}, this makes the right hand side of the KE zero. To find a nontrivial answer we need to obtain a first order addition $J_{k12345}^{(1)}$ to J_{k12345}. To calculate $J_{k12345}^{(1)}$ one takes the "time" derivative of J_{k12345}, using the equation of motion (4.26) and inserts the zeroth order approximation for the tenth correlation function (this is similar to equation (4.28), but a product of five pair correlators involving ten wavevectors). $J_{k12345}^{(1)}$ can then be expressed as

$$J_{k12345}^{(1)} = Be^{i\Delta\omega z} + \frac{A_{k12345}}{\Delta\omega}, \tag{4.29}$$

where $A_{k12345} = 3T_{k12345}^* n_k n_1 n_2 n_3 n_4 n_5 \left(\frac{1}{n_k} + \frac{1}{n_1} + \frac{1}{n_2} - \frac{1}{n_3} - \frac{1}{n_4} - \frac{1}{n_5} \right)$ and $\Delta\omega = \omega_k + \omega_1 + \omega_2 - \omega_3 - \omega_4 - \omega_5$. The first term of (4.29) is a fast oscillating function, its contribution to the integral (4.27) decreases with z and is negligible at z larger than $1/\omega_k$, and as a result we will ignore the contribution arising from this term. The second term is substituted in equation (4.27),the relation $Im(\Delta\omega) \sim -\pi\delta(\Delta\omega)$ is applied because of integration around the pole, and the KE is derived,

$$\begin{aligned} \frac{\partial n_k}{\partial z} = & 18\pi \int |T_{k12345}|^2 f_{k12345}\, \delta(k + k_1 + k_2 - k_3 - k_4 - k_5) \\ & \times \delta(\omega_k + \omega_1 + \omega_2 - \omega_3 - \omega_4 - \omega_5) dk_1 dk_2 dk_3 dk_4 dk_5, \end{aligned} \tag{4.30}$$

with T_{123456} being the six-wave interaction coefficient for the system and

$$f_{k12345} = n_k n_1 n_2 n_3 n_4 n_5 \left(\frac{1}{n_k} + \frac{1}{n_1} + \frac{1}{n_2} - \frac{1}{n_3} - \frac{1}{n_4} - \frac{1}{n_5} \right). \tag{4.31}$$

The KE has important exact power law solutions. These solutions are known as KZ solutions, namely from the discovery by Zakharov and their analogies to the Kolmogorov spectrum seen in classical turbulence theory. Moreover, the KE also contains thermodynamical equilibrium solutions, that correspond to the relaxation of energy and wave action within the system to equilibria. These solutions are limiting cases of the more generalized Rayleigh-Jeans distribution,

$$n_k = \frac{T}{\omega_k + \mu}, \tag{4.32}$$

where T is the temperature and μ is a chemical potential.

One can predict the scaling of the KZ solutions by considering a dimensional analysis argument upon an inertial interval in k-space where the fluxes of both energy and wave action are constant. We have seen that in the long-wave model, equation (4.25) implies that the six-wave interaction coefficient scales as

$$T_{123456} \sim |k|^0. \tag{4.33}$$

Thus, the scaling of the KE in terms of wavenumber k and wave action density n_k is,

$$\dot{n}_k \sim |k|^2 n_k^5. \tag{4.34}$$

For the direct cascade of energy, the KZ spectrum is realized when there exists a constant, non-zero energy flux P_k that is scale independent,

$$P_k = \int^k \omega_k \dot{n}_k dk \sim |k|^0. \tag{4.35}$$

Equations (4.34) and (4.35) gives the scaling of n_k for the direct cascade to be,

$$n_k = C|k|^{-1}, \tag{4.36}$$

where C is an arbitrary constant. Similarly, the wave action cascade implies a constant wave action flux flowing towards low wavenumbers, i.e. the wave action flux Q_k scales as

$$Q_k = \int^k \dot{n}_k dk \sim |k|^0, \tag{4.37}$$

consequently generating an inverse KZ wave action spectrum of

$$n_k = C|k|^{-\frac{3}{5}}. \tag{4.38}$$

The inverse cascade spectrum is of a finite capacity type, in a sense that only a finite amount of the cascading invariant (wave action in this case) is needed to fill the infinite inertial range. (Indeed, the integral of $n_k \sim k^{-3/5}$ converges at $k = 0$). In these cases the turbulent systems have a long transient (on its way to the final thermal equilibrium state) in which the scaling is of the KZ type. This is because the initial condition serves as a huge reservoir of the cascading invariant. Note that

the situation here is not specific for WT only and it is valid generally for turbulence. For example, it is valid for Navier-Stokes turbulence, i.e. the Kolmogorov-Obukhov spectrum, which is also finite capacity.

4.3.7 Modulational Instability and the Creation of Solitons

Closeness of equation (4.4) to integrability means that we should expect not only random waves but also soliton-like coherent structures. In the inverse cascade setup, solitons appear naturally. Indeed, the wave turbulent description (equation (4.30)) breaks down when the inverse cascade reaches some low k's. Modulational instability (MI) develops at these scales, which results in the filamentation of light and its condensation into coherent structures - solitons.

The inverse cascade of photons is a very important process in the creation of solitons. It provides the means, via nonlinear wave interaction to allow wave action to reach lower wavenumbers. Once the intensity at these wavenumbers passes a certain threshold, MI can take over. MI of a wave packet occurs when the nonlinearity of the wave packet increases such that the linear dynamics (defined by the linear frequency $\omega_k = k^2$) become Bogoliubov modified, that is to say that the wave packet no longer propagates linearly. As a consequence, the wave packet's dynamics are no longer determined by the linear dispersion, but now by the Bogoliubov dispersion relation or frequency. In focusing nonlinear states, this Bogoliubov frequency can become imaginary when the wave intensity is high enough, resulting in an instability of exponential growth of the wave envelope. This process was first discovered in the context of water waves, where it is originally known as the Benjamin-Feir instability [30].

One can characterize MI by deriving the Bogoliubov frequency [31], - the nonlinear wave frequency that takes into account the first order effect of weak nonlinearity. To derive such a relation, one must expand the wave function $\psi(x,z)$ around a condensate. The description of the condensate can be calculated by assuming an x-independent solution of the evolution equation, i.e. $\psi(x,z) = \psi_c(z)$. Looking for a small perturbation around this condensate, this expansion can be written in either physical or Fourier space and is given by either

$$\psi = \psi_c\,(1+\phi) \quad \text{or} \quad a_k = \psi_c\,(\delta(k)+\phi_k)\,. \tag{4.39}$$

where $|\phi|$, $|\phi_k| \ll 1$.

The condensate is defined as the $k = 0$ mode, which corresponds to an x-independent state. We can determine its dynamics by considering an x-independent solution $\psi_c(z)$ to equation (4.4). We find that $\psi_c(z) = \psi_0 \exp(-i\omega_c z)$, with $\omega_c = -\varepsilon_0 n_a^4 l_\xi^2 k_0^2 |\psi_0|^2/8q$. $\psi_c(z)$ describes the background rotation of the condensate with frequency ω_c. Substituting ansatz (4.39) into system (4.4) and linearizing to the first order in ϕ_k, gives a nonlinear evolution equation for the perturbation ϕ_k. Finally, one

makes the assumption of a single monochromatic plane wave solution for ϕ_k of the form $\phi_k = A\exp(ikx - i\Omega_k z) + \text{c.c.}$, where A is a complex constant, and c.c. means complex conjugate. Equating the exponentials, one can derive the Bogoliubov formula or the MI condition for a perturbation upon a condensate.

$$2q\Omega_k = \sqrt{\left(1 + \frac{|\psi_0|^2\varepsilon_0 n_a^4 l_\xi^4 k_0^2}{2K}\right)k^4 - \frac{|\psi_0|^2\varepsilon_0 n_a^4 l_\xi^2 k_0^2}{2K}k^2}, \tag{4.40}$$

where $|\psi_0|^2$ is the average density of the condensate, and Ω_k is the frequency of the waves upon the condensate. To obtain the frequency of the original wave function $\psi(x,z)$, we must add back the condensate shift (or the frequency of the condensate) to the Bogoliubov frequency Ω_k. Therefore, the Bogoliubov dispersion relation for a weakly nonlinear wave packet is $\omega_k = \omega_c + \Omega_k$, where ω_c is the condensate frequency shift and Ω_k is the MI condition for ϕ_k for the weakly nonlinear wave packet upon the condensate, equation (4.40).

4.4 Numerical Method

We numerically solve equation (4.4) using a standard pseudo-spectral method with periodic boundary conditions. We de-alias on half the wavenumbers to remove any aliasing errors when computing the cubic nonlinear term. We set a resolution of 2048 points in physical space and apply a fourth order Runge-Kutta method to solve in "time" z. We set the "time step" to be smaller than the CFL condition and the smallest linear time of evolution to ensure the simulation is properly resolved. We compute the energy of each term in equation (4.5) to ensure that the linear energy is greater than the nonlinear and moreover, that the leading nonlinear term dominates the sub-leading one, i.e. that the long-wave limit is satisfied. Weak nonlinearity is verified by parameter J (see equation (4.20)), but not too weakly nonlinear that we experience "frozen turbulence" [32]. To increase stability of the numerical scheme, we integrate the linear terms exactly and apply the time stepping algorithm to the nonlinear terms only by using integrating factors.

4.5 Experimental and Numerical Results

Both experimental and numerical setups are configured for decaying OWT, where an initial condition is defined and allowed to develop absent of any forcing or numerical dissipation. Experimentally, we have injected photons at intermediate spatial scales, where intermediate means around a wavenumber $k = k_0$ in between $k = 0$ and dissipation scale occurring at $k = k_D$. At this purpose, the intensity of the input beam is modulated with a patterned intensity mask, and in order to impose an initial condition close to the random phase approximation required by the theory, we have

randomize the phases by a phase modulator. This is made by creating through the SLM a random distribution of diffusing spots with the average size $\sim 35\ \mu m$, which is relatively larger than the liquid crystal electrical coherence length l_ξ fixing the dissipative scale.

The numerical initial condition is more idealized and strictly localized at a small-scale range: we excite five wavenumbers with constant amplitude around $|k_f| \sim 1.5 \times 10^2\ mm^{-1}$, and the phase of ψ_k is random and independent at each k. Moreover, we have applied a Gaussian filter in physical space to achieve a beam profile comparable to that of the experiment.

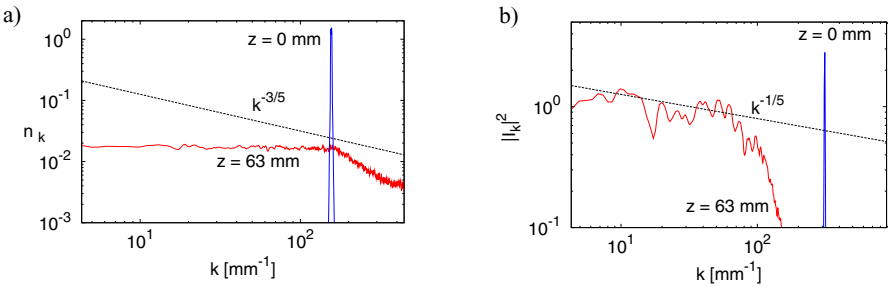

Fig. 4.4 a) Numerical spectrum of a) the wave action n_k, and b) the light intensity, $N_k = |I_k|^2$ at distances $z = 0\ mm$ and $z = 63\ mm$.

The numerical wave action spectrum is shown in Fig. 4.4a at two different distances, we see at $z = 0\ mm$ the peak from the initial condition at high wavenumbers, then at $z = 63\ mm$ we see evidence of an inverse cascade, as the majority of the wave action is situated towards low wavenumbers. However, at low wavenumbers we do not see the spectrum matching our theoretical KZ prediction of $n_k \sim |k|^{-3/5}$, this is because of high nonlinearities towards low wavenumbers causing a breakdown of the WTT. The higher nonlinearity towards low wavenumbers causes soliton formation out of the weakly nonlinear waves, and as a result we observe a flattening of the wave action spectrum. However, it remains to be found why the inverse wave action spectrum disagrees with the WTT prediction in the same run, and whether we could confidently say that what we see is a KZ spectrum. Note that even in weak wave turbulence, the KZ spectrum may not be realized, e.g. if the interaction of scales is nonlocal. In the other words, the presence of wave turbulence (claimed in this paper) does not automatically imply the presence of KZ spectra (for which we see an indication but not a solid proof).

Experimentally, we measure the light intensity $I(x,z) = |\psi|^2$ and not the phases of ψ and, therefore, the spectrum n_k is not directly accessible. Instead, we measure the spectrum of intensity $N(k,z) = |I_k(z)|^2$. The scaling for N_k in the inverse cascade state is easy to obtain from $n_k \sim |k|^{-3/5}$ and the random phase condition, this gives $N_k \sim |k|^{-1/5}$. Numerical and experimental spectra of the light intensity are shown in Figs. 4.4b and 4.5 respectively. In both cases one can see an inverse cascade excitation of the lower k states, and good agreement with the WT prediction $N_k \sim |k|^{-1/5}$.

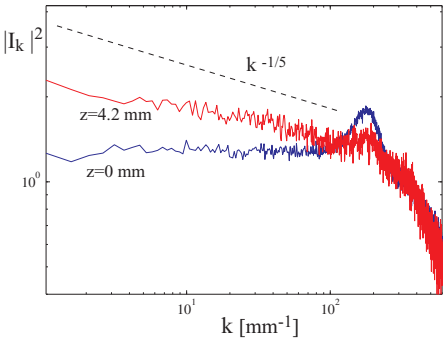

Fig. 4.5 Experimental spectrum of the light intensity, $N_k = |I_k|^2$ at two different distances z.

Note that the numerical spectrum of the light intensity shows a better agreement with the expected KZ scaling than the numerical wave action spectrum. A possible explanation is that averaging over phases can provide a wash-out effect of the WTT breakdown phenomena occurring at low wavenumbers, thus restoring the scaling predicted in the approximation of weak nonlinearities.

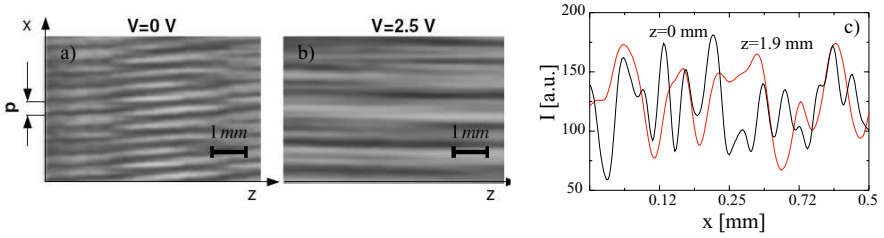

Fig. 4.6 Intensity distribution $I(x,z)$ showing the beam evolution during propagation; a) linear case, b) weakly nonlinear case. c) Two intensity profiles $I(x)$ recorded at $z = 0$ and $z = 1.9$ *mm* in the weakly nonlinear regime, $V = 2.5\,V$.

Experimentally, the inverse cascade can be seen directly by inspecting the light pattern in the $x - z$ plane under the beam propagation evolution. Two magnified images of the intensity distribution $I(x,z)$ showing the beam evolution during propagation are displayed in Fig.4.6. For comparison, in Fig.4.6a and b, respectively, we show the beam evolution in the linear and in the weakly nonlinear (wave turbulence) regime. In Fig.4.6a the initial condition is periodic with an uniform phase and no voltage is applied to the liquid crystal layer ($V = 0$). We see that the linear propagation is characterized by the periodic recurrence of the pattern with the same period, a phase slip occurring at every Talbot distance, this one being determined by p^2/λ with p the period of the initial condition and λ the laser wavelength [33]. In Fig.4.6b the voltage on the liquid crystal cell is switched on, $V = 2.5\ V\ rms$, and the initial condition is periodic with the same period as in Fig.4.6a but with random phases.

In this case, the initial period of the pattern is becoming larger as the light beam propagates forward along z. If a random phase distribution would have been chosen in the linear case, then, a speckle pattern would have developed along propagation [34], therefore destroying the initial modulation and preventing a direct comparison of the linear and weakly nonlinear case.

While the linear propagation leads to Talbot intensity carpets [35], with the initial intensity distribution reappearing periodically along the beam propagation direction z, the weak nonlinearity leads to wave interaction, so that, as the beam propagates, the different spatial frequencies components mix-up and the periodic occurrence of the Talbot carpet is broken. In Fig.4.6c we show two intensity profiles taken in the nonlinear case at different stages of the beam propagation. The inverse cascade is accompanied by a smoothing of the intensity profiles and amplification of low wavenumbers as the beam propagates forward inside the nematic layer.

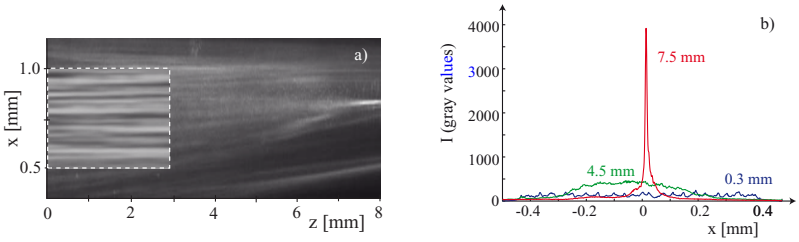

Fig. 4.7 a) Experimental results for intensity distribution $I(x,z)$ for the same parameter values for Fig.4.6. Area marked by the dashed line is shown at a higher resolution (using a larger magnification objectif). b) Linear intensity profiles $I(x)$ taken at different propagation distances, $z = 0.3$, 4.5 and 7.5 *mm*

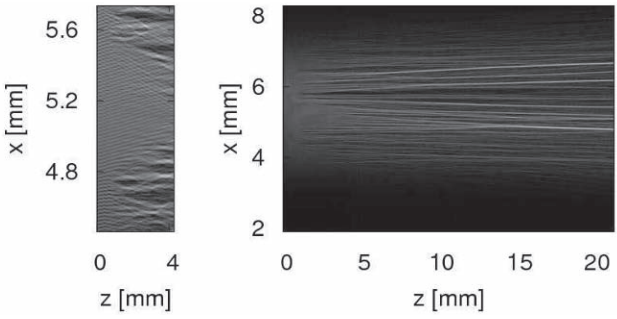

Fig. 4.8 Numerical results for intensity distribution $I(x,z)$. The frame on the left is a magnified section of the initial propagation of the beam.

Example zooms of the intensity distribution $I(x,z)$ showing the beam evolution during propagation in the experiment and in the numerics are displayed in Fig. 4.7 and Fig. 4.8 respectively. The experimental data shown in Fig. 4.7 have

been recorded for the same parameter values as for Fig.4.6. In the high resolution inset on Fig. 4.7 one can visually observe that the typical scale increases along the beam which corresponds to an inverse cascade process. Further, in both Fig. 4.7 and Fig. 4.8 one can see formation of coherent solitons out of the random initial field, such that one strong soliton is dominant at the largest distance z (the soliton peak intensity in Fig.4.7 is ~ 800 times greater than the initial light intensity).

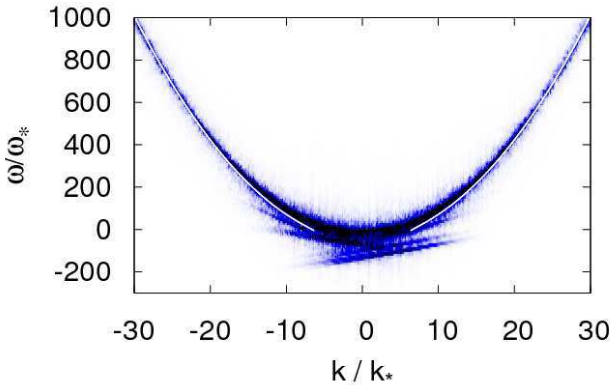

Fig. 4.9 The $k-\omega$ spectrum of the wave field at $z = 2.1$ *m*. $\omega_* = 1/256ql_\xi^2$ and $k_* = 1/\sqrt{128}l_\xi$. The Bogoliubov dispersion relation is shown by the solid line.

Separating the random wave and the coherent soliton components can be done via performing an additional Fourier transform with respect to "time" z over a finite z-window. Such numerically obtained (k, ω)-plot is shown in Fig. 4.9. There, the incoherent wave component is distributed around the wave dispersion relation, which is Bogoliubov-modified by the condensate (equation (4.40)) and shown by a solid line in Fig. 4.9. This distribution is narrow for large k which corresponds to weak nonlinearity, and it gets wider toward low k, which corresponds to a growth of nonlinearity and breakdown of the WT applicability conditions. For these low k values one can see pieces of slanted lines (under the dispersion curve). Each of these lines corresponds to a coherent soliton, whose speed is equal to the inclination slope. We observe that the formation of solitons is seen in the (k, ω)-plot as straight line "peeling" with a gradient tangential to the dispersion curve. Experimental realization of the (k, ω)-plot will be performed in next future by employing a higher depth resolution camera.

4.5.1 Direct cascade of energy

Finally, we numerically investigated the direct energy cascade. We found that the direct cascade prediction is an infinite capacity spectrum. This means that unlike

the inverse cascade, one cannot realize the KZ prediction in a decaying simulation. Therefore, we ran a numerical simulation of equation (4.4), but with the additional terms that correspond to additive forcing $+iF$, and dissipation $-iD$. We forced with constant amplitude and random phases at three wavenumbers at the low wavenumber region and applied hyper and hypo-viscosities of the form $D = \nu_1 \partial^8 \psi / \partial x^8 + \nu_2 \partial^{-8} \psi / \partial x^{-8}$. We ran the simulation, and then averaged the wave action spectrum once the simulation reached a steady state. We show the direct wave action spectrum with the WTT KZ prediction in Fig. 4.10. We see a good agreement with the KZ spectrum for about a decade in wavenumber space. There is some slight noise at high wavenumbers, due to the simulation not completely reaching a true steady state. This regime is not accessible in the experiment because the system is not large enough to let the cascade to develop over a significant wavenumber interval. Further experiments are in progress in order to increase the size of the system and to observe the direct cascade.

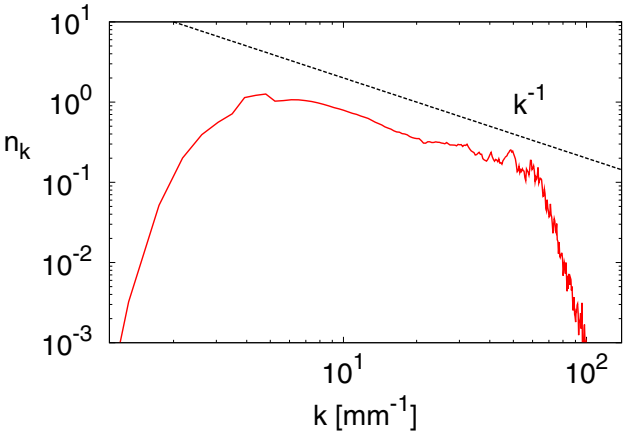

Fig. 4.10 The numerical direct wave action spectrum of energy with the predicted KZ spectrum of $n_k = k^{-1}$.

4.6 Conclusions

In conclusion, we have presented an experimental implementation of the 1D OWT regime, accompanied by numerical simulations and theory. We observe an inverse cascade of photons toward the states with lower wavenumbers in both the experiment and numerics, the predicted intensity spectrum is seen clearly in the experiment plot, with a reasonable trend in the numerical plot. The wave action spectrum in the numerical plot is vaguely seen over a short region, we argue that decaying OWT isn't the ideal setup for seeing the KZ spectrum, because of the high lev-

els of nonlinearity at lower wavenumbers and the presence of solitons where WTT breaks down. Furthermore, we have shown that after the initial inverse cascade to low wavenumbers, we see the development of solitons by MI, then the further merging of these solitons into one dominate soliton at later times. Finally, we also verified numerically the KZ prediction for the direct cascade, with a good agreement for about a decade in wavenumber space.

4.7 Acknowledgements

This work has been partially supported by the Royal Society's International Joint Project grant *Vortices, turbulence and photon condensation in a nonlinear optical experiment*.

References

1. S. Dyachenko, A.C. Newell, A. Pushkarev, and V.E. Zakharov, Physica D **57**, 96 (1992)
2. V. Zakharov, F. Dias, and A. Pushkarev, Physics Reports, **398**, 1 (2004)
3. S. Nazarenko, and V. Zakharov, Physica D **201**, 203 (2005)
4. C. Connaughton, C. Josserand, A. Picozzi, Y. Pomeau, and S. Rica, Phys. Rev. Lett. **95**, 263901 (2005)
5. S. Nazarenko, and M. Onorato, Physica D **219**, 1 (2006)
6. F.T. Arecchi, G. Giacomelli, P.L. Ramazza, and S. Residori, Phys. Rev. Lett. **67**, 3749 (1991)
7. G.A. Swartzlander, Jr. and C.T. Law, Phys. Rev. Lett. **69**, 2503 (1992).
8. C. Barsi, W. Wan, C. Sun, and J.W. Fleischer, Opt. Lett. **32**, 2930 (2007).
9. V. E. Zakharov, V. S. Lvov, and G. Falkovich, *Kolmogorov Spectra of Turbulence*, (Springer-Verlag, 1992).
10. U. Bortolozzo, J. Laurie, S. Nazarenko, and S. Residori, J. Opt. Soc. Am. B **26**, 2280 (2009).
11. M. Peccianti, C. Conti, and G. Assanto, Phys. Rev. E **68**, 025602 (2003).
12. A.J. Majda, D.W. McLaughlin, and E.G. Tabak, J. Nonlinear Sci. **6**, 944 (1997).
13. D. Cai, A.J. Majda, D.W. McLaughlin, and E.G. Tabak, Physica D, **152**, 551, (2001).
14. V.E. Zakharov, A.N. Pushkarev, V.F. Shvets, and V.V. Yan'kov, JETP Lett. **48**, 83 (1988).
15. B. Rumpf, and A.C. Newell, Phys. Rev. Lett. **87**, 5 (2001).
16. B. Rumpf, and A.C. Newell, Physica D, **184**, 162 (2003).
17. B. Barviau, B. Kibler, A. Kudlinski, A. Mussot, H. Millot, and A. Picozzi, Opt. Express **17**, 7392 (2009).
18. A. Eisner and B. Turkington, Physica D, **213**, 85 (2006).
19. R. Jordan, and C. Josserand, Phys. Rev. E, **61**, 1 (2000).
20. K.Ø. Rasmussen, T. Cretegny, and P.G. Kevrekidis, Phys. Rev. Lett. **84**, 17 (2000).
21. R. Jordan, B. Turkington, and C.L. Zirbel, Physica D, **137**, 353-378 (2000).
22. A. Picozzi, S. Pitois, and G Millot, Phys. Rev. Lett. **101**, 093901 (2008).
23. S. Pitois, S. Lagrange, H.R. Jauslin, and A. Picozzi, Phys. Rev. Lett. **97**, 033902 (2006).
24. V.I. Petviashvili, and V.V. Yan'kov, Reviews of Plasma Physics, 14, (1987).
25. I.C. Khoo, *Liquid Crystals: Physical Properties and Nonlinear Optical Phenomena* (Wiley, New York, 1995).
26. P.G. De Gennes and J. Prost, *The Physics of Liquid Crystals*, (Oxford Science Publications, Clarendon Press, second edition, 1993).
27. M. Peccianti, C. Conti, G. Assanto, A. De Luca, and C. Umeton, Nature **432**, 733 (2004).

28. C. Conti, M. Peccianti, and G. Assanto, Opt. Lett. **31**, 2030 (2006).
29. R. Fjortoft, Tellus **5**, 225 (1953).
30. T.B. Benjamin and J.E. Feir, J. Fluid Mech., **27**, 417-430 (1967).
31. N.N. Bogoliubov, J. Phys. U.S.S.R. 11, 23 (1947).
32. A.N. Pushkarev, Eur. J. Mech. B/Fluids **18**, 345-352 (1999).
33. H.F. Talbot, *Phil. Mag.* **9**, 401 (1836).
34. J. W. Goodman, *Statistical Optics* (John Wiley, New York, 1985).
35. M. Berry, I. Marzoli, and W. Schleich, Phys. World, June 2001, 1 (2001).

Part II
Localized structures in pattern forming systems

Chapter 5
Localized Structures in the Liquid Crystal Light Valve Experiment

Umberto Bortolozzo, Marcel G. Clerc, René G. Rojas, Florence Haudin and Stefania Residori

Abstract We will review the conditions for the appearance of coherent or localized states in a nonlinear optical feedback system, with particular reference to the Liquid Crystal Light Valve (LCLV) experiment. The localized structures here described are of dissipative type, that is, they represent the localized solutions of a pattern-forming system. We will show that different types of localized states are observed in the system and can be selected depending on the control parameters: round localized structures that interact forming bound-states, triangular localized structures, characterized by the presence of phase singularities, localized peaks, appearing above a structured background. Then, we will discuss the nonvariational behaviors of such coherent states, like the bouncing of round localized structures and the chaotic front propagation for the triangular ones. We will present the full model equations for the LCLV system as well as a one-dimensional spatially forced Ginzburg-Landau equation, which is the simplest model accounting for the phenomenology observed in the experiment. We will show how, by using a properly intensity/phase modulated input beam, we can either induce a large pinning effect or control the dynamics of large

Umberto Bortolozzo
INLN, Université de Nice Sophia-Antipolis, CNRS, 1361 route des Lucioles 06560 Valbonne, France e-mail: Umberto.Bortolozzo@inln.cnrs.fr

Marcel G. Clerc
Departamento de Física, Facultad de Ciencias Físicas y Matemáticas, Universidad de Chile, Casilla 487-3, Santiago, Chile, e-mail: marcel@galileo.dfi.uchile.cl

René G. Rojas
Instituto de Física, Pontificia Universidad Católica de Valparaíso, Casilla 4059, Valparaíso, Chile e-mail: rene.rojas@ucv.cl

Florence Haudin
INLN, Université de Nice Sophia-Antipolis, CNRS, 1361 route des Lucioles 06560 Valbonne, France e-mail: Florence.Haudin@inln.cnrs.fr

Stefania Residori
INLN, Université de Nice Sophia-Antipolis, CNRS, 1361 route des Lucioles 06560 Valbonne, France, e-mail: Stefania.Residori@inln.cnrs.fr

O. Descalzi et al. (eds.), *Localized States in Physics: Solitons and Patterns*,
DOI 10.1007/978-3-642-16549-8_5,

arrays of localized structures, addressing each site independently from the others. Finally, the propagation properties of localized structures will be presented.

5.1 Introduction

Non equilibrium processes often lead in nature to the formation of spatially periodic and extended structures, so-called patterns [2, 2]. The appearance of a pattern from a homogeneous state takes place through the spontaneous breaking of one or more of the symmetries characterizing the system [4]. In some cases, it is possible to localize a pattern in a particular region of the available space, so that we deal with localized instead of extended structures. From a theoretical point of view, localized structures in out of equilibrium systems can be seen as a sort of dissipative solitons [19]. Experimentally, during the last years localized patterns or isolated states have been observed in many different fields. Examples are domains in magnetic materials [5], chiral bubbles in liquid crystals [6], current filaments in gas discharge experiments [7], spots in chemical reactions [8], oscillons in granular media [9, 10], localized fluid states in surface waves [9] and in thermal convection [12], solitary waves in nonlinear optics [13, 14, 15, 16, 17, 18, 48, 20]. All these localized states can be considered to belong to the same general class of localized structures, that is, they are patterns that extend only over a small portion of a spatially extended system.

In optics, solitary waves have first been predicted to appear in bistable ring cavities [13], then, they have been largely studied not only for their fundamental properties but also in view of their potential applications as elementary bits of information [21, 22, 23, 24]. Sometimes named as cavity solitons, optical localized structures have been observed in photorefractive media [25], in lasers with saturable absorber [26], in Liquid-Crystal-Light-Valves (LCLVs) with optical feedback [14, 15, 16, 17, 18], in Na vapors [27] and more recently in semiconductor micro-cavities [20].

Here, we will review the conditions for the appearance of coherent or localized states in a nonlinear optical feedback system, with particular reference to the Liquid Crystal Light Valve (LCLV) experiment [28]. We will show that different types of localized states are observed in the system and can be selected depending on the control parameters: round localized structures that interact forming bound-states [29], triangular localized structures, characterized by the presence of phase singularities [30], localized peaks, appearing above a structured background [31]. Then, we will discuss the nonvariational behaviors of such coherent states, like the bouncing of round localized structures [32] and the chaotic front propagation for the triangular ones [33].

We will present the full model equations for the LCLV system as well as a one-dimensional spatially forced Ginzburg-Landau equation, which is the simplest model accounting for the phenomenology observed in the experiment [34] and for the tilted snaking bifurcation diagram [35]. Then, we will show how, by using a properly intensity/phase modulated input beam, we can either induce a large pin-

ning range or control the dynamics of large arrays of localized structures, addressing each site independently from the others [36]. Finally, we will present the propagation properties of localized structures [37].

5.2 The Liquid Crystal Light Valve Experiment

5.2.1 Description of the setup

The experimental setup, shown in Fig.8.3, consists of a LCLV with optical feedback, as it was originally designed by the Akhmanov group [38]. The LCLV is composed of a nematic liquid crystal film sandwiched in between a glass window and a photoconductive plate over which a dielectric mirror is deposed. Coating of the bounding surfaces induces a planar anchoring of the liquid crystal film (nematic director **n** parallel to the walls). Transparent electrodes covering the two confining plates permit the application of an electric field across the liquid crystal layer. The photoconductor behaves like a variable resistance, which decreases for increasing illumination. The feedback is obtained in the following way: the light which has passed through the liquid-crystal layer, and has been reflected by the dielectric mirror inside the LCLV, is sent back onto the photoconductor of the LCLV. This way, the light beam experiences a phase shift which depends on the liquid crystal reorientation and, on its turn, modulates the effective voltage that locally is applied to the liquid crystals.

The feedback loop is closed by an optical fiber bundle and is designed in such a way that diffraction and polarization interference are simultaneously present [28]. The presence of diffraction leads to the spontaneous generation of self-organized patterns, which display a typical spatial period scaling as $\sim \sqrt{\lambda |L|}$, where λ is the laser wavelength and L is the optical free propagation length in the feedback loop [39]. On the other hand, the presence of polarization interference leads to bistability between different spatial states. Setting $L = 0$ eliminates diffraction effects, so that in this case the system exhibits bistability between homogeneous states and front propagation [25].

To obtain localized structures the optical free propagation length is usually fixed to $L = -8\ cm$. For this value of L the transverse size of a single localized structure, which scales as $\sqrt{\lambda |L|}$, is about 250 μm. At the linear stage for the pattern formation, a negative propagation distance selects the first unstable branch of the marginal stability curve, as for a focusing medium [41]. Moreover, an input and feedback polarizer are inserted in such a way to form with the liquid crystal director an angle of 45° and -45°, respectively. For this parameter setting and close to the point of Fréedericksz transition, there is coexistence between a periodic pattern and a homogeneous solution. The Fréedericksz transition point is attained for an applied r.m.s. voltage V_0 of approximately 3 V, with a frequency of 5 kHz [25]. By increasing V_0, successive branches of bistability are excited. Most of the experimental observations here reported were obtained close to one of the points of nascent bistability onto the

different bistable branches. There, the bistable behavior observed is similar to the one observed close to the Fréedericksz transition point [25].

The input beam has a Gaussian profile with a transverse size of approximately 2 *cm*, whereas a diaphragm before the LCLV selects a central active zone with a diameter of 1 *cm*. The input intensity I_{in} usually varies in between 0.3 and 1 mW/cm^2. As shown in Fig.8.3, the setup includes also a spatial light modulator (SLM) connected to a personal computer (PC) and inserted in the optical path of the input beam I_{in}. The SLM is a twisted nematic liquid crystal display that can be used either without polarizers or in between crossed polarizers providing, respectively, phase or intensity modulations that are used to control the spatial profile of the input beam.

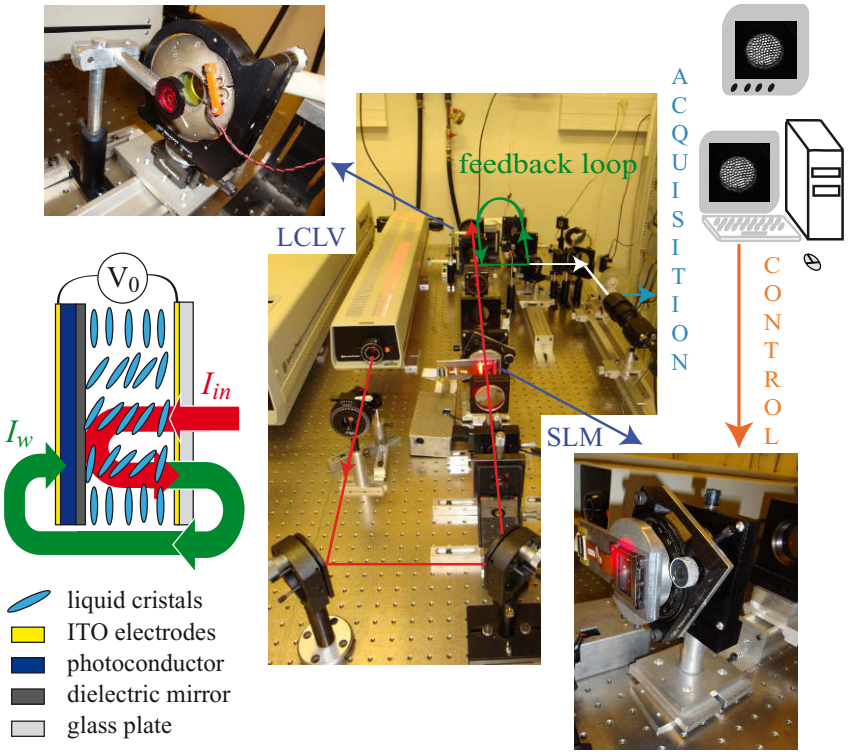

Fig. 5.1 Experimental setup: the LCLV is illuminated by a plane wave collimated beam (red line in the central picture); the beam reflected by the LCLV (green line) is sent back to the photoconductor through a beam-splitter, a mirror and, finally, an optical fiber bundle. In the upper left inset is shown an enlarged picture of the LCLV. A schematic representation is displayed below: V_0 is the voltage applied, I_{in} and I_w are the input and feedback intensity, respectively. A small portion of the beam (white line), is extracted from the feedback loop through a beam-splitter and sent to the acquisition line that is composed by a lens, a mirror and a computer interfaced CCD camera. In the bottom right inset is shown an enlarged image of the SLM that is computer interfaced and used to control the spatial profile of the input beam.

5.2.2 The optical feedback: model equations

The theoretical model for the LCLV feedback system was previously derived in [32] and consists of two coupled equations, one for the average director tilt $\theta(\mathbf{r}_\perp,t)$, $0 \leq \theta \leq \pi/2$, and one for the feedback light intensity I_w. The average director tilt $\theta(\mathbf{r}_\perp,t)$ accounts for the average orientation angle of the liquid crystal molecules with respect to the longitudinal direction of the nematic layer, $r_\perp$ denotes the transversal direction of the liquid crystal layer. For $\theta = 0$ ($\theta = \pi/2$) all the molecules are parallel (orthogonal) to the confining walls, which corresponds, respectively, to a planar and a homeotropic alignment of the liquid crystals [42].

When one applies an electric voltage V_0 along the longitudinal direction of the nematic layer, all the molecules in the bulk reorient in such a way to align with the direction of the applied field, because of their positive dielectric anisotropy. Hence, liquid crystal molecules are under the influence of two opposite torques, the elastic restoring torque and the electric torque. The equation for the average director tilt around equilibrium reads as

$$\tau\partial_t\theta = l^2\nabla_\perp^2\theta - \theta + \theta_c(V), \tag{5.1}$$

where l is the electrical coherence length, τ the local relaxation time and $\theta_c(V)$ the equilibrium average director tilt. There is a critical value of the voltage–V_{FT}–for which the electric force overcomes the elastic one, so that the molecules reorient. This process is called *Fréedericksz transition* [42].

In the LCLV, we must take into account the response of the photoconductor. In the absence of optical feedback, the response of the valve is phenomenologically described by the following model, as originally proposed in [32],

$$\theta_c = \begin{cases} 0 & V \leq \Gamma V_{FT} \\ \pi/2\left(1 - \sqrt{\Gamma V_{FT}/V}\right) & V > \Gamma V_{FT} \end{cases}, \tag{5.2}$$

where $V = \Gamma V_0$ is the voltage that effectively applies to the liquid crystal layer and Γ is the impedance of the LCLV dielectric layers. Experimentally and theoretically, we have a very good agreement with the observation of the average equilibrium director tilt and the formula (5.2). In Fig.5.2a the measured equilibrium director tilt θ_c is plotted as a function of V_0 together with a best fit by using Eq.(5.2). Note that other models for the director tilt are reported in the literature [14, 16], which, however, do not provide a satisfactory agreement with the experimental data for our light-valves.

When we consider the optical feedback, the relaxation and diffusive dynamics of the average director tilt is largely enriched because the voltage that effectively applies to the liquid crystal layer becomes a function of the average director tilt. It, precisely, reads as

$$V(\theta) = \Gamma V_0 + \alpha I_w(\theta), \tag{5.3}$$

where I_w is the feedback intensity arriving onto the photoconductor and α is a phenomenological parameter summarizing, in the linear approximation, the response of the photoconductor. After a free propagation length L, the feedback light intensity is given by

$$I_w = \frac{I_{in}}{4} \mid e^{i\frac{L\lambda}{4\pi}\nabla_\perp^2} \left(1 - e^{-i\beta\cos^2\theta}\right) \mid^2, \tag{5.4}$$

the diffraction being accounted for by the operator $e^{i\frac{L\lambda}{4\pi}\nabla_\perp^2}$. The overall phase shift experienced by the light traveling forth and back through the liquid crystal layer is $\beta cos^2\theta$, where $\beta = 2kd\Delta n$ with $k = 2\pi/\lambda$ the optical wave number ($\lambda = 633$ nm), $d = 15$ μm the thickness of the liquid crystal layer and $\Delta n = 0.2$ the difference between the extraordinary ($\parallel$ to $\mathbf{n}$) and ordinary ($\perp$ to $\mathbf{n}$) refractive index of the liquid crystals.

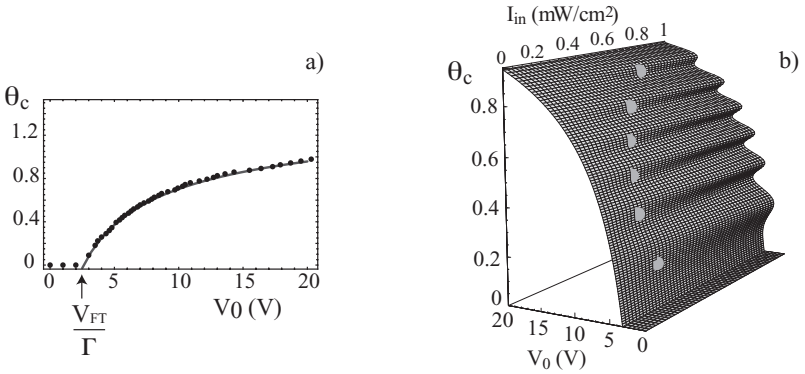

Fig. 5.2 a) Equilibrium average director tilt θ_c as a function of the applied voltage V_0 when there is no optical feedback; circles are experimental points, the solid line is a best fit with Eq.(5.2). b) The multi-valued function $\theta_c(V_0, I_{in})$ representing the equilibrium average director tilt when the optical feedback is present; shaded areas mark the locations of the nascent bistability points.

By inserting Eq.(5.4) into Eq.(5.1), the dynamics of the LCLV with optical feedback is described by

$$\tau\partial_t\theta - l^2\nabla_\perp^2\theta + \theta = \begin{cases} 0 & V \leq \Gamma V_{FT} \\ \pi/2\left(1 - \sqrt{\frac{\Gamma V_{FT}}{\Gamma V_0 + \alpha I_w(\theta, \nabla_\perp^2)}}\right) & V > \Gamma V_{FT} \end{cases}. \tag{5.5}$$

Above the Fréedericksz transition and by neglecting the spatial terms–which is equivalent to consider a free propagation length equal to zero–we can find a closed expression for the homogeneous equilibrium solutions

$$\theta_c = \pi/2\left(1 - \sqrt{\Gamma V_{FT}/(\Gamma V_0 + \alpha I_{in}[1 + \cos(\beta\cos^2\theta_0)])}\right).$$

The multi-valued function $\theta_c(V_0, I_{in})$, representing the equilibrium average director tilt when the optical feedback is present, is shown in Fig.5.2b. The value of V_{FT} is set to 3.2 V_{rms}, as measured for the LCLV [25, 43]. For small intensity of the optical feedback ($I_{in} \ll 1$), the system has one equilibrium state, however when I_{in} is increased the system exhibits multiple stability. In agreement with the bistability branches observed experimentally, several points of nascent bistability can be distinguished.

5.3 Experimental Observations of Optical Localized Structures

5.3.1 Round localized structures: interaction and dynamics

Optical localized structures are observed in the experiment when diffraction and polarization interference are simultaneously present. Round localized structures are characterized by interactions, that are mediated by the oscillations present on their tails [44]. A quantitative experimental evidence of the crucial role played by the oscillatory tails in determining the interaction forces between localized structures is given in [17]. The oscillatory tails of localized structures, and, therefore, their interactions, are tailored by acting on the spatial frequency bandwidth q_B of the optical feedback loop, which can be experimentally controlled by means of a variable aperture placed in the Fourier plane.

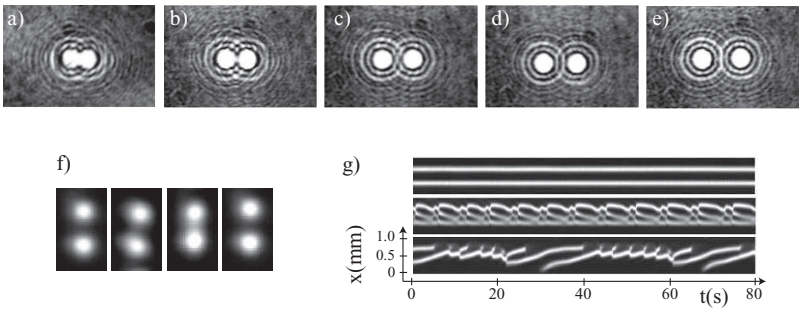

Fig. 5.3 Upper panels: bound states of localized structures obtained for $V_0 = 4.5\ V$, $I_{in} = 0.5\ mW/cm^2$ and $q_b = 3.6$; all states a)-e) are obtained by inducing a pair of localized structures with an increasing initial distance between centers, and letting the system evolve up to the formation of a stationary bound state. Lower panels: bouncing dynamics of localized structures observed at $V_0 = 12.2\ V$ and $I_{in} = 0.95\ mW/cm^2$; f) successive snapshot showing two localized structures bouncing one over the other; g) space-time diagrams showing two stationary localized structures (top), two localized structures with periodic oscillations of their positions (middle) and aperiodic bouncing (bottom).

While for monotonically decreasing tails one would expect only attractive or repulsive forces, oscillatory tails induce oscillatory signs of the interactions, and

thus produce both attractive and repulsive forces, depending on the distance between the centers of a pair of localized structures. In the upper part of Fig.5.3 we display a set of different bound states of localized structures obtained for $V_0 = 4.5\ V$, $I_{in} = 0.5\ mW/cm^2$ and $q_b = 3.6$, where $q_b \equiv q_B/q_{diff}$ is the system bandwidth normalized to the diffractive wave number $q_{diff} = \sqrt{\pi k/|L|}$. We notice that bound states form a set that can be ordered following a precise rule, given by counting the number of maxima and minima that occur along the segment connecting the centers of the two localized structures. This number n has been identified as the bound state order number [17].

Concerning the dynamics of localized structures, it can be shown that close to the point of nascent bistability, the model for the LCLV can be reduced to a Swift-Hohenberg type equation with the inclusion of nonvariational effects [32]. The amplitude equation is a Lifshitz normal form

$$\partial_t u = \eta + \mu u - u^3 + \nu \partial_{xx} u - \partial_{xxxx} u + \beta u \partial_{xx} u + \gamma (\partial_x u)^2, \tag{5.6}$$

where u is the amplitude of the first deformation mode of the average director tilt θ, η is a symmetry breaking parameter, μ is the bifurcation parameter, $\nu \partial_{xx} u$ is the diffusion, $\partial_{xxxx} u$ describes a super diffusion, accounting for the short distance repulsive interaction, and the terms proportional to β and γ are, respectively, the nonlinear diffusion and convection.

As a consequence of the nonvariational dynamics, localized structures show complex behaviors, such as the bouncing of two adjacent localized structures. In order to study this effect, one-dimensional experiments have been carried out by inserting in the feedback loop a rectangular mask with a width of 0.5 *mm* and a length of 20 *mm* [32]. The dynamics of localized structures have been recorded and analyzed. Successive snapshots showing the bouncing of two localized structures one over the other are shown in Fig.5.3f. The corresponding spatiotemporal plots are displayed in Fig.5.3g. The middle panel shows the periodic oscillations for the positions of the two structures observed for $I_{in} = 0.95\ mW/cm^2$ and $V_0 = 13.2\ V$. In the top panel it is shown the spatiotemporal plot corresponding to stationary localized structures, as observed for a slightly decreased input intensity, $I_{in} = 0.90\ mW/cm^2$, and for the same value of V_0. The bottom panel displays the spatiotemporal diagram corresponding to aperiodic oscillations in the structure positions, as observed for $V_0 = 13.3\ V$ and $I_{in} = 0.90\ mW/cm^2$.

5.3.2 *Triangular localized structures: bistability and phase singularities*

When the input intensity I_{in} and the voltage V_0 are set in such a way to excite multistable states, it has been observed the bistability between two different types of localized structures, namely the usual ones, characterized by a circular symmetry, and the triangular ones characterized by a broken symmetry and a higher amplitude peak

[30]. The two localized structures not only differ in shape but also are separated by a discrete gap in their peak intensity. If used as pixels for information storage, these localized structures represent three-state variables, instead of the common two-state variables (bits) that a common localized structure can encode, thus allowing an increased information storage for the same given area of the recording medium.

As we have seen in the previous section, round localized structure have a circular symmetry, with a bright central peak connected to the dark background via a series of small amplitude oscillations. Triangular localized structures are characterized by a triangular symmetry, observed both in the central peak and in the tails. For comparison, a round and a triangular localized structure, as observed for the same experimental parameters in the coexistence region, are shown in Fig.5.4 a and b, respectively. Numerical simulations faithfully reproduce the observations. In Fig.5.4c it is displayed a triangular localized structure resulting from numerical simulations of the LCLV model equations. We notice that triangular localized structures are characterized by a rich structure of phase singularities appearing as black holes on the intensity pattern. Phase singularities are nucleated by pairs (positive and negative) from around the peak to the oscillating tails [45]. The presence of phase singularities is evidenced in Fig.5.4d by plotting the lines $Im(E) = 0$ and $Re(E) = 0$, whose intersections mark their exact locations.

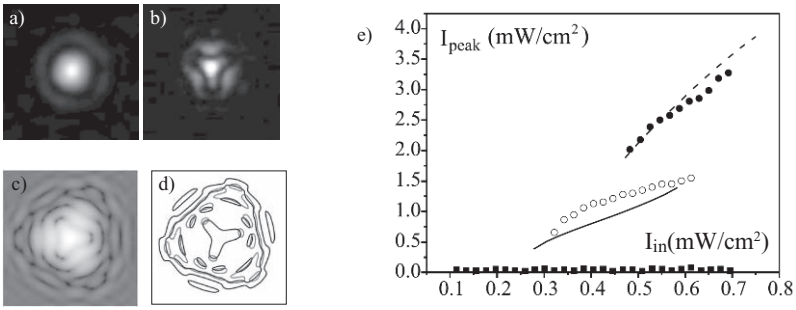

Fig. 5.4 a) Round and b) triangular localized structures as observed in the LCLV experiment for the same parameter values. c) Numerically calculated intensity distribution of a triangular localized structures plotted in logarithmic gray scale; corresponding contour lines $Re(E) = 0$ (black) and $Im(E) = 0$ (grey) showing the locations of phase singularities. e) State diagram showing the bistability between the round and triangular localized structures. Experimental points: squares, low uniform state; open circles, round localized structures; solid circles, triangular localized structures. Numerical lines: continuous, round localized structures; dashed, triangular localized structures.

Each of the two localized structures coexisting in the bistable region can be switched on by an appropriate addressing pulse. Lower intensity pulses trigger a round localized structure, whereas higher intensity pulses create a triangular localized structure. The experimental state diagram is shown in Fig.5.4, together with its numerical counterpart. Here it is plotted for each localized structure the peak intensity I_{peak}. Starting from a very low value of input intensity I_{in} and gradually increasing it, the lower uniform solution is the only state observed up to

$I_{in} = 0.32\ mW/cm^2$. From this value on, round localized structures are observable. At $I_{in} = 0.61\ mW/cm^2$ round localized structures loose their stability, and the system jumps to the branch of triangular localized structures. If, starting from a triangular localized structure, the pump is decreased, the structure remains stable down to $I_{in} = 0.47\ mW/cm^2$, and then decays to a round localized structure. If, instead, starting from $I_{in} = 0.61\ mW/cm^2$, the pump is increased, the triangular localized structure exists up to $I_{in} = 0.69\ mW/cm^2$, and then destabilizes via a transition to a delocalized irregular pattern. The transition to a pattern state occurs through a space-time chaotic dynamics and complex front propagation phenomena that are associated with the creation/annihilation of phase singularities [33].

5.3.3 Bipatterns and localized peaks

In the LCLV experiment it exists a range of parameters for which bistability occurs between two pattern states. In this case, we observe the appearance of localized peaks, that is, high amplitude peaks nucleate spontaneously over a lower amplitude pattern [31]. An experimental snapshot showing localized peaks over an hexagonal pattern and a typical bifurcation diagram allowing for the appearance of localized peaks are displayed in Fig.5.5a and inset, respectively. An unifying description close to a spatial bifurcation of localized states is given in [34, 49], which accounts for the appearance of localized peaks over a lattice spontaneously generated by the system itself.

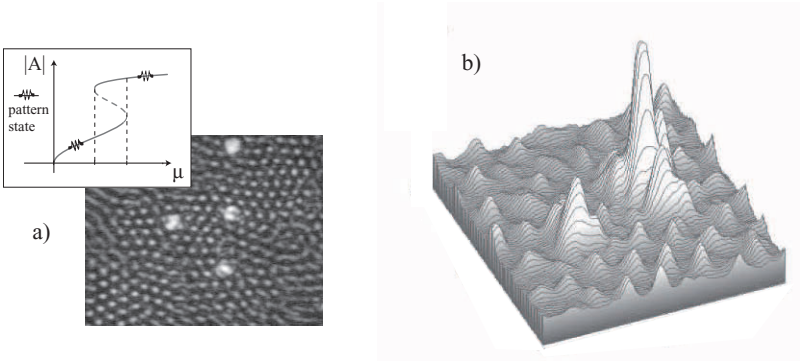

Fig. 5.5 a) Experimental snapshot showing localized peaks over an hexagonal pattern; $V_0 = 12.3\ V$ and $I_{in} = 0.38\ mW/cm^2$. In the inset: a typical bifurcation diagram allowing for the appearance of localized peaks; μ is the bifurcation parameter. c) Experimental intensity profile showing two localized peaks with different amplitudes coexisting over an hexagonally patterned background; $V_0 = 12.3\ V$ and $I_{in} = 0.41\ mW/cm^2$.

Experimentally, we fix the voltage applied to the LCLV at $V_0 = 12.3\ V$ and we increase the input intensity. At $I_{in} = 0.33\ mW/cm^2$ we observe a first bifurcation

that leads to the appearance of an hexagonal pattern. Then, by increasing I_{in}, we observe the spontaneous creation of localized peaks, which are triggered by amplitude and phase fluctuations of the underlying pattern. When continuing to increase I_{in}, localized peaks with a third higher value of the amplitude appear and coexist with the lower amplitude peaks, in a similar way as shown in the previous section for the round and triangular localized structures coexisting over an uniform background. The coexistence of the two localized peaks with different amplitude is shown in Fig.5.5b. At even higher I_{in}, higher amplitude peaks dominate over lower ones and start to invade all space. By doing this, they form large aggregations that propagate with a complex front dynamics until a final pattern is formed, which is largely dominated by spatiotemporal chaos.

5.3.4 1D spatially forced model

As we have seen in the previous section, the main ingredient for the appearance of localized peaks is the coexistence of two spatially periodic states, and this, in some sense, regardless the way in which the two patterns have been created. In order to provide a generic description of such a situation, we have considered in [34] a one-dimensional spatially extended system that exhibits a sequence of spatial bifurcations, the primary bifurcation is super-critical while the secondary one is of subcritical type, as shown in the inset of Fig.5.5a. Let $\mathbf{u}(x;t)$ be a vector field that describes the system under study and satisfies the partial differential equation $\partial_t \mathbf{u} = \mathbf{f}(\mathbf{u}, \partial_x, \{\lambda_i\})$, where $\{\lambda_i\}$ is a set of parameters.

For a critical value of one of the parameters, the system exhibits a spatial instability at a given wave number q_c. Close to this spatial instability, we use the Ansatz $\mathbf{u} = A(X,T)e^{iq_c x}\hat{u} + \bar{A}(X,T)e^{-iq_c x}\hat{\bar{u}} + \cdots$ and the standard amplitude equation reads as [4]

$$\partial_T A = \mu A - \nu |A|^2 A + \alpha |A|^4 A - |A|^6 A + \partial_{XX} A, \tag{5.7}$$

where μ is the bifurcation parameter and $\{\nu, \alpha\}$ control the type of the bifurcation (first or second order depending on the sign of these coefficients). Higher-order terms are ruled out by scaling analysis, since $\nu \sim \mu^{2/3}$, $\alpha \sim \mu^{1/3}$, $|A| \sim \mu^{1/6}$, $\partial_t \sim \mu$, $\partial_x \sim \mu^{1/2}$, and $\mu \ll 1$. Note that this approach is phase invariant ($A \to Ae^{i\varphi}$), but the initial system under study does not necessarily have this symmetry.

Eq.(5.7) allows the coexistence between two different spatially periodic states and, thus, admits front solutions connecting the two states. A single localized structure can be constructed by considering the interaction of two fronts. However, Eq.(5.7) does not exhibit stable localized states, because the scale separation used to derive it has ruled out the fast oscillations, an approximation that is no valid near the front's core. Indeed, in these locations the slowly varying envelope $A(X,T)$ has oscillations of the same (or comparable) size as the small scale of the underlying pattern. In order to take into account this effect, denominated as the non-adiabatic

effect [46, 47, 10], we have computed the corrections of the amplitude equation by including the non-resonant terms [49]. The amended amplitude equation reads as

$$\partial_T A = \mu A - \nu |A|^2 A + \alpha |A|^4 A - |A|^6 A + \partial_{XX} A + \sqrt{\mu} \sum_{m,n\geq 0}^{N} g_{mn} \frac{\partial_X \left[A^m \bar{A}^n\right]}{i q_c (m-n-1)} e^{-i\frac{q_c(1+n-m)}{\sqrt{\mu}}X}, \tag{5.8}$$

where g_{mn} are real numbers of order one and N is the degree of the highest non-linearity. The resulting amplitude equation is parametrically forced in space by the non-resonant terms. It is important to remark that the non-resonant terms are proportional to the spatial derivative of the envelope, therefore they do not change the uniform states. Also notice that the original symmetries $\left\{x \to -x, A \to \bar{A}\right\}$ and $\left\{x \to x + x_o A \to A e^{i q_c x_o}\right\}$ have been restored.

As a consequence of the spatial forcing the front interaction becomes oscillating, that is, alternates between attractive and repulsive forces, thus allowing to stabilize localized structures. The dynamical evolution and bifurcation diagrams of localized patterns can be deduced. It can be shown that for decreasing δ or increasing η the family of localized patterns disappears by successive saddle-node bifurcations and only localized structures with one peak survive, which is in agreement with the experimental observations [31, 50].

5.4 Control of Optical Localized Structures

As shown in Fig.8.3, the experiment comprises a control line, which includes a SLM interfaced with a personal computer and placed on the optical path of the input beam. When the SLM is inserted in between crossed polarizers it provides intensity modulation on the input beam profile, which is used to impose a spatially periodic forcing of the optical feedback. On the other hand, when the polarizers are removed, the SLM provides phase modulations, that are used to control the motion of localized structures [36], as we will see in the following sections. Other control techniques, based on SLM, have been employed in LCLV experiments [51, 52, 53] and semiconductor microcavities [54].

5.4.1 Pinning range and localized structures

For a diffraction length L close to zero and with interference polarization in the feedback loop, bistable regimes can be reached between two homogeneous orientation states of the average tilt angle θ [25]. In this case, front propagation is observed and studied between two spatially uniform orientation states [43]. Recently, we have studied the driven front propagation occurring when the two coexisting states be-

come spatially periodic [55]. By introducing the spatial forcing, the fronts exhibit a large pinning effect, as well as spatially oscillating motion outside the pinning region.

By using the SLM placed as shown on Fig.8.3, sinusoidal modulations of the input light can be induced in such a way that the homogeneous states are transformed into patterned ones. When the modulations are 2-D a large pinning effect is also observed, allowing to create stable localized structures of different size. By using a dedicated software, intensity masks are produced and sent to the SLM, so that the general expression for the input beam profile becomes $I_{in}(\mathbf{r}) = A + B\sin(\mathbf{q}\cdot\mathbf{r})$, where the amplitudes A and B can be controlled by changing the transmittance of the SLM and $\mathbf{q}$ is the spatial wave vector of the grid. By changing the voltage V_0 in the bistability range, we identify a pinning range and, for a given initial condition and a given voltage V_0, it is possible to stabilize localized structures with different sizes. In Fig.5.6 we show three different localized structures obtained with an hexagonal modulation of the input beam profile, for slightly different values of the voltage V_0 applied to the LCLV.

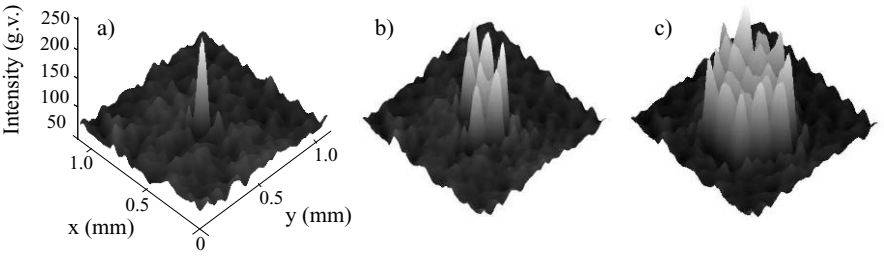

Fig. 5.6 Different localized structures observed with an hexagonal modulation of the input beam profile: a) : $V_0 = 5.543\ V$, b) : $V_0 = 5.582\ V$ and $V_0 = 5.742\ V$.

For one-dimensional systems close to the pinning range, localized states are predicted to exist and to show snaking bifurcation diagrams [56]. However, in 2D cases no a definite theory exists up to now. Our observations in the LCLV experiment demonstrate the existence of the pinning range and its role in the stabilization of localized structures.

5.4.2 Controlled storage of localized structures matrices

Storage of localized structures matrices has been demonstrated by introducing a phase grid on the input beam profile [36]. Numerically, it has been demonstrated for a Kerr-like system that localized structures behave like single particles moving in the presence of phase/intensity gradients [57]. In the case of the LCLV experiment, numerical simulations have shown that phase gradients are more efficient in displac-

ing localized structures than intensity gradients are, and that localized structures go towards the maxima of the phase, so that a phase grid is able to pin localized structures on its local maxima [58]. By using the SLM a phase grid is imposed on the input beam, so that the light intensity on the photoconductor is

$$I_w = \frac{I_{in}}{4} \mid D_\perp \cdot \left[e^{i\varphi_{SLM}(x,y)} \left(1 - e^{-i\beta \cos^2 \theta} \right) \right] \mid^2, \tag{5.9}$$

where $\varphi_{SPM} = \varepsilon(cosKx + cosKy)^2$ is the input phase modulation, $K = 0.015\ rad/\mu m$. The period of the spatial grid is chosen in order to match the size of the localized structures, therefore we can bring them as close one to the other as the maximum packing limit. The parameter ε ranges from 0.2 to 0.6 *rad*. The lower limit is dictated by the minimum modulation amplitude capable to overcome the crosstalk between localized structures, whereas the maximum limit has not to exceed the value for which the homogeneous stationary solution becomes unstable in favor of the pattern state.

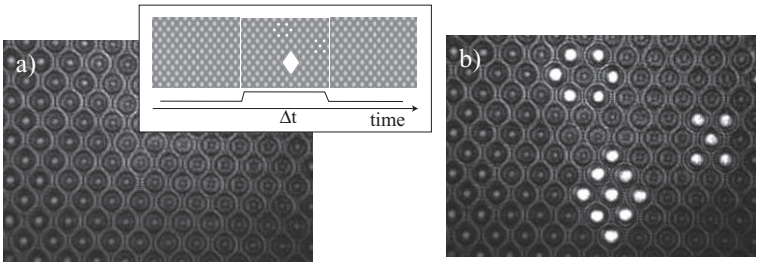

Fig. 5.7 Writing of localized structures over a grid: the empty grid in a) is addressed by an image sent through the SLM for a short writing time Δt, as shown in the inset; the final state in b) is the stationary distribution of localized structures recorded on the grid.

When traveling in the optical feedback loop, the beam undergoes diffraction so that the initial phase modulation is converted into an intensity modulation [59] and phase maxima give rise to low amplitude intensity maxima on the photoconductor. In Fig.5.7a it is displayed an instantaneous snapshot of the empty grid, as observed on the photoconductor side of the LCLV. To write localized structures on the grid, either we send a sequence of local pulses or we flash an image through the SLM. Once created localized structures move towards the closest local maximum of the intensity and remain attached there. By sending through the SLM an image containing the information to be stored, we can write any arbitrary configuration of localized structures. Fig.5.7b shows the final stationary distribution of localized structures obtained after the writing process.

5.5 Propagation Properties of Optical Localized Structures

Diffraction of optical beams is a rich field of classical optics and numerous works aim at developing new beams with smart properties such as, for example, the self-reconstructing Bessel [60] or Airy beams [61]. With this idea of capturing the properties of free propagation of new types of optical beams, we have investigated the diffraction behavior of optical localized structures [37]. Indeed, despite the numerous works dedicated in the past two decades to optical localized structures, an analytical expression describing their transverse field profile $E(x,y)$ is still lacking, so that no prediction can be provided on their evolution under free propagation. Nevertheless, it is a crucial issue to characterize their propagation if one can manage to use localized structures in future applications, for example as optical bits of information. Due to the balance between Kerr non-linearity and diffraction, one expects special diffraction properties to exist for localized structures. In this section, we present an experimental characterization of the propagation properties of localized structures in the LCLV experiment.

A convenient way to represent the diffracted beam of a localized structures is to represent the $I(x,z)$ intensity profile, called irradiance. Experimentally, localized structures are followed during their free propagation by extracting through a beam splitter a small portion of the feedback beam and by recording their evolution starting from a reference plane, $z = 0$ *cm*, which coincides with the photoconductor side of the LCLV. By displacing together the screen and the CCD camera on the acquisition line, the irradiance of the localized structures can then be extracted from the recorded movie.

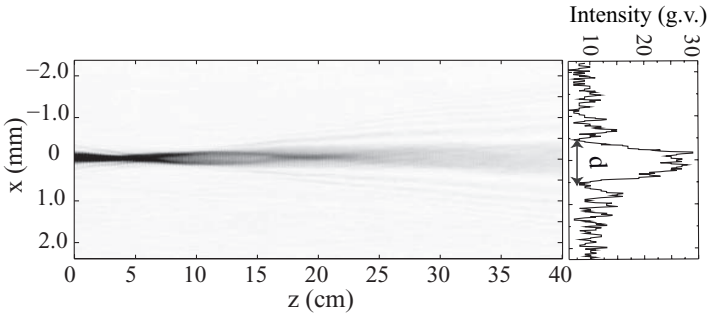

Fig. 5.8 Irradiance of a localized structure in the x,z plane. In the inset it is shown a radial profile in the plane $z \approx 40$ *cm*.

A typical irradiance of a localized structure is shown in Fig.5.8. The diffraction length was fixed to $L = -8$ *cm*. In the reference plane, the localized structure appears, as usual, as a round structure with oscillations in the tails. For propagation distances smaller than $2|L|$, the irradiance brings into evidence new features of the localized structure. In particular, the localized structure focuses at a given z whereas it has a ring or hole shape in a plane close to $z = |L|$. A second focalization exists

in a successive plane. The diffraction length was changed to characterize the position of the main focus and the hole structure with respect to $|L|$. The dependencies of the positions of these two events were found to vary linearly with $|L|$ [35]. Furthermore, a Gaussian type divergence for large value of z has been found for the distance d between the two first minima on both sides of the central peak of the localized structure. The far-field is characterized by the appearance of an increasing number of oscillating wavelets around the central peak, representing the diffraction rings developing at large propagation distance, as shown in the inset of Fig.5.8.

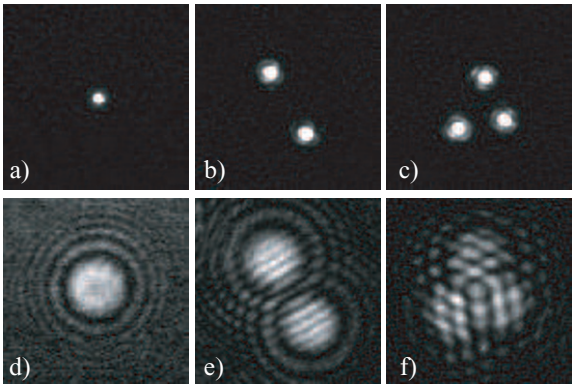

Fig. 5.9 Transverse profiles of a) one, b) two and c) three localized structures close to the focalization plane; d), e) and f) corresponding transverse profiles of the same localized structures recorded in the far-field.

Considering that the size of a single localized structure is increasing with diffraction, one expects the possibility for localized structures to overlap in the far-field, where they can interfere even though in the near field they appear as totally non interacting. This is shown in Fig.5.9, where the same localized structures are displayed for comparison in the focalization plane and in the far-field. Fig.5.9b and c show two and three localized structures that are not interacting in the near-field. Due to diffraction, interference patterns are clearly visible in the far-field, as shown in Fig.5.9e and f. For the two localized structures (Fig.5.9e), the interference pattern is made of stripes whereas for the three localized structures (Fig.5.9 f), it is an hexagonal pattern. These results suggest the interesting idea that depending on the plane z chosen to observe the localized structures, they can either look as ”particle-like” and independent objects or, when looking further on their propagation, they can behave as ”waves” that interfere coherently. Similar analogies of particle-wave duality in a pattern forming system have been also pointed out in parametrically excited surface waves [62].

5.6 Conclusions

In conclusion, we have shown that different types of localized structures can be observed in the LCLV experiment, whenever bistability is present between different spatial states. These can be either uniform or patterned states, so that localized structures correspondingly appear over an homogeneous or spatially modulated background. By introducing either intensity or phase modulations of the input beam, we have shown that we can control and manage localized structures at a high degree, addressing single pixels over large arrays or creating differently sized localized patterns. The full model for the LCLV experiment shows a good agreement with the experimental observations, whereas suitable normal forms derived close to the points of nascent bistability qualitatively accounts for the main dynamical behaviors of localized structures. Finally, investigation of the propagation properties of localized structures have revealed new interesting features related with the dual particle-wave character of the localized patterns.

References

1. G. Nicolis and I. Prigogine, *Self-organization in Non Equilibrium systems*, (J.Wiley & sons, New York, 1977).
2. L.M. Pismen *Patterns and Interfaces in Dissipative Dynamics*, (Springer Series in Synergetics, Berlin Heidelberg 2006).
3. For a review on pattern formation see e.g. M. Cross and P. Hohenberg, Rev. Modern Phys. **65**, 581 (1993).
4. N. Akhmediev and A. Ankiewicz, *Dissipative Solitons*, (Springer, Berlin, 2005).
5. H.A. Eschenfelder, *Magnetic Bubble Technology*, (Springer Verlag, Berlin 1981).
6. S. Pirkl, P. Ribiere and P. Oswald, Liq. Cryst. **13**, 413 (1993).
7. Y. A Astrov and Y. A. Logvin, Phys. Rev. Lett. **79**, 2983 (1997).
8. K-Jin Lee, W. D. McCormick, J. E. Pearson and H. L. Swinney, Nature **369**, 215 (1994).
9. P. B. Umbanhowar, F. Melo and H. L. Swinney, Nature **382**, 793 (1996).
10. M. G. Clerc, P. Cordero, J. Dunstan, K. Huff, N. Mujica, D. Risso, and G. Varas, Nature Physics **4**, 249 (2008).
11. O. Lioubashevski, H. Arbell and J. Fineberg, Phys. Rev. Lett. **76**, 3959 (1996); O. Lioubashevski, Y. Hamiel, A. Agnon, Z. Reches and J. Fineberg, Phys. Rev. Lett. **83**, 3959 (1999).
12. K. Lerman, E. Bodenschatz, D.S. Cannell and G. Ahlers, Phys. Rev. Lett. **70**, 3572 (1993).
13. D. W. Mc Laughlin, J. V. Moloney and A.C. Newell, Phys. Rev. Lett. **51**, 75 (1983).
14. R. Neubecker, G. L. Oppo, B. Thuering and T. Tschudi, Phys. Rev. A **52**, 791 (1995).
15. P. L. Ramazza, S. Ducci, S. Boccaletti and F. T. Arecchi, J. Opt. B **2**, 399 (2000).
16. Y. Iino and P. Davis, J. of Appl. Phys. **87**, 8251 (2000).
17. P. L. Ramazza, E. Benkler, U. Bortolozzo, S. Boccaletti, S. Ducci and F. T. Arecchi, Phys. Rev. E **65**, 066204-1 (2002).
18. S. Residori, T. Nagaya and A. Petrossian, Europhys. Lett. **63**, 531 (2003).
19. B. Schäepers, M. Feldmann,T. Ackemann and W. Lange, Phys. Rev. Lett. **85**, 748 (2000).
20. S. Barland et al., Nature **419**, 699 (2002).
21. G. S. McDonald and W. J. Firth, J. Opt. Soc. Am. B **10**, 1081 (1993).
22. M. Tlidi, P. Mandel and R. Lefever, Phys. Rev. Lett. **73**, 640 (1994).
23. M. Brambilla, L. A. Lugiato and M. Stefani, Europhys. Lett. **34**, 109 (1996).
24. W. Firth and A. J. Scroggie, Phys. Rev. Lett. **76**,1623 (1996).

25. M. Saffman, D. Montgomery and D. Z. Anderson, Opt. Lett. **19**, 518 (1994).
26. V.B. Taranenko, K. Staliunas and C.O. Weiss, Phys. Rev. A **56**, 1582 (1997).
27. B. Schaepers, M. Feldmann,T. Ackemann and W. Lange, Phys. Rev. Lett. **85**, 748 (2000).
28. S. Residori, Physics Reports **416**, 201 (2005).
29. P. L. Ramazza, E. Benkler, U. Bortolozzo, S. Boccaletti, S. Ducci and F. T. Arecchi, Phys. Rev. E **65**, 066204 (2002).
30. U. Bortolozzo, L. Pastur, P. L. Ramazza, M. Tlidi and G. Kozyreff, Phys. Rev. Lett. **93**, 253901 (2004).
31. U. Bortolozzo, R. Rojas and S. Residori, Phys. Rev. E **72**, 045201(R), (2005).
32. M. G. Clerc, A. Petrossian and S. Residori, Phys. Rev. E. **71**, 015205 (R) (2005).
33. S. Residori, U. Bortolozzo and P. L. Ramazza, J. Low Temp. Phys. **145**, 277 (2006).
34. U. Bortolozzo, M. G. Clerc, C. Falcon, S. Residori and R. Rojas, Phys. Rev. Lett. **96**, 214501 (2006).
35. U. Bortolozzo, M. G. Clerc and S. Residori, Phys. Rev. E **78**, 036214 (2008).
36. U. Bortolozzo and S. Residori, Phys. Rev. Lett. **96**, 037801 (2006).
37. U. Bortolozzo, F. Haudin and S. Residori, Opt. Lett. **33** 2698 (2008).
38. S.A. Akhmanov, M.A. Vorontsov and V.Yu. Ivanov, JETP Lett. **47**, 707 (1988); M.A. Vorontsov and W.B. Miller, in *Self-Organization in Optical Systems andApplications in Information Technology*, Ed. by M.A. Vorontsov and W.B. Miller (Springer, Berlin, 1995).
39. E. Pampaloni, P. L. Ramazza, S. Residori and F. T. Arecchi, Phys. Rev. Lett. **74**, 259 (1995).
40. M. G. Clerc, S. Residori and C. S. Riera, Phys. Rev. E **63**, 060701 (R), (2001).
41. F. T. Arecchi, S. Boccaletti, S. Ducci, E. Pampaloni, P. L. Ramazza and S. Residori, J. of Nonlinear Opt. Phys. & Materials **9**, 183 (2000).
42. P. G. de Gennes and J. Prost, *The Physics of Liquid Crystals*, (Oxford Science Publications, Clarendon Press, second edition, 1993).
43. S. Residori, A. Petrossian, T. Nagaya, C. Riera and M. G. Clerc, Physica **D 199**, 149 (2004).
44. I. S. Aranson, K. A. Gorshkov, A. S. Lomov and M. I. Rabinovich, Physica **D 43**, 435 (1990).
45. P. L. Ramazza, U. Bortolozzo and L. Pastur, J. Opt. A: Pure Appl. Opt. **6** 266, (2004).
46. M. G. Clerc and C. Falcon, Physica A **356**, 48 (2005).
47. D. Bensimon, B. I. Shraiman and V. Croquette, Phys. Rev. A **38**, R5461 (1988).
48. Y. Pomeau, Physica D, **23**, 3 (1986).
49. U. Bortolozzo, M. G. Clerc, F. Haudin, R. G. Rojas, and S. Residori, Advances in Nonlinear Optics **2009**, 926810 (2009).
50. U. Bortolozzo, M. G. Clerc and S. Residori, New J. of Physics **11**, 093037 (2009).
51. B. Gütlich, H. Zimmermann, C. Denz, R. Neubecker, M. Kreuzer and T. Tschudi, Appl. Phys. B **81**, 927 (2005).
52. B. Gütlich, H. Zimmermann, C. Cleff and C. Denz, Chaos **17**, 037113 (2007).
53. C. Cleff, B. Gütlich and C. Denz, Phys. Rev. Lett. **100**, 233902 (2008).
54. F. Pedaci, P. Genevet, S. Barland, M. Giudici and J. R. Tredicce, Appl. Phys. Lett. **89**, 221111 (2006).
55. F. Haudin, R. G. Elías, R. G. Rojas, U. Bortolozzo, M. G. Clerc and S. Residori, Phys. Rev. Lett. **103**, 128003 (2009).
56. P. Coullet, C. Riera and C. Tresser, Phys. Rev. Lett. **84**, 3069 (2000).
57. W. J. Firth and A. J. Scroggie, Phys. Rev. Lett. **76**, 1623 (1996).
58. U. Bortolozzo, P. L. Ramazza and S. Boccaletti, Chaos **15**, 013501 (2005).
59. G. D'Alessandro and W. J. Firth, Phys. Rev. Lett. **66**, 2597 (1991).
60. J. Durnin, J. J. Miceli and J. H. Eberly, Phys. Rev. Lett. **58**, 1499 (1987).
61. G. A. Siviloglou, J. Broky, A. Dogariu and D. N. Christodoulides, Phys. Rev. Lett. **99**, 213901 (2007).
62. Y. Couder, S. Protière, E. Fort and A. Boudaoud, Nature **437**, 208 (2005).

Chapter 6
Convectons

Arantxa Alonso, Oriol Batiste, Edgar Knobloch and Isabel Mercader

Abstract A horizontal layer containing a miscible mixture of two fluids can generate dissipative solitons called convectons when heated from below. The physics of the system leading to this behavior is explained, and the properties of the resulting convectons are described. The convectons are shown to be present in a parameter regime known as the pinning region containing a multiplicity of stable convectons of odd and even parity. These lie on solution branches that snake back and forth across the pinning region and illustrate a phenomenon known as homoclinic snaking. Examples of single pulse and multipulse convectons in periodic and closed containers are exhibited and compared with similar states described by the Swift-Hohenberg equation. Time-dependent states in the form of localized traveling waves are computed and distinguished from convectons that drift.

6.1 Introduction

Many fluid systems exhibit spatially localized structures in both two [29]–[3] and three [15, 40] dimensions. Of these the localized structures or *convectons* arising in

Arantxa Alonso
Departament de Física Aplicada, Universitat Politècnica de Catalunya, Barcelona, Spain e-mail: arantxa@fa.upc.edu

Oriol Batiste
Departament de Física Aplicada, Universitat Politècnica de Catalunya, Barcelona, Spain e-mail: oriol@fa.upc.edu

Isabel Mercader
Departament de Física Aplicada, Universitat Politècnica de Catalunya, Barcelona, Spain e-mail: isabel@fa.upc.edu

Edgar Knobloch
Department of Physics, University of California, Berkeley CA 94720, USA e-mail: knobloch@berkeley.edu

O. Descalzi et al. (eds.), *Localized States in Physics: Solitons and Patterns*,
DOI 10.1007/978-3-642-16549-8_6,

binary fluid convection are perhaps the best studied. These states are similar to localized structures studied in other areas of physics [2] despite the fact that fluid systems must always be confined between boundaries. On the other hand in fluid systems the length scale is typically set by the layer depth or the distance between any confining boundaries instead of being an intrinsic length scale selected by a Turing or modulational instability. As a result when we speak of localized states in binary fluid convection we mean states that are localized in the horizontal direction only. In this sense the problem resembles laser systems in short cavities in which the standing wave structure in the longitudinal direction remains of paramount importance [28].

In fluids dissipation, whether through viscosity or thermal diffusion, is generally of great importance. For example, it is responsible for the presence of a nonzero threshold value of the Rayleigh number, a dimensionless measure of thermal forcing, for convection to occur. As a result the dissipative solitons of interest in the present article are strongly dissipative and hence require strong forcing for their maintenance. States of this type cannot be understood in terms of (an infinite-dimensional) Hamiltonian system with small forcing and dissipation.

In this article we survey the properties of localized states in binary fluid convection in a horizontal layer of depth h heated from below. Binary liquids, such as water-ethanol [36, 49] and water-salt mixtures [22] or mixtures of He^3-He^4 at cryogenic temperatures [1], are characterized by a cross-diffusion effect called the Soret effect that describes the diffusive separation of the lighter and heavier molecular weight components of the mixture in an imposed temperature gradient. Specifically, if C is the concentration of the heavier component then its flux is proportional to $-\nabla C - C_0(1-C_0)S_T\nabla T$, where S_T is the Soret coefficient, T is the temperature and C_0, $0 < C_0 < 1$, is the mean concentration. Thus when $S_T > 0$ the heavier component migrates, on a diffusive time scale, towards the colder boundary and vice versa. On the other hand, in the anomalous case in which $S_T < 0$ the heavier component migrates towards the hotter boundary. As a result if a mixture with a negative Soret coefficient is heated from below the destabilizing temperature gradient sets up, in response, a stabilizing concentration distribution. The competition between these two effects leads to complex behavior, including time-dependence at onset of convection [34, 8].

In the absence of motion the temperature T satisfies Laplace's equation. When the top and bottom plates confining the fluid have a larger heat capacity than the fluid the boundaries may be considered to be good thermal conductors in the sense that any fluid motion will not significantly distort the temperature of the plates. Under these circumstances we may suppose, to a good approximation, that the temperature of the bounding plates is fixed, $T = T_0 + (\Delta T/2)$ at $z = 0$ and $T = T_0 - (\Delta T/2)$ at $z = h$. In the conduction state the temperature distribution is therefore $T(z) = T_0 + \Delta T[(1/2) - (z/h)]$. Convection distorts this conduction profile and we write $T(x,z,t) = T_0 + \Delta T[(1/2) - (z/h) + \theta(x,z,t)]$, where $\theta(x,z,t)$ captures the effects of the fluid motion. Owing to the Soret effect the conduction state is also associated with a concentration distribution of the heavier molecular weight component, $C(z) = C_0 + \Delta C[(1/2) - (z/h)]$, where $\Delta C = -C_0(1-C_0)S_T\Delta T$, and we write $C(x,z,t) = C_0 + \Delta C[(1/2) - (z/h) + \Sigma(x,z,t)]$ to describe the stirring ef-

fect of the fluid motion. It is tempting to think of ΔC as an imposed concentration difference across the layer, but this is incorrect since the boundary conditions on C are not that C is fixed on the boundaries but that the flux of the heavier component vanishes on the boundaries, i.e., that $\eta_z = 0$ on $z = 0, 1$, where $\eta \equiv \theta - \Sigma$.

In the following we nondimensionalize the governing equations using the depth h as the unit of length and the thermal diffusion time h^2/κ in the vertical as the unit of time. The system is then described by the dimensionless equations [9]

$$\mathbf{u}_t + (\mathbf{u}\cdot\nabla)\mathbf{u} = -\nabla P + \sigma R[(1+S)\theta - S\eta]\hat{\mathbf{z}} + \sigma\nabla^2\mathbf{u}, \tag{6.1}$$

$$\theta_t + (\mathbf{u}\cdot\nabla)\theta = w + \nabla^2\theta, \tag{6.2}$$

$$\eta_t + (\mathbf{u}\cdot\nabla)\eta = \tau\nabla^2\eta + \nabla^2\theta, \tag{6.3}$$

together with the incompressibility condition $\nabla\cdot\mathbf{u} = 0$. Here $\mathbf{u} \equiv (u, w)$ is the dimensionless velocity field in (x, z) coordinates and P is the pressure. The system is specified by four dimensionless parameters,

$$R \equiv \frac{\alpha g \Delta T h^3}{\kappa\nu}, \quad S \equiv \frac{\beta}{\alpha} C_0(1-C_0)S_T, \quad \sigma \equiv \frac{\nu}{\kappa}, \quad \tau \equiv \frac{D}{\kappa}, \tag{6.4}$$

referred to, respectively, as the Rayleigh number, separation ratio, Prandtl number and Lewis number. Here $\alpha \equiv -\rho_0^{-1}(\partial\rho/\partial T)_0 > 0$ is the coefficient of thermal expansion, $\beta \equiv \rho_0^{-1}(\partial\rho/\partial C)_0 > 0$ is the corresponding coefficient describing the concentration dependence of the fluid density ρ, g is the acceleration due to gravity, ν is the kinematic viscosity and D is the molecular diffusivity of the heavier component; the subscript 0 indicates reference values, computed at $T = T_0$, $C = C_0$. Thus σ and τ specify the properties of the fluid (typically for liquids $\sigma = O(1)$ while $\tau = O(10^{-2})$), while the parameter R specifies the strength of the applied temperature difference imposed across the system, and plays the role of an easily controllable bifurcation parameter. The parameter S is proportional to the Soret coefficient S_T and characterizes the mixture since it measures the concentration contribution to the buoyancy force due to cross-diffusion.

When S or equivalently S_T is sufficiently negative, (i) the primary steady state bifurcation becomes subcritical since any convection that mixes the two components will decrease the stabilizing effect of the concentration stratification produced in response to the destabilizing thermal stratification, and hence make convection easier, and (ii) the primary instability of the conduction state $\mathbf{u} = \theta = \eta = 0$ becomes a Hopf bifurcation [33]. With periodic boundary conditions and identical boundary conditions at the top and bottom this bifurcation is a Hopf bifurcation with $\mathrm{O}(2)\times Z_2$ symmetry, where $R_x \in \mathrm{O}(2)$ acts by $(u(x,z),\, w(x,z),\, \theta(x,z),\, \eta(x,z)) \to (-u(-x,z),\, w(-x,z),\, \theta(-x,z),\, \eta(-x,z))$ relative to a suitable origin, and $R_z \in Z_2$ acts by $(u(x,z),\, w(x,z),\, \theta(x,z),\, \eta(x,z)) \to (u(x,1-z),\, -w(x,1-z),\, -\theta(x,1-z),\, -\eta(x,1-z))$; the continuous part of the symmetry O(2) corresponds to translations in x. The presence of this symmetry is important, and is responsible, for example, for the bifurcation of a circle of periodic states from the conduction state at the primary bifurcation. Its effect on the Hopf bifurcation is more profound [31]: the

bifurcation results in two branches of time-dependent oscillations, traveling waves (hereafter, TW) and standing waves (hereafter, SW) both of which typically bifurcate subcritically and are unstable [24], although the TW may acquire stability at finite amplitude. In contrast, in a closed container this bifurcation breaks apart into successive bifurcations to time-periodic *chevron* states called $\mathrm{SW}_{0,\pi}$. These states are characterized by the presence of a source in the center of the container that emits waves that travel outwards towards the boundaries; the waves may be emitted either in phase (SW_0) or out of phase (SW_π) [26, 7]. The appearance of chevrons already within linear theory is a consequence of a boundary-induced change in the unstable eigenfunction [7]. Moreover, the imposition of lateral boundaries shifts the bifurcation to TW-like states to finite amplitude: these states are no longer *rotating waves* but they break the symmetry of the chevron states, i.e., these are states in which one or other propagation direction predominates. In addition, entirely new states may arise through a secondary Hopf bifurcation from one of the chevron states. These states, called *blinking* states [8, 6], consist of waves that periodically reverse direction, and have no analogue in the corresponding problem on a periodic domain. Indeed, the presence of these states can be related to the loss of translation invariance when lateral boundaries are imposed. A detailed discussion of the effect of such boundaries on the Hopf bifurcation can be found in [26].

In periodic domains with larger spatial period the TW typically lose coherence and break up into a spatio-temporally chaotic state known as dispersive chaos [6]–[39].

In the following we describe some solutions of Eqs. (1)-(3) with the boundary conditions $\mathbf{u} = \theta = \eta_z = 0$ on $z = 0, 1$ appropriate to no-slip, fixed temperature, no-mass-flux boundary conditions, and either (i) periodic boundary conditions (hereafter, PBC) in the horizontal with dimensionless period Γ, (ii) Neumann or stress-free boundary conditions (hereafter, NBC) $u = w_x = \theta_x = \eta_x = 0$ on $x = \pm\Gamma/2$, or (iii) insulating closed container boundary conditions (hereafter, ICCBC), $\mathbf{u} = \theta_x = \eta_x = 0$ on $x = \pm\Gamma/2$. Only a single horizontal dimension will be included resulting in patterns that are two-dimensional, with one extended dimension only. The results described below are for parameter values that have been used in experiments on water-ethanol mixtures.

6.2 Convectons with periodic boundary conditions

In Fig. 10.1(a) we show the results for a $\Gamma = 60$ periodic domain with the parameters $S = -0.021$, $\sigma = 6.22$, $\tau = 0.009$ used in [37]. The figure represents a bifurcation diagram that shows the dimensionless convective heat flux across the layer as a function of the imposed Rayleigh number R. Steady spatially periodic overturning convection (hereafter, SOC) is strongly subcritical, and acquires stability (solid line) above the termination point of the TW branch. The latter bifurcates subcritically from the primary Hopf bifurcation at $R = R_H \approx 1760.8$ corresponding to the onset of convective instability; the SW are not shown. Dispersive chaos is present

for $R > R_H$ and is stable; this state is indicated in Fig. 10.1(a) using solid dots. The time-independent convectons discussed below emerge from this state with increasing R via relaxation oscillations as described in [9]. Figure 10.1(b) shows a typical transient once stable convectons are present, showing the decay of dispersive chaos into a stable, time-independent convecton. The growth of this structure suppresses motion outside the convecton. Thus the formation of the convecton may be viewed as a type of nonlinear focusing instability. The void region outside the convecton fills with waves if the convecton region extends beyond the absolute instability threshold [9].

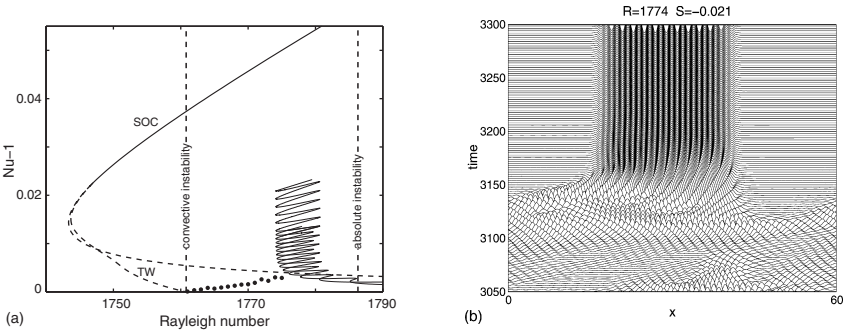

Fig. 6.1 (a) Bifurcation diagram showing the time-averaged convective heat flux per unit length across the layer, $Nu-1 \equiv \Gamma^{-1}\int_{-\Gamma/2}^{\Gamma/2}\theta_z(x,z=1)\,dx$, as a function of the Rayleigh number R when $\Gamma = 60$. The conduction state loses instability at a Hopf bifurcation ($R = R_H \approx 1760.8$). Steady spatially periodic convection (SOC) acquires stability at a parity breaking bifurcation marking the destruction of a branch of spatially periodic traveling waves (TW) originating in the primary bifurcation. Small amplitude dispersive chaos (solid dots) is present for $R > R_H$ and leads into the pinning region ($1774 < R < 1781$) containing a multiplicity of stable localized states of both even and odd parity. (b) Space-time plot showing the midplane temperature $\theta(x,z=1/2,t)$ as a function of time for $R = 1774$ starting from a random small amplitude initial condition. Parameters: $S = -0.021$, $\sigma = 6.22$, $\tau = 0.009$, $\Gamma = 60$. From Ref. [9].

Figure 10.1(a) reveals that the convectons are organized into a pair of branches corresponding to steady states with well defined parity: even states are invariant under R_x and satisfy $(u(x,z),\, w(x,z),\, \theta(x,z),\, \eta(x,z)) = (-u(-x,z),\, w(-x,z),\, \theta(-x,z),\, \eta(-x,z))$, while odd states are invariant under $R_x \circ R_z$ and satisfy $(u(x,z),\, w(x,z),\, \theta(x,z),\, \eta(x,z)) = -(u(-x,1-z),\, w(-x,1-z),\, \theta(-x,1-z),\, \eta(-x,1-z))$. These branches, L_{even} and L_{odd}, respectively, snake back and forth across an interval of Rayleigh numbers called the snaking or pinning region. This interval is quite small for the separation ratio used here, but widens as $|S|$ increases. The pinning region contains a large multiplicity of stable convectons of different lengths and either parity. However, the pinning regions for the even and odd parity convectons are not identical – the pinning region for the odd convectons is generally noticeably narrower than that of even parity convectons [9, 41, 42].

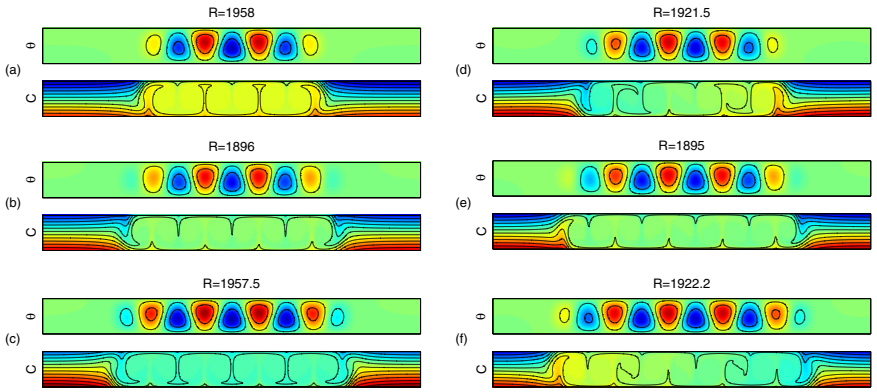

Fig. 6.2 (Color online) (a)-(c) Even parity convectons at successive saddle-nodes on the L_{even} branch with PBC. States (a,c) are on the right of the pinning region, while (b) is on the left. (d)-(f) Odd parity convectons at successive saddle-nodes on the L_{odd} branch with PBC. States (d,f) are on the right of the pinning region, while (e) is on the left. The states are visualized in terms of contours of constant temperature fluctuation θ and contours of constant concentration C. Here and elsewhere all solution profiles use the same color table to indicate the amplitude of the temperature and concentration fields. The states on the right of the pinning region are characterized by strong vortices at either end of the structure and hence strong entrainment; those on the left of the pinning region have weak vortices in the front regions, and very little concentration is entrained. Parameters: $S = -0.1$, $\sigma = 7$, $\tau = 0.01$, $\Gamma = 14$. From Ref. [42].

To understand the properties of these states we show in Fig. 10.2 a series of convectons computed in a smaller domain, with period $\Gamma = 14$. The states are visualized in terms of contours of constant temperature fluctuation θ and contours of constant concentration C. Here and elsewhere all solution profiles use the same color table to indicate the amplitude of the temperature and concentration fields. The figure shows even and odd convectons at successive saddle-nodes on the L_{even} and L_{odd} branches (not shown). The figure reveals that the end vortices repeatedly change direction as one proceeds upwards, from saddle-node to saddle-node, along the right boundary of the pinning region, as additional vortices are nucleated pairwise at the edges of each convecton. As a result the convectons at the right boundary are characterized by strong entrainment of concentration, leading either to a change in the mean concentration within the convecton (even parity convectons) or a concentration gradient within the convecton (odd parity convectons). In contrast, the saddle-nodes along the left boundary correspond to transitions between successive states, and at these the end vortices are very weak, with almost no entrainment taking place (Fig. 10.2). Thus the convectons on the left of the pinning region are characterized by homogenized concentration that is equal to the average concentration.

Figure 7.3 indicates that the convectons form by excavating a hole in the concentration distribution much as described for localized traveling waves by Riecke [46]. This self-trapping resembles closely what happens in optical systems when a laser "burns" a hole through a nonlinear medium by locally altering the index of refrac-

tion. In general these types of mechanisms are associated with a finite threshold – in our language they are subcritical. This is the case for the SOC branch in the binary convection problem since an increase in the convection amplitude increases the mixing of the concentration field thereby decreasing its stabilizing effect and allowing convection to proceed at lower Rayleigh numbers. Moreover, when convection is enhanced locally the same process may result in the formation of a localized structure, at least within a well-defined range of Rayleigh numbers . Figure 7.3 also shows that the convecton profile, once formed, is insensitive to the spatial period Γ. This period only serves to define the available supply of C that can be pumped horizontally by odd convectons or entrained by even convectons.

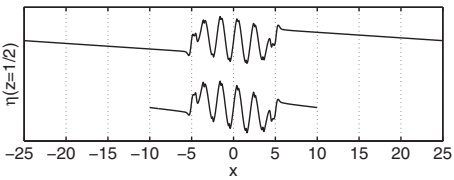

Fig. 6.3 Profiles of $\eta(x,z=1/2)$ for odd parity convectons of the same length at $R=1919$ in domains with PBC and $\Gamma = 20,50$. The profiles are identical except for an overall offset due to different values of the horizontal midplane concentration jump across the convectons generated by the flow within. Parameters: $S=-0.1$, $\sigma=7$, $\tau=0.01$.

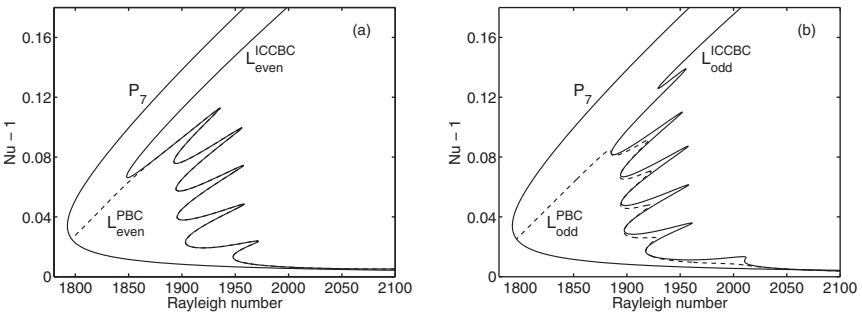

Fig. 6.4 Comparison of the bifurcation diagrams in a $\Gamma = 14$ domain with PBC and ICCBC. (a) Even parity localized states; the two branches coincide until the domain is almost filled. (b) Odd parity localized states; the two branches differ throughout as a consequence of the suppression of horizontal pumping by odd convectons in the presence of ICCBC. Parameters: $S=-0.1$, $\sigma=7$, $\tau=0.01$. From Ref. [42].

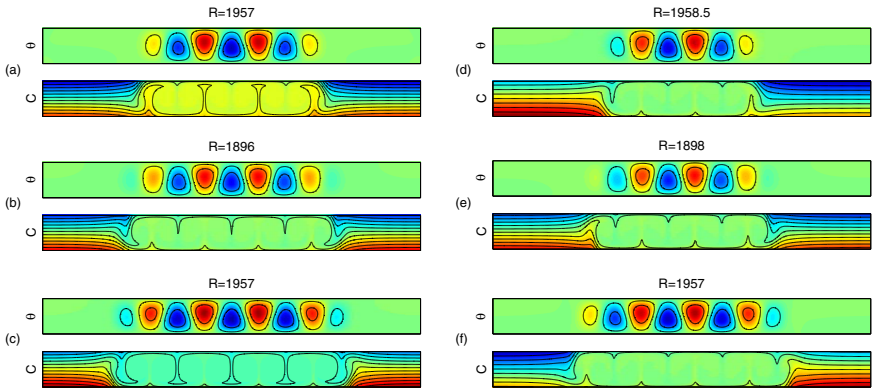

Fig. 6.5 (Color online) (a)-(c) Even parity convectons with ICCBC in a $\Gamma = 14$ container at successive saddle-nodes on the L_{even} branch. States (a,c) are on the right of the pinning region, while (b) is on the left. (d)-(f) Odd parity convectons with ICCBC in a $\Gamma = 14$ container at successive saddle-nodes on the L_{odd} branch. States (d,f) are on the right of the pinning region, while (e) is on the left. The states on the right of the pinning region are characterized by strong vortices at either end of the structure and hence strong entrainment; those on the left of the pinning region have weak vortices in the front regions, and very little concentration is entrained. Parameters: $S = -0.1$, $\sigma = 7$, $\tau = 0.01$. From Ref. [42].

6.3 Convectons with ICCBC

When the boundary conditions are changed to ICCBC (or CCBC as in [41]) the translation invariance is broken and the symmetry that remains is the symmetry $Z_2 \times Z_2 \sim D_2$ generated by R_x and R_z. Figures 7.4(a,b) show the bifurcation diagrams for (a) even and (b) odd states in a $\Gamma = 14$ domain when ICCBC are imposed at $x = \pm\Gamma/2$ and compare the results with those of the corresponding PBC case. As discussed in [41, 42] the traditional snaking diagram is greatly perturbed by this type of boundary condition. Instead of coexistence between snaking and periodic branches the snaking branches now turn continuously into large amplitude states that take the place of the competing periodic states. These large amplitude states fill the container but are not periodic – instead they contain defects that allow the state to adjust to the imposed boundary conditions – and in this they resemble states known as mixed mode states that are also present in the PBC case [42, 13]. This is so for both even (Fig. 7.4a) and odd (Fig. 7.4b) parity states. Localized states computed with ICCBC at successive saddle-nodes are shown in Fig. 7.5. In addition, the ICCBC increase substantially the width of the pinning region for the odd parity states and hence exert an effect on odd parity convectons even when the convectons are localized well away from the walls. Indeed, the width of the pinning region for the odd parity states is now identical to that of even parity states [41, 42].

Figure 7.4(a) shows that until the domain fills with convection the even parity convecton branches with ICCBC and PBC track one another very closely, indicating that the pinning of the fronts to the structured state between them that is responsible

for the snaking behavior of the convecton branches is unaffected by the lateral walls whenever the convecton has even parity. Figure 7.4(b) shows that this is not the case for odd parity convectons, suggesting that the horizontal pumping of concentration by odd parity convectons is responsible [41]. However, the snaking behavior with ICCBC still resembles the PBC case qualitatively, and indeed the left boundaries of the two pinning regions coincide (see below).

As explained in [41] odd parity convectons in the presence of closed container boundary conditions should be thought of as being one half of a two-convecton state filling a domain of length 2Γ obtained by reflecting the odd convecton in $x = \pm\Gamma/2$. Such a reflection yields exact solutions in the case of Neumann boundary conditions and results in a state in which the pumping effects of oppositely oriented odd convectons cancel out, producing a more or less spatially uniform concentration (and temperature) in the void region between them (Figs. 7.5d,f), and eliminating the mean concentration gradient present in odd convectons computed with PBC (Figs. 10.2d,f). The concentration level on either side of the convecton depends on whether the convectons pump towards one another or away from one another, and in a domain of period 2Γ the resulting concentration jump balances the pumping action of the individual convectons. It is for this reason that the two-convecton state with equidistant convectons matches, at least approximately, the solutions found here with insulating no-slip boundary conditions at $x = \pm\Gamma/2$.

To confirm this scenario we examined in [42] the flux balance in the fore and aft regions of the odd parity convecton shown in Fig. 7.5(d). We denote the midplane concentration to the left of the convecton by C^- and to the right by C^+; the mean midplane concentration inside the convecton is $\bar{C}$. We suppose that the convecton pumps concentration from right to left with flux F. Then flux balance at the left front of the convecton, required for the existence of a steady state, leads to the estimate $F \approx \tau(C^- - \bar{C})/\delta$, while that at the right front leads to $F \approx \tau(\bar{C} - C^+)/\delta$. Here δ is the width of the front region, assumed to be the same fore and aft. It follows that $\bar{C} \approx (C^+ + C^-)/2$, a conclusion that agrees very well with the computations shown in Figs. 7.5(d,f). The same argument applied to odd or even convectons at a left saddle-node leads to the prediction $C^- = \bar{C} = C^+$ since $F = 0$ (no entrainment by end vortices). This is so for both PBC (Fig. 10.2) and ICCBC (Fig. 7.5) since the boundary conditions exert little influence when $F = 0$, in agreement with the computations reported in Figs. 10.2(b,e) and Figs. 7.5(b,e). This prediction explains, moreover, why the left boundary of the pinning region for odd convectons is unaffected by the boundary conditions (Fig. 7.4b) – and hence coincides with the left boundary of the even convecton snaking region – while the right boundary is affected dramatically. Finally, the above argument also explains the depletion of the concentration outside the even convecton in Fig. 7.5(a) and its enhancement outside the even convecton in Fig. 7.5(c).

In Fig. 7.6(a) we show a different type of convecton. This convecton is also computed with ICCBC but instead of being located in the center of the container it is attached to one of the walls. Despite this difference the branch of these convectons also snakes, and with each turn a new cell appears at the free end of the convecton. As a result the direction of the entraining vortex changes at each turn, and so

does the homogenized concentration within the structure (Fig. 7.6a). In contrast, the center convectons such as those shown in Fig. 7.5(a) grow by adding a *pair* of cells, one on each side, and so undergo only half the number of back and forth oscillations before the domain is filled as the wall-attached convectons.

To understand the origin of the wall-attached convecton we show in Fig. 7.6(b) the corresponding state with NBC. These (unphysical) boundary conditions allow one to reflect the structure in the boundary $x = \Gamma/2$ and obtain a continuous solution of Eqs. (1)-(3) on the doubled domain, i.e., an even convecton located in the center of a domain of period 2Γ. Structures of this type are well understood, and in particular snake in the usual fashion. Since the domain is twice as large the convecton branch with NBC undergoes twice as many back and forth oscillations before the domain is filled as an even convecton branch in a domain of length Γ, and this fact is reflected in the number of turns executed by the solution branch in Fig. 7.6(b). This behavior in turn resembles closely that observed in Fig. 7.6(a) even though the latter states cannot be reflected in the boundary $x = \Gamma/2$. It should be mentioned that the temperature field $\theta(x,z)$ does not fully reveal the difference between ICCBC and NBC solutions which is more visible in the velocity field $w(x,z)$ since $w(\pm\Gamma/2,z) = 0$ in the former but not in the latter (Figs. 7.6a,b).

6.4 Multiconvectons

In Fig. 6.7 we show bound states of two convectons in a domain with NBC at $x = 0,\Gamma$. Figure 6.7(a) shows a state consisting of two "even" parity convectons of opposite sign, where the sign refers to the direction of the outer cells. In fact the

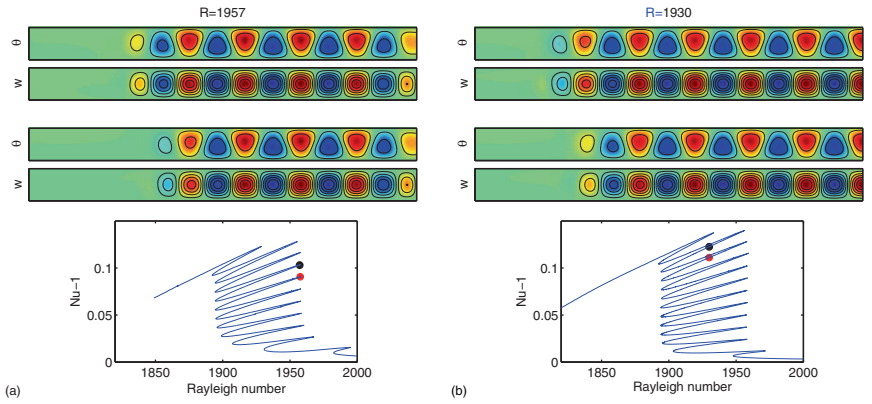

Fig. 6.6 Wall-attached convectons with (a) ICCBC, and (b) NBC in terms of $\theta(x,z)$ and $w(x,z)$. The corresponding bifurcation diagrams are shown at the bottom, with the black dots referring to the (longer) upper states and the red dots referring to the (shorter) states in the middle panels. Parameters: $S = -0.1$, $\sigma = 7$, $\tau = 0.01$. From Ref. [43].

individual convectons are slightly distorted by their interaction and near the end of the branch (open dot) cease to look even. However, the overall structure has exact odd parity with respect to $x = 0$ and, as expected, also snakes although the snake is not well developed: since the effective domain per convecton is now only $\Gamma/2$ the domain fills up rapidly and the snaking branch terminates on a branch consisting of identical 13 cells with odd parity and a well-defined wavenumber (not shown). Figure 6.7(b) shows a different odd parity multiconvecton. This one consists of one central odd parity state and two wall-attached convectons related by odd parity. With NBC the structure can be reflected in the end walls and still satisfy Eqs. (1)-(3). The resulting structure consists of an alternating array of odd and even states of opposite sign, and also snakes. This branch also terminates on the odd parity 13 cell branch, at the same location (open dot) as the branch in Figure 6.7(a) – as the termination point is approached, the voids fill in and the two solutions come to resemble one another. Thus the termination point can be viewed as a bifurcation from a constant amplitude state to different types of hole-like states.

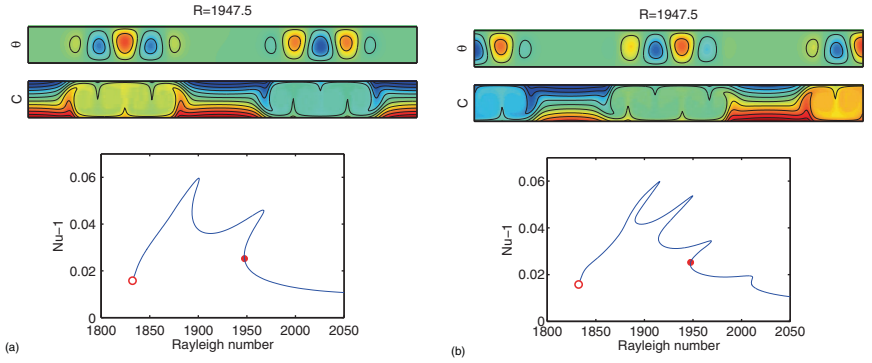

Fig. 6.7 Odd parity multiconvectons with NBC. (a) A bound pair of "even" parity convectons of opposite sign. (b) A bound pair of "odd" parity convectons. Lower panels show the bifurcation diagrams with the red dot indicating the location of the profile shown in the upper panel. The open dots indicate the termination point of each branch; this point is the same for both branches and lies on a branch with 13 identical cells (not shown). Parameters: $S = -0.1$, $\sigma = 7$, $\tau = 0.01$. From Ref. [43].

6.5 Localized traveling waves

Figure 6.8(a) shows the decay of an unstable even parity convecton at $R = 1947$ into a spatially localized traveling wave (hereafter, LTW). Both the waves within the packet and the packet itself travel to the left, although the speed of the latter is quite slow. Wave packets of this type are frequently found in experiments, both in rectangular [44, 30] and periodic [35] domains, and have also been found in simulations [51, 4]. In the present case the LTW coexist with time-independent convectons

and the latter evolve into LTW when they are unstable with respect to asymmetric (i.e., phase) perturbations. The LTW are quite different from the drifting localized structures that form when the symmetry of Eqs. (1)-(3) with respect to $x \to -x$ is weakly broken [21]. The latter take the form of solitary waves, i.e., waves that are steady in an appropriately moving reference frame – the speed of this frame must be determined as an eigenvalue of a nonlinear eigenvalue problem. In contrast, the LTW consist of two frequencies, one from the motion of the wave packet and the other from the waves within the packet.

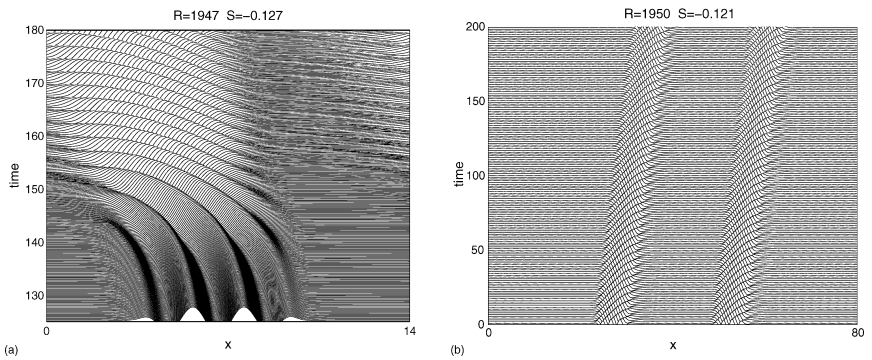

Fig. 6.8 (a) A space-time plot showing the evolution of an even parity convecton into a spatially localized traveling wave (LTW). (b) A space-time plot showing a bound state of two LTW. Parameters: (a) $R = 1947$, $S = -0.127$, $\Gamma = 14$; (b) $R = 1950$, $S = -0.121$, $\Gamma = 80$.

Figure 6.8(b) shows that in larger domains the LTW can also form bound states; these consist of two or more LTW traveling with a common speed. These states form as a result of the overlap of the oscillatory tails of the leading and trailing structures, and the resulting mutual entrainment. Similar structures form in flowing liquid films [12] and indeed as secondary structures on top of an already developed traveling wave state [48].

6.6 Interpretation

The properties and organization of the states described above resemble those familiar from parallel studies of a much simpler problem, the Swift-Hohenberg equation on the real line,

$$u_t = ru - (\partial_x^2 + 1)^2 u + f(u)\,, \tag{6.5}$$

where $f(u) = f_{23}(u) \equiv b_2 u^2 - u^3$ (hereafter, SH23) or $f(u) = f_{35}(u) \equiv b_3 u^3 - u^5$ (hereafter, SH35). Like Eqs. (1)-(3) Eq. (5) is reversible with respect to $x \to -x$, $u \to u$; SH35 has, in addition, the symmetry $x \to x$, $u \to -u$ analogous to the midplane symmetry R_z of Eqs. (1)-(3). Both SH23 and SH35 have been extensively

studied (see [19] for a review). On the real line, when $b_2 > \sqrt{27/38}$, resp. $b_3 > 0$, the primary branch P of periodic states bifurcates subcritically, and is therefore initially unstable. With increasing amplitude it turns around and acquires stability in a saddle-node bifurcation. At a point M, the Maxwell point, the energy of the state P vanishes and is therefore equal to the energy of the trivial state $u = 0$. At this point, $r = r_M$, fronts can be constructed connecting the $u = 0$ state to P and back again, and consequently steady spatially localized structures of arbitrary length all coexist. However, because the state P is structured, the fronts cannot move freely when r is perturbed from r_M: the fronts are pinned to the heterogeneity of the state P between them [10], and consequently will only move once $|r - r_M|$ becomes sufficiently large. This physical argument relies on the existence of a free energy for SH23 and SH35 but explains why multiple distinct spatially localized equilibria should be present in a "pinning region" surrounding the Maxwell point.

There are in fact two (SH23) or four (SH35) distinct branches of localized states, labeled L_ϕ, and selected by beyond-all-orders effects [38, 23], that bifurcate from $u = 0$ simultaneously with the P branch (Fig. 6.9). For SH23 $\phi = 0, \pi$, corresponding to even parity states with, respectively, maxima and minima at the symmetry point $x = 0$. For SH35 there are in addition to $L_{0,\pi}$ also two branches of odd parity states characterized by $\phi = \pi/2$ (positive slope at $x = 0$) and $\phi = 3\pi/2$ (negative slope at $x = 0$). In contrast to SH23 the $\phi = 0, \pi$ solitons are now related by the symmetry $u \to -u$ of SH35 and likewise for the $\phi = \pi/2, 3\pi/2$ solitons. At small amplitude these localized structures are spatially extended but become strongly localized by the time they enter the pinning region. Once in the pinning region the L_ϕ branches begin to snake, adding extra oscillations on either side of each soliton profile while preserving the overall symmetry of the profile. Analysis of the Swift-Hohenberg equation shows that the width of the pinning region is the same for all the snaking branches, and that the wavelength of the periodic structure enclosed within the localized state varies across the pinning region, with the structure compressed for $r < r_M$ and stretched for $r > r_M$ [19]. Stability computations indicate that solitons on branches with a positive slope are stable while those on branches with a negative slope are unstable [17, 18]. The asymmetric states located on the "rungs" connecting the different snaking branches [17, 18] that are responsible for the *snakes-and-ladders* structure of the pinning region are never stable.

Figures 10.1(a) and 10.2 show that much of the phenomenology associated with the pinning region as described by SH35 also applies to convection in binary mixtures. This is so despite the fact that the fluid problem is not variational in time, and no energy playing the role of a Lyapunov function can be defined. This is because the snaking behavior shown in Fig. 10.1(a) is in fact a consequence of the formation of a heteroclinic *cycle* between a trivial state (conduction) and a periodic state (convection), i.e., a solution profile that connects the trivial state at $x = -\infty$ to the periodic state, with a second connection from the periodic state back to the trivial state as $x \to \infty$. In generic systems the formation of this type of orbit is a higher codimension phenomenon but in systems that are *reversible* in space the return connection follows from the equivariance of the equations with respect to $x \to -x$, and the heteroclinic cycle may become generic or *structurally stable*. Numerical computations

suggest that this is the case for binary fluid convection: the pinning or snaking interval is filled with heteroclinic connections between the trivial and periodic states. The boundaries of this region correspond to tangencies between the unstable (stable) manifold of the conduction state and the center-stable (center-unstable) manifold of the periodic state [50]–[10]; an energy function is not required at any stage of this argument. Moreover, since the midplane reflection symmetry of Eqs. (1)-(3) with identical boundary conditions at top and bottom plays the same role as the symmetry $u \to -u$ of SH35, four branches of spatially localized convectons bifurcate from the conduction state together with the branch P of periodic states, provided only that the problem is posed on the whole real line. When these are followed numerically by decreasing the Rayleigh number their amplitude grows while their length shrinks. Once their amplitude and length are comparable to the amplitude and wavelength of steady spatially periodic convection on the SOC branch (Fig. 10.1a) all four convecton branches enter the pinning region and begin to snake back and forth across it (Fig. 10.1a) as the convectons grow in length by nucleating additional convection rolls at both ends. With periodic boundary conditions in the horizontal this process continues until the length of the convecton becomes comparable to the available spatial domain when the convecton branches turn over towards the saddle-node of the periodic branch and leave the pinning region [11, 3, 13]. The bifurcation terminating the convecton branches can be interpreted as a bifurcation of holes from a periodic state. Once again there are four branches, with phases $\phi' = 0, \pi/2, \pi, 3\pi/2$. These branches also snake once they enter the pinning region from above and the hole deepens and gradually fills with the conduction state. On the real line these eight snaking branches remain distinct but on periodic domains with finite period they (generally) connect pairwise [13]. Thus in periodic domains of finite period we expect four branches of convectons. For other boundary conditions, it is necessary, however, to distinguish between convectons and holes since these are no longer related by $\Gamma/2$ translation [42, 43].

We mention that we expect rung-like secondary branches to be present in Fig. 10.1(a) as well. However, in contrast to SH35, in the convection problem these states are expected to correspond to drifting solitary waves, and these are not computed in this article – states of this type are only stationary in SH35 because of its variational structure.

Figure 6.9(b) shows a branch of two-pulse states computed for SH23 resembling the bound state of two convectons shown in Fig. 6.7(a) and consisting of two identical equally spaced localized states. For parity reasons this branch cannot bifurcate from the primary branch P_{19} which contains 19 wavelengths per period Γ and so bifurcates from the next branch P_{18} containing 18 wavelengths. Instead the snaking branch that bifurcates from P_{19} corresponds to bound states of nonidentical states as shown in Fig. 6.9(c) resembling the state shown in Fig. 6.7(b). However, the correspondence is not precise since SH23 does not have the required additional symmetry $u \to -u$.

The one qualitative difference, beyond the presence of time-dependence, between binary fluid convection and a model equation such as the Swift-Hohenberg equation is the observed difference in the widths of the snaking regions for odd and even par-

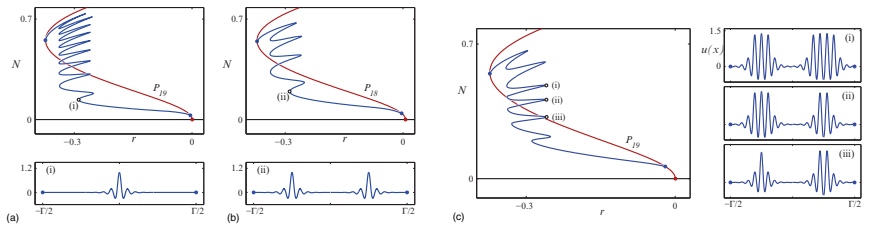

Fig. 6.9 Bifurcation diagram for the Swift-Hohenberg equation SH23 showing the norm $N \equiv \Gamma^{-1} \int_{-\Gamma/2}^{\Gamma/2} u^2 \, dx$ as a function of the parameter r. (a) The branch P_{19} of 19 wavelengths within Γ together with the branch L_0 of convectons with maxima at $x = 0$. (b) Equally spaced two-pulse states cannot bifurcate from P_{19} and instead bifurcate from a subsequent branch P_{18}. Unequally spaced two-pulse states lie on isolas (not shown). (c) Branch of unequal two-pulse states bifurcating from P_{19}. Sample profiles are included. From Ref. [20].

ity convectons. This difference increases with increasing $|S|$ since the width of each region increases with the subcriticality of the periodic branch. We have attributed this fact to the pumping effect associated with odd parity convectons whereby heavier fluid is pumped across the convecton from one side to the other depending on the direction of the vortices in the front regions bounding the convectons. In periodic domains this effect necessarily generates a linear concentration profile between adjacent convectons, while in closed containers it leads to convectons with different background concentrations fore and aft. We have seen that the former effect is responsible for the different widths of the snaking regions for odd and even parity convectons and provided a heuristic explanation why this difference disappears in closed containers.

6.7 Summary

In this article we have summarized the properties of strongly dissipative solitons called convectons that are found in binary fluid convection. We have identified, using a combination of direct numerical simulation and numerical branch following, odd and even convectons in periodic domains, and examined the effects on these structures of lateral boundaries. Because of the horizontal concentration pumping by odd convectons lateral boundaries have a nontrivial effect on the properties of these states and we have explained how and why these boundaries change the width of the pinning region for odd convectons back to that of even convectons. We have also shown examples of wall-attached convectons and different types of two-pulse states. Finally we have shown how these time-independent localized structures relate to localized traveling waves. These results illustrate the richness of this system but in no way represent a systematic study of its properties.

The behavior described here is by no means unique. Stable convectons, including wall-attached convectons, were originally discovered by Ghorayeb and Mojtabi [29] in natural doubly diffusive convection, i.e., convection in a vertical cavity driven by imposed horizontal temperature and concentration differences across the cavity. These states are also associated with snaking behavior [11], this time resembling SH23 since midplane reflection symmetry is now absent [13]. Convection in an imposed vertical magnetic field also exhibits convectons [14, 27] and similar behavior is present in surface tension driven convection in a binary mixture [3]. Similar behavior has been conjectured [32] to be present in other subcritical fluid systems such as plane Couette flow. The reason is simple: the basic mechanism responsible for the creation of these structures is generic in systems that are reversible in space. This is the case for each of the above examples, and provided a heteroclinic cycle between a trivial (homogeneous) and a periodic (structured) state forms as a parameter is varied the associated pinning region in all its richness will be present, and with it the types of behavior described here. Indeed, recent work on plane Couette flow [47] identifies states localized in the cross-stream direction that are of precisely this type. The one significant difference between different fluid systems lies in the stability properties of the localized structures. There is in general no reason why stability should follow the predictions from a variational system like the Swift-Hohenberg equation since nonvariational systems admit additional modes of instability. In general this question must be answered on a case by case basis, by explicit stability computations.

Acknowledgements This work was supported by DGICYT under grant FIS2009-08821 and by the National Science Foundation under grant DMS-0908102.

References

1. G. Ahlers and I. Rehberg, Phys. Rev. Lett. **56**, 1373 (1986).
2. N. Akhmediev and A. Ankiewicz (eds), *Dissipative Solitons*, Lect. Notes in Physics **661**, Springer, Berlin (2005).
3. P. Assemat, A. Bergeon and E. Knobloch, Fluid Dyn. Res. **40**, 852 (2008).
4. W. Barten, M. Lücke, M. Kamps and R. Schmitz, Phys. Rev. E **51**, 5662 (1995).
5. O. Batiste and E. Knobloch, Phys. Rev. Lett. **95**, 244501 (2005).
6. O. Batiste and E. Knobloch, in *Bifurcation Theory and Spatio-Temporal Pattern Formation*, W. Nagata and N. Sri Namachchivaya (eds), Fields Institute Communications **49**, 9 (2006).
7. O. Batiste, I. Mercader, N. Net and E. Knobloch, Phys. Rev. E **59**, 6730 (1999).
8. O. Batiste, E. Knobloch, I. Mercader and M. Net, Phys. Rev. E **65**, 016303 (2001).
9. O. Batiste, E. Knobloch, A. Alonso and I. Mercader, J. Fluid Mech. **560**, 149 (2006).
10. M. Beck, J. Knobloch, D. J. B. Lloyd, B. Sandstede and T. Wagenknecht, SIAM J. Math. Anal. **41**, 936 (2009).
11. A. Bergeon and E. Knobloch, Phys. Fluids **20**, 034102 (2008).
12. A. Bergeon and E. Knobloch, Proc. 3rd Int. Symp. on Bifurcations and Instabilities in Fluid Dynamics, Nottingham, UK (August 2009).
13. A. Bergeon, J. Burke, E. Knobloch and I. Mercader, Phys. Rev. E **78**, 046201 (2008).
14. S. Blanchflower, Phys. Lett. A **261**, 74 (1999).

15. S. Blanchflower and N. O. Weiss, Phys. Lett. A **294**, 297 (2002).
16. C. S. Bretherton and E. A. Spiegel, Phys. Lett. A **96**, 152 (1983).
17. J. Burke and E. Knobloch, Phys. Rev. E **73**, 056211 (2006).
18. J. Burke and E. Knobloch, Phys. Lett. A **360**, 681 (2007).
19. J. Burke and E. Knobloch, Chaos **17**, 037102 (2007).
20. J. Burke and E. Knobloch, Discrete and Continuous Dyn. Syst. Suppl., pp. 109-117 (2009).
21. J. Burke, S. M. Houghton and E. Knobloch, Phys. Rev. E **80**, 036202 (2009).
22. D. R. Caldwell, J. Fluid Mech. **64**, 347 (1974).
23. S. J. Chapman and G. Kozyreff, Physica D **238**, 319 (2009).
24. T. Clune and E. Knobloch, Physica D **61**, 106 (1992).
25. P. Coullet, C. Riera and C. Tresser, Phys. Rev. Lett. **84**, 3069 (2000).
26. G. Dangelmayr and E. Knobloch, Nonlinearity **4**, 399 (1991).
27. J. H. P. Dawes, J. Fluid Mech. **570**, 385 (2007).
28. Q. Feng, J. V. Moloney and A. C. Newell, Phys. Rev. A **50**, R3601 (1994).
29. K. Ghorayeb and A. Mojtabi, Phys. Fluids **9**, 2339 (1997).
30. R. Heinrichs, G. Ahlers and D. S. Cannell, Phys. Rev. A **35**, 2761 (1987).
31. E. Knobloch, Phys. Rev. A **34**, 1538 (1986).
32. E. Knobloch, Nonlinearity **21**, T45 (2008).
33. E. Knobloch and D. R. Moore, Phys. Rev. A **37**, 860 (1988).
34. E. Knobloch, D. R. Moore, J. Toomre and N. O. Weiss, J. Fluid Mech. **166**, 409 (1986).
35. P. Kolodner, Phys. Rev. A **43**, 2827 (1991).
36. P. Kolodner, C. M. Surko and H. Williams, Physica D **37**, 319 (1989).
37. P. Kolodner, J. A. Glazier and H. L. Williams, Phys. Rev. Lett. **65**, 1579 (1990).
38. G. Kozyreff and S. J. Chapman, Phys. Rev. Lett. **97**, 044502 (2006).
39. I. Mercader, A. Alonso and O. Batiste, Eur. Phys. J. E **15**, 311 (2004).
40. I. Mercader, A. Alonso and O. Batiste, Phys. Rev. E **77**, 036313 (2008).
41. I. Mercader, O. Batiste, A. Alonso and E. Knobloch, Phys. Rev. E **80**, 025201(R) (2009).
42. I. Mercader, O. Batiste, A. Alonso and E. Knobloch, Fluid Dyn. Res. **42**, 025505 (2010).
43. I. Mercader, O. Batiste, A. Alonso and E. Knobloch, J. Fluid Mech., submitted.
44. E. Moses, J. Fineberg and V. Steinberg, Phys. Rev. A **35**, 2757 (1987).
45. Y. Pomeau, Physica D **23**, 3 (1986).
46. H. Riecke, Phys. Rev. Lett. **68**, 301 (1992).
47. T. M. Schneider, J. F. Gibson and J. Burke, Phys. Rev. Lett., in press.
48. A. Spina, J. Toomre and E. Knobloch, Phys. Rev. E **57**, 524 (1998).
49. V. Steinberg, J. Fineberg, E. Moses and I. Rehberg, Physica D **37**, 359 (1989).
50. P. D. Woods and A. R. Champneys, Physica D **129**, 147 (1999).
51. H. Yahata, Prog. Theor. Phys. **85**, 933 (1991).

Chapter 7
Morphological Characterization of Localized Hexagonal Patterns

Daniel Escaff Dixon

Abstract The localization of a static hexagonal pattern in a uniform background is studied. Based on a numerical analysis of a prototype model (a Swift-Hohenberg type equation) it is shown that the range of existence of these localized states depended on their shape and size. A morphological classification of these localized structures is performed in order to characterize this phenomenon. A heuristic description of the localization process (based on a wall interaction approach) is proposed, which supplies a good physical picture of what is observed numerically.

7.1 Introduction

Thermodynamic equilibrium is characterized by uniform (without dynamic) spatiotemporal behavior, namely, a state where all the intensive quantities are constant in space and time [1]. When a system is forced to be far from equilibrium these intensive quantities could display a complex spatiotemporal behavior, called self-organization or synergy [2, 3]. To wit, by moving some control parameter related to the distance from equilibrium, the uniform state becomes unstable and the system exhibits the formation of a self-organized structure. A nice example of self-organization is the formation of periodic cellular patterns [4], i.e. a periodic array of cells which demands long range coordination between the different parts of the system. In two-dimensions the basic geometries are three: stripes, hexagons and squares. There are also more irregular patterns which do not follow these geometries. Nature is full of these non-equilibrium manifestations: as convective systems or periodically driven fluid in hydrodynamics [4, 5]; the Turing instability in chemical reactions [6, 7]; or the pigmentation patterns in biology [8], to mention a few examples. Theoretically, these processes can be modeled by writing partial dif-

Daniel Escaff Dixon
Complex Systems Group, Facultad de Ingeniería y Cs. Aplicadas, Universidad de los Andes, Av. San Carlos de Apoquindo 2200, Santiago, Chile. e-mail: descaff@uandes.cl

O. Descalzi et al. (eds.), *Localized States in Physics: Solitons and Patterns*,
DOI 10.1007/978-3-642-16549-8_7,

ferential equations for some order parameter, which is related with the intensive quantities that exhibit the complex spatiotemporal behavior.

Over the last decades much effort has been devoted to the study of localized static cellular patterns [9] (to fix ideas in a uniform background). These localized states are usually related with a hysteretic behavior in the pattern formation, although that coexistence of extended states is not strictly necessary. An essential mechanism responsible for the localization of the pattern is the *pinning effect* [10, 11, 12]. Due to the periodicity of the cellular pattern the pinning effect acts as a periodic "force" capable of trapping the patterns in a region of space. Through this effect these localized structures are structurally stable (in the Andronov sense), namely, they are robust to a parametric perturbation. This structural stability makes it possible to observe them in many experimental contexts [9, 14].

For one-dimensional systems the bifurcation scenario of these localized static cellular patterns has been entirely characterized. By using the fact that any static structure should be a solution of an ordinary set of differential equations, a geometrical picture for the appearance and disappearance of these localized structures can be constructed [6] (based on a horseshoe-like analysis). Essentially, this type of analysis predicts a cascade of saddle-node bifurcations, which accounts for the appearance and disappearance of these localized structures, known as the *snaking bifurcation* [16, 17]. In simple words, a localized state can be classified by the number of cells that are spatially localized, i.e. the size of the localized structure. There is then an infinite discrete set of possible localized states; the range of existence (at the parameter space) depends on the size of the localized structure.

For two-dimensional systems the scenario is more complicated, even with quasi-one-dimensional configurations, as front connecting stripe patterns with a uniform state, that could exhibit unexpected dynamics in the new dimension [16, 18, 19]. In the case of hexagons, it has been observed that not only does the size play an important role in the localization process, but the shape of the localized state does as well [20]. The aim of this chapter is to perform a morphological characterization of localized hexagonal patterns in order to elucidate their bifurcation features. Namely, how the existence range (at the parameter space) of the different species of localized structures is affected by their shape and size. In order to do this characterization a prototype model for hexagon formation is introduced in section 11.2. In section 11.3 the morphological characterization is performed, and detailed numerical analysis of the prototype model is given in order to sustain the morphological characterization. In section 7.4 a heuristic description of the localization process is presented, based on a wall interaction approach. The case of a localized line of cells is separately commented in section 11.7, because it can exhibit qualitatively different features. Finally, in section 11.7 we summarize our results and provide conclusions.

7.2 Prototypical Model for Hexagon Formation

A prototype model, which exhibits coexistence between a stable uniform state and a hexagonal pattern, is a variant of the famous Swift-Hohenberg equation [21], which has the form [22]

$$\partial_t u = \varepsilon u + \nu u^2 - u^3 - \left(\nabla^2 + q^2\right)^2 u, \tag{7.1}$$

where ∇^2 is the Laplace operator in two dimensions, u is the order parameter, ε is the control parameter (related with the distance to equilibrium), q is the characteristic wave number of the system, and ν is a parameter related to the breaking of the up-down symmetry ($u \longrightarrow -u$) which is essential to observing the formation of hexagons. Since (7.1) has the symmetry $u \longrightarrow -u$ and $\nu \longrightarrow -\nu$ simultaneously, only the case $\nu > 0$ (up-hexagons) will be studied.

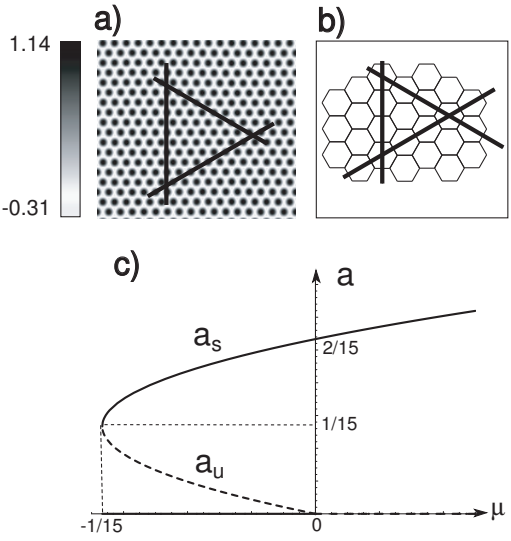

Fig. 7.1 (a) Density plot of the order parameter from a direct numerical simulation of model (7.1), for $\varepsilon = 0.01$, $\nu = 1$ and $q = 0.7$. (b) Pictorial representation of the hexagonal pattern. (c) Typical hysteresis loop of model (7.1) computed from a enveloped equation approach, where a represents the amplitude of the pattern and $\mu = \varepsilon/\nu^2$.

The uniform solutions $u = 0$ became unstable when $\varepsilon > 0$ and the system exhibits the formation of a hexagonal pattern. Fig. 10.1(a) displays a typical hexagonal pattern from a numerical simulation of equation (7.1), while Fig. 10.1(b) shows a pictorial representation of the pattern. The appearance of the pattern shows hysteresis, namely, if the control parameter is moved back to the region $\varepsilon < 0$ the hexagons persist for some values of ε sufficiently close to the critical point $\varepsilon = 0$. Fig. 10.1(c) shows a typical hysteresis loop computed from an enveloped equation approach (i.e. a perturbation near the limit $\nu \sim \sqrt{|\varepsilon|} \to 0^+$, for technical details see [23]). The amplitude of the pattern as function of the control parameter ($\mu = \varepsilon/\nu^2$) is presented there, where solid lines represent stable patterns while dashed lines represent unstable patterns. Therefore, there is a coexistence region where both the uniform and the hexagonal phases are stable. Inside this region we expect to observe local-

ized structures. For instance, by fixing the parameter $\nu = 1$ and $q = 0.7$, a numerical measure of the coexistence range gives us $\varepsilon \in [-0.162, 0]$.

7.3 Localized Hexagonal States: Geometrical Considerations and Morphological Characterizations

One of the main features of hexagonal patterns is their crystalline nature. They behave as a two-dimensional solid crystal, with three privileged directions where it is possible to make a perfectly flat cutting of the hexagonal net (namely without cutting the cells). In Fig. 10.1(a) and (b) an explicit drawing is shown of these directions of symmetry. As it is intuitively expected, the pinning effect occurs just when the wall (the interface between the hexagonal and the uniform phase) coincides with one of these directions [11, 20, 23]. Therefore, to construct a localized structure, the net must be cut along these directions of symmetry, just as when cutting a diamond. Fig. 10.1(a)-(f) displays typical localized states obtained by a direct numerical simulation of model (7.1). Since the hexagonal net must be cut along its directions of symmetry, only four types of corners are allowed: with *internal* angles of $\pi/3$ or $2\pi/3$; or with *external* angles of $\pi/3$ or $2\pi/3$.

Therefore, we can perform a morphological classification of the localized structures. When the localized domain is convex, there are two types of corners with internal angles of $\pi/3$ or $2\pi/3$. Then, we define two morphological categories, introducing the following nomenclature: *n-convex structure*, with $n = 0$, if there are no internal angles of $\pi/3$ (see Fig.10.2(a)), otherwise $n = 1$ (see Fig.10.2(b)). When the localized domain is not convex, we have in addition external angles of $\pi/3$ or $2\pi/3$. Then, we define four morphological categories, introducing the following nomenclature: *mn-nonconvex structure*, with $m = 0$ or $n = 0$, if there are no external or internal angles of $\pi/3$, respectively, otherwise $m = 1$ or $n = 1$. Fig.10.2(c) shows a 00-nonconvex structure, Fig.10.2(d) a 01-nonconvex structure, Fig.10.2(e) a 10-nonconvex structure and Fig.10.2(f) a 11-nonconvex structure.

A fully numerical study of the different species of localized domain has been performed by fixing the parameters $\nu = 1$ and $q = 0.7$, and only moving the control parameter ε (using a pseudo-spectral method). The pinning range for an isolated flat wall can be estimated $\varepsilon \in [-0.157, -0.093]$. To wit, for $\varepsilon > -0.093$ the hexagonal phase propagates over the uniform one, and for $\varepsilon < -0.157$ the uniform phase propagates over the hexagonal one, but for $-0.157 < \varepsilon < -0.093$ the flat interface movement is locked.

Fig.10.2(g) shows a numerical experiment performed for $\varepsilon = -0.151$ (i.e. inside the pinning rage), taking as the initial condition a 1-convex structure generated with $\varepsilon = -0.15$. Here this kind of localized state destabilizes, becoming a 0-convex structure. In general, for $\varepsilon < -0.15$ it is not possible to observe 1-convex or $n1$-nonconvex structures. In Fig.10.2(h) a destabilization process of a 0-convex structure is shown, for $\varepsilon = -0.155$, in this case the final state is a completely uniform state. In the range $\varepsilon \in [-0.157, -0.155]$, in spite of the fact that the pinning effect

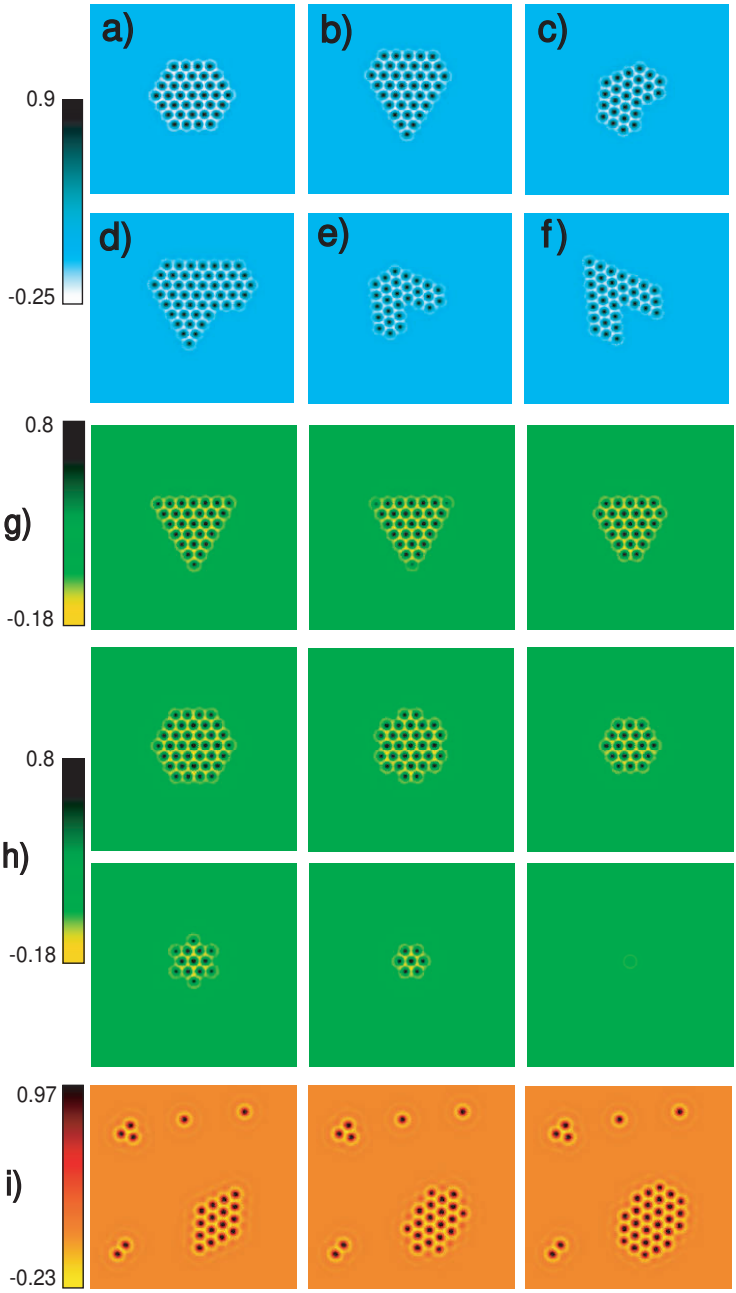

Fig. 7.2 Density plot of the order parameter from a direct numerical simulation of model (7.1), for $\nu = 1$, $q = 0.7$ and: (a) $\varepsilon = -0.12$; (b) $\varepsilon = -0.12$; (c) $\varepsilon = -0.12$; (d) $\varepsilon = -0.135$; (e) $\varepsilon = -0.14$; (f) $\varepsilon = -0.135$; (g) $\varepsilon = -0.151$ (temporal evolution, time runs from left to right); (h) $\varepsilon = -0.155$ (temporal evolution, time runs from left to right and from top to bottom); (i) $\varepsilon = -0.09$ (temporal evolution, time runs from left to right).

is still acting (an isolated flat wall remains at rest in this range), it is not possible to observe localized structures of any category (convex or nonconvex). It is important to notice that the destabilization processes (see Fig.10.2(g) and Fig.10.2(h)) start from the corners of the structure.

On the other hand, in the other border of the pinning range the opposite behavior is observed. Fig.10.2(g) shows a numerical experiment performing for $\varepsilon = -0.9$ (i.e. outside the pinning rage), taking as initial condition a 1-convex structure generated with $\varepsilon = -0.93$ surrounded by smaller localized structures. In this case the cells, far from the corners, are not able to confine the pattern, and it begins to propagate from these places, while the smaller structures remain static. Namely, the corners are stronger to contain the spread of the pattern.

Notice that the introduced classification is neither suitable to the 1-cell structure, which is a genuine isotropic structure (see Fig.7.3(a), for more details of localized isotropic structures see [24]), nor applicable to those structures where is not possible to define a corner, such as in the case of a line of cells (see Fig.7.3(b)). For instance, in the case of 3-cells structures, there are three possibilities: a line, an equilateral triangle or a corner in an angle of $2\pi/3$ (see Fig.7.3(c)), where the equilateral triangle is the only suitable to be sorted as a 1-convex structure. Another interesting phenomenon is the presence of holes inside the localized structure. These types of objects can be sorted in our morphological categories (non-convex domain). When the hole is far from the border of the structure, the behavior will be the same predicted for the longest structures by our calculations. If the hole is close to the border this behavior will change due to the wall's interaction explained below.

Table 7.1 summarizes our results. Notice that the range of existence of the smallest localized structures is quite different from the longer ones. Therefore, the existence of a localized structure is strongly affected by its size. For the longest structures (typically, more than ten cells), the morphological category seems to be the main feature.

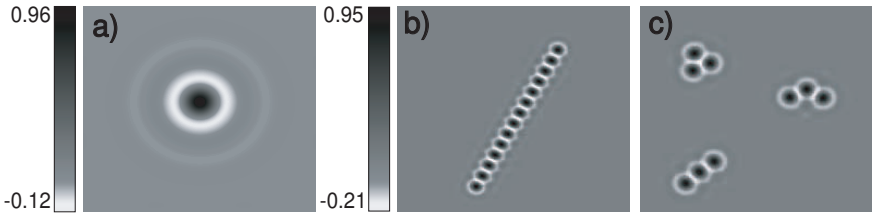

Fig. 7.3 Density plot of the order parameter from a direct numerical simulation of model (7.1), for $\nu = 1$, $q = 0.7$ and: (a) $\varepsilon = -0.088$; (b) $\varepsilon = -0.095$; (c) $\varepsilon = -0.11$.

Table 7.1 Range of Existence of the Different Species of Localized States for $\nu = 1$ and $q = 0.7$.

Morphological Features	minimum ε	maximum ε
Isolated wall	-0.157	-0.093
0-convex	-0.154	-0.093
1-convex	-0.15	-0.093
00-nonconvex	-0.154	-0.113
10-nonconvex	-0.154	-0.129
01-nonconvex	-0.15	-0.113
11-nonconvex	-0.15	-0.129
3-cells (equilateral triangle)	-0.149	-0.086
3-cells ($2\pi/3$ corner)	-0.146	-0.106
2-cells	-0.146	-0.084
1-cell	-0.142	-0.056
Line of cells	-0.146	-0.093

7.4 Heuristic Description of the Localization Process

To understand the mechanisms behind these numerical results, one must realize that a localized pattern is a domain surrounded by walls (in one of the three symmetry directions of the hexagonal net). These walls are under stress, which comes from three different sources: (1) the preference of the system for the hexagonal phase or the uniform phase, which leads to the propagation of one phase over the other; (2) the interaction between the long spatial scale of the interface with the small spatial scale of the cellular pattern, the pinning or trapping effect; and (3) the presence of other walls that surround the localized pattern. Therefore, when these three effects cancel each other, the localized structure exists.

The two first effects have been widely discussed along the literature [11], however stress coming from the wall interaction has been just considered recently [20, 23]. To get an intuitive picture of the process one can first consider an isolated wall (i.e. the two first effects) in the limit $\nu \sim \sqrt{|\varepsilon|} \ll 1$, keeping $q \sim \mathcal{O}(1)$. To wit, working near this limit we assume that equation (7.1) is a weakly nonlinear regimen. Then, it is possible to construct a static equilibrium condition for the position longitudinal P of the envelope of the front (for technical details see [11, 20, 23]), that is the wall is motionless if

$$-\beta + \Gamma \cos(qP) = 0. \tag{7.2}$$

The first term $-\beta$ is related with the tendency of the system to propagate one phase over the other, it is proportional to the distance of the control parameter to the Maxwell point, namely, the point where both phases are equivalent. The second term accounts for the pinning or trapping effect, which is capable of locking the front propagation in the range of the control parameter $|\beta/\Gamma| < 1$, the *pinning range*.

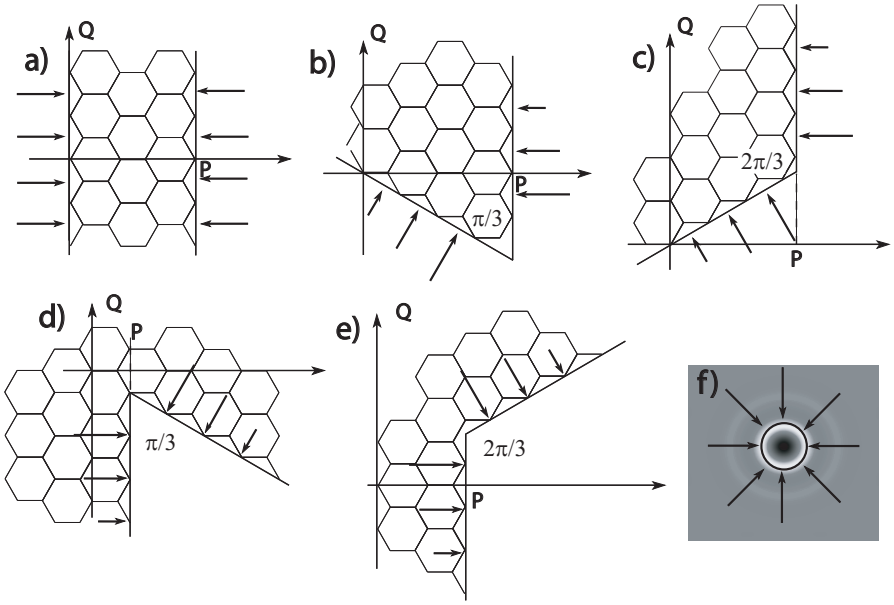

Fig. 7.4 Pictorial view of the wall interaction for (a) parallel walls; (b) $2\pi/3$ internal corner; (c) $\pi/3$ internal corner; (d) $2\pi/3$ external corner; and (e) $\pi/3$ external corner; (f) the isotropic one-cell structure.

To study how the presence of the other walls modifies (7.2), one can focuses on the interaction of two walls. There are five types of configurations: parallel walls; or forming one of the four possible angles, related to the morphological categories.

For parallel walls, the configuration is motionless if it satisfies the static equilibrium condition

$$-\beta + \Gamma \cos(qP) + \Xi_{\parallel} \exp(-\lambda P) = 0, \tag{7.3}$$

where $\Xi_{\parallel} > 0$ and $\lambda > 0$ are numerical constants (see [20, 23] for explicit evaluation of these coefficients). In this case, P means the position of one wall with respect to the other, i.e. the size of the structure (see Fig.7.4(a)). Note that this case is quasi-one-dimensional, and the relation (7.3) predicts the same bifurcation structure deduced for one-dimensional systems in [6, 16, 25], namely, the range of existence of a localized cellular pattern depends on its length (number of cells).

The relation (7.3) could be interpreted qualitatively as follows: a small structure feels an extra-stress, stronger than a longer one, which comes from its smaller size. Since $\Xi_{\parallel} > 0$, the wall interaction is attractive (as in one-dimension [25, 26]), i.e. this extra-stress acts like a *self-compressing effect*, which explains the shift in the range of existence of the smallest structures (see Table 7.1). Fig.7.4(a) shows a pictorial view of the wall interaction for parallel walls, while Fig.7.4(f) draws an extension of this concept for the isotropic one-cell structure.

For a corner in an internal angle of α ($\pi/3$ or $2\pi/3$), the following static equilibrium condition is obtained (see [20, 23] for technical details)

$$-\beta + \Gamma \cos(qP) + \Xi_\alpha \exp\left(-\sqrt{3}\lambda d/2\right) = 0, \tag{7.4}$$

where

$$d = 2\left[\cos(\alpha) P + \sin(\alpha) Q\right]/\sqrt{3} \tag{7.5}$$

is the distance to the corner, and $\Xi_\alpha > 0$ a numerical constant. Hence, when we get closer to the corner, the stress increases [see Fig.7.4(b) and (c)]. This effect comes intuitively from the fact that, near the corner, both walls are closer, and the self-compressing effect is stronger. From (7.4) we can also deduce that, for a fixed Q, the extra-stress, produced by the wall interaction, is bigger in the case of a $\pi/3$ corner than in the case of a $2\pi/3$ corner (the walls are closer in the former case).

Notice that the relation (7.4) predicts a strong curvature at the corners, which is corrected for the high order terms of our perturbative expansion. Since we are neglecting the surface tension, curvature is not relevant. Actually, one of the main hypotheses behind this analysis, is that curvature effects can be neglected in the case of hexagons. That is, if the interface curvature is not capable of eliminating or creating a cell, it is not relevant in a first approximation. If so, there would be a cell interaction that could be modeled in a wall interaction framework (not in a continuous one). Moreover, this tells us that when we match two walls, the matching is smooth at the corner.

For corners associated to the external angles of $\pi/3$ or $2\pi/3$ the static equilibrium condition takes the form

$$-\beta + \Gamma \cos(qP) - \tilde{\Xi}_\alpha \exp\left(-\sqrt{3}\tilde{\lambda} d/2\right) = 0, \tag{7.6}$$

with $\tilde{\Xi}_\alpha > 0$. Then, in this case the extra-stress (from the interaction of walls) is negative, e.g. such types of structures tend to disappear when the hexagonal pattern is energetically favorable ($\beta < 0$), which agrees with numerical observations (see Table 7.1). In this case the self-compressing effect acts over the uniform phase (see Fig.7.4(d) and (e)).

Therefore, in spite of the size of the localized structure, it always has corners and at these regions the self-compressing effect remains relevant. Since the types of corners are related to the morphological category of the structure, this is a *shape effect*.

7.5 The Case of a Localized Line of Cells

As mention before, the case of a line of cells deserves an independent analysis. Table 7.1 shows the existence range of this species of localized structure fixing the parameters $\nu = 1$ and $q = 0.7$. For $\varepsilon < -0.146$ the localized state vanishes and prevails

the uniform state $u = 0$, but for $\varepsilon > -0.093$ the destabilization process is qualitatively different from the other species. Fig.7.5 shows this destabilization process: the cells from the center of the structure stretch and start to propagate stripes. These stripes are asymmetric objects in the sense that the spatial oscillations are centered in a positive value of the order parameter u, as is expected in a system that has broken symmetry $u \longrightarrow -u$. When the elongation of the cells reaches the ends of the structure, the system nucleates hexagons at these points which begin to spread filling the remaining space. After the transient dynamics the system converges to the localized state shown in the last picture of Fig.7.5, which seems to be an stationary state.

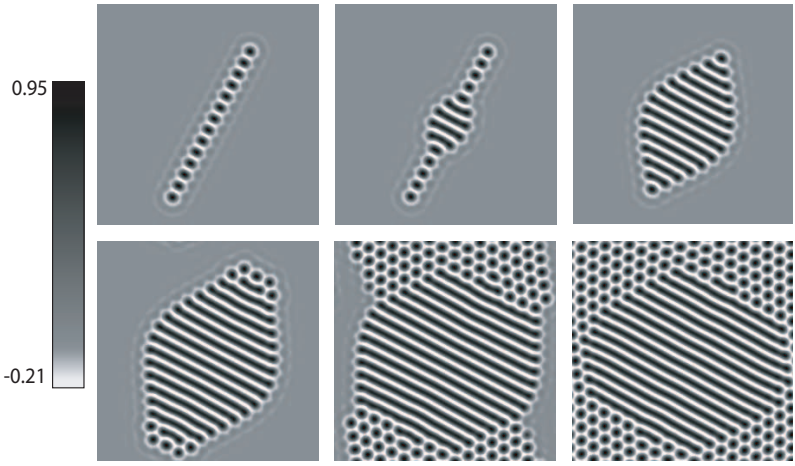

Fig. 7.5 Density plot of the order parameter from a direct numerical simulation of model (7.1) for $\nu = 1$, $q = 0.7$ and $\varepsilon = -0.092$. Time runs from left to right and from top to bottom.

Probably, this localized state (the last picture of Fig.7.5) is a particular feature of model (7.1). In fact, it is not predicted by universal argument performed through amplitude equations [27], i.e. we do not necessarily expect to observe these structures in an arbitrary instability with the same symmetries of model (7.1). The numerical experiment shown in Fig.7.5 is related to high non-linear behavior. Actually, when decreasing a little bit ν (which rules the magnitude order of non-linear saturation) none of these processes are observed. Fig.7.6 displays the same type of numerical experiment performing for $\nu = 0.9$, where the systems behaves as it is intuitively expected from the heuristic description of the last section.

7.6 Conclusions and Perspective

Due to the crystalline nature of a hexagonal pattern, the localized hexagonal structures are like crystals, whose shapes are related to the symmetry direction (as one-dimensional crystalline planes) of the hexagonal net. While for localized structures that link two uniform states in 2-dimensions, the surface tension (or curvature effects) is a fundamental feature of the localization process (that are like raindrops), in this case it seems to be negligible. For these crystals their morphological category and their size play a fundamental role in the localization.

Heuristic description via wall interaction supplies a good physical interpretation of the mechanisms involved in the localizations of the pattern. Namely, in addition to the well known pinning phenomenon, there is a self-compressing effect, induced by the attractive wall interaction. This makes the phenomenology richer in the sense that the process of localization depends on the size and shape of the structure. It is also suggested that localized structures appear by saddle-node bifurcations, due to the appearance of zeros of the static equilibrium conditions.

Furthermore, this process seems to be similar for holes in the hexagonal net. Preliminary numerical simulations show deformations in the surrounding pattern, probably induced by boundary conditions, which change the phenomenology. A way to avoid this problem is to consider holes inside of a localized pattern. In this case the wall interaction will be worked in the same manner as in simple connect domains. Then, they are non-convex structures that can be sorted in our morphological categories and are suitable for the same kind of analysis performed in this report.

Another interesting phenomenon is the destabilization of a line of cells. It could exhibit qualitatively different features compared to the other species of localized

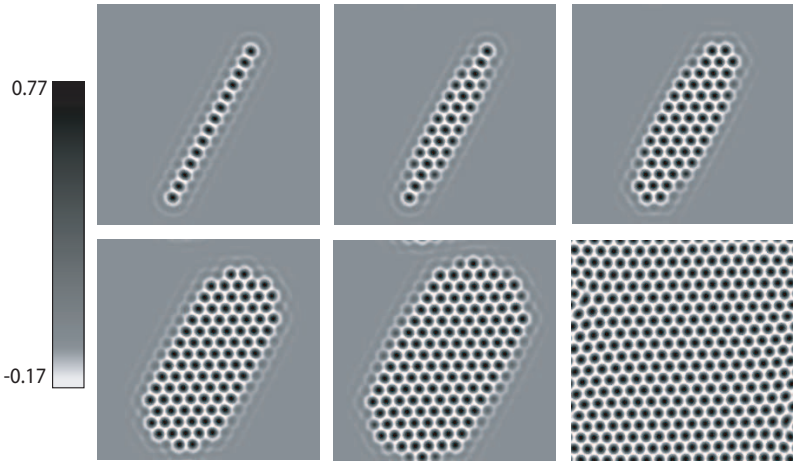

Fig. 7.6 Density plot of the order parameter from a direct numerical simulation of model (7.1) for $\nu = 0.9$, $q = 0.7$ and $\varepsilon = -0.075$. Time runs from left to right and from top to bottom.

states. However, it is related to high non-linear behavior, and near to the weakly non-linear regime the destabilization process behaves as our perturbation method predicts.

Acknowledgements I would like to thank FONDECYT Project No. 11090280 and FAI ING-002-09 for financial support.

References

1. H. B. Callen, *Thermodynamic and an Introduction to Thermostatistics* (Copyright, USA, 1985).
2. G. Nicolis and I. Prigogine *Self-Organization in Nonequilibrium Systems* (John Wiley & Sons, New York, 1977).
3. H. Haken *Synergetics* (Springer, Berlin, 1983).
4. M.C. Cross and P.C. Hohenberg, Rev. Mod. Phys. **65**, 851 (1993).
5. S. Chandrasekhar, *Hydrodynamic and Hydromagnetic Stability* (Dover Publications, New York, 1981).
6. A.M. Turing, Phil. Trans. R. Soc. B **237**, 37 (1952).
7. V. Castests, E. Dulos, J. Boissonade and P De Kepper, Phys. Rev. Lett. **64**, 2953 (1990).
8. J. D. Murray, *Mathematical Biology* (Springer-Verlag, Berlin, 1989).
9. E. Knobloch, Nonlinearity, **21**, T45 (2008).
10. Y. Pomeau, Physica D **23**, 3 (1986).
11. B.A. Malomed, A.A. Nepomnyashchy and M.I. Tribelsky, Phys. Rev. A **42**, 7244 (1990).
12. H. Sakaguchi and H. Brand, Physica D **97**, 274 (1996).
13. H. Arbell and J. Fineberg, Phys. Rev. Lett. **85**, 756 (2000).
14. U. Bortolozzo, M. G. Clerc and S. Residori, New J. Phys. **11**, 093037 (2009).
15. P. Coullet, C. Riera and C. Tresser, Phys. Rev. Lett. **84**, 3069 (2000).
16. J. Burke and E. Knobloch, Chaos **17**, 037102 (2007).
17. M. Beck, J. Knobloch, DJB. Lloyd, B. Sandstede and T. Wagenknecht, SIAM J. Math. Anal. **41**, 936 (2008).
18. A. Hagberg, A. Yochelis, H. Yizhaq, C. Elphick, L. Pismen and E. Meron, Physica D **217**, 186 (2006).
19. M. G. Clerc, D. Escaff, D. and R. Rojas, EPL **83**, 28002 (2008).
20. D. Escaff, O. Descalzi and J. Cisternas, Prog. of Theo. Phys **121**, 29 (2009).
21. J. Swift and P.C. Hohenberg, Phys. Rev. A **15**, 319 (1977).
22. M. Bestehorn and H. Haken, Z. Phys B **57**, 329 (1984).
23. D. Escaff and O. Descalzi, Int. J. of Bifur. Chaos **19**, 2727 (2009).
24. DJB. Lloyd, B. Sandstede, Nonlinearity **22**, 485 (2008).
25. M.G. Clerc and C. Falcon, Physica A **356**, 48 (2005).
26. B.A. Malomed and A.A. Nepomnyashchy, Phys. Rev. A **42**, 6009 (1990).
27. S. Ciliberto, P. Coullet, J. Lega, E. Pampaloni and C. Perez-Garcia, Phys. Rev. Lett. **65**, 2370 (1990).

Part III
Localized structures for optical applications

Chapter 8
Cavity Solitons in Vertical Cavity Surface Emitting Lasers and their Applications

Massimo Giudici, Francesco Pedaci, Emilie Caboche, Patrice Genevet, Stephane Barland, Jorge Tredicce, Giovanna Tissoni and Luigi Lugiato

Abstract Cavity solitons (CS) are single peak localized structures which form over a homogeneous background in the section of broad-area non linear resonator driven by a coherent holding beam. They can be switched on and off by shining a writing/erasing local laser pulse into the optical cavity. Moreover, when a phase or amplitude gradient is introduced in the holding beam, *CS* are set in motion along the gradient with a speed that depends on gradient strength. The ability to address *CS*

Massimo Giudici
Université de Nice Sophia Antipolis, Centre National de la Recherche Scientifique, Institut Non Linéaire de Nice, 1361 route des lucioles, Valbonne, France e-mail: Massimo.Giudici@inln.cnrs.fr

Francesco Pedaci
Université de Nice Sophia Antipolis, Centre National de la Recherche Scientifique, Institut Non Linéaire de Nice, 1361 route des lucioles, Valbonne, France

Emilie Caboche
Université de Nice Sophia Antipolis, Centre National de la Recherche Scientifique, Institut Non Linéaire de Nice, 1361 route des lucioles, Valbonne, France

Patrice Genevet
Université de Nice Sophia Antipolis, Centre National de la Recherche Scientifique, Institut Non Linéaire de Nice, 1361 route des lucioles, Valbonne, France e-mail: patrice.genevet@inln.cnrs.fr

Stephane Barland
Université de Nice Sophia Antipolis, Centre National de la Recherche Scientifique, Institut Non Linéaire de Nice, 1361 route des lucioles, Valbonne, France

Jorge Tredicce
Université de Nice Sophia Antipolis, Centre National de la Recherche Scientifique, Institut Non Linéaire de Nice, 1361 route des lucioles, Valbonne, France e-mail: Jorge.Tredicce@inln.cnrs.fr

Giovanna Tissoni
INFM-CNR and CNISM, Dipartimento di Fisica e Matematica, Università dell'Insubria, Via Valleggio 11, 22100 Como, Italy e-mail: giovanna.tissoni@uninsubria.it

Luigi Lugiato
INFM-CNR and CNISM, Dipartimento di Fisica e Matematica, Università dell'Insubria, Via Valleggio 11, 22100 Como, Italy e-mail: luigi.lugiato@uninsubria.it

O. Descalzi et al. (eds.), *Localized States in Physics: Solitons and Patterns*,
DOI 10.1007/978-3-642-16549-8_8,

and to control their location as well as their motion makes them interesting for all-optical processing units. In this chapter we report on several functionalities of *CS* that have been experimentally implemented in a Vertical Cavity Surface Emitting Laser (VCSEL) biased below threshold. We show that *CS* positions in the transverse section of the resonator can be reconfigured according to a phase landscape introduced in the holding beam. *CS* drifting propelled by a phase gradient in the holding beam can be used for realizing an all-optical delay line. Information bits are written in form of *CS* at a point of the device and a time delayed version of the written information can be read elsewhere along the gradient direction. *CS* existence and functionalities are deeply affected by presence of device defects generated during the fabrication process and randomly distributed through the device section. The sensitivity of *CS* to parameters gradients can be used to probe these defects, otherwise not detectable, and mapping their positions. Finally, a periodic flow of moving *CS* can be obtained by the interplay between a device defect and an external parameter gradient. This suggests the possibility of engineering a *CS* source directly onto the device.

8.1 Introduction

Optical morphogenesis has been widely investigated in the last twenty years [1, 2, 3]. Its success is partly due to possible applications to all-optical information processing. In particular, the idea of using optical patterns for encoding information in the transverse structure of the field has opened a new approach to parallel all-optical information processing. The transverse plane is thought as a blackboard on which light spots can be written and erased in any desired location and in a controlled way. In fact, optical patterns have been proven to be unsuitable for this operation because the intensity peaks are strongly correlated with one another, so that they cannot be manipulated as independent objects. Instead, this operation becomes possible using *localized structures* (LS).

LS are ubiquitous in nature; they form in large aspect-ratio media where two or several solutions coexist in the parameter space [4, 5, 6]. They have been predicted and experimentally observed in many different systems, several of them are described in this book: gas discharges [7], reaction-diffusion systems [8], fluids [9], magnetic fluids [10], traveling-wave convection [11]. In optics LS have been predicted in non linear optical cavities [12, 8] and they have been experimentally reported in photorefractive oscillators [14], in liquid crystal light valves [15, 16], in sodium vapors [17]. When LS are realized in semiconductor micro-cavities their attractive properties are combined with the advantages of semiconductor media for applications, namely fast response, miniaturization and low fabrication costs [18, 19]. LS in semiconductor microcavities are the subject of this chapter.

Single-peak localized structures, also called *cavity solitons* (CS), have been theoretically predicted in broad area semiconductor micro cavity injected by a coherent beam (holding beam, HB) [20, 21]. *CS* addressing is obtained by injecting a narrow

beam coherent and in phase with the holding beam (writing beam, WB) [22]. The same beam, out of phase with respect the holding beam, can be used to erase individually a cavity soliton. Moreover, any parameter gradient induces a drift of *CS* [8], allowing for reconfiguration of *CS* positions and other processing operations. In the case of a phase (intensity) modulation in the holding beam, *CS* tend to move to the nearest local maximum of the phase (intensity) profile.

From the experimental point of view, *CS* have been observed in an electrically biased broad-area Vertical Cavity Surface Emitting Lasers (VCSELs) used below threshold in the amplifying regime [23] and *CS* existence domain in the parameter space has been characterized in [13]. *CS* were observed also in optically pumped VCSELs [25] and in electrically biased VCSELs above threshold [26]. These works have disclosed one of the main drawbacks of CS: their stability requires a rather fine control in terms of the detuning between the VCSEL cavity resonance and the injected field frequency (the tolerance on this parameter is of the order of 10 GHz). On the other hand, the *CS* switching time has been characterized in [14, 28], where response times of less than one nanosecond have been shown using a coherent writing beam, thus assessing the potential of *CS* for applications. More recently, the property of CSs to drift in a phase gradient have been experimentally evidenced, thus providing some proof-of-principle demonstrations of *CS* applications like an all optical delay line [29] and a reconfigurable array of light bits [30].

One of the main outcomes of all these experimental analysis concerns the homogeneity of the VCSEL resonator along its transverse section. While *CS* theory has been developed in the frame of a perfectly homogeneous system, real devices where *CS* are achieved appear to be extremely inhomogeneous. Long scale (over more than 100 μm) inhomogeneities have strongly affected the first experimental observation of *CS* [23, 13, 31] and have been progressively eliminated during the manufacturing evolution of the VCSEL devices. On the other hand, the state-of-the-art fabrication of these broad-area semiconductor lasers is unable to avoid the formation of small-scale defects (between few microns to few tens of microns). These defects affect *CS* addressing [31], *CS* drift [29], *CS* positioning [30] and they need to be considered when envisaging *CS* applications. In this chapter we describe the main achievements in terms of *CS* applications and how they are affected by device defects. A perspective on further developments of *CS* based applications will be given in the conclusions.

8.2 CS motion

The stability analysis of *CS* solution in a passive injected resonator [8] reveals in 1D the existence of a neutral mode stemming from the translational symmetry of the equations describing the system. A neutral mode has a zero eigenvalue and therefore it is excited by an arbitrarily small spatial variation of any system parameter [32]. Since the spatial profile of this mode is the gradient of the *CS* itself, its excitation implies transverse drift of CS. Singular perturbation theory can be used to

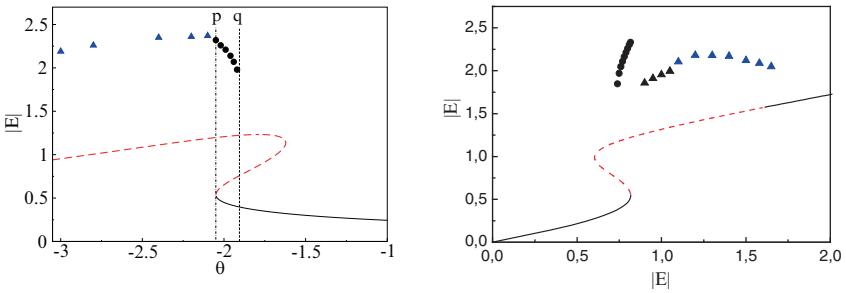

Fig. 8.1 Stationary solutions for an homogeneous device, as a function of the cavity detuning parameter θ (left panel) and of the input field amplitude E_I (right panel). The solid (dashed) line represents the stable (unstable) homogeneous steady state. Circles (triangles) represent the maximum intensity of stable CSs (patterns). Other parameters are: I = 2.0024 and E_I = 0.792 (left), I = 2. and θ = - 2. (right). The region between the two lines p and q in the left panel is the stability region of CSs corresponding to $-2.06 \leq \theta \leq -1.905$.

estimate the speed of the *CS* [33, 34]. The results indicate that the *CS* behaves as an overdamped Aristotelian particle, whose velocity (instead of acceleration) is proportional to the external force. In view of applications, it is advisable that the direction and the modulus of this force are controllable. Then, the most suitable parameter for introducing a gradient is the holding beam phase. Such a gradient can be obtained by tilting the direction of the holding beam with respect to the VCSEL cavity axis or by inserting a spatial phase modulator along the holding beam path. Besides, a phase variation of the holding beam does not affect directly the existence of *CS*, as it would be the case for an intensity variation of the holding beam.

8.2.1 Numerical Analysis of CS motion in a constant phase gradient

In order to analyze the effect of a holding beam phase gradient on *CS* drift, we numerically integrate the equations described in [21]. This model describes a broad area VCSEL, biased below threshold, in the paraxial and mean field limit approximations and it reads :

$$\frac{\partial E}{\partial t} = -\left[(1+i\theta)E - 2C(1-i\alpha)(N-1)E - E_I - i\nabla_\perp^2 E\right], \tag{8.1}$$

$$\frac{\partial N}{\partial t} = -\gamma\left[N + (N-1)|E|^2 - I - d\nabla_\perp^2 N\right], \tag{8.2}$$

where E is the normalized slowly varying envelope of the electric field and N is the carrier density, γ is the ratio between the non radiative recombination rate $\gamma_{\|}$ and the cavity decay rate κ ($\gamma = \gamma_{\|}/\kappa$), θ is the cavity detuning parameter $\theta = (\omega_c - \omega_0)/\kappa$, with ω_0 being the injected frequency and ω_c the cavity frequency. E_I is the normalized input field, I is the normalized injected current, $2C$ is the bistability parameter, α is the linewidth enhancement factor, $\nabla^2_{\perp}$ is the transverse Laplacian and d is the carrier diffusion coefficient.

Time is scaled to the photon lifetime κ^{-1} and the spatial variables x and y are scaled to the square root of the diffraction parameter a; for this kind of cavities we can assume a time unit of about 10 ps and a space unit of about 4.5 μm [21]. Where not differently stated, in the numerical simulations reported in this paper the following parameters have been fixed: $C = 0.45$, $\alpha = 5$, $\gamma = 0.01$, $d = 0.052$. Our control parameters are then θ, E_I and I.

In Fig. 8.1 we plot the S-shaped input-output curve for the homogeneous stationary solution of Eqs. (8.1, 8.2), showing the intracavity field amplitude as a function of θ (left panel), and E_I (right panel). The broken part of the curves shows the unstable region where, due to a modulational instability, the system generates a spatially modulated solution. As a function of θ, CSs coexist with the stable low-intensity homogeneous solution for $-2.06 \leq \theta \leq -1.905$ (that is, between the two dashed lines p and q in the left panel), while for $\theta < -2.06$ only patterns exist.

In the model a linear gradient is introduced in the holding beam phase by putting $E_I = E_{I0} \exp(i\mathbf{K} \cdot \mathbf{x})$. For the parameters we used, the CS speed v as a function of K is plotted in Fig. 8.2. We obtain typical values in the range of several μm/ns. v depends linearly on K on a large range, where the perturbative limit is still valid, and then it saturates. For higher values of K, the moving CS solution is not stable anymore. This is quite surprising, since holding beam phase is not a critical parameter for the CS existence. An explanation can be found in [8], where the problem of drifting CS in an injected cavity is treated analytically upon some approximations. It turns out that the addition of a constant phase gradient in the holding beam generates two extra terms in the field equation. The first one transforms the time derivative of the field into a convective derivative, thus indicating that travelling CS are the solutions of the field equation. The second term effectively modifies the value of the cavity detuning parameter θ, according to the following relation

$$\theta_K = \theta + aK^2, \tag{8.3}$$

being a the diffraction parameter. For large values of K, this leads eventually to a destabilization of CS, as shown in Fig. 8.2. CS drift speed is limited by the microresonator response times and in particular by the carrier lifetime which is usually longer than the photon lifetime in semiconductor cavities. Finite carrier response time prevent from an instantaneous reorganization of the carrier profile during CS propagation, thus leading to deformation of the travelling CS shape and slowing down [39]. In Fig. 8.2b we plot the CS drift speed for two different values of K as a function of γ. These curves are obtained by integrating Eqts. (8.1,8.2). We have explored the range of values from 0.001 (0.01 being the likely value in our exper-

iment, corresponding to a carrier lifetime of 1 ns) to beyond unity (where photon lifetime becomes the limiting factor).

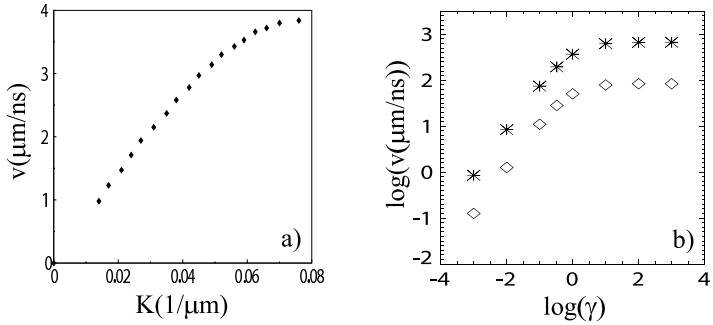

Fig. 8.2 a): *CS* drift speed versus phase gradient in the holding beam. Other parameters as in Fig. 8.1. b): Log-log plot of *CS* drift speed versus γ for $\theta = -2$ and for two values of the gradient: stars $K = 2.38 \times 10^4 m^{-1}$; diamonds $K = 1.91 \times 10^5 m^{-1}$.

8.2.2 Experimental Evidence of CS motion in a constant phase gradient

The experimental setup for generating *CS* in broad area VCSEL is based on a master/slave configuration, where the master is a tunable laser providing the holding beam, and the slave is a VCSEL microresonator. A scheme of this experimental set up is shown in Fig. 8.3. The master laser is driven by a stable (up to 10 μA) current supply and it is temperature controlled to 0.01^oC. It provides a continuous output beam of 70 mW at 150 mA current driving, with a FWHM bandwidth lower than 300 KHz and a tunable wavelength in the range $960 - 980$ nm. This beam is amplified by an optical amplifier, it is spatially filtered and, through a telescope, its waist is brought to 300 μm before being injected into the VCSEL resonator. The polarization of the holding beam is controlled as well as its power by polarization optics and by an Acousto-Optic Modulator. Before injection the maximum power of the holding beam is of about 15 mW. It is worth to point out that the master laser as well as the optical amplifier are optically isolated from back reflections of the following optics (return losses $>$ 40 dB).

The master laser has a secondary output beam (20 mW at 150 mA) whose waist is sized to 10 μm that can be used as local perturbation for writing and erasing *CS* (writing beam, WB). When a chopped writing beam is required, a fast (rise and fall time less than 1 ns) electro-optic modulator (EOM) is inserted in the WB path. Then the EOM provides WB pulses at a fixed rate in the KHz range, each pulse having a width of 100 ns. The phase relationship between the WB and the holding beam

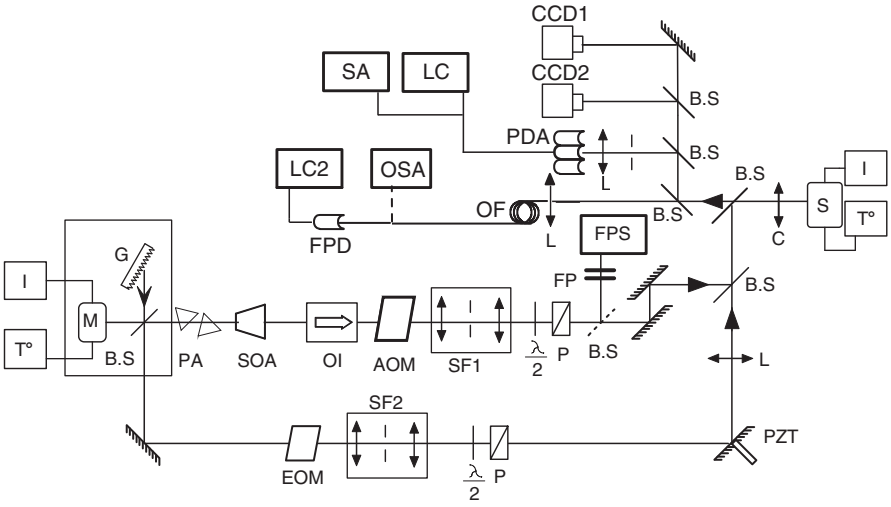

Fig. 8.3 Scheme of the experimental setup: *M*: high power edge emitter laser. *I*: current driver stabilized up to 0.01 mA, T^O: temperature controller, *G*: grating, *OI*: optical diode, *L*: Lens. *FP* Fabry-Perot resonators. *SOA*: semiconductor optical amplifier. *FPS* oscilloscope for visualizing *FP* signal. *EOM*: electro-optical modulator. *AOM*: acousto-optical modulators. *PA*: anamorphic prisms. *S.F*1: beam expander-configurator with spatial filtering, *S.F*2: beam reducer-configurator with spatial filtering. *S*: broad-area vertical cavity surface emitting laser. *C*: collimator. *CCD* camera *PD*: photo-detector. *PDA*: avalanche photo-detectors linear array. *PZT*: piezo-electric ceramic. *M*: mirror. *BS*: beam-splitters. *PM*: power meter (optional). $\lambda/2$: $\lambda/2$ waveplates. *P*: polarizers. *OF*: optical fiber. *LC*: digital scope. *SA*: power spectrum analyzer. *OSA*: optical spectrum analyzer. *FPD*: 8 GHz bandwidth detector. *LC*2: digital scope.

can be varied through a piezo-electric element mounted on the back of one of the mirrors directing the WB towards the VCSEL cavity.

The slave laser, where *CS* are generated, is provided by Ulm Photonics and it is an oxidized bottom-emitter InAs/InGaAs VCSEL with Bragg mirrors consisting of 20.5 pairs on the bottom side and 30 pairs on the top side, and 3 quantum wells emitting around 970 nm at threshold [35]. Its diameter ranges from 150 to 250 μm, according to the sample we used. It is current and temperature stabilized as the master laser. For *CS* generation, at least for the regimes described in this chapter, the VCSEL is biased above transparency and below threshold; it is operated in an amplifying regime. The production of perfectly planar, and thus homogeneous VCSELs with such a broad section is a very challenging task. Bottom-emitter configuration allows for a rather homogeneous current injection through the whole device section, though some weak current crowding on the device border is observed. As a consequence, lasing operation at the threshold of the solitary VCSEL occurs around the circular border of the device. In terms of homogeneity of the longitudinal length of the VCSEL resonator across the transverse section, we can distinguish between a long range (over distances larger than 100 μm) homogeneity and a short range (over distances ranging few microns to few tens of microns) homogeneity. While the devices we are using today can be considered perfectly homogeneous on the long scale

range (the cavity resonance is shifted of only 3 GHz over 200 μm), the state-of-the-art fabrication process does not fully prevent from formation of small size "defects" in the transverse plane of the laser. They consist of local spatial variations of the semiconductor resonator characteristics (thickness, electrical and/or optical properties, optical gain) [36]. A defect is a (small) region where the values of parameters are different compared to the values in the rest of the device, thus affecting *CS* existence [31] and preventing from *CS* addressing through the whole transverse section of the device [13]. Local defects may trap, annihilate, or deviate moving CS, as it will be shown in section 8.4.

The light injected into the VCSEL, together with the output of the VCSEL itself, are sent to the detection system through a beam splitter. The time averaged near field VCSEL profile is recorded by a CCD camera (1 ms time of exposure). When fast detection and spatial resolution are both required we monitor the near field output by a linear array of six avalanche photo-diode detectors (APDs) having a bandwidth of 350 MHz. The detectors output are monitored by two synchronized digital oscilloscopes (Lecroy 7200A: 500 MHz analog bandwidth, 1Gs/s and HP Infinium 54831b: 600 MHz analog bandwidth, 2Gs/s) for simultaneous monitoring of six channels. Ultrafast detection of a small region of the transverse plane of the VCSEL is enable using a single 8 GHz detector. A 6 GHz scope (Lecroy Wavemaster) is then used.

Experimental control parameters are: detuning between the frequencies of the cavity resonance and of the injected signal, intensity of the injected field, VCSEL pumping current. For the experiments described in this chapter these parameters are set in the region where *CS* are stable [13].

CS drift in the transverse plane of the device can be induced by introducing a constant phase gradient in the holding beam. This is obtained by tilting the last beam splitter in the injection path, which aligns the holding beam with respect to the optical axis of the VCSEL. While in a perfect homogeneous device the phase gradient direction fixes the trajectory of the cavity soliton, the presence of device defects may determine a deviation from this trajectory in the transverse plane of the VCSEL. On the other hand, in order to detect drifting cavity soliton, it is necessary to know their trajectory in order to place correctly the detectors linear array. Then it is necessary to confine cavity soliton movement along a well determined direction. This confinement is obtained by shaping the holding beam in form of a stripe parallel to the phase gradient. The resulting holding beam intensity gradient confines tightly the cavity soliton within the stripe.

In order to build this intensity channel we modify slightly the set-up of Fig. 8.3 either by inserting a cylindrical lens before the VCSEL collimator either by inserting a Mach-Zender interferometer in the holding beam path. In the first case we obtain an holding beam in form of fringes, as shown in Fig. 8.4a, in the second case we obtain an holding beam in form of a stripe as shown in Fig. 8.4b. The visibility of these fringes is close to one and their size is adjusted to be sufficiently large to allow for *CS* existence.

The motion of a cavity soliton is shown in Fig. 8.4c. In this experiment the holding beam is injected in form of a single stripe, thus forming a propagating channel

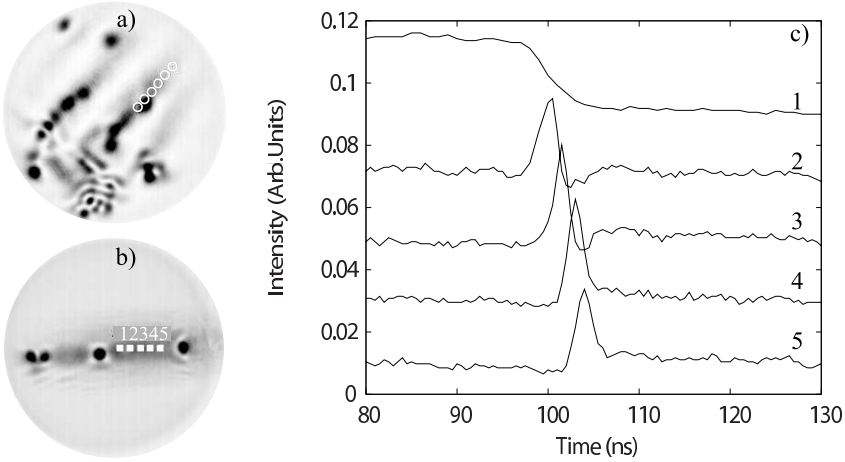

Fig. 8.4 a): Time averaged near field of the VCSEL with the injection in form of fringes obtained by inserting a Mach-Zender interferometer. CCD camera exposure time about 1 ms. The positions and sizes of the regions seen by the detectors of the linear array are marked as white circles. The VCSEL current is 510 mA, holding beam intensity = 15 mW. A phase gradient is introduced in the direction of the fringes. b): Time-averaged near field of the VCSEL with the injection in form of a single stripe obtained by inserting a cylindrical lens before injection into the VCSEL. The positions of the detectors in the transverse plane are indicated by squares. The area monitored by each detector has diameter less than 7.2 μm and the separation between neighboring detectors is 8.9 μm. A phase gradient is introduced in the direction of the fringes from left to right. CCD camera exposure time about 1 ms. In both profiles a) and b) the intensity increases from white to black. c): Time resolved *CS* drift along the stripe of panel b). The cavity soliton passes in front of the detectors named from 1 to 5. The output of each detector is plotted, displaced vertically by 0.02 units for clarity. Detector 1 monitors the point addressed by the writing beam, applied at time $t = 0$.

for *CS* monitored by the linear array of detectors. A constant phase gradient is introduced in the direction of the stripe from left to right. A cavity soliton is ignited by a writing beam pulse at point 1 within the intensity channel. This writing beam acts as a strong amplitude gradient that holds the generated CS, whose drift starts as soon as the WB is removed. The cavity soliton emission peak is successively picked up by detectors 2 - 5. The distance between points 1 and 5 is 36 μm, the delay of the CS peak registered in 5 with respect to the departure in 1 is 7.5 ns, so the *CS* average speed is about 4.7 μm/ns. The drift length of 36 μm is the largest obtainable in our available devices, because of the presence of device defects trapping or annihilating CS. In Fig. 8.4b trapped *CS* are clearly visible in the middle of the intensity channel and on the right of the detector 5.

8.3 Applications of *CS* movement

8.3.1 CS drift in a constant gradient

The result shown in Fig. 8.4 provides clear evidence of *CS* drift in the transverse plane of the VCSEL induced by a constant phase gradient in the holding beam. Though the length of the *CS* drift is limited by the presence of device defects, the experimental evidence provided is a proof of principle of two importants *CS* applications.

The first one is an optical shift register, a device where a set of m data slot is shifted linearly of one position when the device is activated. Shift register can be configured for serial to parallel conversion since the input is a m-bits data packet written at one point of the device and it is converted in a $m \times 1$ array of bits stored in the register. This operation can be accomplished all optically by drifting *CS*, as shown in Fig. 8.4. We have implemented, as a first approximation to a bit value of "1", a perturbation in the form of a writing beam pulse creating a cavity soliton (point 1). Under the effect of the phase gradient this cavity soliton drifts along the injection channel. A second bit can be written once the first cavity soliton has cleared the point 1 and so on. A set of bit packet is therefore written in form of *CS* and these data are shifted along the injection channel. One can retrieve the parallel optical bit sequence by placing a linear array of detectors along this channel. The serial input information is distributed in a parallel optical output line with some delay that, in principle, depends on the speed of the structure.

The second one is the delay line, a device able to delay the arrival of a new data packet when a router is busy. All-optical routers require all optical delay lines in order to preserve high-speed switching of data packets [37]. In practice in a delay line a series of bits applied at one point in space are recovered, after a delay, at a different position. A delay line using *CS* is based on injecting an optical bit stream into an optical resonator, creating a *CS* that drifts transversely with a controllable velocity. Fig. 8.4 is an example of this functionality. As for the shift register, we have implemented to a "1", a perturbation in the form of a writing beam pulse creating a *CS* (point 1). This *CS* drifts in a well defined direction with a well defined speed and it is read elsewhere in the transverse plane of the VCSEL device (for example by detector 5).

The performance of a delay line is assessed by two specifications: the bandwidth at which they can process information and a number called M resulting of the multiplication between the device bandwidth and the amount of time a signal is delayed. For digital signals M corresponds to the maximum number of bits which can be stored in a delay line [38]. In our system, the delay Δt is given by $\Delta t = L/v$ where L is the drift length and v is the *CS* drifting speed. The amount of the delay can be varied straightforwardly by shifting the position of the read out point of the bit stream, i.e. L. While v can be controlled with the gradient strength, it is not advisable to decrease v for increasing Δt since v limits the writing rate of the CSs, i.e the system bandwidth. This can be understood when considering that the incoming

bit stream is addressing a single point of the device and that a CS, once written, must clear out the addressing point before the next bit could be written. Numerical simulations indicate that a *CS* should have drifted around five diameters between one writing pulse and the next (i.e. during the "return to zero" (RZ) stage of the bit stream), in order to avoid interactions which might introduce timing jitter and hence bit-errors. If we call τ_0 the RZ time of incoming signal, the above described condition reads $\tau_0 > 5\phi/v$ where ϕ is the *CS* diameter. In our proof-of-principle demonstration $\tau_0 > 10.6$ ns. Since a *CS* can be written in around one ns [14], we infer that the total bit interval cannot be less than 11.5 ns, which limits the bandwidth to about 90 Mb/s and leads to $M \approx 0.7$. Though M may appear quite modest in this first experimental demonstration, these two *CS* applications present a remarkable potential for improvement. Larger values of M can be straightforwardly obtained in our scheme using resonators of larger transverse dimension and improved homogeneity. Although challenging, there are in principle no barriers to manufacturing delay lines several millimeters long, gaining more than two order of magnitude on the value of M. On the other hand, both M and the bandwidth can be improved by increasing the *CS* drifting velocity. This is limited by the semiconductor microresonator response times, as shown Fig. 8.2b. This curve indicates that *CS* speed can be significantly increased by increasing γ. This can be achieved by known methods to shorten carrier lifetime (see e.g., [40, 41]) and very fast gain recovery times compatible with 200 GHz modulation bandwidth have recently been demonstrated in quantum dot amplifiers [42]. For carrier lifetimes in the ps range, *CS* delay-line and shift register operation would be above 10 Gbit/s. The numerical result of Fig. 8.2b, together with the good perspectives of enlarging the device transverse dimension and improving its homogeneity, suggest that there is great potential for achieving both large M and high bit-rate shift registers and delay lines based on CS.

Moreover, *CS* based all-optical data processing offers robust pulse reshaping of the incoming optical pulse. Because of the threshold response of the *CS* excitation, amplitude fluctuations of the incoming signal will be eliminated, improving the quality of the output signal. The bit length will also be formatted to the same value fixed by the ratio between the *CS* size ϕ and the drift speed v. This reshaping of the bit stream can be useful in telecom networks to avoid deterioration of the signal and it offers an alternative method to all-optical pulse restoring [43, 44]. On the other hand, a *CS* based delay line is not convenient for delaying analogue signals or binary signals where information is stored in the bit length (NRZ coding for example).

8.3.2 Experimental realization of reconfigurable CS arrays

CS motion in parameter gradients suggests the possibility of reconfiguring *CS* positions across the transverse section of the VCSEL according to a given parameter landscape. This operation appears very interesting when the parameter landscape can be easily controlled and reconfigured. This is the case of the holding beam phase

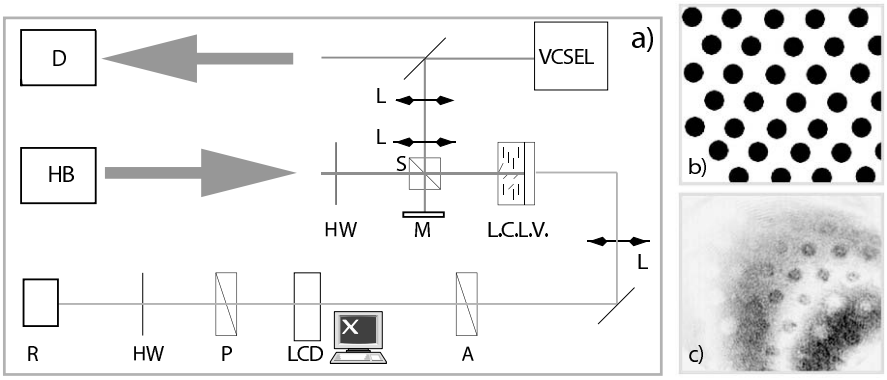

Fig. 8.5 a): Experimental setup of the spatial light modulator introduced in Fig. 8.3. *R*: 658 nm laser; *HW*: half waveplate; *M*: mirror (optional); *P*:polarizer; *LCD*: computer controlled liquid crystal display; *L.C.L.V*: liquid crystal light valve; *S*: cube splitter, *A*: polarisation analyzer. The holding beam (holding beam) (indicated by arrow pointing *H*) reads the LCLV on the reading side before being injected in the VCSEL. Arrow pointing *D* indicates the output beam going to detection part of set-up, see Fig. 8.3. b): Computer generated profile used to drive the LCD. The LCD modulates the intensity profile of the red beam impinging on the rear side of the LCLV. c): Self interference profile of the holding beam in the plane of the VCSEL evidencing the acquired phase profile. Intensity increases from white to black.

that can be configured by using a PC controllable spatial light modulator (SLM). In order to control the holding beam profile, we insert in the set up shown in Fig. 8.3 the SLM system described in Fig. 8.5 a. Since no PC controlled liquid crystal display (LCD) is available at 980 nm, we use a liquid crystal light valve (LCLV). A LCLV is a two sides electro-optical device [16]: the reading side is composed by a liquid crystal layer and a dielectric mirror, while the writing side is composed by a photoconductor layer. Since the liquid crystal molecules will orient according to the (local) voltage drop they experience, the (local) index of refraction is proportional to the spatial profile of the intensity $I_w(x,y)$ impinging on the writing side. Then, an incoming beam reflected by the reading side acquires a phase profile corresponding to $I_w(x,y)$. We use a LCLV readable at 980 nm by the holding beam and written by a red laser beam whose intensity profile is modulated by a PC controlled LCD. Then, the LCLV acts as a wavelength buffer, transferring the computer generated intensity profile to a corresponding phase profile in the holding beam. For the LCLV we used, we have measured a maximum phase modulation depth for the reading beam of the order of $\Delta\phi = 2.5$ rad ($0.8\ \pi\ \pm 0.05$ rad). This maximum value was obtained for writing intensity of the order of 0.1 mW/cm^2 and an applied AC voltage to the two sides of the LCLV of $2.2V$ peak to peak at a frequency of 9 KHz. In order to inject a pure phase gradient, the reflecting surface of the LCLV is imaged into the VCSEL output mirror. Nevertheless a small amount of intensity modulation is hard to avoid, due to imperfect imaging of the LCLV on the VCSEL and/or small intensity effects in the LCLV. Along the VCSEL transverse section, this intensity modulation is less than 15% of the total intensity injected average on the VCSEL size.

It is worth to point out that this scheme allows also for creating pure holding beam intensity profiles. This is obtained by adding a properly oriented polarizer in front of the LCLV reading side. We prefer to work with the phase profile of the holding beam because, as already mentioned, variations of the holding beam intensity affect directly the existence of the CS (see Fig. 8.1, right panel). Then, a holding beam intensity profile demands to be carefully controlled for avoiding the introduction of spots in the VCSEL section where *CS* existence conditions are not fulfilled.

The phase profile obtained for the holding beam can be monitored by adding an additional mirror *M* (see Fig. 8.5a to form with the LCLV a Michelson interferometer. The phase profile is then converted in amplitude profile and it can be acquired by the CCD camera monitoring the near field of the VCSEL. For this purpose the VCSEL needs to be unbiased and the cavity resonance mistuned with respect the holding beam frequency, in these conditions it acts as a linear reflector for the Michelson fringes. While performing the experiment, the path to the mirror *M* is blocked and holding beam has a pure phase modulation.

In figure 8.5b we show an example of the applied phase profile, the black spots determine in the injection beam a phase jump of 0.8 π rad with respect to the white background. The transition between these two values, which is steplike in the LCD, results in a phase slope in the injection beam of 0.1 π rad/μm, as measured in the interferogram in Fig. 8.5c. This spatial bandwidth limitation is due to the imaging and downscaling processes. In order to evidence the possibility of reconfiguring the *CS* positions according to a predefined phase landscape in the holding beam, we set the system parameters to values compatible with *CS* existence [13]. The near field emission of the VCSEL for a homogeneous holding beam phase profile is shown in fig. 8.6a. In this situation the red beam writing LCLV is blocked and no phase modulation is present on the injection beam. The VCSEL emission shows a rather complex intensity profile, where no stationary localized structures can be clearly observed. We observe some filamented structures where fast detection reveals the presence of an irregular spatio-temporal dynamics and some bright spots localized along two straight lines, one horizontal in the lower part of the device and the other one about 45° from the horizontal. As we will show in the next section, this kind of near field emission is dominated by device defects. In Fig. 8.6b the writing beam is applied on the LCLV, imposing to the holding beam the phase profile shown in Fig. 8.5b. *CS* appear in the near field output of the VCSEL with a geometry that, at least in a large portion of the device section, reproduces the landscape of the phase profile of the holding beam. The device inhomogeneities prevent from extending to the whole VCSEL section the *CS* array imposed by the holding beam phase. In Fig.8.6c we show *CS* positioning when the phase grid has a square symmetry instead of hexagonal as the one in Fig. 8.5b. Also under this geometry *CS* positions follows the phase landscape showing the possibility of reconfiguring the *CS* arrays.

It is worth to remark that the residual holding beam intensity profile associated to the phase profile has a negligible effect on *CS* positioning of Fig. 8.6b. This has been verified by comparing Fig. 8.6b with the intensity holding beam profile. This comparison reveals that *CS* positions correspond to minima of residual intensity

profile and, according to [34], they would be unstable positions in absence of the phase profile.

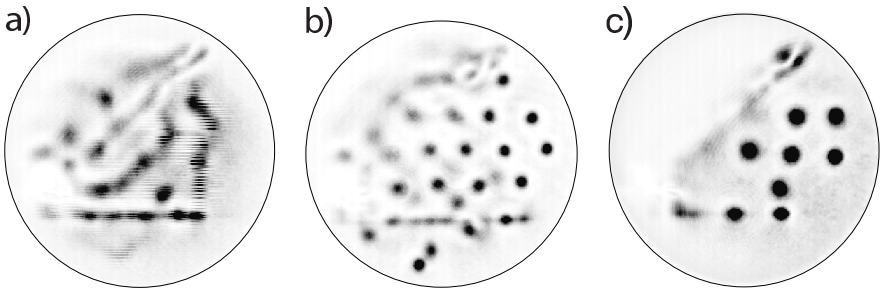

Fig. 8.6 a): VCSEL near field output under homogeneous holding beam injection. VCSEL is electrically driven at 560 mA, the total injected power is around 15 mW. b): VCSEL near field output when the phase modulation is introduced in the holding beam. The hexagonal phase modulations is shown in Fig. 8.5. c): VCSEL near field output when the phase modulation introduced in the holding beam has a square geometry, VCSEL biasing is now J=567 mA. Intensity increases from white to black.

Device inhomogeneities and defects prevent from configuring *CS* positions according to the phase landscape through the whole transverse section. For example, in Fig. 8.6a the horizontal defect line at the bottom of the device section and the defect line at 45^o crossing the transverse section from left to right remain a pinning point for structures despite the presence of the phase landscape. In order to overcome these limitations more homogeneous devices are a possible solution. Alternatively phase landscapes with stronger pinning force, i.e. with larger phase gradient, could be implemented in order to overcome the device defects pinning force. From this point of view, it is worth to point out that, in our experiment, we were quite limited by the poor performances of our SLM in terms of the dynamical range of the phase variation as a function of the $I_w(x,y)$. As previously described, the phase modulation depth of the SLM saturates at very low value of $I_w(x,y)$ at approximately $0.8\ \pi$ of phase variation with respect to the case where $I_w(x,y) = 0$. This low modulation depth limits the maximum value of phase gradient that can be implemented and, therefore, the consequent pinning force. Moreover, the low value of $I_w(x,y)$ saturating the phase variation made impossible to create landscapes having more than two values for the phase. The improvement of the SLM is today technologically achieved by new commercial available liquid crystal on silicon (LCOS) microdisplays in the near infrared range that can reach more than $2\ \pi$ phase contrast. Moreover, since they are PC controlled, they have 8 bits dynamical range. Another possible solution is to use deformable mirrors.

To conclude the description of this *CS* functionality, we emphasize that a phase landscape can be used to configure *CS* positions. The pinning force engendered by phase gradient can win the pinning force of some device defects, thus allowing for *CS* reconfiguration. Other device defects lead to spontaneous formation of *CS* which are anchored on the defect and cannot be moved by the phase gradient engendered

by the landscape applied. In the next section we will analyze in details the characteristics of device defects and their influence on the *CS* drift.

8.4 CS motion and device defects

The detrimental role of device defects on *CS* applications has been shown in the preceding sections. As previously mentioned, we call defect any local variation of a structural parameter of the device on a scale ranging from a few microns to a few tens of microns, i.e. having a size comparable to the *CS* size. These inhomogeneities are typically generated during the device growth or postprocessing stages and, at the state of the art of the broad-area VCSEL fabrications, they cannot be avoided [36]. Several structural parameters can be involved: the resonator length (Bragg reflectors layers thickness variations and/or interface roughness), the optical gain and the refraction index (transverse inhomogeneity of doping level). Moreover, conventional quality screening of the finished device such as spontaneous emission profile or electronic microscope imaging of the VCSEL do not allow for detection of these defects. Their influence on *CS* operations is a consequence of the tight stability conditions of *CS* in terms of the system parameters and of the sensitivity of *CS* speed in presence of parameter gradients. In particular, *CS* existence domain in terms of cavity detuning parameter θ is very narrow, as shown in Fig. 8.1. *CS* survive in an interval of 0.155κ; which corresponds, in physical units, to a frequency range of 15 GHz. In terms of the optical length of the resonator through the device section, a variation of less than one angstrom extended on an area corresponding to the *CS* size would affect detrimentally *CS* stability. Then, it is not surprising that *CS* existence is affected by tiny device inhomogeneities, that do not affect the spontaneous emission profile. As a consequence, even if system parameters are set such that the largest part of the device allows for *CS* stability, there are points and/or regions where *CS* existence is not possible. In these regions, we are in a parameter range such that only the homogeneous solution or the pattern solution shown in Fig. 8.1 are stable and *CS* cannot be ignited by local perturbations, using a writing beam, for example, as shown in [13].

The presence of these regions explains also why, despite control parameters are optimized for CS, the experimental profiles obtained show extended structures and single light peaks (see, for example, Fig. 8.6a that are not individually controllable. Single light peaks are particularly intriguing because of their similarity with CS; the impossibility of switching them off by a local perturbation reveals that they are monostable structures whose characteristics are imposed by the device defect underneath. Numerical simulations are very useful to understand the nature of these structures, as it will be shown in Section 8.4.3.2.

On the other hand, a parameter variation through the device section implies the existence of a gradient in this parameter and it inevitably induces a drift of the CS [32]. Then, small scale defects behave as a attractive or repulsive regions for CS, thus modifying their motion and imposing strong constraints on their positions.

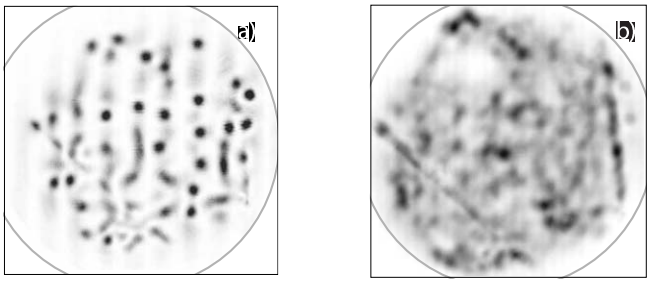

Fig. 8.7 a): An example of near field output of the injected VCSEL in the case of holding beam in form of vertical fringes, *CS* are present along them and, in this direction, there is no external parameter gradient imposing any movement. Intensity increases from white to black. The fringes are then shifted horizontally. This image corresponds to one frame of the movie realized when shifting the fringes. b): Device section scanned by *CS* passages. Points of the section are represented in a grey scale according to how often a *CS* pass over it: from white (less visited) to black (more visited). The latter correspond to the most repelling defects, the last to the most attractive ones.

Actually, the sensitivity of *CS* existence and drift on device defects suggests that they can be used as a tool to probe a VCSEL section and reveal its defects. Such a method will allow for detecting any structural defect whether it is located onto its external surface or buried into the device and thus not detectable otherwise [33].

8.4.1 CS force microscope

In order to implement *CS* movement to reveal device defects we inject an holding beam in form of fringes, as previously done for the CS-based delay line. The width of these fringes is chosen in order to allow for *CS* existence (fringe separation is fixed at about 26 μm). No other parameter gradient is introduced into the system; in particular, we take care of eliminating any phase gradient, both longitudinally and transversally to the fringes. This is obtained by proper setting the angles of the interferometer arms, leading to a flat phase profile. Finally it is possible to change the orientation of the fringes by acting on the two arms of the interferometer. The holding beam intensity profile confines *CS* in the direction orthogonal to the fringes, but *CS* are free to move along the fringes (see Fig. 8.7, a). By piezoelectrical control of the position of one of the interferometer mirrors, we shift the fringes position in the direction orthogonal to the fringes. *CS* are then dragged in the direction of the fringes motion, thus exploring the entire device section. In absence of local defects, *CS* would move along straight lines parallel to the fringes shift direction. In the real system, on the contrary, the trajectory followed by the *CS* will be affected by any defect found along the path, which will displace the *CS* perpendicularly to its (forced) motion. *CS* dragging occurs on a time scale much slower than the time-

scales of the medium, thus *CS* migrate adiabatically towards their stable positions. Their trajectory is affected by the local defects encountered: points of the plane visited by *CS* will indicate attracting local defects, while regions that are avoided will correspond to repulsive inhomogeneities. Trajectories are recorded by making a movie of the VCSEL near field output as the fringes are scanned along the whole transverse plane. All frames (one is shown in Fig. 8.7a are then summed and normalized. The same operation is repeated for different directions of fringes, covering homogeneously the 2π angle. Again all frames are added and normalized resulting in a device map indicating statistically how often *CS* visit each point of the device. Attracting defects will be located in correspondence of the most visited point of the device section. Instead repulsive defects will be located at the less visited points, since all *CS* trajectories will avoid these points. The map of the device defects obtained in shown in Fig. 8.7b. In a perfectly homogenous laser this image would be homogeneously gray, indicating that all the positions of the transverse plane have the same probability to be visited.

It is worthwhile to note that, for each device we can associate a different map as the one shown in Fig. 8.7b and that, for each device, the associated map is always the same after any realization, thus indicating that the defects indicated are really structural defects of the device and do not depend on initial conditions of the experiment.

8.4.2 Modeling of an inhomogeneous device

In the model the presence of device defects can be described by introducing local variations of the cavity detuning parameter θ. This parameter, which is critical for *CS* existence (as shown in Fig. 8.1, left panel), takes into account any variation of the resonator optical length. Through the device section, the profile of θ is represented in the form $\theta(x,y) = \theta_0 + \delta\theta(x,y)$, where $\delta\theta(x,y)$ is a normally distributed stochastic process with zero mean and finite spatial correlation length. While the amplitude of $\delta\theta(x,y)$ determines the depth (or height) of device defects, the correlation length is related to the defect size. We implement this distribution in Eqs. (8.1,8.2) assuming defect size of the order of CS, i.e. defect diameters of 10-15 μm. Distribution amplitude is a critical parameter in order to get numerically VCSEL emission profiles similar to the ones obtained experimentally (see, for example, Fig. 8.6a.

While defects may pin CS, the experimental evidences show that, in certain points of the device section, *CS* do not exist anymore and addressing by local perturbation is not possible there. Accordingly, the distribution amplitude is chosen wide enough for θ to span over a range larger than the one where *CS* exist, being θ_0 chosen in the region where *CS* are stable. The resulting profile contains defects having only an attracting and/or repulsive role on *CS* but also defects large enough to affect the stability of CS.

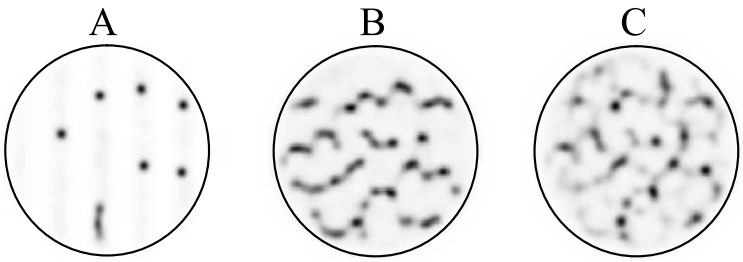

Fig. 8.8 a): Numerically simulated VCSEL output in the case of an holding beam in form of fringes, reproducing the experimental situation of 8.7 (intensity grows from white to black). b): *CS* trajectories after complet horizontal scan of the vertical fringes along the device section. c)Superposition of *CS* trajectories for different fringes orientation and resulting device section scanned by *CS* passages. Points of the section are represented in a grey scale according to how often a *CS* pass over it: from white (less visited) to black (more visited). The former corresponds to the most repelling defects, the latter to the most attractive ones.

In order to assess the validity of the interpretation given to the results presented in Section 8.4.1 in terms of device defects, of their effect on *CS* dragging and of their modeling, we have numerically simulated the operations described in Section 8.4.1 using eqs. (8.1,8.2). The holding beam has been introduced in form of fringes as in the experiment, and these fringes were shifted orthogonally to their orientation at a velocity slow enough for the system equations to follow adiabatically. In Fig. 8.8b we show the trajectory of *CS* obtained after a scan of fringes in a single direction. They were obtained by adding all the frames of the movie obtained while shifting the fringes as the one shown in Fig. 8.8a (exactly as in the experiment). We repeated the same procedure for different directions of the fringes (angles $n\pi/4$, with $0 < n < 7$) and adding all the frame we have obtained the map shown in Fig. 8.8c. The similarity with Fig. 8.7 is striking, but the great advantage of the numerical simulations is that we know the defect distribution. The map can be therefore directly compared with the spatial distribution of θ introduced, thus confirming that this distribution is mapped by our method based on dragging CS. In Fig. 8.9 most visited regions (attracting defects) correspond to regions where θ value is more negative than θ_0, while repelling defect corresponds to regions where θ value is less negative than θ_0. The regions where θ is such that standard *CS* are unstable are delimited by the thick lines: green regions correspond to high intensity structures (that are always on) that strongly attract *CS*. Red regions correspond to repulsive regions where only the low intensity solution is stable, and *CS* cannot survive.

8.4.3 Interaction between phase gradient and defects: the CS tap

We have shown how device defects distributed through the VCSEL section affect *CS* operations in presence of gradients. If we consider a single device defect sur-

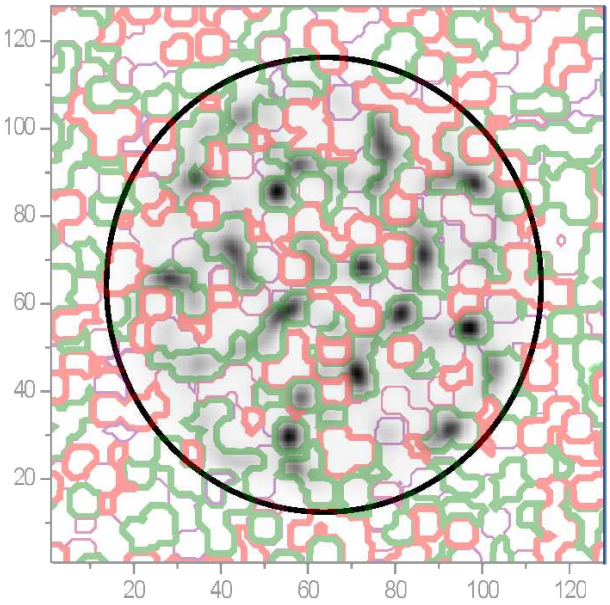

Fig. 8.9 Fig. 8.8c is superposed with the spatial distribution of θ using in the simulations: thick red delimits regions where $\theta > -1.90$, thick green delimits regions where $\theta < -2.05$. Thin lines delimit regions where θ takes intermediate values: thin violet $-2.05 < \theta < -1.975$ and thin magenta $-1.975 < \theta < -1.90$ Here $\theta_0 = -2$, $I = 2$ and $E_I = 0.8$.

rounded by a region homogeneous enough for allowing *CS* stability, the presence of an external parameter gradient may results in an interesting *CS* spatio-temporal dynamics. In particular, we have observed that the interaction between a defect and a phase gradient in the holding beam may induce the spontaneous formation of a regular sequence of *CS* originating from the defect and moving in the gradient direction [46], thus forming a sort of *CS* "tap". The length of the drift depends on the extension of the homogeneous region surrounding the defect, since other defects may stop *CS* drift as shown in Section 8.3.1.

8.4.3.1 Experiment

The experimental set-up is similar to the one used in Section 8.3.1. The holding beam has an intensity profile in form of fringes in order to confine *CS* drift along straight channels. One of these propagation path is monitored by a linear detector array in the near field of the VCSEL output, as shown for example in Fig. 8.4a. The holding beam phase gradient is introduced in the direction of the fringes to propel *CS* along them. System parameters are optimally set for allowing *CS* existence in the largest part of the device. As already mentioned, despite these conditions, some attractive defects are deep enough to lead to the formation of structures whose char-

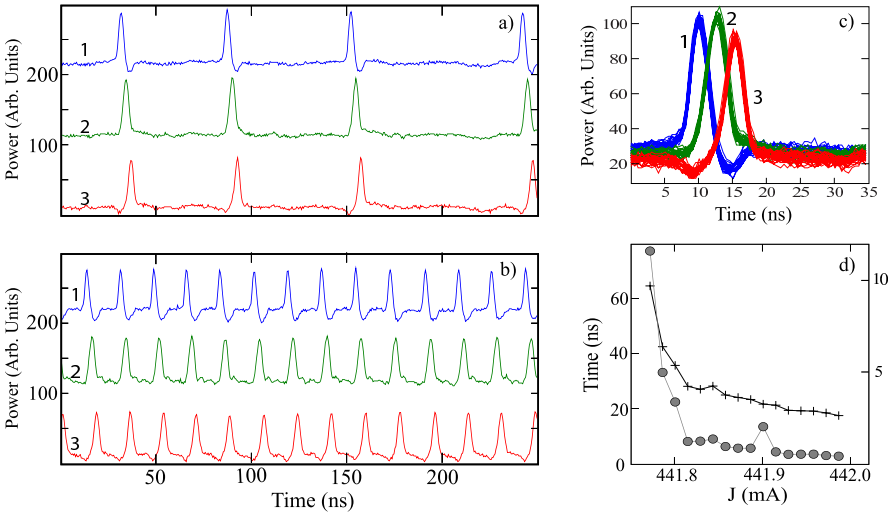

Fig. 8.10 a): Intensity outputs from a linear array of four detectors placed along a channel line and separated by 9 μm. Detector 1 monitors the defect point where the structure forms, no intensity is monitored by the last detector of the array (detector 4) and its trace is not shown. Each trace is vertically shifted for clarity. The VCSEL current is $J = 441.76mA$ and holding beam intensity is 15 mW. b): As in a) except for VCSEL current which is $J = 442.0mA$. c): For the case depicted in a), we superimpose fifty spatio-temporal sequences monitored by three detectors. d): Average period of the sequence in a) $< T >$ (crosses, with left vertical scale) and its standard deviation $\sigma(T)$ (circles, with right vertical scale) as a function of J.

acteristics are strongly dependent on the defect underneath. These structures experience also a pinning force engendered by the attractive nature of the defect. When the monitored fringe encompasses such device defects and the applied holding beam phase gradient is strong enough to win the pinning force, a regular sequence of drifting *CS* springing from the defect may appear. In Fig. 8.4a, we show the near field emission of the VCSEL when injected by an holding beam in form of intensity fringes, the positions of the detectors along the fringe monitored are indicated. *CS* drift occurs at fast time scale and it cannot be resolved by CCD camera which provides time-averaged images. Instead the position of deep device defects is clearly indicated by the presence of bright structures which form upon them.

In Fig. 8.10a and in Fig. 8.10b we show the time traces corresponding to the VCSEL intensity output picked up by three fast detectors $1-3$ placed along the channel line when a constant phase gradient in the holding beam. In particular, detector 1 monitors a device defect (that we call point 1 from now on) where, if the the phase gradient is removed, a stationary structure spontaneously appears. The phase gradient has the same direction of the monitored fringe. Each detector records a regular pulsing signal with an average period $< T >= 63ns$ and the time traces are strongly correlated to each other with a time delay (Δt) of 3.0 ns for two neighbor detectors in the direction of the gradient. Small increase of the VCSEL pumping current J (lower panel) decreases dramatically the period of the pulsing signal down

to $< T >= 17.5ns$, while both Δt and the pulse width are almost unaffected. These time series indicate the presence of a drifting *CS* that is originated from the structure appearing at point 1, it immediately starts to drift along the channel due to the phase gradient with a speed of 3.0 $\mu m/ns$, and eventually it dies out after detector 3. The periodic flow of *CS* outside the defect is characterized by the period T, corresponding to the time separation between the passage of two consecutive *CS* on a point of the VCSEL transverse section.

In Fig. 8.10c we superimpose fifty realizations of structure generation in 1 with the following evolutions monitored by the other two detectors. Even if we consider the situation where the process is characterized by the strongest dispersion, the traces recorded by the detectors 2 and 3 superimpose perfectly. This indicates that the spatial evolution of the *CS* is always the same after structure formation in point 1, confirming the existence of a deterministic force pushing CS. In Fig. 8.10 d) we plot the average value of period T and its standard deviation σ_T as a function of J. Even in the case of largest σ_T, T is larger than σ_T of almost an order of magnitude, thus indicating the regularity of the process. By increasing J this regularity is further increased and, for $J > 441.8$ mA the signal is periodic. The two observations of Fig. 8.10c and d) indicate the occurrence of a regular flow of *CS* drifting in the direction of the phase gradient. The formation time of the structure in point 1 determines the period of the sequence T and it is dramatically affected by a variation of the pumping current of the device, while its drifting speed is not.

It is important to point out that, if the channel line is changed in the experiment (by changing the gradient direction together with the orientation of the fringes and moving the detector array accordingly), other defect points of the device originating a regular flow of *CS* can be revealed. Their positions are randomly distributed throughout the transverse section of the device. In Fig. 8.10 the drift of the *CS* along the channel is interrupted after detector 3 by the interaction with another defect which, in this case, annihilates the structure. The distance covered by the drifting *CS* before vanishing depends on the defect-free length of the channeling path. As previously mentioned, we have observed drifting lengths spanning from 10 μm to 30 μm.

8.4.3.2 Numerical Simulations

Numerical simulations have been performed in order to get insights on the above describe dynamics. A single defect is introduced in eqs. (8.1), (8.2) assuming a supergaussian spatial profile of θ:

$$\theta(x,y) = \theta_0 - \theta_d exp\left[-\left(\frac{(x-x_0)^2+(y-y_0)^2}{\sigma_d^2}\right)^3\right] \tag{8.4}$$

where θ_0 is chosen in the range where *CS* are stable ($p < \theta_0 < q$, see Fig. 8.1, left panel). According to the experimental observations, the defect size is assumed comparable with the *CS* size: σ_d = 11.25 μm which means a defect diameter at

half depth of 21.2 μm. The sign of θ_d determines the attractive ($\theta_d > 0$) or repulsive ($\theta_d < 0$) nature of the defect. θ_d determines the depth of the defect and the steepness of the defect walls, i.e. the value of the gradient of θ. Equations (8.1,8.2) have been integrated with all other parameters set in order to allow for *CS* existence outside the defect.

In the case of an attractive defect, we have observed that, if the defect depth is sufficiently large, a high intensity structure spontaneously form upon the defect, thus leading to output profiles similar to the ones experimentally observed (see, for example, Fig. 8.6a. Numerical simulations confirm that this happens when only the high intensity solution is stable within the defect. The same bifurcation occurs in the homogeneous device shown in Fig. 8.1 when $\theta < p$ and patterns developed throughout the entire device section. Actually, the single peaked structure generated on the defect can be intuitively viewed as a "portion" of a pattern, the characteristics of which are strongly dependent on the defect size and shape. In particular, it is important to point out that the bifurcation value of θ leading to the structure formation in the defect (θ_c) is slightly different (more negative) from the bifurcation value p calculated in the homogeneous case and it depends on the defect characteristics. For the defect size considered here, pattern solution becomes monostable for $\theta < \theta_c = -2.114$. The structure generated on the attractive defect is also pinned by the defect because of the force engendered by the gradient of θ at the defect walls.

In order to analyze numerically the interaction between these defects and a constant phase gradient in the holding beam, we introduce in Eq. 8.1 $E_I = E_{I0} \exp(i\mathbf{K} \cdot \mathbf{x})$, as shown in 8.2.2. If the force engendered by this gradient is strong enough to win the pinning force of the defect, the structure described above leaves the defect and a regular flow of drifting *CS* springing out of the defect settles down, as shown in Fig. 8.11.

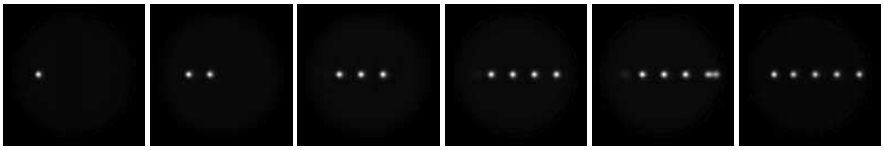

Fig. 8.11 Sequence of snapshots showing the spatio-temporal dynamics of drifting CSs in the transverse section of the VCSEL in presence of a defect. Intensity increases from black to white. The position of the defect corresponds to the high intensity structure visible in the first panel, and the phase gradient is directed rightwards. Defect characteristics: θ_0 = - 2.0472, θ_d = 0.25, σ_d = 11.25 μm. Other parameters: E_I = 0.792, I = 2.0024, K = 0.052 μm^{-1}, and t_i = 5 ns is the time after initiation of the phase gradient in the numerical simulation.

This spatio-temporal behavior corresponds to the one experimentally shown in Fig. 8.10. It can be understood by considering the characteristics of the defect above described and the fact that, outside the defect, *CS* solution is stable. As the structure leaves the defect pushed by the phase gradient, it becomes a *CS* and it keeps on travelling in the direction of the gradient with a speed depending on K. In the

defect, once the structure has gone away, the system must relax back to the high intensity state, which is the unique stable solution. Therefore, the structure forms deterministically in the defect as a result of the (local) evolution of the system to the equilibrium. This structure is pushed outside the defect by the phase gradient and the process starts again, originating a periodic flow of drifting CS.

As in the experimental time traces, the separation between two pulses (T) is determined by the time τ_f required to regenerate the structure at the defect once the preceding one has gone ($T \approx \tau_f$), though numerical simulations show that other situations are possible for deeper defects. This relaxation process depends critically on the parameter values inside the defect. In particular, it depends on how far these values are from the critical ones at which the homogeneous solution loses its stability. The divergence of τ_f, as the control parameter approaches the bifurcation point, is a well known behavior of systems close to bifurcation (critical slowing down) [47]. For zero dimensional bistable systems, the critical slowing down is characterized by a typical dependence of the relaxation time on the bifurcation parameter. This is given by the inverse of a square root law of $|\mu - \mu_c|$, with μ being the generic parameter and μ_c its critical value at the bifurcation [47]. The fits of the numerical curves of τ_f reveal a similar scaling as a function of θ and of E_I, as shown in Fig. 8.12a and 8.12b, though the scaling exponent is different from $\frac{1}{2}$.

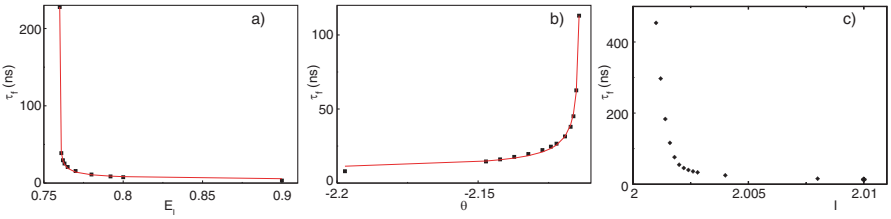

Fig. 8.12 Structure formation time τ_f on a defect as a function of different parameters.
a): As a function of the holding beam amplitude E_I. At $t = 0$, the holding beam amplitude is suddenly increased from the value $E_I = 0.1$ to the new stationary value E_I. The fitting function is $\tau_f = \tau_0 + (E_I - E_{I,c})^b$, $\tau_0 = 5.18$ ns, $E_{I,c} = 0.79063$, $b = -0.58$. Other parameters values are $\theta_0 = -2.0472$, $\theta_d = 0.2$, $I = 2.0024$, $K = 0\ \mu m^{-1}$.
b): As a function of the value of θ at the defect bottom. The defect profile is introduced in the numerical simulations at $t = 0$, starting from the stationary solution corresponding to the perfectly homogeneous case. The fitting function is $\tau_f = \tau_0 + (\theta_c - \theta)^b$, $\tau_0 = 7.27ns$, $b = -0.76$, $\theta_c = -2.114$. Others parameters: θ_0 = - 2.0472, I = 2.0024, E_I = 0.792, K = 0 μm^{-1}.
c): As a function of VCSEL bias current I. The defect profile is introduced in the numerical simulations at $t = 0$, starting from the stationary solution corresponding to the perfectly homogeneous case. Here θ has been varied with I in order to take into account the redshift of the cavity resonance due to Joule heating. Defect characteristics: θ_d = 0.2, θ_0 = -2.0472. Other parameters: K=0. μm^{-1} and $E_I = 0.792$.

Concerning the VCSEL bias, it appears that changing this parameter does not correspond only to change the parameter I in the equations. A change in the VCSEL bias implies also a variation of θ because of the change of the semiconductor

refractive index caused by Joule heating [14]. In order to take into account this double effect in the model, we have introduced phenomenologically the dependence of θ on I by putting $\theta(I) = \overline{\theta} - 5(I - \overline{I})$, being $\overline{\theta}$= - 2.0472 and $\overline{I}$ = 2.0024. The dependence of τ_f as a function of I is plotted in Fig. 8.12c, and it is similar to the one experimentally obtained in Fig. 8.10d. It is worthwhile to note that I cannot be increased arbitrarily since eventually the homogeneous solution becomes unstable even outside the defect and CSs do not exist anymore. This explains why value of $< T >$ cannot be further reduced in Fig. 8.10d. Finally, it is well known that noise is much more effective in the vicinity of the bifurcation, thus explaining why the fluctuations of $< T >$ in Fig. 8.10d are larger for low I.

Defect depth and shape affect the characteristics of the reported spatio-temporal dynamics for CS, but the onset of the periodic flow of drifting *CS* is rather robust versus defect characteristics. Three ingredients are necessary: outside the defect *CS* solution must be stable, inside the defect only the high intensity solution is stable and the phase gradient must be strong enough to push the structure outside the defect.

The formation of a regular sequence of CSs springing from a device defect and moving in the gradient direction, that we called *CS* "tap", may be useful in *CS* applications. First off all, defect-like spots can be engineered in the transverse plane of the device in order to create device built-in *CS* sources, thus avoiding the use of a writing beam to generate CS. The generation rate of these spots can be set by engineering the defects characteristics. Thus, defects with different height/depth and size could be engineered to obtain simultaneously *CS* sources with different properties in the same device.

CS generation rate can be set by controlling the system parameters and/or by engineering the defect characteristics. The flow behavior upon variations of the device pumping current suggests that, by means of a weak modulation of the pumping current, it may be possible to modulate the distance between *CS*, keeping constant the value of the phase gradient generating the motion. Moreover, it may be even possible to stop the *CS* generation without perturbing the *CS* stability nor their speed outside the defect, by simply varying the pumping level across the critical value where the formation time of the structure goes to infinity (see Fig. 8.12c).

This sensitivity of *CS* generation on the pumping current suggests the possibility of realizing a delay line for digital signals where a bit value of "1" is stored as a drifting *CS* and the input signal to be delayed is used for modulating the VCSEL pumping current. This represents an optoelectronic method to store information bits in form of moving CS, thus realizing a serial to parallel converter.

Finally, the *CS* flow can also be modified by injecting an optical perturbation onto the defect originating the flow. In particular, it is possible to interrupt the *CS* flux for a certain interval of time by injecting a Gaussian incoherent beam in the defect position, without varying all the other parameters. This acts as an erasing beam and, as long as it is on, it stops the *CS* emission. When the injected beam is switched off, a new *CS* is spontaneously created in the defect and the *CS* flux starts again. We obtain therefore a perfect control on *CS* emission, and this would permit us to realize a delay line where information is encoded by erasing pulses in a periodical sequence

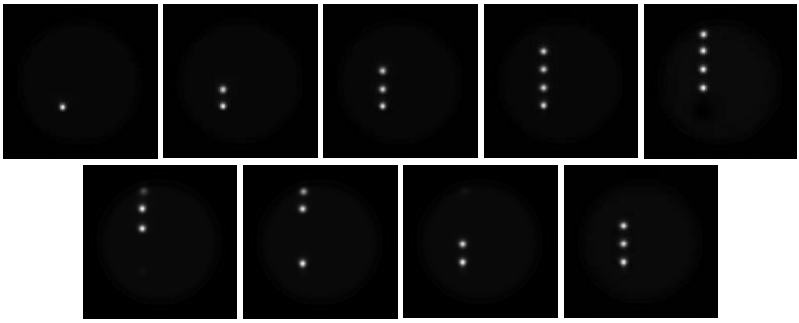

Fig. 8.13 Sequence of snapshots illustrating different stages of continuous creation and inhibition of CSs The defect position corresponds to the *CS* in the first frame, and the phase gradient is directed upwards. The injection starts just before frame number 5 and stops after frame 6. From left to right the frames are taken every 12 ns, starting at the $4th$ ns (the entire simulation lasting 100 ns). Parameters are: $\theta_d = 0.2$, $\theta_0 = -2.0$, $I = 2.$, $E_I = 0.8$, and $K = 0.042\mu m^{-1}$. Intensity increases from black to white.

instead of writing them. At variance with the use of a writing beam, this operation can be realized by using an optical perturbation not necessarily coherent with the holding beam, thus simplifying remarkably the experimental scheme. In Fig. 8.13 we show a sequence of snapshots illustrating different stages of continuous creation and inhibition of CSs.

8.5 Conclusions

In this chapter we have illustrated some examples of applications of *CS* in semiconductor microcavities. Though these operations are still at the stage of proof-of-principle, *CS* appear as promising tools for all-optical signal processing. The possibility of inducing *CS* drift by introducing a phase gradient in the holding beam enables the conception of *CS* based devices as the shift register and the optical delay line. The same property allows for the creation of *CS* reconfigurable arrays within the device section. In this case the desired geometry is introduced in the holding beam phase by a spatial phase modulator.

The main limitations of *CS* based applications come from the VCSEL resonator homogeneity. The state-of-the-art of the fabrication process cannot prevent the formation of device defects in the transverse section of the device. They affect *CS* existence, thus preventing from using the entire transverse section for *CS* addressing. Moreover, they can attract or repel drifting CS, thus affecting the operations based on CS drift.

Reversing the point of view, the sensitivity of *CS* on the presence of these defects makes them the best tool for a screening of the homogeneity of VCSEL devices. A *CS* based microscope has been demonstrated for detection of device defects.

If the defect is isolated, the presence of a phase gradient in the holding beam may generate a regular flow of *CS* drifting in the gradient direction and springing from the defect. This suggests the possibility of engineering device defects for creating *CS* sources buried in the device, thus avoiding the use of an external writing beam. We have also shown that, by addressing incoherently this defect, it would be possible to encode information bits in the drifting CS.

Finally, for *CS* based devices exportable "outside the laboratory" it is advisable to simplify the experimental scheme and to remove the tight requirements on the parameters of the injected beam. A promising solution is provided by the Cavity Soliton Laser, a device where *CS* are generated without an external injected beam, thus behaving as microlasers. Important steps in this direction have been accomplished recently by three successful implementations of this concept [48, 49, 33]. One of these schemes is treated in a chapter of this book.

Acknowledgements This work was done in the framework of the FET OPEN Project Nr. 4868 FunFACS (Fundamentals, Functionalities and Applications of Cavity Solitons). G. Tissoni acknowledges the financial support of the University of Nice.

References

1. T. Arecchi, S. Boccaletti, G. Giacomelli, G.P.Puccioni, P.L. Ramazza, S. Residori. Physica D **61**, 25 (1992)
2. W. J. Firth, "Self-organization in optical systems and applications in information technology", edited by M. A. Vorontsov and W. B. Miller, p.69, Springer-Verlag, Berlin (1995)
3. L. A. Lugiato, M. Brambilla and A. Gatti, Advances in Atomic, Molecular and Optical Physics 40, edited by B. Bederson and H. Walters, p. 229, Academic, New York (1998)
4. O. Thual and S. Fauve. J. Phys. **49**, 1829-1923 (1988)
5. M. Tlidi, P. Mandel, and R. Lefever. Phys. Rev. Lett. **73**, 640 (1994)
6. P. Coullet, C. Riera, C. Tresser. Phys. Rev. Lett. **84**, 3069, (2000)
7. Yu. Astrov and H. Purwins. Phys. Lett. A **283**, 349 (2001)
8. K. L. Lee, W. D. McCormick, J. E. Pearson, and H. L. Swinney. Nature **369**, 215-218 (1994)
9. J.Wu, R. Keolian, and I. Rudnick. Phys. Rev. Lett. **52**, 1421 (1984)
10. R. Richter and I. V. Barashenkov. Phys. Rev. Lett. **94**, 184503 (2005)
11. E. Moses, J. Fineberg, and V. Steinberg. Phys. Rev. A **35**, 2757 (1987)
12. N. Rosanov and G. Khodova. Opt. Spectrosc. **65**, 449 (1988)
13. W. J. Firth and A. J. Scroggie. Phys. Rev. Lett. **76**, 1623 (1996)
14. M. Saffman, D. Montgomery, and D. Anderson. Opt. Lett. **19**, 518 (1994)
15. A. Schreiber, B. Thring, M. Kreuzer, and T. Tschudi. Optics Comm. **136**, 415 (1997)
16. S. Residori. Physics Reports volume **416**, issue 5-6, p. 201-272 (2005)
17. B. Schæpers, M. Feldmann, T. Ackemann, and W. Lange. Phys. Rev. Lett. **85**, 748 (2000)
18. L. A. Lugiato. IEEE, J. Quant. Electr. **39**, 193 (2003)
19. N. Akhmediev, A. Ankiewicz (eds.). Dissipative solitons, vol. **661** of Lecture Notes in Physics (Springer, New York, 2005); Chapters 3,4,5 and 6
20. M. Brambilla, L. A. Lugiato, F. Prati, L. Spinelli, and W. J. Firth. Phys. Rev. Lett. **79**, 2042 (1997)

21. L. Spinelli, G. Tissoni, M. Brambilla, F. Prati and L. A. Lugiato. Phys. Rev. A **58**, 2542 (1998)
22. M. Brambilla, L. A. Lugiato and M. Stefani. Europhys. Lett. **34**, 109 (1996)
23. S.Barland, J. R. Tredicce, M. Brambilla, L. A. Lugiato, S. Balle, M. Giudici, T. Maggipinto, L. Spinelli, G. Tissoni, T. Knoedl, M. Miller, and R. Jaeger. Nature **419**, 699 (2002)
24. X. Hachair, L.Furfaro, M. Giudici, S. Balle, J. Tredicce, M. Brambilla, T. Maggipinto, I. M. Perrini, G. Tissoni, L. Lugiato. Phys. Rev. A **69**, 043817 (2004)
25. Y. Menesguen, S. Barbay, X. Hachair, L. Leroy, I. Sagnes, R. Kuszelewicz. Phys. Rev. A **74**, 023818 (2006)
26. X. Hachair, F. Pedaci, E. Caboche, S. Barland, M. Giudici, J.R. Tredicce, F. Prati, G. Tissoni, R. Kheradmand, L.A. Lugiato, I. Protsenko, and M. Brambilla. J. of Sel. Topics on Quant. Electr. **12**, 339-351 (2006)
27. X. Hachair, L. Furfaro, J. Javaloyes, M. Giudici, S. Balle, J. Tredicce, G. Tissoni, L. Lugiato, T. Maggipinto, and M. Brambilla. Phys. Rev. A **72**, 013815 (2005)
28. S. Barbay, Y. Menesguen, X. Hachair, L. Leroy, I. Sagnes, and R. Kuszelewicz. Opt. Lett. **31**, 1504 (2006)
29. F. Pedaci, S. Barland, E. Caboche, P. Genevet, M. Giudici, J. Tredicce, T. Ackemann, A. Scroggie, G.L. Oppo, W.J. Firth, G. Tissoni, and R. Jaeger. Appl. Phys. Lett. **92**, 01101 (2008)
30. F. Pedaci, P. Genevet, S. Barland, M. Giudici, and J. Tredicce. Appl. Phys. Lett. **89**, 221111 (2006).
31. R. Kuszelewicz, I. Ganne, I. Sagnes and G. Slekys, and M. Brambilla. Phys. Rev. Lett. 84, 6006 (2000)
32. T.Maggipinto, M.Brambilla, G.K.Harkness, and W.J.Firth. Phys. Rev. E **62**, 8726 (2000)
33. S. Longhi. Phys. Rev. E **55**, 1060 (1997).
34. W.J. Firth and G.K. Harkness, *Asian Journal of Physics* **7**, 665 (1998); G.-L. Oppo, A.J. Scroggie and W.J. Firth. Phys. Rev. E **63**, 066209 (2001)
35. M. Grabherr, R. Jaeger, M. Miller, C. Thalmaier, J. Heerlein, R. Michalzik, and K.J. Ebeling. IEEE Photon. Tech. Lett. 10, pp. 1061–3, 1998
36. J. L. Oudar, R. Kuszelewicz, B. Sfez, J. C. Michel and R. Planel. Opt. Quant. Electron. **24**, S193 (1992)
37. R.W. Boyd, D. Gauthier, and A.L. Gaeta. Opt. & Photon. News **17**, 18 (2006)
38. R. Tucker, P. Ku, and C. Chang-Hasnain. Electron. Lett. **41**, 208 (2005)
39. G. Tissoni, L. Spinelli, I. Perrini, M. Brambilla, T. Maggipinto and L.A. Lugiato. J. Opt. Soc. Am. B **16**, 2095 (1999)
40. E.A. Avrutin, J.H. Marsh, and E.L. Portnoi. IEE Proc.- Optoelectron. **147**, 251 (2000)
41. A . Garnache, S. Hoogland, A. C. Tropper, I. Sagnes, G. Saint-Girons, and J. S. Roberts. Appl. Phys. Lett. **80**, 3892 (2002)
42. S. Dommers, V. V. Temnov, U. Woggon, J. Gomis, J. Martinez-Pastor, M. Laemmlin and D. Bimberg. Appl. Phys. Lett. **90**, 033508 (2007)
43. J. Lucek and K. Smith. Opt. Lett. **18**, 1226-1228 (1993)
44. M. Pantouvaki, M.J. Fice, R. Feced, E.P. Burr, R. Gwilliam, A.B. Krysa, J.S. Roberts and A.J. Seeds, IEEE Phot. Tech. Lett. **16**, 617 619 (2004)
45. F. Pedaci, G. Tissoni, S. Barland, M. Giudici and J. Tredicce, Appl. Phys. Lett. **93**, 111104 (2008)
46. E. Caboche, F. Pedaci, P. Genevet, S. Barland, M. Giudici, J. Tredicce, G. Tissoni, and L. Lugiato. Phys. Rev. Lett. **102**, 163901 (2009)
47. S. Cribier, E. Giacobino, and G. Grynberg. Optics Comm. **47**, 170-172 (1983); F. Mitschke, C. Boden, W. Lange and P. Mandel. Optics Comm. **46**, 135-140 (1983)
48. Y. Tanguy, T. Ackemann, W. J. Firth, and R. Jaeger. Phys. Rev. Lett. 100, 013907 (2008)
49. P. Genevet, S. Barland, M. Giudici, and J.R. Tredicce. Phys. Rev. Lett. 101, 123905 (2008)
50. T. Elsass, K. Gauthron, G. Beaudoin, I. Sagnes, R. Kuszelewicz and S. Barbay. Appl. Phys. B, 2009, doi:10.1007/s00340-009-3748-9

Chapter 9
Cavity Soliton Laser based on coupled micro-resonators

Patrice Genevet, Stéphane Barland, Massimo Giudici, and Jorge R. Tredicce

Abstract We report on the experimental observation of localized laser structures in a compound laser system consisting of two mutually coupled broad-area Vertical Cavity Surface Emitting Lasers (VCSELs), one of which is operated as a saturable absorber. As cavity solitons appearing in a VCSEL driven by a coherent driving beam, these localized structures coexist with a dark homogeneous background and they can be individually addressed by a local perturbation. On the other hand, they are generated in a laser device (hence called Cavity Soliton Laser, CSL) that does not require a driving field. We explore the parameter space of the CSL to map the region of existence of the localized laser structures and to give evidence of multi-peaks and ring-like laser states. We describe the bifurcation diagram associated to the formation of these complexes which, as the single-peak structures, can be switched by means of a local addressing beam. Localized laser structures have multistable emission frequency associated to coexisting compound cavity longitudinal modes.

Patrice Genevet
Université de Nice Sophia Antipolis, Centre National de la Recherche Scientifique, Institut Non Linéaire de Nice, 1361 route des lucioles, Valbonne, France e-mail: patrice.genevet@inln.cnrs.fr

Stéphane Barland
Université de Nice Sophia Antipolis, Centre National de la Recherche Scientifique, Institut Non Linéaire de Nice, 1361 route des lucioles, Valbonne, France

Massimo Giudici
Université de Nice Sophia Antipolis, Centre National de la Recherche Scientifique, Institut Non Linéaire de Nice, 1361 route des lucioles, Valbonne, France e-mail: Massimo.Giudici@inln.cnrs.fr

Jorge Tredicce
Université de Nice Sophia Antipolis, Centre National de la Recherche Scientifique, Institut Non Linéaire de Nice, 1361 route des lucioles, Valbonne, France e-mail: Jorge.Tredicce@inln.cnrs.fr

O. Descalzi et al. (eds.), *Localized States in Physics: Solitons and Patterns*,
DOI 10.1007/978-3-642-16549-8_9,

9.1 Introduction

In the last decade an intensive experimental and theoretical work has been developed on localized structures. These structures appear in a large variety of large aspect ratio physical systems, where pattern formation is not ruled by the boundary conditions [1, 2, 3, 4, 5, 6, 7]. Their properties are very interesting for applications, especially when they form in optical systems. Localized structures can be individually addressed and positioned, which makes them very attractive for the optical treatment of information [8]. Several demonstrations of localized structures implementation to all-optical information processing have been experimentally provided [9, 10, 11, 12]. In optical resonators driven by an external electromagnetic field, localized structures have often been named Cavity Solitons. A large amount of theoretical and experimental work has been developed to analyze cavity solitons existence domain in semiconductor media [13, 14], allowing for fast response and miniaturisation.

Despite the large amount of investigations on localized structures, some questions concerning their bifurcation diagram describing the formation of complex localized patterns [15] are still under debate. In one dimensional systems, the bifurcation diagram showing the domain of stability of single-peak, double peak and up to N-peaks localized structures has been established in the case where a stationary homogeneous state coexists with a stationary pattern solution, as it is the case for optical systems injected by an external field [16, 17]. The different kinds of localized structures appear as a consequence of direct and inverse saddle node bifurcations. Such series of bifurcations leads to the so-called snaking region which describes the coexistence of a very large number of different localized structures. As all of them are stable in a measurable region of parameter space, it is expected to observe a high degree of multistability between the different coexisting states [18]. However experimental observations have shown that such large coexistence of localized structures is not found, at least in bidimensional systems [6]. Instead of the expected bifurcation of the system towards the upper (patterned) branch, the commonly observed behavior is the sequential nucleation of an increasing number of distant single-peak structures as a parameter is increased [3, 10, 19, 20]. This disagreement between experimental and theoretical results was recently attributed to an anomalous slant of the snaking region, which means that not all states coexist and are stable simultaneously, but that, for each parameter value, only a subset of these states is stable. More recently, it was demonstrated that an intrinsic slant will appear just as a consequence of the continuous translational symmetry [21]. Other mechanisms may include an additional saddle node bifurcation of the complete pattern solution [22] or the appearance of a non local coupling yielding to long range interactions among localized structures [20]. If experimental observations confirmed that all the states are not stable in the same parameters zone, leading to a slant of the homoclinic snaking bifurcation diagram [23], the role that could be played by the device inhomogeneities has not been fully understood yet. Besides, the ”slanted snake” picture captures only the stability of a single localized state, while the superposition of in-

dependent localized states, appearing at separate points of the space, will inevitably complicate the situation [15].

In the present chapter, we propose to extend the analysis of the localized states bifurcation diagram to the case of laser systems. At difference with passive systems (as, for example, the coherently driven VCSEL resonator), in laser systems there is no external field imposing its phase, thus they are phase invariant. This symmetry increases the complexity of the theoretical description. The analysis described above based on the coexistence of two stationary solutions, i. e. an homogenous and a pattern solution having the same reference frequency, does not apply since there is no external injected field fixing the frequency of the system. In fact, we are not aware of any general theory existing for phase invariant systems that could predict the bifurcation sequence leading from single-peak localized structure to more complex states.

The system we analyze consists of two coupled broad-area Vertical Surface Emitting Lasers (VCSELs) facing each other and forming a self-imaging compound cavity. While one laser is operated as amplifier, the other is biased below transparency and it behaves as a saturable absorber. Recent experimental results have shown this system can generate independent and switchable localized structures [24]. For its ability of generating localized structures similar to cavity solitons without requiring the presence of an injection field, this compound system has been named Cavity Solitons Laser (CSL). Localized states existence was theoretically predicted in two-levels lasers media with saturable absorber in the limit of fast material response [7, 25] and, more recently, in semiconductor media [26]. In Rosanov and coworkers early theoretical studies, these localized structures appearing in laser systems were named *laser solitons* [27]. Some of these theoretical studies have indicated the possibility of generating multi-humps localized states. We will show experimentally that the organization of localized laser structures leads to a diagram strikingly similar to the homoclinic snaking obtained for injected systems where the phase invariance is broken.

9.2 Experimental Setup

The experimental setup is presented in Fig.9.1 [24, 28]. Two nominally identical VCSELs (L_1 and L_2) are mounted in face to face configuration. They are 200 μm diameter disk-like lasers. L_1 and L_2 are placed in self-conjugate planes and therefore, after one roundtrip, L_1 (resp. L_2) is re-imaged on itself. This configuration allows to compensate for the diffraction occurring between the two VCSELs, hence preserving the high Fresnel number required for the existence of localized structures [29]. Diffraction takes place only within the two VCSEL resonators, which delimit a self-imaging compound cavity. A 20% reflection beam splitter is inserted in the center of the cavity to extract output beams from the compound system. We underline that the results presented in this paper could not be obtained using a 50% reflection beam splitter, indicating that the amount of coupling between the devices

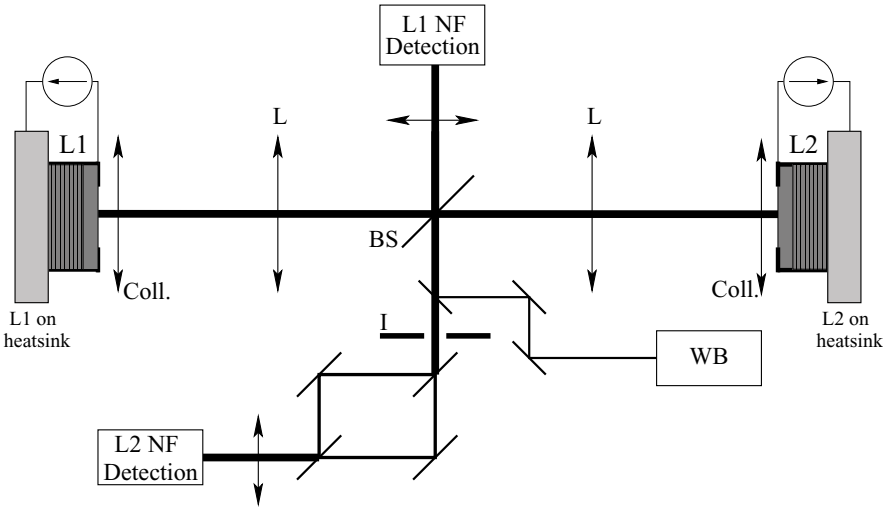

Fig. 9.1 Schematic drawing of the experiment. L_1: Laser above the transparency, L_2: Laser below the transparency, BS: beam splitter. Detection of L_1 (resp. L_2) includes a CCD camera monitoring the near-field of L_1 (resp. L_2) and a fast detector to monitor the local temporal behavior. For phase profile analysis we add the Mach-Zehnder interferometer in the L_2 detection path.

must be sufficiently high. The near-field profiles of both VCSELs are imaged on a charge coupled device (CCD) camera, allowing for the simultaneous monitoring of L_1 and L_2. The self-imaging condition is obtained experimentally by comparing onto a single CCD camera the image of the near-field emission profile of L_2 with the near-field emission profile of L_1 reflected by the output mirror of L_2 (the two resonators being uncoupled due to a large detuning between their resonances, as described in Section 9.3). If, after reflection, the near-field profile of L_1 is imaged also onto the CCD camera and this image has the same size as the near-field image of L_2, then self-imaging condition is reached.

L_1 and L_2 lase at around 980 nm, they are obtained from the same wafer and they are nominally identical, both have a solitary threshold of about 400 mA. Their substrate temperatures (T_1^o and T_2^o) and pumping currents (I_{L1} and I_{L2}) are stabilized. To operate as a laser with saturable absorber, the two lasers forming the compound system work in different regimes. The amplification is obtained by biasing L_1 at high current values, while the saturable absorption is obtained by biasing L_2 below transparency (below 40mA). The index of refraction of the semiconductor medium depends both on substrate temperature and on pumping current through Joule heating. The mismatch between the cavity resonances, implied by a difference in the bias currents, can be therefore compensated by controlling the individual substrate temperatures (T_1^o and T_2^o), thus enabling coupling between the two resonators. The coupling level between the two resonators depends also on the reflectivity of the beam splitter inserted in the cavity for extracting output beams. In order to maximize the coupling, we choose the beam splitter with the minimal reflectivity still

enabling extraction of detectable output beams. In our experiment, the reflection of the beam splitter is 20%. In order to ignite cavity solitons we used a 15 μm size writing beam (WB) generated by an external-cavity tunable laser mounted in Littman configuration. The WB is applied to a point of the transverse profile of the absorbing resonator (L_2) acting as a local optical perturbation of the compound system. A Mach-Zehnder interferometer on the L_2 detection path is used to study the localized structures coherence properties.

9.3 Bistability regime

Laser solitons can be obtained in presence of a bistable response of the output field [7]. As previously explained, in our laser system bistability is achieved by biasing L_2 below its transparency value and thus operating it as a saturable absorber. For enabling L_2 absorption of the electromagnetic field amplified by L_1 the cavity resonances of the two micro-resonators should match. This matching is achieved by properly tuning the micro-resonators substrates temperatures.

When these parameter settings are done, the bistability response versus the amplifier bias current is captured by monitoring the emitted intensity of a small region of the transverse profile (Fig. 9.2). The results of this measurement are shown in Fig. 9.2 lower panel, for different bias current values of the absorber. As the amplifier bias current is increased, we remark that the emitted intensity drops to spontaneous emission level for 320 mA $< I_{L1} <$ 400 mA. This zone has been identified as the parameter region where the cavity resonances are close enough to allow for interaction and therefore for the absorption to take place. The origin of this sudden drop in the emitted intensity can be understood by considering that the cavity resonance of L_1 is continuously changed when the amplifier current is swept. By increasing I_{L1}, the L_1 cavity resonance is red-shifted proportionally to I_{L1} due to Joule heating. For $I_{L1} = I_{L2} = 0$ the temperature of L_2 substrate has been set to an higher value than the one of L_1. Then, as the bias current of L_1 is upward scanned, the induced red shift of L_1 resonator resonance will eventually compensate the initial detuning between the resonances. When interaction occurs, the absorption by L_2 reduces the emitted intensity until bleaching occurs due to saturation. If we modify the difference between the temperatures of L_1 and L_2 at $I_{L1} = I_{L2} = 0$, the interaction zone will occur at a new I_{L1} value which correspond to the new amount of current necessary to compensate the initial detuning between the two resonances. We notice that the drop in intensity is not observed when the relative difference of the micro-resonators substrates temperatures is reversed. In this case, an increasing of I_{L1} moves L_1 cavity resonance away from the L_2 cavity resonance and the interaction never occurs. It is worth to point out that when the two devices interact, the presence of absorption by L_2 can also be monitored by the presence of a light induced current in the device bias circuit.

For low current values in the absorber resonator, *i.e.* high absorption levels, [Fig. 9.2, lower panel a) with I_{L2} around 16 mA], the emitted intensity exhibits the char-

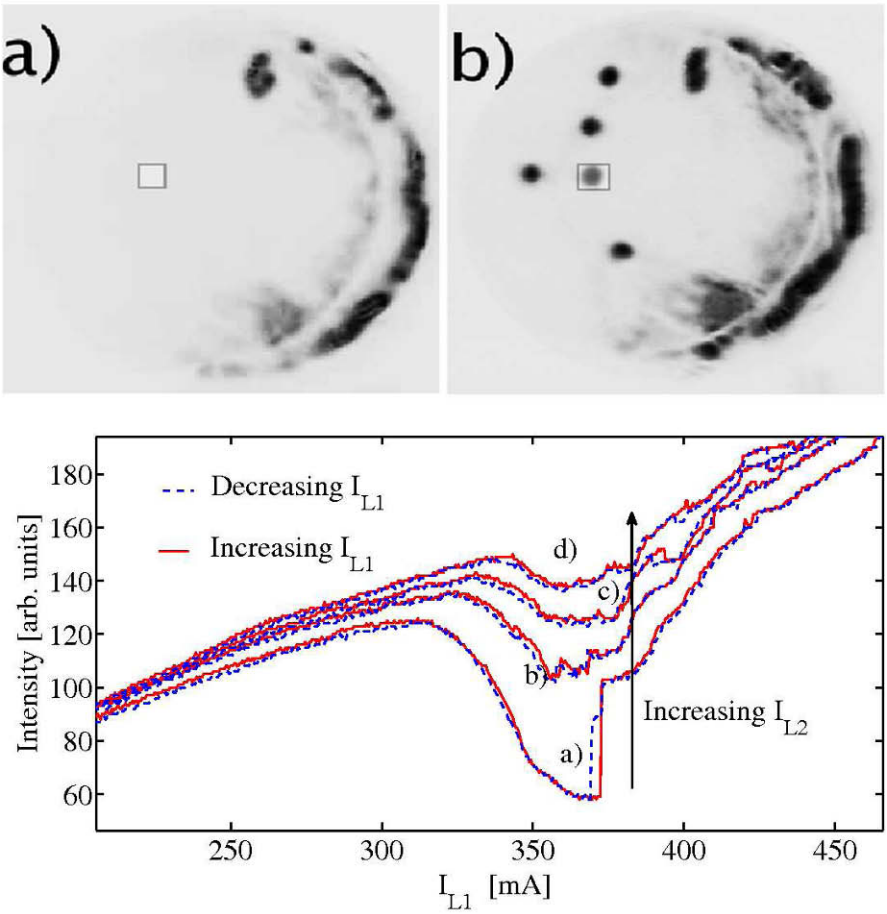

Fig. 9.2 Upper panel: Typical near-field profile of the system before (a) and after (b) the switching of five single-peak structures. To capture the bistability response, a region of about 15 μm diameter is monitored. This region is indicated by the square. Intensity increases from white to black
Lower Panel: Local intensity output emitted by the system when scanning I_{L1} with a fixed difference of packages temperature. Different curves are shown for different values of I_{L2}. The continuous curves correspond to upward scanning I_{L1} while the dashed part of the curves corresponds to downward scanning I_{L1}. In curve a) I_{L2}=16 mA, in curve b) I_{L2}=30 mA, in curve c) I_{L2}=38 mA, and in curve d) I_{L2}=46 mA. For sufficiently low values of I_{L2} an hysteresis cycle appears.

acteristic hysteresis cycle resulting from the bistable response of the system. This regime persists on a range of around 10 mA variation of I_{L2}. The abrupt transitions at the edge of the bistable cycle correspond to the appearance, in the recorded area of the near-field profile, of a bright isolate spot of laser radiation having a diameter

of approximately 10 μm, as the one presented in Fig.9.2 upper panel. The optical spectrum of this structure reveals a well pronounced peak characteristic of laser emission which is absent in the case of the homogeneous solution. If the current in the absorber is too high, the bistable response is lost [Fig. 9.2 lower panel b), c), d)] and the intensity drop is less pronounced.

In [24], we have proven that an external writing beam (WB) of around 15 μm diameter can be used for the independent control of the observed bright spots. The parameters are set in the bistable zone and the system is initially prepared in the low intensity branch. The application of the optical perturbation at two sufficiently distant points in L_2 transverse section ignites two independent bright spots, thus allowing for interpreting these structures as single-peak laser solitons. The same WB can be used to switch them off independently. For this operation we have followed the indications of numerical simulations where erasing of laser solitons is obtained by applying a perturbation of suitable duration [30]. We have experimentally observed this behavior for parameters set sufficiently close to the lower edge of the bistability region [28]. The limitation in optical power of our optical perturbation did not allow us to control, for the same parameters values of the system, both the switching on and off using different perturbations duration. On the other hand, laser solitons have been independently switched off by dragging them in regions of the transverse section of the system where inhomogeneities destabilize laser solitons [24]. These device inhomogeneities affects also the existence of cavity solitons in the coherently driven schemes, as described in the chapter on cavity solitons in VCSEL of this book.

We have previously shown that our compound system can be interpreted as a laser with saturable absorber when the interaction between the cavities occurs. The parameters zone where the interaction occurs can be obtained for different combinations of values of the temperature difference and of the amplifier current. We can, for example, set the interaction zone at different I_{L1} values by changing the initial temperature difference between the resonators. In this way we have obtained a broad parameters region where single-peak laser solitons are stable [28]. This flexibility in the control parameters has also permitted the observation of more complex localized states. The next subsection will be devoted to the description of the bifurcation sequence that, from the single-peak laser solitons state, leads to multi-humps states.

9.3.1 Multistable Regime

The formation of clusters of localized states is currently a focus of experimental and theoretical investigations in optics. A general theory describing the appearance of these clusters of localized structures has been developed in the frame of a Swift-Hohenberg equation in one spatial dimension and in the case where a stationary homogeneous solution coexist with a stationary pattern state [16]. This is the case of injected optical resonator, where the frequency of both solutions are fixed by the injected field frequency. It turns out that a front connecting these two solutions is

stationary in a finite parameter region called ”locking range”. The bifurcation diagram of a single-peak localized state shows that the intensity of this state ”snakes” up towards higher intensity levels, zig-zagging to and from across the locking range. While the positive slope ”zig” corresponds to stable branches of localized states, the negative-slope ”zag” are unstable branches. The number of peaks of the localized state associated to a stable branch is increased by two at each zig-zag [32]. Hence, localized states with an increasing number of peaks coexist in the parameter space. This peculiar bifurcation diagram has been named ”homoclinic snaking” because all these localized states are homoclinic to the homogeneous solution. At variance with these theoretical predictions, the sequential formation of an increasing number of peaks upon the variation of a parameter is often observed in experiments [23, 10], indicating that the bifurcation diagram would exhibit a certain degree of slanting, breaking the alignement of the stability branches of different localized states versus the parameter value. Different hypothesis on the mechanism leading to the slant of the homoclinic snaking bifurcation diagram has been formulated [20, 22].

On the other hand, there are no indications that a bifurcation diagram of localized structures similar to the homoclinic snaking could exist also in laser systems, where the homogeneous solution corresponds to a non-lasing state with an undefined frequency and phase. In the early description of laser solitons of Rosanov, these structures arise as a heteroclinic connection of two fixed points of zero amplitude which represent the non lasing state [7]. In order to shed some light on the bifurcation diagram of the Cavity Soliton Laser, we have experimentally investigated the bifurcation diagram of a single-peak laser soliton. We have found that our system supports the existence of clusters of laser solitons and complexes, which could be considered as bound states of two or more coherent single-peak laser solitons. The appearance of these multi-humps states arises from a secondary bifurcation of the laser soliton solution. While this analysis has been performed monitoring a small region of the transverse section of the cavity soliton laser, we have also analyzed the global bifurcation diagram of the entire device.

9.3.2 Local bifurcation diagram

The bifurcation diagram of a single-peak laser soliton is obtained by monitoring a small surrounding region, as described in the previous section to evidence the bistability regime. The control parameter is the amplifier current I_{L1}, which has been used to draw the bistability curve of Fig. 9.2. The bifurcation diagram of the single-peak soliton laser depends critically on the system parameters. In upper panel of Fig. 9.3, we show the evolution of the bifurcation diagram for different values of the absorber current I_{L2}. For clarity the different diagrams are vertically shifted for increasing values of I_{L2}. We observe that for high current value in L_2 ($I_{L2} \geq 26$ mA) and thus low absorption in the system, the sequence of bifurcations is such that there is no distinguishable multistability. When I_{L1} is scanned upward, the system jumps from the non-lasing state towards the single-peak laser soliton (indicated with A).

Increasing more the pumping current, a secondary bifurcation takes place and a two-peaks structure (indicated as *B*) appears followed by a ring-like state (indicated with *C*). When I_{L1} is scanned downward from the upper state, a bistability is observed between the ring-like structure with the double-peak structure for $I_{L1} \approx 368$ mA and between the single-peak laser soliton with the homogeneous solution for $I_{L1} \approx 362$ mA. No clear coexistence is observed between these four states. Decreasing I_{L2} to $22 - 24$ mA, we remark that the system jumps directly from the homogeneous solution to a complex structure (two-peaks or ring-like structure) when scanning upward I_{L1}, instead, when I_{L1} is scanned downward, the intensity reaches the homogeneous intensity level by successive abrupt jumps corresponding to this sequence of transitions: from ring-like structure to two-peaks structure to single-peak structure to homogeneous solution. The homogeneous structure coexist with two ($I_{L2} = 24$ mA) or with all the three lasing structures ($I_{L2} = 22$ mA). For lower absorption values ($I_{L2} = 16$ mA), the single-peak laser soliton state is not spontaneously reached anymore, while the two-peaks structure coexists with the homogeneous solution.

The upper panel of Fig.9.3 demonstrates that the bifurcation diagram of localized states can be modified by changing the level of absorption. Since there is no general theory that applies to cavity soliton laser it is difficult to argue on the origin of this behavior; we hope that these experimental findings may stimulate further theoretical investigations of localized structures in laser scheme.

The abrupt jumps observed in the bifurcation diagram for $I_{L2} = 22$ mA and $I_{L2} = 24$ mA suggest the presence of multistability but such behavior can not be evidenced by scanning I_{L1} all the way up from the homogeneous state and then all the way down. In order to confirm the coexistence between single and multi-humps structures, we have performed a measurement aimed at exploring the complete stability domain of each structure. This can be determined by preparing the system on each state and scanning up and down I_{L1} to find the switching values towards the upper and lower branch. The full stability diagram obtained is shown in Fig. 9.3, lower panel. The black arrows designate the stability of each state. The green dashed arrows designate the parameters zone where a localized structure coexists with the homogeneous solution while the red one corresponds to bistability between structures. The single-peak soliton laser branch is denoted by the letter a). The branch associated to the double peak structure is marked by the letter b) and the letter c) designate the ring-like structure. As previously described, this curve is obtained for a peculiar setting of parameters and it changes when the absorption level is modified. In particular, a change in I_{L2} affects the size of the region of bistability with the homogeneous solution (green dashed arrows). The same happens to the region of coexistence between adjacent states (red dashed arrows). For the particular parameters setting we used to obtain this diagram, the homogeneous state, the single-peak soliton laser and the double peaks structures are simultaneously stable. For 295.5 mA $< I_{L1} <$ 297.5 mA the system is multistable. We notice that the slant in the coexistence of the states is clearly visible in the lower panel of Fig. 9.3 and it indicates that the size of the region of coexistence between a localized state and the homogeneous solution shrinks with the increasing of the structure size.

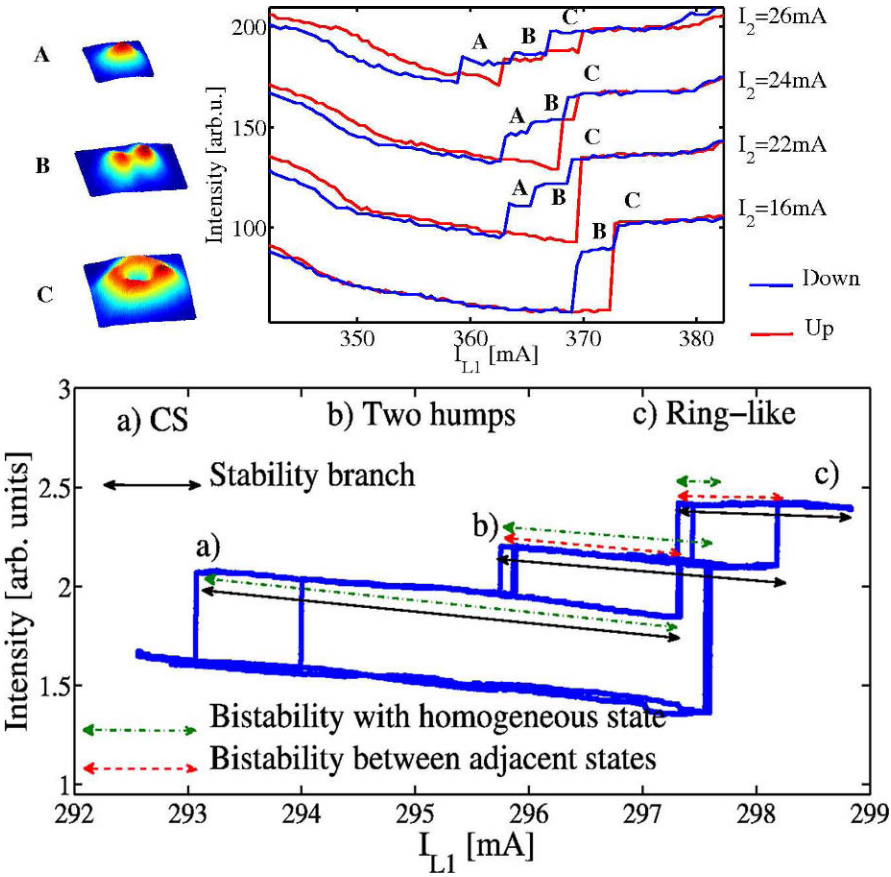

Fig. 9.3 Upper panel: Local intensity output emitted by the system when I_{L1} is ramped up and down, for different values of I_{L2}. The monitored region of the transverse section of the system has a diameter of 30 μm. I_{L1} is scanned very slowly to preserve the stability of the temperature controller). Red curve: I_{L1} scanned upward, Blue curve: I_{L1} scanned downward. Curves for different values of I_{L2} are vertically shifted for clarity. a) Intensity profile of one-peak laser soliton. b) Intensity profile of two peaks laser soliton. c)Intensity profile of a ring-like lasing structure.
Lower panel: Local intensity output emitted by the system as shown in the upper panel for $I_{L2} \approx 24$ mA. I_{L1} is properly scanned to explore the stability of all branches (full black arrows), i.e. of each localized state. The green dashed arrows designate the parameters region for each localized state where it is bistable with the homogeneous solution. In this region, a writing beam could be used to switch on the localized structure considered. The red dashed arrows designate the region of bistability between different structures. Multistability is present in the parameter regions where the red and green dashed arrows overlap.

9.3.3 Towards the whole bifurcation diagram

The local bifurcation diagram presented in Fig.9.3 has been obtained by considering only a region of 30 μm diameter in the transverse profile of the system. The bifur-

cation sequence exhibits a very complex bifurcation diagram when considering a larger region of emission. To better understand the bifurcation diagram of the whole system, we first increase the diameter of the observed area to around 80 μm. We perform the same measurement as in Fig. 9.3, upper panel, for two I_{L2} values. The results are shown in Fig. 9.4.

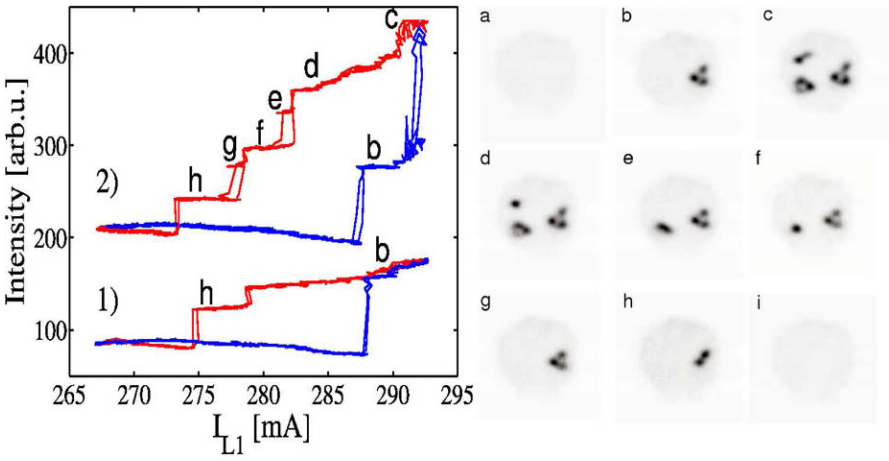

Fig. 9.4 Left panel: Local intensity output emitted by the system when I_{L1} is ramped up and down, for two values of I_{L2}: $I_{L2} = 20$ mA, 2) $I_{L2} = 22$ mA. The monitored region of the transverse section of the system has a diameter of 80 μm. Right panel: For each branch indicated by a letter in the left panel we show the corresponding near-field emission profile of the monitored region.

The curve denoted by 1) is obtained for $I_{L2} = 20$ mA. As shown in Fig.9.3, upper panel, for this value of I_{L2} the laser soliton structure is not reached spontaneously. A three-humps structure switches on (b) when I_{L1} is ramped up and becomes unstable, the system switches to the two-peaks state, when I_{L1} is decreased (h). If the absorption level is varied by changing I_{L2}, the bifurcation diagram concerning the monitored region is dramatically affected as shown by curve 2) in Fig. 9.4. Indeed, for the same I_{L1} scanning range, the near-field profile shows the appearance of new structures that where not present for lower I_{L2}. It is important to underline the difference between the local bifurcation diagram described in Fig. 9.3, which was restricted to the evolution of a single localized state, with a bifurcation diagram taking into account the evolution of several mutually independent localized states occupying different spatial regions of the system. In the next section we will characterize the coherence properties of these separate localized states versus the coherence properties within the same localized structure.

Fig. 9.4 has been obtained by monitoring the emitted intensity of a 80 μm diameter area when the current in the amplifier is ramped all the way up and all the way down. As discussed, this method cannot capture the full stability diagram because the intermediate states are not fully visited, while others may not be explored at all.

It is interesting to obtained the full stability diagram for the whole transverse profile of the CSL. The result is shown in Fig. 9.5.

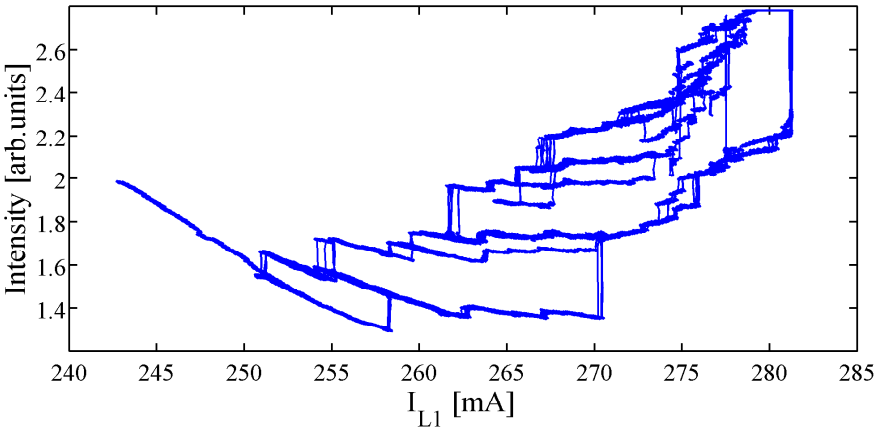

Fig. 9.5 Full bifurcation diagram for the whole transverse section of the system. This figure reveal a high degrees of multistability when several isolated zones are simultaneously observed.

Since a detailed description of each state which can be seen on Fig. 9.4 would be tedious, we will only outline the main features of the organization of these states. The first remark is that a sort of slant in the coexistence of the states is still evident when considering the whole transverse section. The diagram shows also that the switching of independent structures does not occur for the same parameter values. This behavior can be attributed to the inhomogeneities of the VCSEL device that can anticipate or delay the bifurcation point, although other interpretations may be possible [1]. We point out that for I_{L1} value at the beginning of the multistable response of the system (between 250 and about 270 mA), the near-field reveals the switching of isolated localized spots that grow in size when increasing I_{L1}. The growth of these isolated spots with I_{L1} leads eventually to their connection. For higher I_{L1} values, the pattern will invade the whole transverse section of the device. In this case, the fast temporal detection reveals a complex dynamics. This regime is very interesting to be studied but the spatial extension of the experiment requires an appropriate tool for both spatial and temporal detection. Although Fig. 9.5 already displays a remarkable complexity, it is important to note that it shows only the field intensity variable and that it does not give any information on the phase of the field.

[1] The presence of a long range coupling term, for example

9.4 Coherence properties of laser solitons

In order to obtain some information on the phase profile of the CSL emission we perform a near-field interferometric measurement of its output.

Since laser solitons are monochromatic, the mutual coherence of two of them can be studied by looking for interference fringes in the near-field when their respective signals are superimposed and imaged on a slow (*i.e.* time averaging) CCD camera. To realize this measurement, the output signal from the system is separated in two beams (see Fig.9.1). Each beam is directed through a different arm of a Mach-Zehnder interferometer. At the exit of the interferometer, a lens forms two images of the L_2 near-field output on a CCD camera, each image corresponding to a propagation through each arm of the interferometer. This experimental scheme allows us to overlap different spatial regions in the near-field output of the system in order to evaluate their mutual coherence.

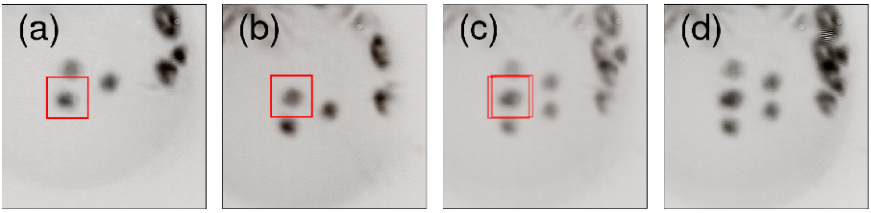

Fig. 9.6 L_2 near-field (NF) intensity distribution after the interferometer. a) The absorber medium NF is imaged from the interferometers first arm. b) The absorber medium NF is imaged from the interferometers second arm. The image is slightly shift down. c) Mathematical sum of the two previous picture. d) The interferogram present no fringes indicating that the two different laser structures are not coherent.

The sequence of near-field measurements presented in Fig. 9.6 summarizes the experiment. The Fig. 9.6a) is the near-field of the compound system observed through one arm of the interferometer, while the other arm is blocked. The Fig. 9.6b) shows the same near-field, imaged through the second arm of the interferometer only. Both images are slightly shifted with respect to each other. The shift is such as there is a superposition, in the CCD plane, between the lower left structure of the Fig. 9.6a) and the upper one of the Fig. 9.6b). This is clearly seen in Fig. 9.6c), which shows the mathematical sum of Fig. 9.6a) and b) [2]. Now, we let the two beams to interfere on the CCD by opening simultaneously both arms of the interferometer. The result of this experiment is presented in Fig. 9.6d). The absence of interference fringes, *i.e.* the fact that the sum of the intensities shown in c) is identical to the intensity of the sum shown in d) indicates that interference terms have been averaged out during the integration time of the CCD. This indicates that the upper structure is not coherent with the lower left one. The same experiment has been performed

[2] We add intensities, pixel by pixel.

with all the combinations of structures present in Fig. 9.6 and the results are identical, indicating that these independent single-peak laser soliton are not mutually coherent. This observation is very interesting when we compare it to the results of the experiment made with double-humps structures. Indeed, we have performed the same measurement but we have overlapped one peak of the double-humps structure to interfere with its neighbor. The results are presented in Fig.9.7. As previously, the first two pictures show the near-field observed through each single arm of the interferometer. The third picture is obtained by computing the mathematical sum of the two previous images while the last picture is the intensity at the interferometer output when the two arms are open. The presence of fringes, whose periodicity and orientation of course depend on the alignment of the two arms of the interferometer, indicate that the two peaks forming the double-humps structure are mutually coherent. The possibility to create multi-humps states in laser with saturable absorption has already been theoretically predicted and the stability of weakly coupled lasers structures has also been investigated [7, 31]. The authors show that stable bound state of two laser solitons can be formed if the phase mismatch between them is 0 or π.

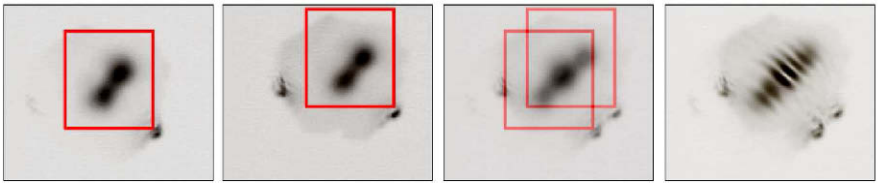

Fig. 9.7 From left to right: Intensity near-field profile of a double hump structure imaged twice on the CCD camera via two different interferometer paths: the first two pictures show the images obtained when either one or the other path is open. The third shows the calculated sum of the two intensity images: the top-right peak is superimposed on the bottom left peak. When both paths are open, the two peaks interfere with each other.

Even if the alignment condition chosen for this particular measurement does not allow us to determine the relative phase of the two humps with respect to each other, it clearly shows that the humps of a composite structure are mutually coherent, while distant laser solitons are not.

9.4.1 Modal properties

The CSL is based on the mutual coupling of two resonators in a long compound cavity (typically 30 cm). Because the gain curve of semiconductor laser is very broad (some nanometers) compared to the free spectral range (FSR) of the compound cavity (about 460 MHz), the number of longitudinal modes capable of being active is very important. The laser solitons could therefore lase on several frequencies, each

one associated to a compound cavity mode. In the following, we will turn our attention to laser solitons emission frequencies. Even if the optical spectrum analyzer shows the appearance of a new and narrow peak when a laser soliton switches on, the resolution of the optical spectrum analyzer (0.1 nm) is not sufficient to disclose the eventual presence of several compound cavity modes, which are separated by only $460MHz$.

A possible method to observe the presence of multiple frequencies in a laser soliton consists of performing an heterodyne measurement, using a stable reference field from a tunable laser. For this purpose, we use an external cavity laser mounted in Littrow configuration whose linewidth is below 1 MHz. The reference field is combined with the cavity solitons signal and sent to an 8 GHz bandwidth photodetector. The beating signal is detected and amplified and then it is recorded by a power spectrum analyzer HP8593.

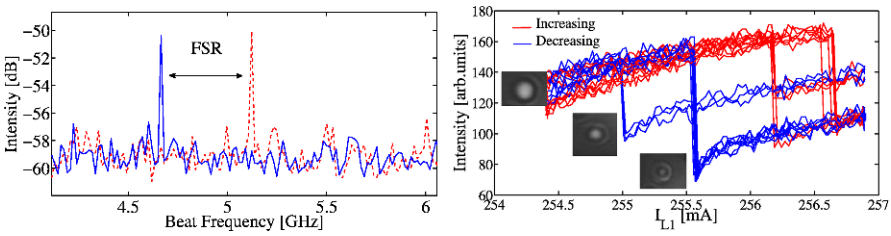

Fig. 9.8 Left panel: Two heterodyne measurements of the laser soliton frequency emission. The two curves indicate that the emission frequency is monochromatic and it takes discrete values associated to the compound cavity modes. Right panel: Interferometric intensity signal of a LS as a function of I_{L_1}. The interferometric intensity signal is obtained integrating the phase profile of the monitored LS. The figure shows the multi-stability of the laser soliton emission frequency. The inset picture are the phase profile resulting from the interference of the laser soliton with a reference beam extracted using the emission at the peak of the laser soliton. Bright zones represent hight intensities.

Fig. 9.8, left panel shows two different realizations of the recorded beating signal. The two curves have been obtained for a small change in the pumping current (around 0.2 mA) such that the laser soliton is kept bistable with the homogeneous zero solution (during this experiment, the total output intensity emitted by the laser soliton is constant). For both heterodyne curves, there is a single peak. This is a clear indication that, in each case, the laser soliton is emitting on a single frequency, but these two frequencies are different. When the current is continuously increased, the beat note remains unique but it undergoes to consecutive sudden jumps of equal frequency intervals. The frequency jumps is around 460 MHz and it corresponds to the free spectral range of the compound cavity.

This measurement is completed by recording the intensity of the signal resulting from the interference of a single-peak soliton lasers with a reference beam extracted from the single-peak soliton under consideration. The reference beam is obtained by enlarging the output beam propagating in one arm of the interferometer and

selecting a region of few micron around the center of the single-peak laser structure. In this way the whole structure interferes with its central part, resulting in the phase profiles shown in Fig. 9.8, left panel. The interferometric signal of the single-peak laser soliton is obtained by integrating its phase profile on the full size of the structure. Since the length difference between the interferometer arms is about $\Delta L = |L1 - L2| \sim 5$cm, the phase difference between the two beams oscillating at ν_n at the end of interferometer is given by: $\Delta\phi_n = k_n \Delta L$ where k_n is the wavevector and ΔL the length difference between the interferometer's arms. The variation of the phase difference associated to a frequency jump of the single-peak laser soliton to the neighbor compound cavity mode is therefore given by:

$$\Delta\phi_{n+1} - \Delta\phi_n = \pi \frac{\Delta L}{L_c}$$

As a result, if the emission frequency of the laser soliton changes, the interferometric intensity detected will also change. To avoid aliasing, the previous equation shows that $\frac{\Delta L}{L_c}$ has to be sufficiently smaller than 1, which is the case here since the compound cavity length is about $L_c \sim 32.5$cm. In these conditions, the sequential mode switching, undetectable by looking at the simple laser soliton emission intensity, will be detected by the variation of the interference intensity at the output of the interferometer. Fig. 9.8, right panel shows the evolution of the interferometric intensity as a function of I_{L1}. When the pumping current is increased upward, the interferometric intensity evolves continuously (due to a continuous frequency shift with the current) until $I_{L1} = 256.2$ mA when the interferometric intensity changes abruptly. This sudden jump is accompanied by a jump of a 460 MHz in the power spectrum recording the heterodyne beat signal, confirming that the laser soliton emission frequency has changed. When the current is decreased, the interferometric intensity does not go back to its initial value for identical I_{L1} value. The emission frequency of the laser soliton is therefore multistable.

We underline that the frequency multistability of a single-hump localized state discussed above constitutes an additional degree of complexity which was not visible on the intensity measurements shown in figure 9.5.

9.5 Conclusions and Perspectives

Until recently, research on the formation of localized structures in semiconductors devices (cavity solitons) has been confined to "optically injected" schemes. In such systems the injected electromagnetic field fixes the phase and the frequency of both cavity solitons and the coexisting homogeneous solution. Cavity solitons existence has been demonstrated and several properties of these structures have been studied. The results of these experiments have been used to propose different devices for all-optical data processing. In spite of these successes, the implementation of cavity solitons in non-prototypical devices is difficult for the extreme sensitivity of cavity solitons stability to the parameters of the injected field. A possible path to avoid this

difficulty is based on the concept of CSL, a device capable of generating localized laser structures without need of an injected field. In this contribution, we show that a CSL can be implemented by using two coupled VCSELs forming a compound system which, under certain conditions, is equivalent to a broad-area laser with saturable absorber. We demonstrate that complex laser structures can form in a CSL. The analysis of their bifurcation diagram reveals multistability between single and double peaks states and between double-peaks and ring-like states. We also show that the organization of these states in parameter space is modified when the system parameters are changed. Starting from local measurements, we extend the monitored area towards the inclusion of the whole transverse section and we show that a high degree of multistability can be observed. We analyze the laser structures coherence properties and we show that double humps structures are equivalent to coherent localized patterns while distant independent single structures are mutually incoherent. We finally perform a frequency analysis and we observe that the laser solitons emission frequency is multistable, a peculiar feature of the system under consideration. Even if the cavity soliton laser in its present form seems difficult to implement in a practical device, we prove that a compound cavity scheme is a reliable system for laser soliton generation. A very recent progress has shown that a monolithic version of laser with saturable absorber can be implemented in a single broad-area VCSEL structure [33]. Another source of interest of the present implementation is related to the frequency multistability associated to the existence of several longitudinal modes of the compound cavity. As a consequence, localized laser structures operating simultaneously on multiple frequencies might be accessible in this experimental scheme and could lead to fully localized states of light or Cavity Light Bullets.

Acknowledgements This work was supported by the STREP Project FunFACS (www.funfacs.org). We would like to thank G. Tissoni, W. Firth, L. Columbo and L. Gil for useful discussions.

References

1. R. Neubecker et al., Phys. Rev. A, 52, 791 (1995)
2. S. Barland et al., Nature, 419, 699 (2002)
3. Yu. A. Astrov et al., Phys. Rev. Lett. 79, 2983 (1997)
4. B. Schäpers et al., Phys. Rev. Lett. 85, 748 (2000)
5. R. Richter et al., Phys. Rev. Lett. 94, 184503 (2005)
6. N. Akhmediev et al., Lecture Notes in Physics, Springer Berlin / Heidelberg (2005)
7. N.N. Rosanov, Spatial Hysteresis and Optical Patterns, Springer-Verlag Berlin / Heidelberg (2002)
8. W. J. Firth and A.J. Scroggie, Phys. Rev. Lett., 76, 1623 (1996)
9. U. Bortolozzo and S. Residori, Phys. Rev. Lett., 96, 037801 (2006)
10. F. Pedaci et al., Appl. Phys. Lett. 89, 221111 (2006)
11. F. Pedaci et al., Appl. Phys. Lett. 92, 011101 (2008)
12. F. Pedaci et al., Appl. Phys. Lett. 93, 111104 (2008)
13. X. Hachair at al., Phys. Rev. A, 043817 (2004)
14. X. Hachair et al., Phys. Rev. A 72, 13815 (2005)
15. E. Knobloch Nonlinearity 21, T45 (2008)

16. P. Coullet, C. Riera, and C. Tresser, Phys. Rev. Lett. 84, 3069 (2000)
17. M. G. Clerc , and C. Falcon, Physica A 356, 48 (2005)
18. J. Burke and E. Knobloch, Phys. Rev. E 73, 056211 (2006)
19. X. Hachair et al., Phys. Rev. A72, 013815 (2005)
20. W. J. Firth et al., Phys. Rev. Lett. 99, 104503 (2007)
21. J. H. P. Dawes, SIAM Journal on Applied Dynamical Systems 7, 186 (2008)
22. U. Bortolozzo, M. G. Clerc and S. Residori, Phys. Rev. E 78, 036214 (2008)
23. S. Barbay et al., Phys. Rev. Lett. 101, 253902 (2008)
24. P. Genevet et al., Phys. Rev. Lett. 101, 123905 (2008)
25. N.N. Rosanov and S.V. Fedorov, Opt. Spectrosc. 72, 782 (1992)
26. M. Bache et al., Appl. Phys. B 81, 913 (2005)
27. A.G. Vladimirov et al., Journal of Optics B: Quantum and Semiclassical Optics 1, 101 (1999)
28. P. Genevet et al., Phys. Rev. A 79, 033819 (2009)
29. L. Lugiato, IEEE J. Quantum Electron, 39, 193 (2003)
30. M. aghdami et al., The European Physical Journal D 47, 447 (2008)
31. A. G. Vladimirov, G. V. Khodova, and N. N. Rosanov, Phys. Rev. E 63, 056607 (2001)
32. W.J.Firth, L. Columbo, and T. Maggipinto, Chaos 17, 037115 (2007)
33. T. Elsass, K. Gauthron, G. Beaudoin, I. Sagnes, R. Kuszelewicz and S. Barbay. Appl. Phys. B, 2009, doi:10.1007/s00340-009-3748-9

Chapter 10
Cavity soliton laser based on a VCSEL with saturable absorber

Giovanna Tissoni, Keivan M. Aghdami, Franco Prati, Massimo Brambilla and Luigi A. Lugiato

Abstract In this Chapter we intend to make a review on our work on cavity solitons in semiconductor lasers with saturable absorbers, with a special attention to the most recent results. We study theoretically a broad-area vertical cavity surface emitting laser (VCSEL) with a saturable absorber, and show numerically the existence of cavity solitons in the system: they exist as solitary structures superposed on a background with zero intensity. Therefore, this system can work as a cavity soliton laser, ensuring maximum contrast and compactness of the device, in comparison with other systems supporting cavity solitons. In particular, in absence of a holding beam, these solitons do not rely on a proper phase of the addressing pulses to be either created or deleted. We also show that the properties of the system are deeply influenced by the radiative recombination of carriers. Taking into account this process, the existence of solitons is shown numerically for a choice of parameters suitable to describe real devices, where the same material is used for the active and the passive parts. Furthermore, we compare three different switching techniques for the control of cavity solitons in a VCSEL based cavity soliton laser, one incoherent and the other two semicoherent with different injection frequencies. We show that the

Giovanna Tissoni
CNISM and INFM–CNR, Dipartimento di Fisica e Matematica, Università dell'Insubria, Como, Italy e-mail: giovanna.tissoni@uninsubria.it

Franco Prati
CNISM and INFM–CNR, Dipartimento di Fisica e Matematica, Università dell'Insubria, Como, Italy e-mail: franco.prati@uninsubria.it

Luigi A. Lugiato
CNISM and INFM–CNR, Dipartimento di Fisica e Matematica, Università dell'Insubria, Como, Italy e-mail: luigi.lugiato@uninsubria.it

Keivan M. Aghdami
Physics Department, Payame Noor University, Mini City, 19569 Tehran, Iran

Massino Brambilla
INFM–CNR, Dipartimento di Fisica Interateneo, Politecnico di Bari, Italy e-mail: m.brambilla@poliba.it

O. Descalzi et al. (eds.), *Localized States in Physics: Solitons and Patterns*,
DOI 10.1007/978-3-642-16549-8_10,

switching dynamics and energies can be very different depending on the type of injection. Finally, we show that in a cavity soliton laser based on a VCSEL with a saturable absorber the solitons can spontaneously move if the ratio of the carrier lifetimes in the amplifier and in the absorber takes appropriate values. The direction of the motion is arbitrary, while its velocity is determined by the parameters of the system. In devices with a finite cross section the CS describes different trajectories depending on the shape of the boundary of the pumped region. For a circular pump the CS moves on circular trajectories along the boundary. This dynamical regime can be exploited to create controllable trains of pulses, together with frequency and amplitude modulation.

10.1 Introduction

Cavity Solitons (CSs) are intensity peaks of the coherent field emitted by optical resonators, generated through nonlinear light–matter interaction which leads to self-localization within the cavity. CSs occur in broad area optical devices, under conditions where a patterned state of radiation coexists with a stable homogeneous background of low intensity. The resulting profile thus shows a number of bright circular spots embedded in a darker background [1].

A favorable condition for the generation of CSs is the coexistence of two branches for the homogeneous stationary solution of the device, with the lower branch stable and the upper one affected by a pattern forming instability. The CSs form as portions of the pattern emerging from the upper branch, sitting on the homogeneous lower branch. Such a condition can be realized in a VCSEL with injected signal with the VCSEL operating above transparency but below threshold [2, 3, 4, 5], or above threshold [6].

Another configuration that can produce CSs is the VCSEL with saturable absorber. It is well known that the presence of the saturable absorber makes the laser bifurcation subcritical, and the lasing solution coexists with the non-lasing one in a certain range of pump values. Hence, in this case the contrast between the CSs and the background is maximum, because the background consists of pure spontaneous emission. This system works as a Cavity Soliton Laser (CSL), in the sense that it emits only CSs, whose number and position can be controlled. With respect to the standard configuration of semiconductor devices used up to now to generate CSs, a further advantage of the CSL is the absence of a holding beam injected from outside, which makes the device more compact and easy to realize.

The formation of localized structures (or autosolitons) in lasers with saturable absorber was the object of investigations in the past. In most cases, the study was limited to the case of inertialess medium (class-A lasers) [7, 8, 9], but more recently it was extended to class-B lasers [10, 11]. When more localized structures are stable and can be switch on and off independently of one another they are also called Cavity Solitons (CS). The first theoretical prediction of the existence of CSs in a VCSEL with saturable absorber has been given in [12, 13].

In the framework of the FunFACS project [14] three different schemes of CSL were experimentally investigated. In one case, a CSL with frequency–selective feedback has been realized [15, 16], in the other case the system consists in two coupled VCSELs, one of which acting as a saturable absorber [17]. In the third case, a miniaturized device has been realized by means of a monolithic VCSEL with an intracavity saturable absorber [18].

In this paper we address the problem of how a CS can be switched on and off in a VCSEL–based CSL, comparing different injection techniques, in the monolithic scheme. The question is not trivial because, with respect to driven systems, where the driving field provides a reference phase, in a CSL such reference phase is absent. Hence, the usual coherent technique, consisting in injecting a localized beam in phase with the driving field to create a CS, and in opposition of phase to delete it, is not applicable, and optical switching in a CSL is necessarily incoherent.

Incoherent switching was reported also in a system with a holding beam such as the driven VCSEL below threshold. In [19] the injected beam is orthogonally polarized with respect to the holding beam. In [20] the injected beam is oscillating at a frequency which lies inside the pump window of the system. In this case the beam produces a change in the pump profile creating a local excess of carriers which in turn modifies the profile of the electric field.

In the case of a CSL based on a VCSEL with a saturable absorber, it was demonstrated numerically in [12, 13] that a CS can be switched on and off using a coherent beam oscillating at the frequency of the empty cavity longitudinal mode closest to the gain maximum, *i.e.* slightly detuned with respect to the CS. The control injection parameters are the amplitude and/or duration of the pulse, while its phase does not play any role.

Here we consider three different injection techniques. When we speak of incoherent injection, it means that we consider an optically pumped device, and inject an incoherent pulse which incoherently sums to the pump field as in [20]. If the injected field is coherent and almost resonant to the laser field, we say that injection is semicoherent, because in the switching process we do not make use of any particular phase relationship. In this case we consider two possibilities: the injected field oscillates at the cavity frequency, as in [12] and [13], or it oscillates at the CS frequency.

In the CSL based on the VCSEL with frequency–selective feedback [15, 16], the control of the CS is realized both with an injected beam orthogonally polarized with respect to the laser field as in [19], and with an injected beam polarized as the laser field, as in [12] and [13]. In the monolithic scheme [18], the injection has been made at the pump frequency.

In driven systems it is known that a CS can be set in motion by applying an appropriate intensity or phase gradient [21]. Spontaneous motion of a CS has also been reported due to thermal effects [22, 23, 24]. Here we consider another mechanism which can induce the motion of a CS in a CSL. The mechanism is an instability of the stationary CS which occurs for proper values of the ratio r of the carrier lifetimes in the two sections of a CSL based on a VCSEL with a saturable absorber. In

a range of value of r the equilibrium between light and matter breaks, and the CS is forced to move.

The phenomenon has been already predicted in class-B lasers with a saturable absorber [11]. Our model, however, is more appropriate for semiconductor devices, because it incorporates features typical of semiconductors such as the alpha factors of both materials, carrier radiative recombination [25, 13] which were neglected in [11].

This Chapter is structured as follows: in Section 10.2 we present the rate equation model describing a VCSEL with saturable absorber, we study the bistability condition and the instabilities, both dynamical and pattern-forming. In Section 10.3 we present the three different switching techniques and compare the switching dynamics and switching energy, while in Section 10.4 we study the CS stability, describing the dynamical instability giving rise to spontaneous CS motion. In Sections 10.5 we consider CS motion in a finite device and its applications. Finally, Section 10.6 is devoted to conclusions.

10.2 The model

We consider a rate-equation model for the intracavity field and the carrier populations in the two media [12, 13]:

$$\dot{F} = [(1-i\alpha)D + (1-i\beta)d - 1 + i\nabla_{\perp}^2]F\,, \tag{10.1}$$

$$\dot{D} = b_1[\mu - D(1+|F|^2) - B_1 D^2]\,, \tag{10.2}$$

$$\dot{d} = b_2[-\gamma - d(1+s|F|^2) - B_2 d^2]\,. \tag{10.3}$$

F is the slowly varying amplitude of the electric field, D and d are population variables related to the carrier densities in the active and passive material, respectively. In this model we take into account the effects of radiative recombination of carriers in both media through the quadratic decay terms $-B_1D^2$ and $-B_2d^2$, representing spontaneous emission due to band-to band recombination processes involving one electron and one hole. The parameters α and b_1 (β and b_2) are the linewidth enhancement factor and the ratio of the photon lifetime to the carrier lifetime in the active (passive) material, μ is the pump parameter of the active material and γ measures absorption in the passive material, s is the saturation parameter. Time is scaled to the photon lifetime, and space to the diffraction length. Typically a time unit is ~ 4 ps and a space unit $\sim 4\ \mu$m.

For more details on the definition of these parameters see [12].

In the following we will always assume $B_1 = B_2 = B$ and $s = 1$. This choice allows to simplify the analysis of the homogeneous stationary solution (HSS) and it is the most reasonable one when the active and the passive part of the device are made with the same material.

An estimation of the magnitude of the parameter B can be made considering that $B \sim B_{sp} N_0 \tau_{nr}$, where B_{sp} is the spontaneous emission coefficient, N_0 is the

transparency density and τ_{nr} is the nonradiative decay rate. Assuming $B_{sp} \sim 10^{-10}$ cm^3/s [26], $N_0 \sim 10^{18}$ cm^{-3}, and $\tau_{nr} \sim 10^{-9}$ s, we obtain $B \sim 10^{-1}$.

If $B_1 = B_2 = B$ and $s = 1$ the trivial HSS of Eqs. (10.1–10.3) reads

$$F_0 = 0, \quad D_0 = \frac{\sqrt{1+4B\mu}-1}{2B}, \quad d_0 = \frac{\sqrt{1-4B\gamma}-1}{2B}. \tag{10.4}$$

while the nontrivial HSS is

$$F_s = \sqrt{I_s}\mathrm{e}^{-i\omega t}, \tag{10.5}$$

$$D_s = \frac{\sqrt{(1+I_s)^2+4B\mu}-1-I_s}{2B}, \tag{10.6}$$

$$d_s = \frac{\sqrt{(1+I_s)^2-4B\gamma}-1-I_s}{2B}, \tag{10.7}$$

where the stationary intensity I_s is given implicitly by the equation

$$D_s + d_s = 1, \tag{10.8}$$

and the laser frequency is

$$\omega = \alpha D_s + \beta d_s. \tag{10.9}$$

10.2.1 Bistability

From Eq. (10.8) one can obtain an explicit expression for the pump parameter μ as a function of the stationary intensity I_s. With an exchange of the axes it is then possible to draw a plot of I_s as a function of μ. The shape of the curve depends on the parameters γ and B. Under certain conditions the laser bifurcation is subcritical and there is bistability between the non trivial and the trivial HSS over a finite range of μ.

To study the nature of the laser bifurcation we observe that in the limit $I_s \ll 1$ of laser very close to threshold Eq. (10.8) can be written as

$$\mu \approx \mu_{thr} + aI_s, \tag{10.10}$$

where

$$\mu_{thr} = (1+B)\left(1+\frac{1-\sqrt{1-4B\gamma}}{B}\right)-\gamma, \tag{10.11}$$

$$a = \frac{(1+B-\sqrt{1-4B\gamma})^2 - B(1+B)}{B\sqrt{1-4B\gamma}}. \tag{10.12}$$

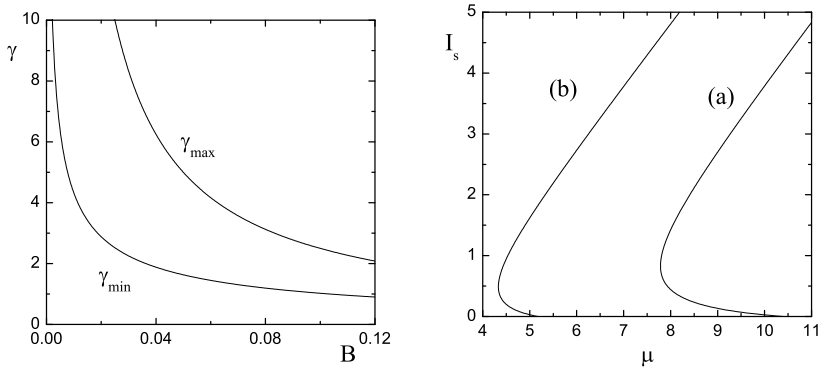

Fig. 10.1 Left: Plots of γ_{min} and γ_{max} as functions of B. For a given B, the nontrivial HSS and the trivial one coexist if γ lies between the two curves. Right: Stationary intensity as a function of the pump parameter μ for (a) $B = 0.04$, $\gamma = 5$, and (b) $B = 0.1$, $\gamma = 2$.

μ_{thr} is the laser threshold, which reduces to $\mu_{thr} = 1 + \gamma$ if $B = 0$ [12]. The sign of a determines whether the laser bifurcation is supercritical or subcritical. The bifurcation is subcritical if $a < 0$, which is equivalent to the condition $\gamma > \gamma_{min}$, with

$$\gamma_{min} = \frac{1}{2}\sqrt{\frac{(1+B)^3}{B}} - \frac{B}{2} - \frac{3}{4}, \tag{10.13}$$

Eqs. (10.4), (10.11) and (10.12) show that there is also an upper limit for the parameter γ. In fact, the presence in those equations of the term $\sqrt{1-4B\gamma}$ implies that it must be $\gamma < \gamma_{max}$, with

$$\gamma_{max} = \frac{1}{4B}. \tag{10.14}$$

These results are in sharp contrast with those obtained neglecting quadratic recombination. In [12] it was shown that in order to have bistability it must be $s > 1$ and $\gamma > (s-1)^{-1}$. The inclusion of the quadratic recombination terms allows to relax the condition $s > 1$, but introduces an upper limit for γ.

In the left panel of Fig. 10.1 we plotted γ_{max} and γ_{min} as a function of B. In this paper we considered the the two values $B = 0.04$ and $B = 0.1$. The corresponding intervals of γ for which the stationary solution is bistable are $1.88 < \gamma < 6.25$ for $B = 0.04$, and $1.02 < \gamma < 2.50$ for $B = 0.1$. In order to have a relatively large domain of coexistence of the trivial and nontrivial HSS, for our numerical simulations we have chosen values of γ rather close to the upper limits, *i.e.* $\gamma = 5$ for $B = 0.04$, and $\gamma = 2$ for $B = 0.1$. The corresponding stationary curves are shown in the right panel of Fig. 10.1. Notice that although B is quite small, the laser thresholds differ considerably from the value $\mu_{thr} = 1 + \gamma$ associated with $B = 0$.

10.2.2 Plane wave instabilities

A first check of the stability of the HSS can be performed neglecting any spatial dependence of the perturbations. In this way one immediately shows that: i) the trivial HSS is stable up to $\mu = \mu_{\text{thr}}$, and ii) the negative slope branch of the nontrivial HSS (if it exists) is always unstable.

In addition, a Hopf bifurcation can affect the nontrivial HSS. unstable. This instability has been studied in the past in connection with the phenomenon of Q-switching [27] .

The extension of the instability domain depends crucially on the ratio $r = b_2/b_1$ of the two population decay rates as shown in the left panel of Fig. 10.2. In [12], where $B = 0$, it was demonstrated that the Hopf instability disappears if the ratio is lower than the critical value

$$r_c = \frac{\sqrt{s-1}+\sqrt{\gamma}}{\sqrt{\gamma}s}. \tag{10.15}$$

The bistability condition $\gamma > (s-1)^{-1}$ implied that the critical value was always smaller than 1. As commented above, the situation is different when $B \neq 0$. In that case it is possible to have bistability even with $s = 1$, and in that limit Eq. (10.15) shows that the critical ratio is equal to 1. Moreover, the term B introduces some further positive corrections, and we can write approximately

$$\left(\frac{b_2}{b_1}\right)_c \approx 1 + \frac{3}{2}\left(\frac{B}{\gamma}\right)^{1/3} + \frac{1}{8}\left(\frac{B}{\gamma}\right)^{2/3} + \frac{53}{96}\left(\frac{B}{\gamma}\right). \tag{10.16}$$

The inclusion of quadratic recombination then allowed us to set in our simulations $b_1 = b_2 = b$ without introducing any unwanted plane wave Hopf instability. This choice is consistent with that of $B_1 = B_2 = B$ and $s = 1$ introduced before.

10.2.3 Pattern forming instabilities

The next step consists in checking the stability of the nontrivial HSS with respect to spatially modulated perturbations of the form $\exp(i\mathbf{q}\cdot\mathbf{x})$, where $\mathbf{q}$ is the transverse wavevector and $\mathbf{x}$ the transverse vector.

Numerical simulations show that, at least for the range of parameters considered here, a dynamical instability (imaginary part of the eigenvalue different from zero) with $q \neq 0$ exists only if the system is unstable also with respect to the plane wave $q = 0$. Hence, the condition $b_1 = b_2 = b$ excludes also the existence of dynamical pattern forming instabilities.

The situation is different when one considers the static instability associated with a real eigenvalue. In that case it turns out that the nontrivial HSS is unstable with respect to any transverse wavevector q such that $0 < q < q_{max}$, with

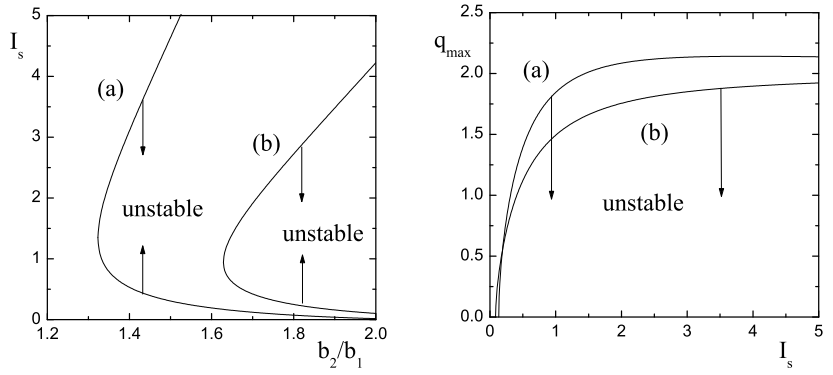

Fig. 10.2 Left: This plot shows how the interval of stationary intensity for which the nontrivial HSS is Hopf unstable varies with the ratio $r = b_2/b_1$ for $b_1 = 0.003$ and (a) $B = 0.04$, $\gamma = 5$, or (b) $B = 0.1$, $\gamma = 2$. The instability disappears for (a) $b_2/b_1 < 1.323$ and (b) $b_2/b_1 < 1.629$. Right: Plots of the pattern forming instability boundary q_{max} as a function of the stationary intensity I_s for $\alpha = 2$, $\beta = 1$, and (a) $B = 0.04$, $\gamma = 5$ or (b) $B = 0.1$, $\gamma = 2$. A comparison with the right panel of Fig. 10.1 shows that the whole upper branch of the stationary curve is unstable in both cases.

$$q_{max}^2 = 2I_s \frac{(\alpha D_s + \beta d_s)(1 + I_s) + 2BD_s d_s(\alpha + \beta)}{(1 + I_s + 2BD_s)(1 + I_s + 2Bd_s)}. \tag{10.17}$$

The instability exists if the right hand side of the equation is positive, and this happens for any I_s larger than a certain value $I_{s,min}$. If the HSS is bistable, it is important to compare $I_{s,min}$ with the intensity $I_{s,TP}$ of the turning point of the stationary curve. As in [12], we found that if $\alpha \geq \beta$ the whole upper branch is unstable. This is confirmed by the right panel of Fig. 10.2, where one must consider that $I_{s,TP} = 0.83$ in case (a) and $I_{s,TP} = 0.49$ in case (b) (see the right panel of Fig. 10.1).

10.3 CS switching techniques

The dynamical equations are integrated using a split–step method with periodic boundary conditions and a 128×128 spatial grid. Typical values of the space and time step were, respectively, 0.25 and 0.01. The effects of spontaneous emission noise were simulated adding to Eq. (10.1) stochastic terms of the form $\sqrt{\beta_{sp}}\,\xi(x,y,t)$ where, for each grid point of coordinate x and y, the functions $\xi(x,y,t)$ are independent Gaussian white noise sources with zero mean and unit variance.

In this Section we consider the set of parameters $s = 1$, $\gamma = 2$, $\alpha = 2$, $\beta = 1$, $b_1 = b_2 = 0.003$, $B = 0.1$. The noise level is $\beta_{sp} = 10^{-10}$ everywhere.

For these parameters stable CS exist in an interval of μ between approximately 4.6 and 5.1, as shown in Fig. 10.3 [13]. While the CS can be switched on relatively

easy over the whole interval, we found that it is easier to switch them off for the smaller values of μ. For that reason here we focus on the case $\mu = 4.6$, indicated by a circle in Fig. 10.3.

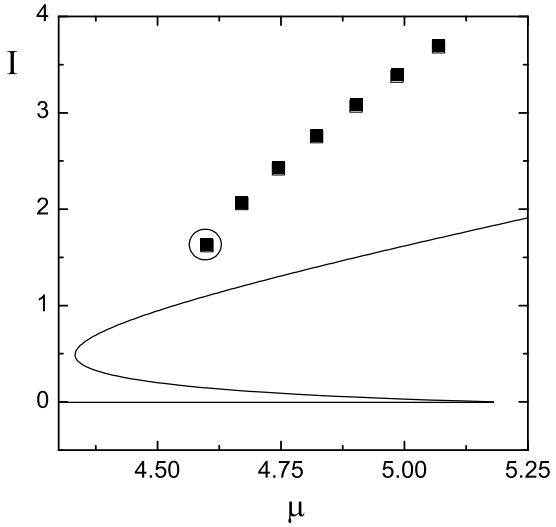

Fig. 10.3 Intensity of the homogenous stationary solution (solid line) and of the CS peaks (squares) as a function of the pump parameter μ. In the interval where CS are stable, they coexist with the trivial homogeneous solution. The non trivial homogeneous solution is unstable everywhere. Parameters are: $r = 1$, $b_1 = 0.003$, $s = 1$, $\gamma = 2$, $B = 0.1$, $\alpha = 2$, $\beta = 1$.

The three injection techniques differ mainly because of the frequency of the injected beam [28], as illustrated in Fig. 10.4. Incoherent injection means that we inject in the laser an incoherent beam oscillating at a frequency ω_p which is much larger than the frequency of laser field. The effect of the injection is to modify locally the pump profile. From the numerical point of view this means that we superimpose to the homogenous pump μ a Gaussian pulse of the form

$$\mu_{inj}(x,y) = \mu_0 e^{\left[-(x-x_0)^2-(y-y_0)^2\right]/w^2}, \tag{10.18}$$

during the injection time t_{inj}.

In semi-coherent injection it is convenient to take the frequency of the injected field ω_{inj} as reference frequency. Hence, a detuning parameter δ defined as $\delta = \omega_{inj} - \omega_c$ appears in Eq. (10.1)

$$\dot{F} = [(1-i\alpha)D + (1-i\beta)d - 1 + i\delta + i\nabla_\perp^2]F, \tag{10.19}$$

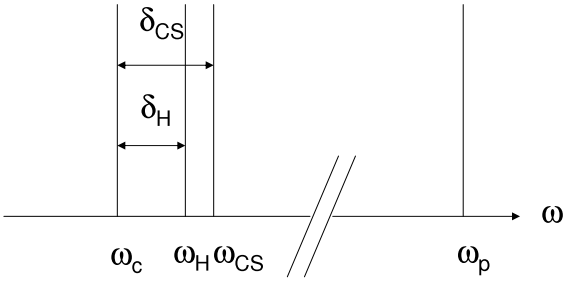

Fig. 10.4 Scheme of the relevant frequencies: cavity frequency ω_c, frequency of the homogeneous solution ω_H, CS frequency ω_{CS}, pump frequency ω_p. The frequency of the injected field is ω_p for incoherent injection, ω_c for semi–coherent injection at the cavity frequency, and ω_{CS} for the semi-coherent injection at the CS frequency.

and injection is simulated in the usual way adding in this equation the term

$$F_{inj}(x,y) = F_0 e^{i\phi_0} e^{\left[-(x-x_0)^2-(y-y_0)^2\right]/(2w^2)}, \tag{10.20}$$

during the injection time t_{inj}. For injection at the cavity frequency $\delta = 0$. For injection at the CS frequency $\delta = \delta_{CS} = \omega_{CS} - \omega_c$. The frequency ω_{CS} of the CS can be determined only numerically. For our choice of the parameters and $\mu = 4.6$ we have $\delta_{CS} \sim 3.91$. Notice that the CS frequency is larger than the frequency of the homogeneous solution, which is $\omega_H = 3$. This fact can be understood considering that the CS frequency is determined by the locking of the various transverse modes that form the CS, and each of them has a frequency larger than the longitudinal mode.

10.3.1 Switching dynamics

The behavior of the dynamical variables during a switching process depends on the type of injection, and it is very different for incoherent and semicoherent injection. With incoherent injection we create locally an excess of carriers in the active material, which means that we act on the variable D. Only after a certain delay this excess of carriers will produce a pulse, or a series of pulses, in the electric field. With semicoherent injection we act directly on the electric field F, inducing variations in

the spatial profile of the population variables which, in turn, affect the subsequent evolution of the electric field.

We describe the dynamics associated with the creation and the deletion of a CS following the behavior of the field intensity I and of the two population variables D and d at the injection point (x_0, y_0). Switching occurs between an off state (the trivial homogeneous solution) and an on state (the CS). For our choice of the parameters the values of the dynamical variables are $I_H = 0$, $D_H = 3.43$, and $d_H = -2.76$ in the off state, and $I_{CS} = 1.66$, $D_{CS} = 1.65$, and $d_{CS} = -0.79$ in the on state. The CS produces a large variation not only in the field intensity but also in the distribution of carriers in the two materials. Hence, the dominant timescales in the switching process are those of the slow dynamical variables D and d.

10.3.1.1 Incoherent injection

An example of creation and deletion of a CS with incoherent injection is shown in Fig. 10.5 a) and b). The injection parameters are indicated in the caption. We used the same amplitude μ_0 and injection time t_{inj}. Yet, for reasons that will become clear in the following, for this type of injection it turned out that a CS can be created only if the beam width w is larger than a given value w_{cre} and deleted only if it is smaller than w_{del}. The values of w_{cre} and w_{del} depend on the other parameters but, in general, we found that $w_{cre} > w_{del}$; hence, it is not possible to use the same beam width for the two processes. In this particular case we used $w = 2$ for creation and $w = 1.2$ for deletion.

During the creation process with incoherent injection we obtain the apparently paradoxical result of creating a hole in D by injecting carriers in the active material. Actually, what happens is very similar to a Q–switching (or gain–switching) process as shown in Fig. 10.5(a). Before injection the system is in the off state. During the initial stage of the injection D grows almost linearly, well above its value at the laser threshold, which is $D_{thr} = 3.76$, I remains very small, and d is fixed at the initial value d_H. Only after a delay of about 40 time units the intensity starts growing in a significant way, and very quickly a large pulse is emitted (notice the logarithmic scale for the intensity I). The pulse causes a strong saturation of the two population variables. At the end of the pulse, D and d have reached values which are not far from the final ones, D_{CS} and d_{CS}. In the following free evolution the system approaches the CS state through damped oscillations of the three dynamical variables.

Deletion of a CS by means of incoherent injection, illustrated in Fig. 10.5(b), is quite intuitive. In this case the main effect of the local injection of carriers is filling the hole produced by the CS in the carrier distribution. An intensity pulse is created anyway, as in the creation process, but it is much less intense. After the end of injection the intensity falls down rapidly to the noise level, while the population variables approach monotonically the off state. In the deletion process the beam width must not exceed a critical value w_{del} because, if the width is too large, not only the hole is filled, but gain is also provided to the region around the CS, thus

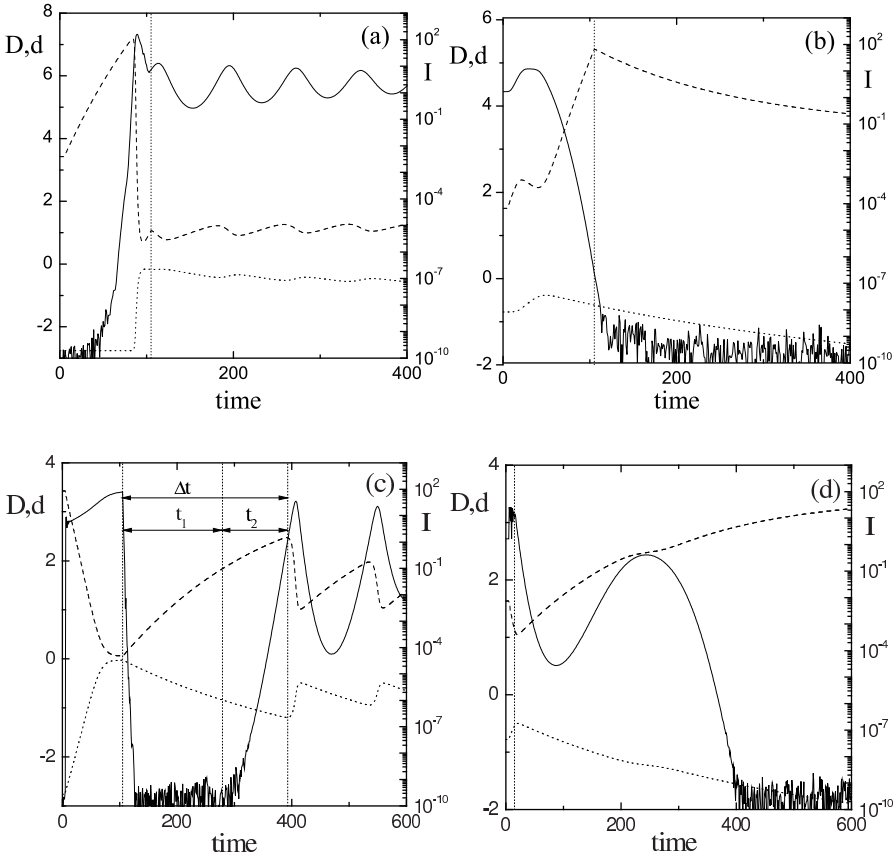

Fig. 10.5 Time evolution of the electric field (solid line), and of active (dashed line) and passive (dotted line) carrier populations during the switching processes. a) and b): Creating and deleting a CS by incoherent injection. In both figures the injection amplitude is $\mu_0 = 20$ and the injection time is $t_{inj} = 100$, and injection starts at $t = 5$. The width of the injected pulse is $w = 2$ for creation (a), and $w = 1.2$ for deletion (b). The vertical dotted lines indicate the end of injection. c) and d): Creating and deleting a CS by semicoherent injection at the cavity frequency. In both cases the injection amplitude is $F_0 = 10$ and the beam width is $w = 2$, and injection starts at $t = 5$. The injection time is $t_{inj} = 100$ for creation (c), and $t_{inj} = 10$ for deletion (d). The vertical dotted lines indicate the end of injection. In (a) the time intervals Δt, t_1 and t_2 are also shown. Their meaning is discussed in the text.

initiating a new creation process. The threshold value w_{del} depends on the other injection parameters, but it is always slightly smaller than the $1/e$ radius of the hole made by the CS in the spatial profile of D which, for the chosen parameters, is about 1.55.

10.3.1.2 Injection at the cavity frequency

The switching dynamics for injection at the cavity frequency is shown in Fig. 10.5 c) and d). In contrast with incoherent injection, we could use the same field amplitude F_0 and beam width w for both creation and deletion, only the injection time t_{inj} is different, because it must be shorter for deletion.

The creation process, illustrated in Fig. 10.5(c) shows many differences with respect to incoherent injection. The intensity I starts to grow immediately, and correspondingly D decreases and d increases. At the end of the injection the field intensity falls down suddenly to the noise level, and the population variables reach values close to zero, which means that both materials are almost completely bleached.

Then a long rebuilding time Δt follows during which the population variables slowly evolve towards the stationary values D_H and d_H which correspond to the off state. In a first stage, of duration t_1, the intensity displays random oscillations around a mean value which is on the order of the noise level β_{sp}. After this stage the intensity starts to grow in an exponential way and, in a time t_2, a new pulse is created in correspondence to the injection point. The growth of the pulse interrupts the evolution of the dynamical variables towards the off state and, after that, the CS state is reached through damped oscillations.

In the deletion process, shown in Fig. 10.5(d), the dynamics at the beginning is not much different from that of the creation process. But in this case the beam is injected for a shorter time. Consequently, the value reached by the field intensity at the end of injection is smaller and the population variables D and d remain sufficiently far from zero. The field intensity can fall down to the noise level or not, as in the case illustrated in the figure. In any case, in the subsequent evolution the rebuilding time is shorter, but when the CS tries to form again, it fails because the population variables have already reached values sufficiently close to those of the off state when the second pulse is generated. For this reason the second pulse remains small and after that the intensity decays to zero forever. A similar behavior was observed in the CSL based on a VCSEL with frequency–selective feedback [15].

The presence of a rather long rebuilding time during creation and of a frustrated revival of the CS during deletion suggest that injection at the cavity frequency is less efficient than incoherent injection, because it requires longer switching times. But when one tries to create and delete several times a CS in the same position with the two different techniques, one finds that the maximum repetition rate is of the same order (about 100 MHz) for both types of injection. The reason is that while the field intensity dynamics is faster for incoherent injection, the population dynamics occur always at the same timescale, and this is what determines the upper limit for the repetition rate. For instance, in the deletion process with incoherent injection

shown in Fig. 10.5(d), if one looks only at the field intensity I it seems that the CS is already off a few tens of time units after the end of injection. Yet, the CS cannot be considered to be completely off until also the population variables D and d reach values close to the off state, and this takes some hundreds time units. Under this respect there are no relevant differences between incoherent injection and injection at the cavity frequency.

10.3.1.3 Injection at the CS frequency

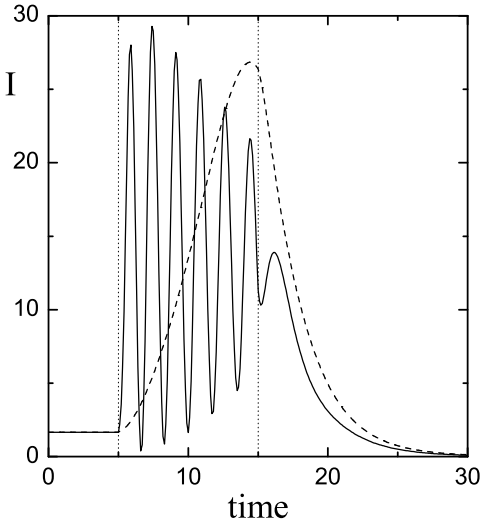

Fig. 10.6 Time evolution of the field intensity during the initial part of the deletion process of a CS for injection at the cavity frequency (solid line) and at the CS frequency (dashed line). All the parameters are the same as in Fig. 10.5(d), except for the amplitude of the injected field for injection at the CS frequency, which is $F_0 = 0.38$. The two vertical dotted lines indicate the period of injection.

The laser dynamics associated with the creation and deletion of a CS when the injected field oscillates at the same frequency as the CS does not differ substantially from that observed with injection at the cavity frequency, in the sense that a long rebuilding time in the creation process and a frustrated revival in the deletion process are present also in this case.

The only relevant difference can be observed in the deletion process, during the injection time. In Fig. 10.6 we compare the intensity dynamics in the initial stage

of the deletion process for injection at the cavity frequency (solid line) and at the CS frequency (dashed line). As for the solid line, this figure is just an enlargement of Fig. 10.5(d) in linear scale. The enlargement allows to appreciate the presence of oscillations in the intensity during the injection time. These oscillations occur at a frequency close to δ_{CS}, indicating that they are due to the beating between the injected field which oscillates at the cavity frequency, and the laser field which oscillates at the CS frequency. When the two fields are frequency matched the oscillations disappear and the deletion process is much more efficient: with the same injection time, a field amplitude $F_0 = 0.38$ instead of $F_0 = 10$ is enough to delete the CS.

10.3.2 Switching energy

In the previous Section we have shown some typical examples of creation and deletion of a CS with some fixed values of the injection parameters. But our numerical simulations showed that a CS can be created and deleted over a large range of values of those parameters. Typically, we fixed the beam width w and then, for different values of the pulse amplitude μ_0 or F_0, we found the minimum and maximum injection time t_{inj} for which a CS can be created and deleted.

The results can be expressed in terms of injection energy, which can be defined as $E_{inj} = \mu_0\, t_{inj}$ for incoherent injection and as $E_{inj} = |F_0|^2\, t_{inj}$ for semicoherent injection. Since we are using scaled variables and parameters, those expression do not allow to get immediately the values of the switching energy in physical units. It is also difficult to compare the switching energy for incoherent and semicoherent injection, because the beam intensity is scaled differently in μ_0 and in $|F_0|^2$. Yet, the comparison is possible for the two kinds of semicoherent injection, which is what we do in this Section.

10.3.2.1 Injection at the cavity frequency

The minimum and maximum injection energy for creating and deleting a CS with this kind of switching are plotted in Fig. 10.7 a) and b). The injection energy necessary to create a CS is typically one order of magnitude larger than to delete it. The behavior of the switching energy as a function of the injected amplitude is similar in the two cases. The minimum and maximum energies approach constant values for large injection amplitude F_0, and the minimum injection energy for deletion in that limit becomes very small. In the opposite limit of F_0 the switching energy increases. A possible explanation is that for small F_0 the injection time increases up to values comparable to the carrier lifetime, and this modifies the interaction between the injected beam and the materials.

In the creation process, if the injection time is too short the system simply returns to the off state after the end of injection; if the injection time is too long we

observe what we call "dancing solitons". This is a dynamical state characterized by the presence of a few intensity peaks (usually two), which remain confined in a small area around the injection point and oscillate or rotate in a seemingly regular way. Sometimes, after a long transient time, whose duration depends on the noise level, they merge and form a single CS, but usually their motion continues for all the time we can reasonably follow it. In the deletion process, if the injection time is too

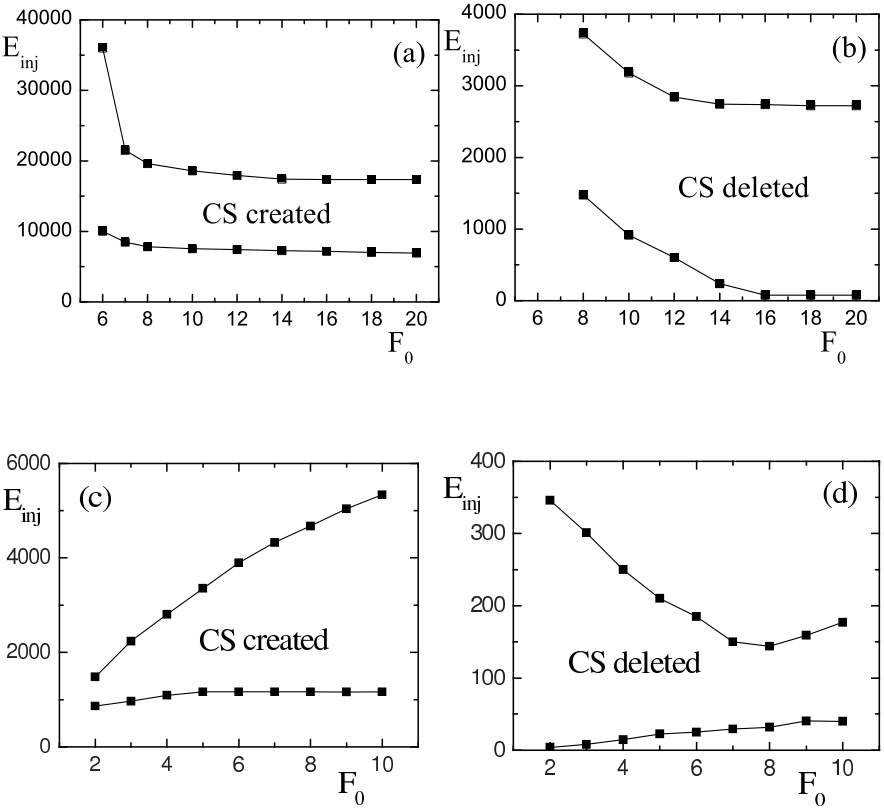

Fig. 10.7 a) and b): Dependence on the injection amplitude F_0 of the minimum and maximum switching energy for creation (a) and deletion (b) of a CS with injection at the cavity frequency. The width of the injected beam is $w = 2$. c) and d): Dependence on the injection amplitude F_0 of the minimum and maximum switching energy for creation (c) and deletion (d) of a CS with injection at the CS frequency . The width of the injected beam is $w = 2$.

short the CS is only partially depleted but after injection it recovers through damped oscillations; if the injection time is too long the intensity after injection falls down

to the noise level as in Fig. 10.5(d), but then the second pulse grows higher and the subsequent evolution is similar to that of Fig. 10.5(c).

10.3.2.2 Injection at the CS frequency

Fig. 10.7 c) and d) show the minimum and maximum injection energy when the injected field is resonant with the CS. A comparison of this figure with Fig. 10.7 a) and b) shows that the injection energy can be much smaller with injection at the CS frequency than with injection at the cavity frequency. This result is due to the fact that smaller values of both the injection amplitude F_0 and of the injection time t_{inj} can be used.

Another relevant difference concerns the behavior of the switching energies as functions of F_0, in particular for the creation process, where we found an asymptotic value for large values of F_0 only for the minimum energy, and both energies, unlike in Fig. 10.7 c) and d), decrease for small F_0. It must be noted that also in this case the switching time increases as the injected amplitude decreases. The increase, however, is slower than the decrease of the intensity F_0^2. A similar behavior was observed in the CSL based on a VCSEL with frequency–selective feedback [15].

The deletion of a CS by injection at the CS frequency is the only process among those studied in this paper, where the phase of the injected beam can play a role. Since the CS and the injected beam oscillate both at the same frequency, their relative phase can influence the deletion process. However, it must be kept in mind that the phase of the CS varies radially as well as its intensity. Since in the injected beam the phase is spatially independent, the relative phase changes from point to point, and what we define as relative phase is actually the relative phase at the CS peak.

The numerical simulations showed a weak dependence of the minimum and maximum energies on this relative phase. What we plotted in Fig. 10.7(d) are the worst results (maximum value of the minimum energy and minimum value of the maximum energy). The boundaries shown in that figure are then those between which the CS can be successfully deleted without any phase control.

The value of the relative phase for which the interval of successful switching energy has its maximum extension is zero. At first glance, this may appear strange, because one can imagine that it is easier to delete a CS by making it to interfere with a beam in opposition of phase. But this is not the case. It must be taken into account that the deletion process is mediated by the two population variables D and d and the action of the deleting beam on them is more efficient when it interferes constructively with the CS.

10.4 Stability of the CS

We study the stability of the CS in the framework of the model equations (10.1)−(10.3).

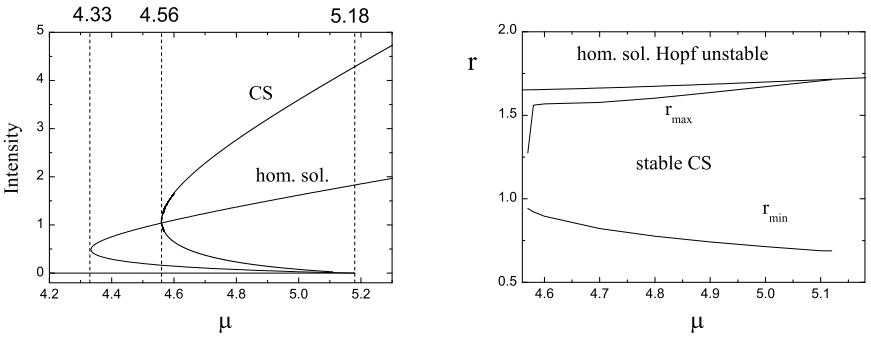

Fig. 10.8 Left: Homogeneous stationary solution and cavity soliton (CS) solution as a function of the pump parameter μ for $s = 1$, $r = 1$, $b_1 = 0.01$, $\gamma = 2$, $B = 0.1$, $\alpha = 2$ and $\beta = 1$. In the case of the CS solution we plot the peak intensity of the soliton. Right: Stability diagram of the stationary CS in the plane of the parameters μ (pump) and r (ratio of carrier lifetimes in the active and in the passive medium). The stationary CS is stable in the region between the two curves r_{min} and r_{max}. Other parameters are as in the left panel.

In this section, the parameters $s = 1$, $\gamma = 2$, $\alpha = 2$, $\beta = 1$, $b_1 = 0.01$, $B = 0.1$ are kept fixed. We use as free parameters the pump μ and the ratio $r = b_2/b_1$ of the carrier lifetime in the active and in the passive medium.

In the left panel of Fig. 10.8 we show the intensity of the homogeneous (plane-wave) and CS solutions as a function of the pump μ, the latter obtained using a standard Newton-Raphson method. The negative slope branches of both solutions are unstable. The non–lasing solution is stable up to the laser threshold, which is $\mu_{th} = 5.18$. The lasing homogeneous solution is everywhere modulationally unstable, because $\alpha > \beta$ [12]. Stable CS may exist in the interval $4.56 < \mu < 5.18$ where the upper branch coexist with the stable non–lasing solution. However, their stability depends strongly on the parameter r. It was found that a necessary condition for the CS to be stable for a given μ is that, for the same μ, the lasing homogeneous solution is stable against a Hopf instability [12]. With our choice of the parameters this means that it must be $r \leq 1.6 - 1.7$.

For smaller values of r, we found that the CS are stable in the interval $r_{min} < r < r_{max}$, as shown in the right panel of Fig. 10.8.

The linear stability analysis of the stationary CS always predicts the existence of three zero eigenvalues, one associated with the phase invariance of the electric field, the other two with the translational invariance along the two transverse directions x and y. In the stability domain $r_{min} < r < r_{max}$ the real part of all the other eigenvalues is negative.

If we cross the boundary $r = r_{max}$ from below, we observe that the real part of a pair of complex conjugates eigenvalues crosses zero. The associated eigenvectors are cylindrically symmetric. As a result, the CS oscillates in amplitude keeping its position in space. The frequency of the oscillations is determined by the imaginary

part of the eigenvalues and the amplitude of the oscillations increases in time. After a transient which can last more than 100 ns the CS dies and the laser jumps to the non-lasing solution.

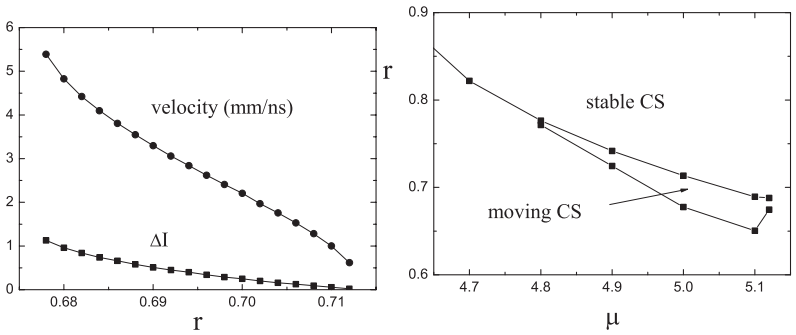

Fig. 10.9 Left: Velocity of the moving CS and difference between the peak intensity of the stationary and of the moving CS as a function of the bifurcation parameter r. $\mu = 5$. Right: Stability domain of the moving CS in the plane of the parameters μ and r.

If, instead, we cross the boundary $r = r_{min}$ from above, a pair of degenerate real eigenvalues changes its sign from negative to positive. To be precise, the two eigenvalues are real everywhere but in a very small interval around r_{min}, where they become complex conjugates. The threshold r_{min} is the value of r at which the real part of the complex eigenvalues crosses zero. The shapes of the associated eigenvectors [29] are very similar to those of the Goldstone modes. These modes, also called neutral modes, are associated to the two null eigenvalues of the translational invariance of the system, and are proportional to the spatial derivatives of the CS profile. They corresponds to the generators of translations, thus their excitation produces a motion of the CS. The mechanism responsible for the motion of the CS is then similar to that of thermal induced motion [24]. The velocity is fixed by the parameters of the system. In two dimensions the direction of motion is completely arbitrary and it is determined only by noise.

As we depart from the instability threshold r_{min} the velocity of the CS increases and its amplitude decreases, as shown in the left panel of Fig. 10.9. For even smaller values of r a further threshold is crossed and after that the moving CS is no longer stable. Depending on the value of μ, the system can either precipitate to the non-lasing solution or develop a turbulent behavior, typical of the region $\mu > \mu_{th}$. The stability domain of the moving CS is shown in the right panel of Fig. 10.9. For numerical convenience the boundaries of the stability domain have been calculated keeping μ fixed and varying r. In a real experiment the opposite must be done. Provided r has a value inside the interval $0.65 < r < 0.75$, the range of pump values μ for which the moving CS exists is quite extended. For such a value of r, it should suffice to decrease μ to observe the transition from the stationary CS to the moving CS.

10.5 Motion of the CS in a finite device

The above analysis have been performed assuming complete translational invariance. A real device, however, has a finite cross section, and it is important to establish how the motion of the CS is influenced by the presence of boundaries. In our equations this ingredient can be introduced in an easy way by assigning a tophat profile to the pump μ. If the tophat is sufficiently sharp the moving CS are reflected when they hit the boundary, and at regime they move along closed orbits. The shape of the orbits depend on the shape of the boundaries. We have considered here a circular pump profile.

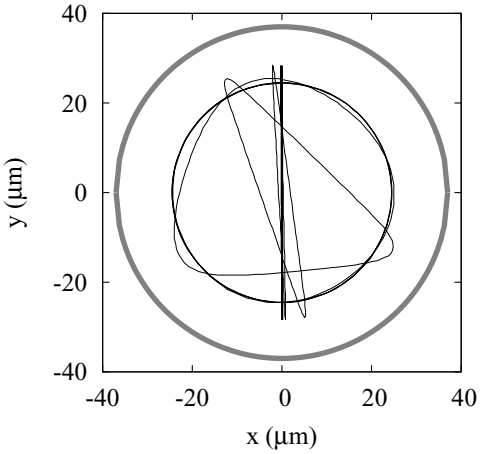

Fig. 10.10 Trajectory of the moving CS in presence of a circular pump. The CS is initially positioned at the center of the square and then it is set in motion in the vertical direction. The thick grey line denotes the pump profile (inside the circle $\mu = 5$, outside $\mu = 0$). Here $r = 0.68$.

10.5.1 Circular pump

In Fig. 10.10 we show the motion of a CS in a device with a circular pump profile. A stationary CS is first switched on at the center, for r = 0.75. Then, the parameter r is reduced to 0.68, in such a way that the CS is forced to move. The direction of motion is usually determined by the noise, but we can control it by shining an address beam in the proximity of the CS. Here we have forced the CS to move in the vertical direction. Fig. 10.10 shows that initially the CS moves along the diameter bouncing at the boundaries. Yet very soon the trajectory departs from the vertical direction because of noise and, after a sequence of bounces, it ends up in a circular

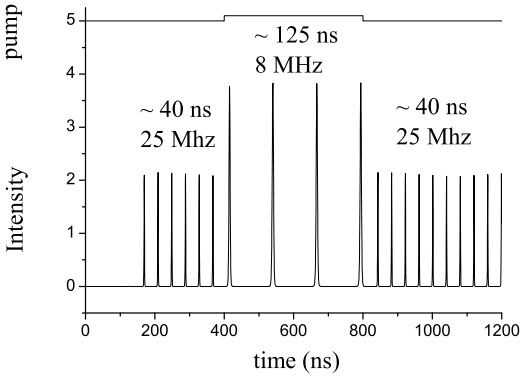

Fig. 10.11 Amplitude and Frequency Modulation of the signal produced by a CS moving along the boundary of a circular pump. Both the amplitude and the frequency of the signal are modulated by a modulation of the pump μ. Here $r = 0.68$.

orbit adjacent to the boundary. The motion can be clockwise or counterclockwise, depending on the noise processes triggering the deflection at the first bounces.

We have devised several application of this new dynamical regime. The first and more intuitive is to put a detector in one point of the trajectory which reveals the periodic motion of the CS. In this way we can realize a train of pulses, whose amplitude and frequency can be adjusted by varying some parameter of the laser, typically the pump μ. In Fig. 10.11 we show how, with a stepwise modulation of μ from 5.0 to 5.1 we can modulate the signal both in amplitude and in frequency.

Our numerical simulations also show that it is possible to pin the moving CS in a given position, stop it for a while, and then release it along the desired direction. In order to do that it is enough to shine on the moving CS a modulated control beam. In our simulations the beam was switched on and off periodically every 4 ns. The control beam acts in this way. When it is on, it attracts the CS exerting a force on it. This causes the CS to reverse the direction of its motion. If we then switch off the control beam, the CS moves along the opposite direction with respect to the initial one. If we switch on again the control beam, the CS is forced to revert again the direction of its motion, and so on. The final direction depends on the number of pulses in the control beam sequence. If the number of pulses is odd, the CS changes its direction, if it is even, the CS continues along the initial direction. Varying the number of pulses we can also stop the CS at the pinning position for the desired time.

10.6 Conclusions

In the first part of this paper we have shown that the inclusion of the quadratic decay terms associated with radiative recombination of carriers in the equations of a broad area VCSEL with saturable absorber has relevant effects on the properties of the CSs, although the coefficient B of these terms is relatively small.

First, CSs exist and are stable even if the saturation intensity and the linear decay rates of carriers are the same in the amplifier and in the absorber, *i.e.* $s = 1$ and $b_1 = b_2$. This contrasts with the results of a previous work [12] where radiative recombination was neglected, and in order to find a sufficiently wide stability range for the CSs the values $s = 10$ and $b_1 = 2b_2$ were considered. The last assumption in particular was probably difficult to obtain experimentally, because it meant that the population dynamics is faster in the amplifier than in the absorber. Instead, the conditions $s = 1$ and $b_1 = b_2$ (that is, r = 1) apply well to devices constituted by the same material in the active and in the passive part (even if some caution must be taken, because the saturation parameter s is defined as $s = a_2/a_1 r$ [12], where a_2 and a_1 are the differential gain in the passive and active medium, which are in principle different, being usually $a_2 > a_1$).

With respect to [12], the introduction of the quadratic recombination of carriers also allowed to decrease by one order of magnitude the ratio of the photon lifetime to the carrier lifetime, which passed from $\sim 10^{-2}$ to $\sim 10^{-3}$, and to increase the linewidth enhancement factor β in the absorber from $\beta = 0$ to the more realistic value $\beta \geq 1$.

We have studied three different kinds of injection techniques for the control of a CS in a CSL: incoherent injection, injection at the cavity frequency and injection at the CS frequency.

We have analyzed the switching dynamics and compared the different behaviors observed for each injection technique. In spite of the relevant differences, we have found that the switching times are comparable for the three injection techniques, since they are determined essentially by the decay rates of the population variables.

With respect to previous studies of incoherent injection in a CSL [15, 16] and in systems with a holding beam [19, 20], we found switching times sensibly shorter, on the order of 1 ns instead of tens/hundreds of ns. In the case of the CSL with frequency–selective feedback [15, 16] the velocity of the process was limited by the length of the external cavity. In optically pumped driven systems [19, 20, 30], the long time scales were attributed to thermal effects. Very recent experimental work in a monolithic CSL shows fast incoherent CS switching [18], showing a good agreement with our numerical analysis.

A bonus of incoherent injection with respect to semicoherent injection is represented by the absence, in the former, of a secondary pulse after the end of injection when the CS is deleted. Because of this secondary pulse, the injection parameters in semicoherent deletion must be chosen accurately, otherwise the pulse can grow too high and the CS forms again. This problem does not exist in incoherent deletion. This is probably the reason why it is possible to delete incoherently a CS almost in

their whole branch of stability, while semicoherent deletion is successful only in the vicinity of the left extremum of the branch (a small interval around $\mu = 4.6$).

In terms of switching energy, we have shown that injection at the CS frequency allows to reduce by a factor of ten the injection energy with respect to injection at the cavity frequency. Yet, its experimental realization is probably not easy, because it requires the a priori knowledge of the CS frequency. However, when a CS is already present, it can be realized by reinjecting part of the output beam inside the cavity to create a new CS or to delete an existing one.

Furthermore, we have shown that in a CSL scheme based on a VCSEL with a saturable absorber there are parametric conditions for which the CS can exist only if it moves in the transverse plane, with a velocity which is fixed by the parameters of the system. The velocity is of the order of some μm/ns. Interesting effects arise when the pump profile is not homogeneous and the translational symmetry of the system is broken. If the pump has a circular profile, the CS moves along the boundary.

A similar circular motion was predicted also for a CS in a semiconductor resonator (passive or amplifier) with optical injection [31]. Two different mechanisms were considered there. If the injected beam is a doughnut mode the CS moves along the intensity maximum of the doughnut driven by its linear phase gradient (2π in a roundtrip around the center). Alternatively, the spontaneous thermal motion [22, 23, 24] can be guided along a circular trajectory by using a ring shaped injected beam, whose intensity gradient is able to confine the spontaneous CS motion to a circle. In the case of injected doughnut the velocity was comparable with that found here, in the thermal case the CS was about one hundred times slower.

As an application of such circular motion we have shown here that the periodic motion in the transverse plane can be transformed in a periodic motion in time, by simply putting a detector in one point along the trajectory. In this way the CSL works as a source of pulses whose amplitude and frequency can be easily controlled varying one system parameter (typically the injected current μ). A delay between the pulses can also be introduced with a suitable sequence of control pulses.

Other applications of spontaneous CS motion can be envisaged: for example, it can be interesting to exploit the spontaneous motion of CS in applications like those already demonstrated in semiconductor amplifiers, such as the delay line [32], the Soliton Force Microscope [33] or the Soliton Tap [34, 35]. In this case, there is no need of external gradients (which would also be difficult to impose to the system in absence of a holding beam) to make the solitons move, making the device more compact and simpler.

In particular, we intend to study the interactions between self-propelled CS and device defects, that could be modelled in this case as local inhomogeneities in the pump profile of the amplifier medium.

Acknowledgements This work was done in the framework of the FET OPEN Project Nr. 4868 FunFACS (Fundamentals, Functionalities and Applications of Cavity Solitons).

References

1. L.A. Lugiato, IEEE, J. Quant. El. **39**, 193 (2003), and references therein.
2. S. Barland, J.R. Tredicce, M. Brambilla, L.A. Lugiato, S. Balle, M. Giudici, T. Maggipinto, L. Spinelli, G. Tissoni, T. Knödl, M. Miller, and R. Jäger, Nature (London) **419**, 699 (2002).
3. X. Hachair, S. Barland, L. Furfaro, M. Giudici, S. Balle, J.R. Tredicce, M. Brambilla, T. Maggipinto, I. Perrini, G. Tissoni, L. A. Lugiato, Phys. Rev. A **69**, 043817 (2004).
4. Y. Menesguen, S. Barbay, X. Hachair, L. Leroy, I. Sagnes, and R. Kuszelewicz, Phys. Rev. A **74**, 023818 (2006)
5. S. Barbay, X. Hachair, T. Elsass, I. Sagnes, and R. Kuszelewicz, Phys. Rev. Lett. **101**, 253902 (2008).
6. X. Hachair, F. Pedaci, E. Caboche, S. Barland, M. Giudici, J.R. Tredicce, F. Prati, G. Tissoni, R. Kheradmand, L.A. Lugiato, I. Protsenko, and M. Brambilla, IEEE J. Sel. Top. Quantum Electron. **12**, 339 (2006).
7. N.N. Rozanov and S.V. Fedorov, Opt. Spectrosc. **72**, 782 (1992).
8. V.B. Taranenko, K. Staliunas, and C.O. Weiss, Phys. Rev. A **56**, 1582 (1997).
9. A.G. Vladimirov, S.V. Fedorov, N.A. Kaliteevski, G.V. Khodova, and N.N. Rosanov, J. Opt. B: Quantum Semiclass. Opt. **1**, 101 (1999).
10. S.V. Fedorov, A.G. Vladimirov, G.V. Khodova, and N.N. Rosanov, Phys. Rev. E **61**, 5814 (2000).
11. S.V. Fedorov, N.N. Rozanov, and N.A. Shatsev, Opt. Spectrosc. **102**, 449 (2007).
12. M. Bache, F. Prati, G. Tissoni, R. Kheradmand, L.A. Lugiato, I. Protsenko, and M. Brambilla, Appl. Phys. B **81**, 913 (2005).
13. F. Prati, P. Caccia, G. Tissoni, L.A. Lugiato, K.M. Aghdami, and H.Tajalli, Appl. Phys. B **88**, 405 (2007).
14. European FET Opern Project FunFACS (Fundamental, Functionalities and Applications of Cavity Solitons).
15. Y. Tanguy, T. Ackemann, and R. Jäger, Opt. Expr. **15**, 16773–16780 (2007).
16. Y. Tanguy, T. Ackemann, W.J. Firth, and R. Jäger, Phys. Rev. Lett. **100**, 013907 (2008).
17. P. Genevet, S. Barland, M. Giudici, and J. R. Tredicce, Phys. Rev. Lett. **101**, 123905 (2008)
18. T. Elsass, K. Gauthron, G. Beaudoin, I. Sagnes, R. Kuszelewicz and S. Barbay, Appl. Phys. B **98**, 327331 (2009) doi:10.1007/s00340-009-3748-9.
19. V.B. Taranenko and C.O. Weiss, Appl. Phys. B **72**, 893–895 (2001).
20. S. Barbay, Y. Menesguen, X. Hachair, L. Leroy, I. Sagnes, and R. Kuszelewicz, Opt. Lett. **31**, 1504–1506 (2006).
21. L. Spinelli, G. Tissoni, M. Brambilla, F. Prati, and L. A. Lugiato, Phys. Rev. A **58**, 2542 (1998).
22. L. Spinelli, G. Tissoni, M. Brambilla, and L.A. Lugiato, Phys. Rev. A **66**, 023817 (2002).
23. G. Tissoni, L. Spinelli, L.A. Lugiato, M. Brambilla, I.M. Perrini, T. Maggipinto, Optics Express, **10**, 1009-1017 (2002).
24. A.J. Scroggie, J.M. McSloy, and W.J. Firth, Phys. Rev. E **66**, 036607 (2002).
25. E.A. Ultanir, G.I. Stegeman, D. Michaelis, C.H. Lange, and F. Lederer, Phys. Rev. Lett. **90**, 253903 (2003).
26. H.C. Casey, Jr., J. Appl. Phys. **47**, 631–643 (1976).
27. T. Erneux, J. Opt. Soc. Am. B **5**, 1063 (1988).
28. K. M. Aghdami, F. Prati, P. Caccia, G. Tissoni, L.A. Lugiato, R. Kheradmand, and H. Tajalli, Eur. Phys. J. D **47**, 447455 (2008).
29. F. Prati, G. Tissoni, L.A. Lugiato, K. M. Aghdami, and M. Brambilla, "Spontaneously moving solitons in a cavity soliton laser with circular section", Eur. Phys. J. D, Special Issue on Dissipative Optical Solitons, accepted (2010).
30. S. Barbay and R. Kuszelewicz, Opt. Express **15**, 12457-12463 (2007).
31. R. Kheradmand, L.A. Lugiato, G. Tissoni, M. Brambilla, H. Tajalli, Optics Express, **11**, 3612-3621 (2003).

32. F. Pedaci, S. Barland, E. Caboche, P. Genevet, M. Giudici, J. R. Tredicce, T. Ackemann, A. J. Scroggie, W. J. Firth, G.-L. Oppo, G. Tissoni, and R. Jger, Appl. Phys. Lett. **92**, 011101 (2008).
33. F. Pedaci, G. Tissoni, S. Barland, M. Giudici and J. Tredicce, Appl. Phys. Lett. **93**, 111104 (2008).
34. E. Caboche, F. Pedaci, P. Genevet, S. Barland, M. Giudici, J. R. Tredicce, G. Tissoni, and L.A. Lugiato, Physical Review Letters **102**, 163901 (2009).
35. E. Caboche, S. Barland, M. Giudici, J. Tredicce, G. Tissoni, and L. A. Lugiato, Phys. Rev. A **80**, 053814 (2009).

Chapter 11
Dynamic Control of Localized Structures in a Nonlinear Feedback Experiment

Mousa Ayoub, Björn Gütlich, Cornelia Denz, Francesco Papoff, Gian-Luca Oppo, and William J. Firth

Abstract Spatial dissipative solitons exhibit a robust form as well as complex dynamic behaviour that make them attractive for applications in the context of all–optical information processing. In this chapter we give an overview of recent experimental and theoretical results on the features of spatial dissipative solitons in a single feedback experiment using a liquid crystal light valve (LCLV) as a model nonlinear medium. In particular, we present techniques for the control of the symmetry and spatial position of localized states in LCLV based experiments. We first discuss the interaction of dissipative solitons with spatially imposed boundary constraints in the feedback loop. This interaction leads to symmetry-breaking phenomena of feedback dissipative solitons. We also present static and dynamic techniques to experimentally control and guide dissipative solitons on modified background by using externally adapted intensity distributions.

Mousa Ayoub
Institut für Angewandte Physik and Center for Nonlinear Science, Westfälische Wilhelms-Universität Münster, Corrensstr. 2/4, 48149 Münster, Germany, e-mail: Ayoubm@uni-muenster.de

Björn Gütlich
Institut für Angewandte Physik and Center for Nonlinear Science, Westfälische Wilhelms-Universität Münster, Corrensstr. 2/4, 48149 Münster, Germany

Cornelia Denz
Institut für Angewandte Physik and Center for Nonlinear Science, Westfälische Wilhelms-Universität Münster, Corrensstr. 2/4, 48149 Münster, Germany, e-mail: denz@uni-muenster.de

Francesco Papoff
SUPA, Department of Physics, University of Strathclyde, 107 Rottenrow, Glasgow, G4 0NG, Scotland, U.K. e-mail: papoff@phys.strath.ac.uk

Gian-Luca Oppo
SUPA, Department of Physics, University of Strathclyde, 107 Rottenrow, Glasgow, G4 0NG, Scotland, U.K. e-mail: gianluca@phys.strath.ac.uk

William Firth
SUPA, Department of Physics, University of Strathclyde, 107 Rottenrow, Glasgow, G4 0NG, Scotland, U.K. e-mail: willie@phys.strath.ac.uk

O. Descalzi et al. (eds.), *Localized States in Physics: Solitons and Patterns*,
DOI 10.1007/978-3-642-16549-8_11,

11.1 Introduction

In the last twenty five years, pattern formation in both conservative and dissipative systems, has been one of the favorite subjects in the field of nonlinear optics. The interaction of light with a nonlinear medium gives rise to the spontaneous emergence of spatial structures as a consequence of an optical instability. Among these, nonlinear localized structures have achieved special attention due to their potential use in information processing.

Due to the wide variety of systems that support the formation of spatial structures, this chapter concentrates on systems that are under constant non equilibrium external conditions. In these systems we talk of *dissipative structures* which may have a macroscopic form in steady state [1, 2], and thus be simultaneously observable and controllable.

Historically, starting from the work of Prigogine in 1977 who introduced the term *dissipative structures*, the interest in this kind of structures has grown continuously due to their model character for high dimensional nonlinear physical phenomena as well as for their application potential. Classical examples of dissipative structures are *Bénard cells* where a pattern of regular hexagonal cells appears on the surface of a liquid, spirals in *Belousov-Zhabotinskii reactions, Taylor vortices, cyclones, hurricanes, and lasers* [3].

In optics, a number of organization processes in time, space or both in time and space, has been reported to lead to the formation of dissipative structures. For example, bistable optical systems show dissipative spatial patterns in the switching behaviour between the lower and the upper branch of the hysteresis curve [4]. Symmetry-breaking instabilities may also lead to the spontaneous formation of dissipative patterns [5, 8], and may arise from the co-operative interaction between light dispersion and diffraction in a nonlinear optical cavity [6, 7, 9].

One of the most interesting structures that may form within nonlinear systems and especially in nonlinear optics are *dissipative solitons*. They are typically stable spatial solitary structures, and differ in nature from conservative solitons [10]. In contrast to conservative systems, dissipative solitons are dynamic objects that experience energy gain and loss during formation and propagation. In this way, they form far away from equilibrium when the overall gain and loss are balanced [10]. In optics, this kind of structures has been found, for example, in semiconductor micro resonators VCSEL [11, 12, 13], photorefractive media [14, 15], a sodium vapor system [16, 17], and liquid crystal light valves [18, 19, 20, 21, 22]. In all these cases, the nonlinearity of the system causes self-focusing of the propagating wave. This nonlinear process balances the broadening that waves experience during propagation due to diffraction. This balance, combined with that of gain and loss, allows the wave to maintain for long times a robust localized shape in space.

For promising applications of dissipative solitons in information processing, such as sensors or probes, the control of these structures and their spatiotemporal complex dynamics becomes even more important. The realization of control schemes for the addressing and selection of a certain target state, is therefore a requirement. The main scope of this chapter is the realization and demonstration of a multitude

of control methods, which allow to statically and dynamically control the absolute positions of these structures. By using an open loop invasive control method where a predefined temporal and/or spatial control signal is imposed onto the nonlinear system, robust position traps and complete addressing of dissipative structures are realized. Furthermore, we study the interaction of dissipative structures with spatial boundaries and their drift motions due to artificially imposed gradients.

11.2 Self-organized localized structures in feedback systems

As mentioned above, the formation of dissipative structures is combined with an organized behaviour such as an optical bistability. This bistable behaviour can provide an all-optical tool to switch the system between two steady states, for example a dark and a bright state, thus swichting the structures on and off. In combination with their robust form as a result of the balance between gain, loss, nonlinearity and diffraction (or dispersion), dissipative solitons can be attractive for applications in the field of all-optical information processing if solitary structures are used as '**optical bits**' [23].

The formation mechanism of dissipative solitons out of a homogeneous background has been understood thoroughly in the last decade. Based on the so-called *modulation instability*, that in simple words is known to break up a wave into small entities or a pulse into short subpulses above a certain threshold, the spatial or temporal intensity profile of a homogeneous or plane wave becomes unstable, and the space-time distribution splits into distinct domains that can be correlated on a long range (pattern) or on a short range (localized structures). Transverse spatial structures are observed in the plane perpendicular to the propagation of the optical wave. From the experimental point of view, patterns emerging in systems in which the optical properties depend on the input light intensity can be achieved using several experimental arrangements. Typical optical setups for pattern formation are shown in Fig. 11.1. In the following, we will focus on experiments implementing the single feedback operation of Fig. 11.1b and capable to support the formation of dissipative solitons. The feedback mechanism causes a nonlinear interaction of the initially perturbed light field so that a modulation instability arises and spatial structures are observed in the output of the light field. Because of the nonlinear interaction and diffraction, the initial wave-front irregularities are either amplified or damped, leading to the formation (or suppression) of patterns in the intensity distribution.

It is possible to understand better the formation of transverse spatial structures in a feedback configuration using a simplified scheme suggested originally by W.J. Firth and G. D'Alessandro [8]. Such a single feedback configuration considers one of the simplest optical nonlinearities i.e. the *Kerr nonlinearity*

$$n = n_1 + n_2 I, \tag{11.1}$$

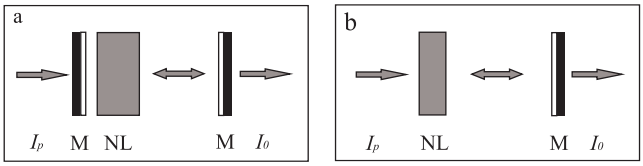

Fig. 11.1 Schematic illustration of different feedback systems that exhibit spontaneous formation of optical structures; a: cavity; b: single feedback scheme. NL: nonlinear medium; M:mirror; I_p: pump intensity; I_o: intensity output.

where the refractive index of the medium n_2 depends linearly on the intensity of the light field. A plane feedback mirror is placed at a distance L after the medium to generate a counterpropagating beam in the Kerr medium neglecting absorption. A spatially extended planar electromagnetic wave E_{in} propagates through the nonlinear medium. According to the refractive index of the nonlinear medium, the optical wave is modulated in its phase. For simplicity, a sinusoidal modulation of the index of refraction is considered in the nonlinear medium: $n = n_1 + \Delta n \cos(k.r)$.

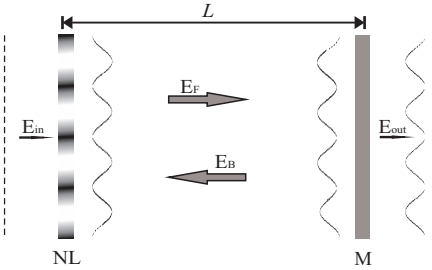

Fig. 11.2 A single feedback scheme suggested by Firth and D'Alessandro in [8]. NL: nonlinear medium, M: mirror, E_{in}: the input field, E_{out}: the output field, E_F: phase modulated field, E_B: the backward field modulated in phase and amplitude.

During the propagation over the distance L to the mirror and back, the modulated beam experiences diffraction. The travelling beam can be easily described by the paraxial wave equation in the slowly varying envelope (SVE) approximation:

$$\frac{1}{c}\frac{\partial}{\partial t}E + (\Delta_\perp^2 E - 2ik_\lambda \frac{\partial}{\partial z}E) = 0, \tag{11.2}$$

where $\Delta_\perp^2 = \partial_x^2 + \partial_y^2$ is the transverse Laplacian and k_λ denotes the wave number of the optical field. Taking into account that the response time of the nonlinear optical media is long compared to the travelling time of the light inside the optical feedback system, the term $\frac{1}{c}\partial_t E$ can be neglected. For the integration over the distance L

$$E_B = \mathscr{D}(E_F) = \exp\left(\frac{-iL}{2k_\lambda}\Delta_\perp^2\right)E_F, \tag{11.3}$$

the transverse Laplacian of the propagation operator $\mathscr{D}$ acts on the modulated wave E_F and converts the phase modulation into an amplitude modulation of the backward field E_B, which in turn can change the refraction index of the medium (see figure 11.2), thereby closing the feedback process [8]. This diffraction process is closely connected to the *Talbot effect* in which the phase modulation is converted into an identical amplitude profile if the light wave propagates freely over a certain distance L_T. For example, a maximum phase modulation at $L_T = 0$ is transformed spatially into a maximal (pure) amplitude modulation at a distance $L_T/4$, but is transversely shifted by π, while the phase modulation becomes zero at this position. Further increasing the propagation distance to $3L_T/4$ results in the transformation of the initial phase distribution into a pure amplitude modulation of the optical field. The Talbot effect allows for a propagation-induced self-mapping between the initial modulation to the intensity modulation at a characteristic distance.

The forward and backward modulated fields superimpose in the nonlinear medium, and the refraction index is then modulated according to the intensity distribution of the resulting field. The refractive index modulation will grow if the gain compensates the losses inside the loop. This gain is proportional to the obtained intensity I and above a certain threshold intensity, the gain dominates. For $(I > I_{th})$ a macroscopic spatial modulation of n will arise with a wavelength Λ and a wave number $k = 2\pi/\Lambda$.

To determine the threshold and the parameter conditions of the spatio-temporal evolution related to the modulation instability quantitatively, a linear stability analysis can be employed for our system. Starting from the uniform stationary solutions of the system $\partial_t \Phi^u = \Delta_\perp^2 \Phi^u = 0$, where Φ^u obeys $\partial_t \Phi = F(r, \Phi, t)$ with F is the nonlinear function of Φ and r are a set of system parameters. A small perturbation such as e. g. a stochastic weak modulation, is then applied in a typical approach of perturbation theory. The resulting system variable $\tilde{\Phi}$ is approximated with a linearized Taylor expansion:

$$\tilde{\Phi} = \Phi^u + \xi \Phi^p, \tag{11.4}$$

where $\xi \Phi^p$ is a small perturbation.

To determine which perturbation will grow in the strongest way we need to solve the following differential equation:

$$\xi \frac{\partial}{\partial t} \Phi = \left. \frac{\partial F}{\partial \Phi} \right|_{\Phi^u} \xi \Phi^p = \mathscr{L}(r) \xi \Phi^p, \tag{11.5}$$

where $\mathscr{L}(r)$ represents the eigenvalues of the differential equation. The generalized solution is given by

$$\Phi^p \propto \exp(\mathscr{L}(r)), \tag{11.6}$$

which can be written as:

$$\exp(\mathscr{L}(r)) = \exp(\lambda(t)) \exp(iwt). \tag{11.7}$$

Here, λ is the growth rate of the initial perturbation that determines if the perturbation will be amplified or damped. The oscillation frequency determines the dynamical behavior of the system. We can distinguish three different cases.

- $\lambda(r) < 0$, stationary uniform solution stable ($\Phi^p damped$)
- $\lambda(r) > 0$, stationary uniform solution unstable ($\Phi^p grows$)
- $\lambda(r) = 0$, neutral/marginal stability.

The transverse field can be treated in terms of spatial frequencies k in Fourier space. Combined with the linear stability analysis, the contour of marginal stability $\lambda(k^2) = 0$ can be determined. A schematic sketch of the occurrence of modulation instability of the uniform solution against a weak modulation, with spatial frequencies k depending on the field intensity, is shown in Fig. 11.3. Every spatial frequency has a certain threshold intensity above which the Fourier component will be amplified.

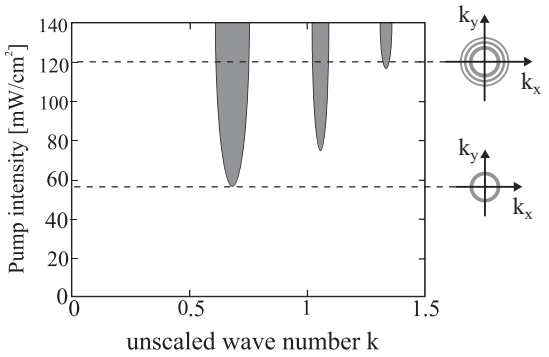

Fig. 11.3 Schematic of modulation instability in a simplified single feedback experiment. Typical marginal stability curves in a plane spanned by the modulus of the transverse wave vector and the pump intensity for the situation of a focusing nonlinearity are shown.

When increasing the field intensity up to the threshold, the primarily homogeneous planar wave solution becomes modulationally unstable against the perturbations at a critical spatial frequency (wave number) k_c [24, 8]. The critical wave number k_c of the first threshold of modulation instability is typically the same that appears in the self-imaging due to the Talbot effect [25]. In Fourier space, k_c represents ring structures centered on the zero order plane wave solution (c.f. Fig. 11.3). At increased intensities, higher order thresholds of the modulation instability, which result in excitation of higher order rings $k^{(n)}$, are observed at the curve of the marginal instability in the linear stability analysis. Generally, distinct spatial modes start to grow from noise at the critical k_c ring and thus not the whole k_c ring becomes excited at the threshold due to symmetry breaking. As a consequence, different spatial patterns and structures evolve spontaneously in the transverse plane of the light field. Most commonly hexagonal patterns are observed just above threshold [8]. In addition to the regularly localized pattern in Fourier space and extended in real space,

single or multiple spot-like structures are also observed in these systems. These dissipative structures are called dissipative solitons.

Emergence of dissipative solitons as a result of balance between loss and gain is based on two fundamental effects; namely, optical bistability [26, 27] and the formation of self-organized optical patterns [10]. The soliton itself can be interpreted as a solution which locally interconnects two homogeneous states [11] or a homogeneous state with a spatially periodic one [29] or even two spatially periodic states [28].

In the following we introduce the mechanisms of the formation of these solitary structures and discuss the features which dominate their spontaneous behaviour in the LCLV single feedback system.

11.3 Localized structures in a single-feedback system using a liquid crystal light valve as a nonlinearity

In our experiments shown in this chapter, the Kerr medium is a reflective liquid crystal light valve (LCLV) acting as a hybrid nonlinear element in a feedback loop. Liquid crystal light valves, in spite of the relative slow response time estimated in the range of 50 ms, are attractive as a nonlinear element in this type of experiments due to the high nonlinear sensitivity and the large aspect ratio. This enables the observation of large areas of patterns and many independent spatial solitons [22].

This device works as an optically addressable spatial light modulator (OaSLM) and as a function of the writing intensity and the external applied voltage. The LCLV is constructed of a set of thin layers, namely two transparent Indium Tin Dioxide-coated glass electrodes, a liquid crystal layer (LC), a dielectric mirror, a sensitive absorber, and a photoconducting layer. The LCLV can be divided into two functional sides — a read and a write side. The principle function of an LCLV is the conversion of a spatial light intensity distribution incident on the photoconduction layer in a modulation of the refractive index of the liquid crystal layer. A read wave passes the (LC) layer, reflects at the dielectric mirror, and leaves the LCLV modulated in its phase and polarization state. The phase shift Φ of the extraordinary wave induced by the LCLV can be written as [30]

$$\tau \frac{\partial}{\partial t}\Phi - l^2 \Delta_{\perp}^2 \Phi + \Phi = S(I_w, V_{ext}). \tag{11.8}$$

where τ denotes the effective response time of the liquid crystals required for their reorientation, l is the effective diffusion length accounting for the restricted spatial resolution of LCLV, and $S(I_w, V_{ext})$ is the saturation function suggested by Lu and Saleh [31] and depends on the writing intensity I_w and the external bias voltage V_{ext} via:

$$S(I_w, V_{ext}) = \Phi_{max} \left\{ 1 - \tanh^2 \left(\frac{V_{lc} - V_{th}}{V_0} \right) \right\}. \tag{11.9}$$

Here, $\Phi_{max} = 2k\Delta n$ is the maximum phase shift induced by the LCLV, k is the wave vector, and Δn is the refractive index modulation. V_{th} and $V_{lc} = S(I_w)V_{ext}$ are the threshold voltage and the voltage dropped to the liquid crystal layer, respectively, and are normalized with respect to V_0. $S(I_w)$ denotes a function describing the intensity dependence of the V_{lc} above the threshold voltage. This model includes temporal and spatial resolution as well as the effects of saturation, thus mimicking the complete response of the material [30].

After illuminating the LCLV with polarized light of a rather low intensity in the range of Milliwatts, the reflected field is modulated in phase and its polarization is changed. A polarizer is used to transfer the phase modulation into an amplitude modulation. The resulting intensity distribution I_w at the write side after free propagation over a distance L can be written as [30]:

$$I_w = \left| \exp\left(\frac{-iL}{2k_\lambda}\Delta_\perp^2\right)(Be^{-ik\Phi}) + C \right|^2 I_p, \tag{11.10}$$

where the amplitude factors B and C are given by $B = \cos\psi_1 \cos\psi_2$ and $C = \sin\psi_1 \sin\psi_2$. ψ_1 and ψ_2 are the angle of the input polarization and the angle of the polarizer axis, respectively, with respect to the optical axis of the liquid crystal layer. If $(\psi_1 = \psi_2 = 0)$, which gives B=1 and C=0, pure phase modulation is induced in the system. In this way, the system can be completely described with the help of the two latter equations.

The experiments shown here have been realized for different arrangements of polarizers, $\psi_1 \neq \psi_2 \neq 0$. In this polarization mode, a rich diversity of optical patterns has been reported [20, 21, 8, 30, 32, 33]. The reason for this diversity is the additional amplitude modulation induced by the modulation of the polarization state. The uniform solution exhibits a more complex behavior than in the phase-only mode. In Fig. 11.4, we show an example of localized structures and of one of the most stable patterns observed in LCLV system driven in this polarization mode.

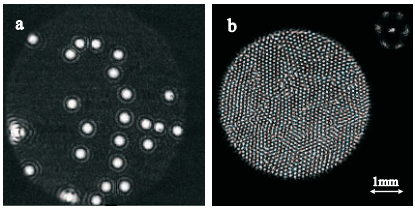

Fig. 11.4 Example of spatial structures in the polarization mode; a: solitary structures at $\psi_1 = -\psi_1 = 44°, V_{ext}$= 4.3 V, and propagation length L=-20 cm; b: a hexagonal pattern at U_{ext}= 4.7 V. The far field is shown in the upper right corner.

A typical experimental setup is shown in Fig. 11.5. The LCLV is driven by a frequency doubled Nd:YAG laser (λ = 532 nm, P = 100 mW). The input I_p is linearly polarized and expanded to 3.5 cm. This uniform wave impinges the read-out side of LCLV where it is internally reflected at the dielectric mirror and modulated in its

phase and polarization state. The modulated wave is then inserted to the feedback loop where the wave passes through the polarizer (P), which transmits the polarization direction ψ_2 with respect to the optical axis of the LCLV. After a distance of free space propagation L, the resulting intensity distribution I_w is reflected at mirrors M, goes through the lenses L, to reach the write side of the LCLV, and thus closing the feedback loop.

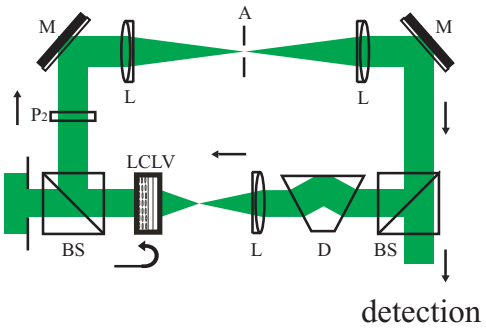

Fig. 11.5 Experimental setup of the LCLV single feedback experiment system. P2: polarizer determining ψ_2, L : lenses, M: mirrors, BS: beam splitter, D: dove prism.

It is worth noting that the LCLV itself provides a self-defocusing nonlinearity. Due to a symmetry in the model equations 11.8 and 11.10 one can simulate self-focusing as well as self-defocusing nonlinearities to balance the diffraction in order to create solitary localized structures. In the experiment, a negative propagation length is realized by imaging a virtual plane in front of the LCLV onto its write side. The far and near field of the feedback wave are also recorded by imaging a fraction of the feedback wave on a CCD camera.

11.3.1 Formation of localized structures

As mentioned above, bright localized states are found in the LCLV system if a bistability of a uniform dark solution with a patterned bright solution exists in polarization mode with a focusing nonlinearity. The results of the linear stability analysis in this case and the corresponding bistability curve for a typical parameter where LCLV single feedback system exhibits solitary structures are shown in Fig. 11.6.

The behavior of the evolving phase Φ shows that at the turning points of the hysteresis curve, the system would become on the one hand unstable against perturbations with $k = 0$ ($\circ$/dotted line). On the other hand, the uniform solution becomes modulationally unstable and forms transversal structures from the switching point ($\diamond$/dashed line). Increasing the input intensity from zero on the lower branch, the homogeneous dark solution remains stable until the threshold of the modulation instability ($\circ$) is reached and the homogeneous solution breaks up and forms patterns.

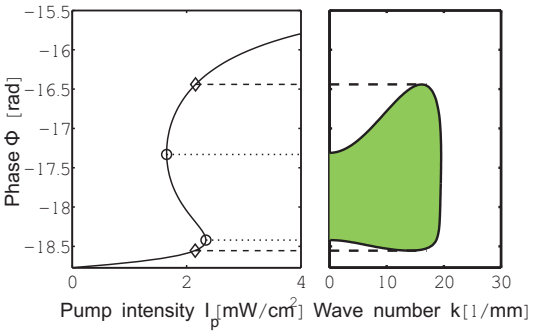

Fig. 11.6 Left: bistability curve found in the stationary uniform solution. Right: results of a linear stability analysis for a focusing nonlinearity in the polarization mode $\psi_1 = -\psi_2 = 40°$. The thresholds of the instability of the uniform solution $(\circ)$ and for the formation of pattern $(\diamond)$ are marked

The pattern solution in turn becomes unstable above the turning point $(\diamond)$ and the system switches to the upper bright steady state. Starting from the uniform bright solution on the upper branch, decreasing the input intensity below the threshold $(\circ)$ leads to break up the bright uniform solution and to forming patterns. Further decreasing the input intensity, the bright patterned solution becomes unstable again at the upper turning point $(\diamond)$ and switches back to the lower branch thus yielding the bistability curve of the system. In the bistability range, bright isolated states emerge on a dark background - in the transverse plane of the feedback beam. They represent localized solitary structures. The localized state itself can be considered as a solution which locally interconnects both previous solutions. The optical bistability, between a uniform unstructured solution and a patterned solution, can be interpreted as a subcriticality. Often the presence of subcriticality is restricted only to small parameter ranges. In Fig. 11.7 the formation of bright solitons in the LCLV experiment is shown.

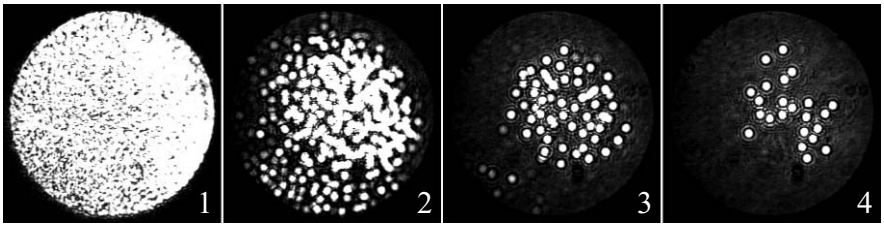

Fig. 11.7 Sequence showing the formation of solitary structures in the LCLV single feedback experiment. Illumination of the LCLV write side first switches the system to the upper bright branch of the bistability curve (1). The addressing illumination is switched off and after transients (2-3) a stationary state with seemingly spontaneous spatially distributed solitary structures evolves (4). Propagation length L = -13 cm

By adjusting the pump intensity I_p to the parameter region where the system shows a bistable behavior and after illuminating the LCLV's side, the system switches initially to a bright state. Solitary structures slowly form on uncorrelated positions. They can be space-filling like optical patterns but local variations of the background lead to random distributions of stationary solitons .

Localized structures may also have a reduced symmetry, where the breaking of the circular symmetry leads for certain ranges of the parameters, to triangular symmetry [34]. In addition to its symmetry, the triangular soliton differs from the circular soliton in central-peak intensity, in its tails, and in size. It has been pointed out that the system features an optical bistability between these two steady localized states. In the following we report on the possibility of controlling the symmetry of localized structures with help of externally imposed boundaries and a suitable nonlinearity strength.

11.4 Boundary-induced localized structures in LCLV

The strong influence of boundaries on regular patterns has already been studied theoretically and experimentally in active and passive nonlinear media [35, 36, 37, 38]. It has been pointed out that boundaries have a strong effect on patterns, yielding symmetries and steady states which do not exist in the extended case. We consider experimentally and numerically how boundaries affect symmetry of solitary structures in LCLV system by applying circular apertures in a range of parameters different from those investigated previously [34].

Solitary structures are observed in polarization modulation with different polarizer configurations; $\psi_1 = \psi_2$ and $\psi_1 = -\psi_2$. We work here mainly with $\psi_1 = -\psi_2$. In our experiment, we use angles of $\psi = 44^\circ$, a free propagation length of $L =$-20 cm, a LC voltage of 4.4 V, and a frequency of 250 Hz. With these parameters, solitary structures begin to appear at $I_w \approx 0.12\ \mathrm{mW/cm^2}$ above the instability threshold. When increasing the input intensity, more solitary structures arise and coexist in the transverse plane of the wave. At higher intensity values, they form a collection of uncorrelated solitary structures. These collections are constituted by moving spots that do not display spatial order.

To apply additional spatial boundaries, an aperture is placed in front of the write side of the LCLV after the solitary structures are formed. The total diameter of the impinging feedback beam on the write side of the LCLV is 2.3 cm, whereas the diameter of the aperture varies from 0.08 to 2 cm. Starting from the aperture diameter 0.9 mm where only a single solitary structure is allowed to pass the aperture, and increasing it slightly, the strong nonlinearity modifies the original circular symmetry in order to fit the aperture area. The sequence of observed structures with increasing apertures but at a fixed input intensity are shown in Fig. 11.8.

The typical circular localized structure breaks up and loses its highest symmetry when enlarging the aperture from 0.90 mm to 0.98 mm where a novel structure with rectangular symmetry emerges. By further increasing the aperture to 1.2 mm, the

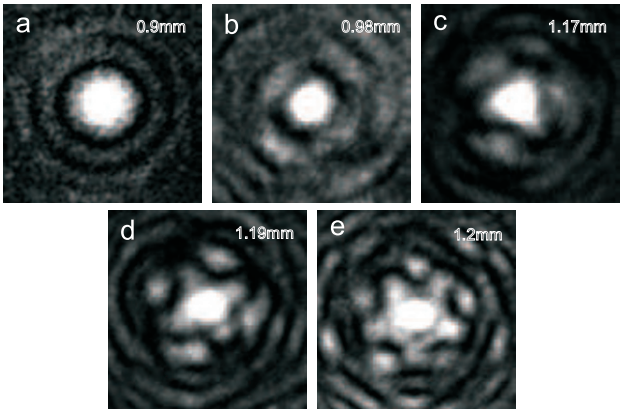

Fig. 11.8 Different symmetries of spatial solitary structures observed at fixed input power and at the aperture sizes shown at the top of each panel. The structures differ from each other in size, symmetry and in the number of the radial oscillations.

structure modifies again and three tails arise. The three tails are arranged symmetrically around the central spot forming a triangular structure similar to the triangular solitons reported in [34]. After the triangular structure, other polygonal symmetries arise when further enlarging the aperture, namely quadratic and pentagonal structures. The central spot has a symmetry corresponding to the number of emerging tails. By further enlarging the aperture, the pentagonal symmetry is destroyed and no clear symmetry is observed. Other symmetries can be observed if the strength of the nonlinearity is large enough to force more structures to fit into the aperture. Experimentally, hexagonal and heptagonal symmetries have been obtained when slightly tuning the nonlinearity by changing the frequency of the applied voltage to 290 Hz, see Fig. 11.9. It is worth noting that the number of tails in the boundary-induced structure is controlled by the aperture size, the LC voltage, the input intensity and the saturation threshold.

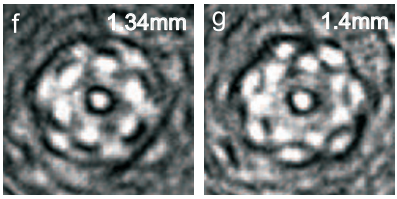

Fig. 11.9 Hexagonal and heptagonal structures appearing when further enlarging the aperture and for higher nonlinearity than in Fig. 11.8.

This experiment demonstrated the transition from *bulk induced* symmetries, where the aspect ratio is large and the emerging structures are independent of the size of the feedback beam, namely the circular and triangular solitary structures, to

boundary induced symmetries which depend on the size of the aspect ratio and the nonlinearity. We have investigated the effect of the input intensity on the behavior of the system in the regime of strong dependence from the boundary conditions. As indicated above, the appearance of lower polygonal symmetries is ruled not only by the size of the imposed aperture, but also by the input intensity. The experimental observations indicate that, if the aperture is kept fixed at 1.2 mm, only the rectangular and triangular symmetries can be observed even at high values of the input intensity. The state diagram for this case is shown in Fig. 11.10

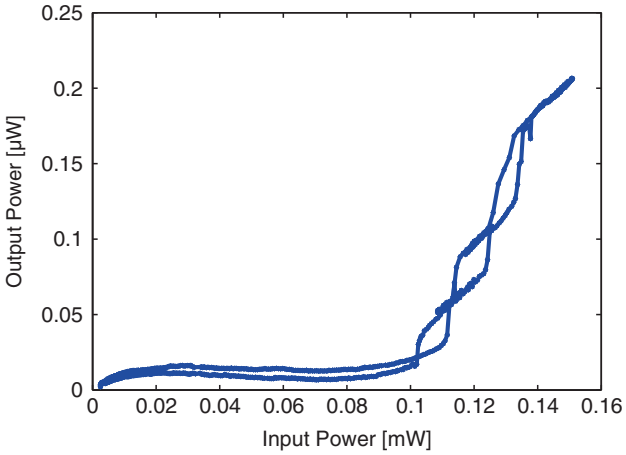

Fig. 11.10 Experimental bistability curve corresponding to the first three symmetries, the circular, rectangular, and triangular one, in the presence of an aperture of size 1.2 mm in the optical feedback path in the polarization mode $\psi_1 = -\psi_2 = 44^\circ$ of the LCLV system.

As shown in Fig. 11.10, the transitions between the observed symmetries when increasing the input intensity are associated with the appearance of boundary-induced bistability regions. If the input intensity is increased, the uniform dark background loses its stability at a certain turning point and the solution switches to a second stable branch of higher output intensity. By further increasing the input intensity, the system loses its stability again and switches to a stable third branch of even higher output intensity. On the other hand, if starting from the third steady state and decreasing the input intensity, the system remains stable until a new turning point before it jumps back to the lower stable branch and so on. The separation of the bistable branches depends also on the polarization configuration. When $\psi_1 = -\psi_2 = 45^\circ$, a maximum separation of the bistability branches representing the steady solutions of the system is obtained.

In comparison with the bistable behavior observed between the circular solitary structure and the triangular one in [34], we observe that the presence of the aperture leads to the generation of an additional steady state corresponding to the intermediate rectangular structure.

Until now we have considered an aperture with diameter of 1.2 mm. To get a complete picture of the ability of the system to support symmetries different from the circular one, the aperture is increased to $\approx$ 1.4 mm, i.e. large enough to allow a pentagonal structure to be observed. The measurements show that at this size of the aperture, the rectangular structure vanishes, and the state diagram depicted in Fig. 11.11 shows four small bistability regions representing four steady states, with a small fifth hysteresis loop corresponding to an unstable hexagonal structure. The hexagonal structure can be stabilized by tuning the applied frequency, i.e. the nonlinearity. Similar multistable behaviors have been described in the numerical simulations of the LCLV system [30].

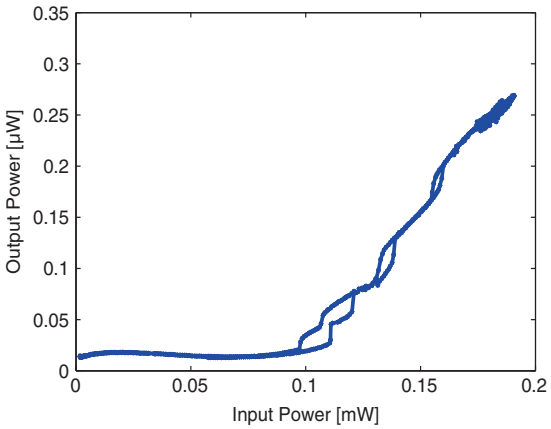

Fig. 11.11 Experimental bistability curve corresponding to the circular, triangular, square and pentagonal symmetries in the presence of an aperture of size 1.4 mm in the optical feedback path in the polarization mode $\psi_1 = -\psi_2 = 44^\circ$ of the LCLV system.

Numerical simulations of Eqs. (11.8)–(11.10) have been performed with a split-step method on 256x256 point grids. The free space propagation of the feedback field is computed by multiplying its Fourier transform by the appropriate phase function and then performing the inverse Fourier transform. To reproduce the experiments, an infinitely absorbing screen with a circular aperture is inserted into the feedback loop so that the diameter and position of the writing beam can be controlled. The position of the aperture is always chosen to be at the grid center.

For the case $\psi_1 = -\psi_2$, dissipative solitons have been found at $\psi_1 = 39^\circ, 40^\circ, 41^\circ$ and L = -18 cm using the model (11.8)–(11.10). As in the experiment, we progressively increase the size of the aperture measured in units of the size of the circular soliton observed without aperture. Fig. 11.12 shows localized structures with rectangular, triangular, quadratic, pentagonal, hexagonal, and heptagonal symmetries observed for apertures of diameters of 1.15, 1.25, 1.82, 2.40, 2.77 and 2.92 times the original circular soliton, respectively and $\psi_1 = 41^\circ$.

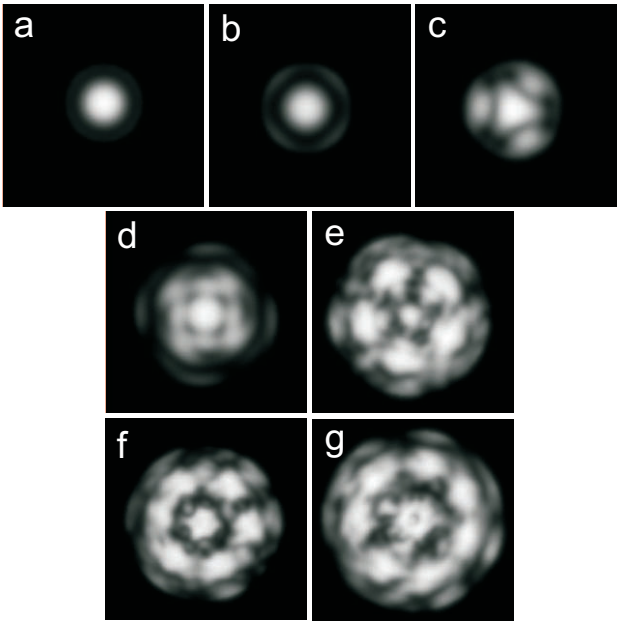

Fig. 11.12 Numerical simulations of solitary structures for the case of $\psi_1 = -\psi_2 = 41^\circ$ when enlarging the aperture to diameters: a) 1.0, b) 1.15, c) 1.25, d) 1.82, e) 2.40, f) 2.77, and g) 2.92 times the original circular soliton size [39].

We note that a similar set of boundary-induced solitary structures can be observed also in the configuration of polarizers $\psi_1 = \psi_2$ [39]. These observations clearly demonstrate the universal nature of the phenomenon of aperture-induced polygonal symmetries.

11.5 Dynamic and static position control of feedback localized states

In contrast to Fourier control, where the intention is to stabilize unstable states of the unaffected system [40, 41, 42, 43, 44], an external amplitude control imposes a stimulus to the nonlinear optical feedback system, which we will name in the following 'forcing' [45, 46, 47, 48]. External amplitude control must be considered as an invasive technique method since it changes the system state in any case. Due the invasive character of the forcing, the response of the system to system solutions not inherently present in the system can be investigated. Furthermore, the adjustment of the control strength is of crucial importance. The strength of the external control must be adjusted such that it does not absolutely dominate the system behavior by itself. In our particular example, the forcing strength must be strong enough to in-

fluence the behavior of feedback solitons, but at the same time must not destroy the ability of the system to support feedback solitons.

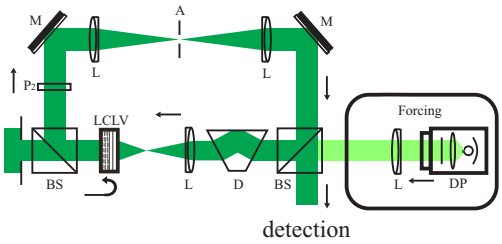

Fig. 11.13 Experimental setup of LCLV system with a digital projector DP that images an incoherent intensity distribution as a forcing

Experimentally the forcing is realized by projecting an incoherent spatial intensity I_f to the LCLV's photoconductive write side as shown in Fig. 11.13. So, it is added to the writing intensity distribution I_w of the unperturbed feedback wave. The spatial distribution of the static or dynamic forcing signal is designed at a computer. The forcing intensity distribution is created by a LCD-data projector. To model the influence of the forcing, I_w in Eq. 11.10 must be replaced simply by the total intensity:

$$I_{tot}(x,y,t) = I_w(x,y,t) + I_f(x,y,t). \tag{11.11}$$

The effect of the forcing onto the feedback system is twofold. First, the offset intensity I_f acts locally similarly to the external bias voltage V_0 in Eq. 11.8, i.e. the operation point of the nonlinearity is shifted locally. Second, the additional intensity distribution I_f induces an offset in the nonlinearly induced phase distribution Φ of the feedback wave. Thus, an additional phase modulation of the feedback wave can be achieved.

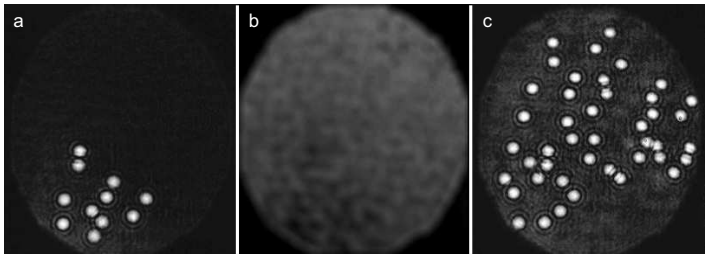

Fig. 11.14 Compensation of inhomogeneous sensitivity; (a): System without compensation; (b): Inverse sensitivity function; (c): System with compensation. The region of existence with the compensation is extended.

In the first experiment, the ability of the added intensity profile to balance spatial inhomogeneities of the background is tested. The spatial distribution of the LCLV's nonlinear sensitivity function via spatial soliton switching is determined as follows. If the sensitivity of the LCLV was homogeneous, localized structures would ignite over the whole aperture with the same forcing intensity level. The intensity levels at which localized states ignite, however, vary from spatial region to spatial region. The local forcing intensity at which a localized state ignites is then a measure of the non-uniformity of the LCLV sensitivity at that position [46]. The inverted sensitivity can then be applied as the control signal for external amplitude to balance the experimental non-uniformity [46]. An experimental example of the result of balancing the LCLV inhomogeneities is shown in Fig. 11.14. We note that a method to map background defects based on linear gradients applied to localized structures has recently been developed to characterize material imperfections in cavity configurations of semiconductor devices [49]. Such method differs from the one presented here in that gradients instead of external forcing ignition is used but the aims and the use of energy localization of the spatial soliton are quite similar. Obviously, the physical size of vertical cavity semiconductor devices [49] is much smaller that that of the LCLV [46] thus making the use of localized states to map non-uniformity and defects a very useful method for the microscopic characterization of homogeneity of nonlinear materials.

The external-forcing compensation method will be extended by introducing a periodic structure to the forcing distribution. We used a chessboard pattern with bright and dark quadratic fields as a forcing signal. To combine the compensation method with the position method, the chessboard was multiplied with the compensation intensity distribution and used as forcing input. The gray scale image of the chessboard intensity distribution is shown in figure 11.15a. In these experiments we showed that the forcing method succeeds in controlling the absolute positions of feedback solitons. However, the quadratic shape of the chessboard fields leaves the feedback solitons a certain range of transverse space to move. Thus, a precise lateral positioning in some areas has not been achieved.

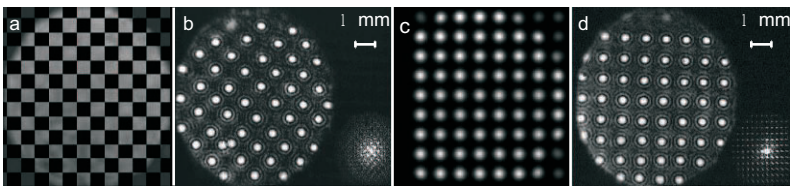

Fig. 11.15 Static position control; (a,c): The forcing input; (b,d): System response.

If the strength of the forcing input is adjusted so that the total intensity level at the LCLV's photoconductive side remains below the switching threshold of localized states, the forcing spatially favors distinct addressing positions. The system keeps its local bistability, and individual feedback solitons can be ignited. Instead of forming at randomly distributed trapping positions, they preferably ignite at the positions

selected by the forcing signal, which are the bright areas of the chessboard pattern as can be seen in Fig. 11.15a,b. To create this image, the forcing and the pump intensity have been kept at a constant level, while the photoconductive writ side was briefly uniformly illuminated to address the solitons. These now form at positions which coincide with the chessboard geometry. In the image the distance between the feedback solitons is d_f=1.1 mm, whereas the soliton peak diameter amounts to d_s=360 μm. However, small distortions from a perfect square grid are observed in the positioning of the feedback solitons. One reason for these distortions in the square grid is a certain range of space, which the localized states still possess within one field of the chessboard. Another reason are the non-ideal imaging properties of the projecting system. For more precise positioning, we then altered the chessboard forcing geometry into the square shaped lattice arrangement with Gaussian shaped control points at the lattice sites as shown in Fig. 11.15c,d. In this case the solitons form perfectly distributed according to the square lattice.

In the experiments described above, the response of feedback solitons to external amplitude control was investigated by observing the final equilibrium state. However, to fully understand the influence of external amplitude control on the feedback solitons, dynamical aspects, which are induced by static amplitude control, must be considered. In the following we then investigate and answer the question how feedback solitons respond to external amplitude forcing, if they are ignited laterally shifted with respect to a local extremum of the amplitude forcing. As a forcing signal we choose a cone shaped intensity distribution with a maximum forcing intensity at the top of the cone, because a cone shape combines a cylinder symmetry with a linear gradient, which points towards the cone maximum from every direction.

A three dimensional image of the cone intensity distribution is shown in figure 11.16. In the experiment, solitons were written at different positions and laterally shifted in respect to the maximum of the cone. The area influenced by the induced gradient is larger than the soliton diameter. So, the feedback soliton is placed into an environment with a linear gradient. This is induced by the cone with its singular accumulation point at the top. Once addressed, the solitons move independently

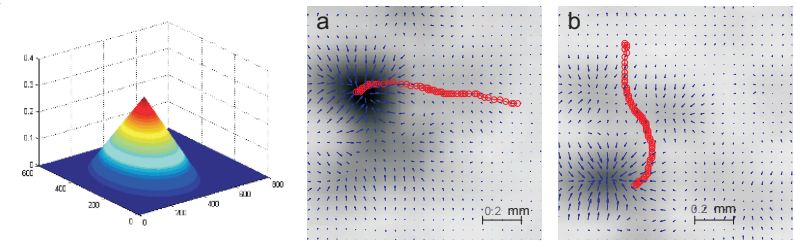

Fig. 11.16 Dynamical position control of a feedback soliton at a conically shaped intensity gradient. The trajectory is indicated by the circle (o).

from the addressing position towards the maximum of the cone intensity, since the amplitude forcing creates a corresponding extremum in the phase gradient of the

feedback wave via the nonlinearity. In figure 11.16a,b examples of the traces of the induced soliton motion are displayed. The track positions of the soliton are marked as a (o). In (a), the soliton is ignited at the right and moves towards the left, while it is addressed at the top and moves towards the bottom in the right hand image (b). The backgrounds depict inverted gray scale image of the system response to the cone forcing. The arrows show the gradient in the intensity distribution which can be use as a rough indicator for the actually induced phase gradient. The trajectories show that the feedback soliton moves towards the position of the cone-shaped forcing's maximal intensity. The final soliton position in figure 11.16a, where the soliton was addressed at the right side of the cone, perfectly coincides with the peak of the cone. In figure 11.16b, where the soliton was addressed above the cone maximum, a small deviation between the final soliton position and the peak position of the cone is observed. Even though the final position and the peak position do not perfectly match in this case, one needs to consider that the soliton peak still covers the area of the cone maximum.

11.6 Gradient induced motion control of feedback localized structures

The previously demonstrated methods for dynamic motion control are not well suited to create drifting solitons for the investigation of interactions with static parameter gradients. The drift motion induced by the motion of a gradient's sharp edge is not smooth enough, and the creation of an appropriate forcing input sequence, which combines a static forcing gradient with a continuous smooth drift motion control in a reliable manner, is a not trivial task.

Therefore, to achieve an easy control of both the static forcing gradient and the drift motion we slightly altered our setup by imposing a permanent global phase gradient in one spatial direction onto the system [22]. A global phase gradient which induces a continuous and smooth drift motion of feedback solitons, can be created if the feedback system is detuned by slightly misaligning either a mirror or one of the lenses. An illustration is shown in figures 11.17a. In order to study the response of feedback solitons to the global phase gradient, five solitons were written at five different spatial positions separated by 0.75 mm perpendicular to the drift direction, and observe the drift motion of the solitary structures. At every addressing position a solitary structure was addressed 50 times. In correspondence to the global phase gradient, the written structures drift from the right to the left. The recorded track positions of the solitons are marked with (•) as in figure 11.17b. The direction of the drift is indicated by an arrow in the lower right corner. Figure 11.17 clearly shows that the drift motion of the feedback spatial solitons is affected by non-uniform backgrounds. By repeating the experiment described here for a larger set of initial positions of the solitons and drift directions, a full map of the background defects and imperfections would became available. Such a task has been recently achieved

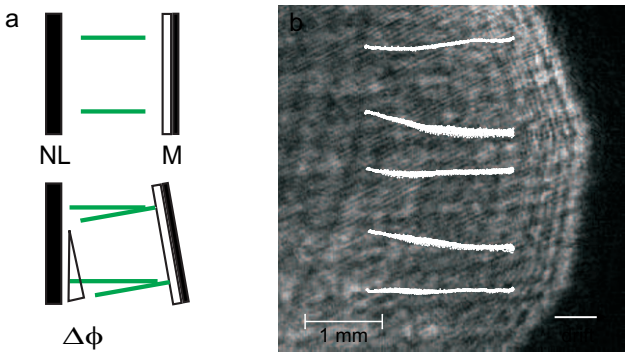

Fig. 11.17 (a)Top: Translational invariant single feedback scheme with a nonlinear optical medium (NL); (Bottom): A small misalignment of the feedback mirror (M) results in a global phase shift $\Delta\Phi$ causing a drift motion; (b): Trajectories of drifting feedback solitons. The trajectories are a superposition of 50 drifting solitons ignited at each of the five addressing positions. Inhomogeneities cause deviations from a straight vertical track and fix the route of the solitons to a trapping route.

in cavity (instead of feedback) configurations of localized states in semiconductor based devices [49].

Now, we demonstrate the possibility of modulating the drift velocity. For this purpose, a hexagonal parameter gradient was chosen as a static background parameter on which drifted solitons will be addressed. The spatial distribution of the hexagonal parameter gradient and the addressing positions of four feedback solitons are shown in figure 11.18a. In the experiment a drift motion of the feedback solitons in direction of the arrow in the bottom left corner was imposed onto the system. We observe a modulation of the velocity of feedback solitons drifting at the hexagonally modulated parameter gradient in the experiment. A sample of the temporal evolution of the instantaneous velocity at a hexagonally shaped control signal with wave number k_h=3.5 mm^{-1} is shown in 11.18b. In correspondence to the control signal, a sine fit matches with the experimental data. This modulation is observed to be on top of the average drift velocity of the feedback solitons which amounts to υ_s = 0.55 mm/s.

Now, we turn from periodic hexagonal parameter gradients to gradients with a simpler line-shaped structure. As before, the interaction of drifting solitons with these line-shaped parameter gradients is examined. A line structure which intended to act as a barrier for drifting solitons is created with a central gap. The spatial distribution of the forcing input is shown in figure 11.19a. The background of the forcing distribution is set to an intermediate gray scale level (80 gray scale) to enable the existence of the feedback solitons. The central part of the line structure is set to a zero gray scale level and this central area is surrounded by a border with higher gray scale level (120 gray scale) than the background intensity. The forcing strength in experiment was adjusted so that feedback solitons could not exist in the dark area of the line structure and the existence was enabled everywhere else. As before, we have indicated the direction of the drift with a small arrow.

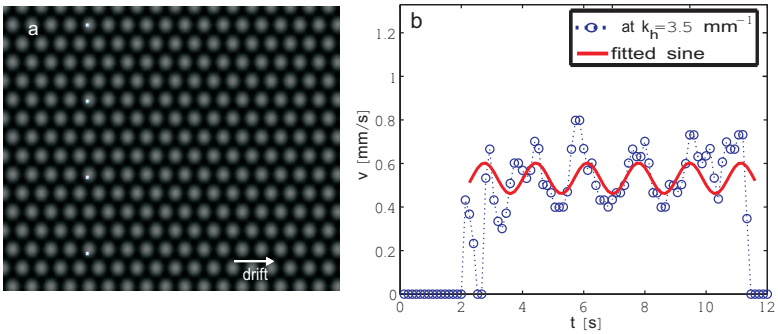

Fig. 11.18 (a): Hexagonal forcing distribution with four addressing positions; (b): Plot of the instantaneous drift velocity of the feedback solitons versus time. The periodic modulations visible in the distribution of the instantaneous drift velocity correspond to the wave number k_h=3.5 mm^{-1} of the hexagon forcing. The modulation of the drift is fitted to a sine function.

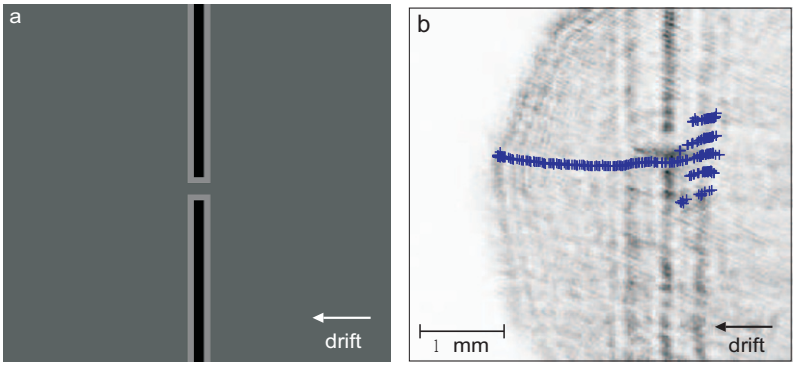

Fig. 11.19 Interactions of feedback soliton with a slit; (a): Gray scale master of the forcing. In the dark area of the line structure the existence of feedback solitons is inhibited. On the gray background and the border drifting solitons can exist drift.; (b): Trajectories (+) of drifting solitons interacting with the slit. The trajectories are a superposition of five sequentially addressed feedback solitons which were ignited at every of the five addressing positions.

Experimentally, optical feedback solitons were addressed at five different positions to the right of the line structure's gap spatially equally separated in y-direction. Influenced by the direction of the global gradient the solitons drift towards the line structure with the gap from right to left. In figure 11.19b, the experimentally tracked positions of the feedback solitons (+) are shown on the top of an inverted gray scale image of the background with activated forcing. The solitons were sequentially addressed at the different addressing position and the experiment was repeated five times for every addressing position. Solitons addressed at the position facing the gap of the line structure can obviously pass the gap, while those addressed at positions above or below are stopped by the barrier. The stopped solitons drift further and are then annihilated in the central dark area of the line, because the system is

not bistable there. Experimentally, we modified both the width of the gap and the border line. In both cases we observed that solitons at a larger parameter range of y-positions are able to pass the gap.

In the following, we check the possibility of guiding of drifting solitons at artificially created trapping trajectories. To create such a guidance structure, the line-shaped structure which before was used as a barrier for localized structures, is inverted. A gray scale image of the master creating a line of guidance for optical solitons is shown in figure 11.20a. As before, an intermediate gray scale level was chosen as a background to create a common area where feedback solitons exist. Instead of a dark line surrounded by a brighter border, the distribution now consists of a brighter line on which a soliton is addressed. The brighter line structure is surrounded by a dark border. The gray scale level of the dark border is set to zero, and the system is adjusted such that solitons are annihilated in the dark areas. Another second soliton is addressed at the same y-position as the guided feedback soliton, but shifted to the left on the x-axis to compare the motion of the trapped guided soliton with an uncontrolled drift motion.

In figure 11.20b–d, three different experimental scenarios of soliton guidance induced by the forcing distribution are shown. The arrows indicate the direction of the induced drift. Figure 11.20b shows the trajectories of both drifting solitons. The localized structure on the right moves parallel to the y-axis downwards and is hence guided by the line structure, whereas the solitary structure on the right only moves influenced by the induced drift in a diagonal direction from an upper left to lower right position. Comparing the y-positions of both drifting solitons one finds that the drift velocity of the guided soliton corresponds to the projection of the freely drifting soliton's velocity onto the y-axis. The motion of the guided soliton is stopped at its final position by an impurity of the system. Figure 11.20c also shows another influence which the spatial system inhomogeneities may have on the guidance of drifting solitons. While the initially guided soliton is stopped by an impurity, the soliton not trapped initially is captured by the guidance structure after permeating its border. Once captured, the soliton continues its drift motion according to the control direction of the guiding line. The third scenario shown in figure 11.20d, adds the loss of guiding structure at a spatial inhomogeneity to the possible influences of spatial impurities. The initially guided soliton in this scenario leaves the guiding structure at an impurity and continues its drift motion according the direction of the global drift. The different behavior of the guided solitons at the impurities is caused by an interplay of two factors. The first factor is small variations in the pump intensity which require small readjustments of the forcing strength. Thus, the relation between forcing strength and the pump intensity slightly varies in the depicted images. The second influence is small variations in the angle of the drift in respect to the guiding line structure which can be read off from motion of the freely drifting solitons. A modified inclination angle between a drift motion and the guiding structure may alter the lateral force pushing a soliton into x-direction. So, a feedback soliton can, depending on the angle of the drift motion, remain trapped or freed or hop onto the guiding structure at an impurity.

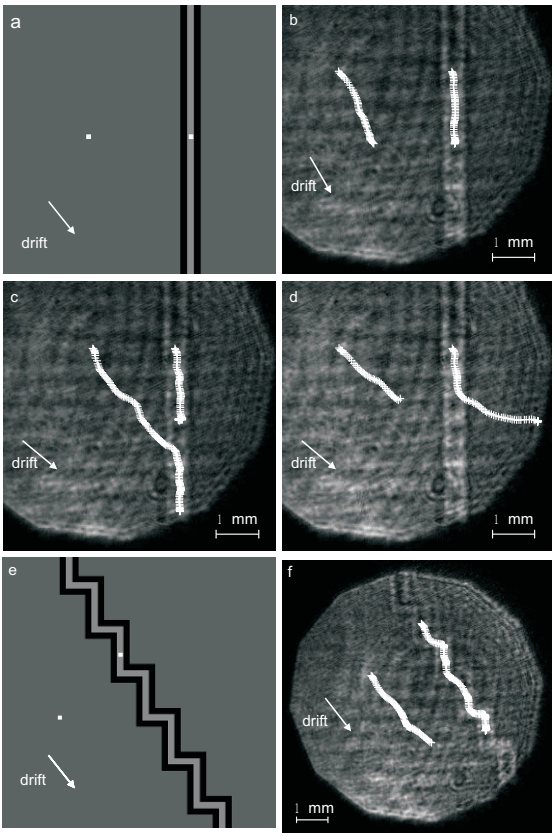

Fig. 11.20 Guidance of drifting solitons; (a, e): Forcing master; (b, f): A drifting soliton addressed at the guiding line follows the path of the guiding, while a freely drifting soliton is moving in correspondence to the general drift direction; (c): Trapping of a freely drifting soliton by the guidance line; (d): Escape of the guided soliton at an impurity.

So far, we demonstrated the one-dimensional guiding of drifting optical solitons. To complete the picture, we test the possibilities of guiding the solitons in x-and y-direction. For this experiment the forcing intensity distribution shown in figure 11.20e was applied int the system. Instead of a straight line, the forcing intensity distribution now consists of a staircase-like structure, which induces guidance into x-direction for a certain distance, and guiding in y-direction will be effected after a sharp turn.

The experimental image of the drifting solitons' trajectories addressed at the staircase guiding structure shown in figure 11.20f, indeed confirms this assumption. As in the preceding experiments the localized state written far from the guiding structure drifts according to the induced drift direction. In the soliton trajectory on the right, which corresponds to the addressing at the guiding structure, the edges consistent with the angles of the staircase guiding structure are clearly visible. This

observation does not apply to for all the edges, as some are smoothed out, and in the central part of the trajectory the smoothing of the staircase is so strong that it is difficult to decide whether the trajectory could also conform to the motion of a freely drifting feedback solitons or not. In any case, the sharp edge of the induced staircase turn of the drifting soliton, is again very well pronounced during the final part of the trajectory. This is a definite indication of the trapping of the drifting soliton by the two dimensional guiding structure.

11.7 Summary

General properties of localized states in single feedback experiments in LCLV have been reviewed. In order to use feedback localized structures in the processing of optical information, full control of their shape and position is required.

We have first demonstrated the interaction of spatial dissipative solitons with inserted boundaries in combination with a suitable nonlinearity. It has been shown that dissipative soliton bifurcates from the circular form to more complex forms when circular apertures are present in the feedback loop. This process showed the transition from bulk-induced symmetries, i.e. the circular and triangular one, to boundary-induced symmetries in a multi-stable behavior of the system.

We have then presented static and dynamic position control of feedback dissipative solitons by using an incoherent external forcing scheme. The forcing method creates robust static trapping positions to which feedback solitons are attracted and at which they form more favorably. The investigation of the drift motion revealed the linear relation between a parameter gradient slope and the gradient induced drift motion of the feedback solitons. For the motion control of drifting solitons the interactions of drifting solitons with different parameter gradients were examined. In the course of these experiments the possibility to create guiding and position selecting control was demonstrated. The methods developed and studied here provide an excellent and very versatile toolbox for controlling of optical dissipative solitons. For all these experimental observations the LCLV system can be considered as a model system. The universal character of localized states allows the operator to export and import control techniques developed in feedabck LCLV experiments to and from cavity configurations. For example position control of cavity solitons [50] as well as mapping of background inhomogeneities [49] have been recently implemented in semiconductor micro-cavities.

References

1. M.C. Cross, P.C. Hohenberg, Rev. Mod. Phys. **65**, 851 (1993)
2. P. Manneville, *Dissipative Structures and Weak Turbulence* (Springer, 1990)
3. E. Schneider, D. Sagan, *Into the Cool: Energy Flow, Thermodynamics, and Life* (Chicago: University of Chicago Press 2005)

4. J.V. Moleney, H.M. Gibbs, Phys. Rev. Lett. **48**, 1607-1610 (1982)
5. L.A. Lugiato, R. Lefever, Phys. Rev. Lett. **58**, 2209-2211 (1987)
6. D.W. McLaughlin, J.V. Moloney and A.C. Newell, Phys. Rev. Lett. **54**, 681 (1985)
7. L.A. Lugiato and C. Oldano, Phys. Rev. A. **37**, 3896 (1988)
8. G. D'Alessandro, W. Firth, Phys. Rev. Lett. **66**, 2597-2600 (1991)
9. A.J. Scroggie, W.J. Firth, G.S. McDonald, M. Tlidi, R. Lefever and L.A. Lugiato, Chaos, Solitons & Fractals **4**, 1323 (1994)
10. N. Akhmediev, A. Ankiewics, *Dissipative Solitons* (Springer, 2005)
11. T. Ackemann, W.J. Firth and G.-L. Oppo, *Advances in Atomic, Molecular, and Optical Physics* **57**, 323-421 (2009)
12. F. Pedaci et al, Appl. Phys. Lett. **92**, 011101 (2008)
13. F. Pedaci, G. Tissoni, S. Barland, M. Giudici, and J. Tredicce, Appl. Phys. Lett. **93**, 111104 (2008)
14. Ph. Jander, A. Desyatnikov, C. Denz, M. Belic, D. Vujic, A. Strinic, IEEE. CNF PROC. EQEC, **217**, (2003)
15. C. Denz, M. Schwab, M Sedlatschek, T. Tschudi, T. Honda, J. Opt. Am B. **15**:p, 2057 (1998)
16. T. Ackemann, Yu.A. Logvin, A. Heuer, W. Lange, Phys. Rev. Lett. **75(19)**, 3450-3453 (2002)
17. M. Pesch, J.-U. Schurek, T. Ackemann, W. Lange, Phys. Rev. Lett. **95**, 143906 (2005)
18. B. Gütlich, C. Cleff, C. Denz, *Drift motion control of solitary structures using parameter gradients* (Optical Society of America, 2007)
19. U. Bortolozzo, S. Residori, Phys. Rev. Lett. **96**, 037801 (2006)
20. B. Thüring, *Spontane Entstehung und Selektion raumzeitlicher Muster in nichtlinear-optischen Rückkopplungssystem* (PhD Thesis, Institute of Applied Physics, Darmstadt University of Technology, 2003)
21. S. Residori, Physics Report, **416**, 201 (2005)
22. C. Cleff, B. Gütlich, and C. Denz, Phys. Rev. Lett. **100**, 233902 (2008)
23. W.J. Firth, C.O. Weiss, *Cavity and feedback solitons* (Optics & Photonics News). **13**, 54-58 (2002)
24. W.J. Firth, J. Mod. Opt. **37(2)**, 151-153 (1990)
25. E. Ciaramella, M. Tamburrini, and E. Santamato, Appl. Phys. Lett. **64**, 3080 (1994)
26. C.M. Bowden, M. Ciftan, H.R. Robl (Eds.), *Optical Bistability I & II* (Plenum Pree, New York, 1981)
27. M. Gibbs (Ed.), *Optical bistability: Controlling light with light* (Academic Press, Orlando, 1985)
28. U. Bortolozzo, M.G. Clerc, C. Falcon, S. Residori, and R. Rojas, Phys. Rev. Lett. **96**, 214501 (2006)
29. B. Gütlich, R. Neubecker, M. Kreuzer, and T. Tschudi, Chaos **13**, 239 (2003)
30. R. Neubecker, G.-L. Oppo, B. Thüring, T. Tschudi, Phys. Rev. A **52**, 791-808 (1995)
31. K. Lu, B.E.A. Saleh, Appl. Opt. **30**, 2354-2362 (1991)
32. B. Thüring, R. Neubecker, M. Kreuzer, E. Benkler.,T. Tschudi, Asian J. Phys. **7**, 453 (1998)
33. P.L. Ramazza, S. Ducci, s. Boccaletti, F.T. Arecchi, J. Opt. B: Quantum Semiclass. Opt. **2**, 399-405 (2000)
34. U. Bortolozzo, L. Pastur, P.L. Ramazza, M. Tlidi, G. Kozyreff, Phys. Rev. Lett. **93**, 253901 (2004)
35. F. Papoff, G. D'Alessandro, G.-L. Oppo, W. Firth, Phys. Rev. A **48**, 634-641 (1993)
36. E. Pampaloni, P.L. Ramazza, S. Residori, F.T. Arecchi, Europhys. Lett. **25(8)**, pp. 587-592 (1994)
37. F. Papoff, G. D'Alessandro, G-L. Oppo, Phys. Rev. A **60**, 648 (1999); F. Papoff, G. D'Alessandro, G-L. Oppo, W.J. Firth, Phys. Rev. Lett. **82**, 2087 (1999)
38. E. Louvergneaux, D. Hennequin, D. Dangoisse, P. Glorieux, Phys. Rev. A **53**, 4435 (1996); G. D'Alessandro, F. Papoff, E. Louvergneaux, P. Glorieux, Phys. Rev. E **69**, 066212 (2004)
39. M. Ayoub, F. Papoff, G.-L. Oppo, and C. Denz, accepted in EPJD (2010)
40. R. Neubecker and E. Benkler, Phys. Rev. E **65**, 066206 (2002)
41. R. Martin, A. J. Scroggie, G.-L. Oppo, and W. J. Firth, Phys. Rev. Lett. **77**, 4007 (1996)

42. E. Benkler, M. Kreuzer, R. Neubecker, and T. Tschudi, Phys. Rev. Lett. **84**, 879 (2000)
43. S. Juul Jensen, M. Schwab, and C. Denz, Phys. rev. Lett **81**, 1614-1617 (1998)
44. P.L. Ramazza, E. Benkler, U. Bortolozzo, S. Boccaletti, S. Ducci and F.T. Arecchi, Phys. Rev. E **65**, 066204-1 (2002)
45. B. Gütlich, H. Zimmermann, C. Cleff, and C. Denz, Chaos **17**, 037113 (2007)
46. B. Gütlich, H. Zimmermann, C. Denz, R. Neubecker, M. Kreuzer, T. Tschudi, Appl. Phys. B. **81**, 927-936 (2005)
47. S. Residori, N. Olivi-Tran, and E. Pampaloni, Eur. Phys. J. D. **12**, 15-20 (2000)
48. B. Gütlich, C. Denz, From Pattern Control to Synchronization: Control Techniques in Nonlinear Optical Feedback Systems. In *Handbook of Chaos Control*, E. Schöll, H.G. Schuster (Edts.), (WILEY-VCH, Weinheim, 2008)
49. F. Pedaci, G. Tissoni, S. Barland, M. Giudici, and J. Tredicce, Appl. Phys. Lett. **93**, 111104 (2008)
50. F. Pedaci, P. Genevet, S. Barland, M. Guidici, J.R. Tredicce, Appl. Phys. Lett. **89**, 221111 (2006)

Part IV
Excitability and localized states

Chapter 12
Interaction of oscillatory and excitable localized states in a nonlinear optical cavity

Damià Gomila, Adrián Jacobo, Manuel A. Matías, and Pere Colet

Abstract The interaction between stationary localized states have long been studied, but localized states may undergo a number of instabilities that lead to more complicated dynamical regimes. In this case, the effects of the interaction are much less known. This chapter addresses the problem of the interaction between oscillatory and excitable localized states in a Kerr cavity. These oscillatory structures can be considered as non punctual oscillators with a highly non-trivial spatial coupling, which leads to rather complicated dynamics beyond what can be explained in terms of simple coupled oscillators. We also explore the possibility of using coupled excitable localized structures to build all-optical logical gates.

12.1 Introduction

Localized states (LS) are commonplace in extended system exhibiting bistability between two different solutions [1]. Physically they imply an equilibrium in a finite region in space between dissipation and driving, and nonlinearity and diffusion.

Damià Gomila
IFISC, Instituto de Física Interdisciplinar y Sistemas Complejos (CSIC-UIB), Campus Universitat Illes Balears, 07122 Palma de Mallorca, Spain, e-mail: damia@ifisc.uib-csic.es

Adrián Jacobo
IFISC, Instituto de Física Interdisciplinar y Sistemas Complejos (CSIC-UIB), Campus Universitat Illes Balears, 07122 Palma de Mallorca, Spain, e-mail: jacobo@ifisc.uib-csic.es

Manuel A. Matías
IFISC, Instituto de Física Interdisciplinar y Sistemas Complejos (CSIC-UIB), Campus Universitat Illes Balears, 07122 Palma de Mallorca, Spain, e-mail: manuel.matias@ifisc.uib-csic.es

Pere Colet
IFISC, Instituto de Física Interdisciplinar y Sistemas Complejos (CSIC-UIB), Campus Universitat Illes Balears, 07122 Palma de Mallorca, Spain, e-mail: pere@ifisc.uib-csic.es

O. Descalzi et al. (eds.), *Localized States in Physics: Solitons and Patterns*,
DOI 10.1007/978-3-642-16549-8_12,

In the nonlinear optics context the spatial coupling is mainly given by diffraction, although diffusion can be also present in some cases.

All these ingredients are present in optical cavities filled with a nonlinear medium [2, 3]. The driving is given by a broad homogeneous holding beam which is shined on a semi-reflecting mirror of the cavity. Part of the light will be reflected, but the rest enters the cavity. If the holding beam is switched off all the energy leave the cavity through the same semi-reflecting mirror, which make the system dissipative. The spatial coupling is provided by the diffraction of the propagating light propagating, which smooth out any spatial inhomogeneity. Finally, a nonlinear medium provides the necessary photon-photon interactions to observe a complex behavior such as the formation of localized states.

Nonlinear optical cavities have long been shown to support localized states, and stationary LS have been advocated for their use as bits in optical memories [4, 5]. An important feature of these LS is that they interact through their oscillatory tails in such a way that they anchor at a discrete set of distances [6, 7, 8]. But LS can also undergo a number of instabilities leading to more complicated dynamical regimes [9, 10]. In this case the role of the interaction is much less known. In particular, we will focus here on the study of the interaction of oscillatory and excitable LS in a Kerr cavity. In this system the dynamics of LS is an intrinsic property of the coherent structures that emerges from the spatially extended nature of the system. Thus, for instance, oscillatory LS are non-punctual oscillators, i.e. oscillators with internal structure or degrees of freedom. As a result, their interaction can not necessarily be reduced to a simple coupling term between punctual oscillators. The interplay between the oscillatory dynamics, the interaction, and the internal structure can affect the dynamics in a nontrivial way. This chapter is an attempt to address this general problem by studying a prototypical case.

12.2 Model

We study the dynamics and interaction of localized states in a prototypical model, namely the Lugiato-Lefever equation, describing the dynamics of the slowly varying envelope $E(\mathbf{x},t)$ of the electric field in a ring cavity filled with a self-focusing Kerr medium (see Figure 12.1). In the mean field approximation, where the dependence of the field on the longitudinal direction has been averaged, and in the paraxial limit, the dynamics of E in two transverse spatial dimensions is described by the following equation [11]:

$$\frac{\partial E}{\partial t} = -(1+i\theta)E + i\nabla^2 E + E_{in} + i|E^2|E, \tag{12.1}$$

where $\mathbf{x} = (x,y)$ is the transverse plane and $\nabla^2 = \partial^2/\partial x^2 + \partial^2/\partial y^2$. The first term on the right-hand side describes the cavity losses, rescaled to 1, E_{in} is the input field, and θ the cavity detuning with respect to input field. Space, time, and the field have been suitable rescaled so that Eq. (12.1) is dimensionless. This model was one of the

first proposed to study pattern formation in nonlinear optics [11], and it was shown later that LS are also observed in some parameter regions [12, 13].

It is important to note that in the absence of losses and input, the intra-cavity field can be rescaled ($E \rightarrow Ee^{i\theta t}$) to remove the detuning term and (12.1) becomes the nonlinear Schrödinger equation (NLSE). As it will be explained later in more detail, the dynamics of LS in this system is connected with the collapse of the 2D solitons in the NLSE.

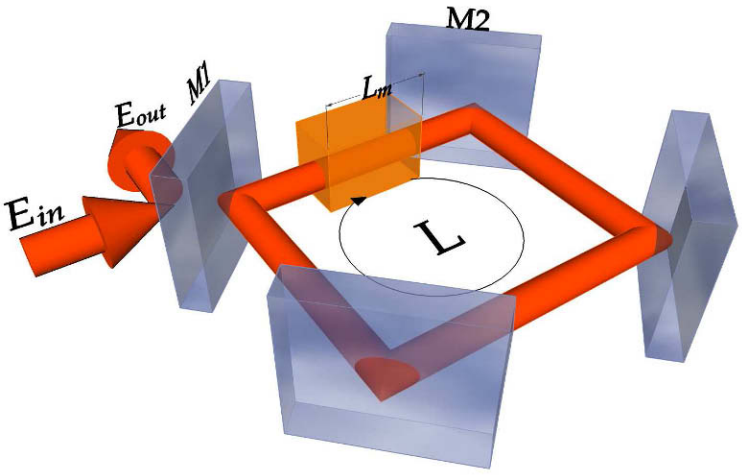

Fig. 12.1 Ring cavity of length L filled with a nonlinear medium of length L_m. Mirror M1 is only partially reflecting, so that the cavity can be driven by E_{in} and read out with E_{out}.

Equation (12.1) has a homogeneous steady-state solution which is implicitly given by $E_s = E_{in}/[1+(i(\theta - I_s)]$, where $I_s = |E_s|^2$. For convenience, we will use in the following the intra-cavity background intensity I_s, together with θ, as our control parameters. It is well known that the homogeneous solution shows bistability for $\theta > \sqrt{3}$. Here we will restrict ourselves to $\theta < \sqrt{3}$ so that I_s is unique once E_{in} is determined. For $I_s > 1$ the homogeneous solution is modulationally unstable and dynamical hexagonal patterns are formed. The bifurcation is subcritical and stationary hexagonal patterns are stable below threshold [14, 15]. In this situation, LS typically exist and their dynamics and interactions are the subject of study in the rest of this chapter.

12.3 Overview of the behavior of localized states

The bistability of the pattern and homogeneous solutions is at the origin of the existence of stable LS that appear when suitable (localized) transient perturbations are applied. The LS can be seen as a solution which connects a cell of the pattern with

the homogeneous solution. While the existence of LS in this bistable regime is quite generic in extended systems [16, 17], their stability strongly depends on the particularities of the system. Using a Newton method it is possible to find the stationary LS solutions with arbitrary precision and determine their stability by diagonalizing the Jacobian. Complemented with numerical simulations, this method allows to gain insight into the structure of the phase space of the system [18, 19, 1].

12.3.1 Hopf bifurcation

Early studies already identified that LS may undergo a Hopf bifurcation leading to a oscillatory behavior [12]. The oscillatory instabilities [20], as well as azimuthal instabilities, were fully characterized later [10]. Interestingly, the oscillations of the LS show the connection of Eq. (12.1) with the NLSE. The growth of an LS during the oscillations resembles the collapse regime observed for solitons in the $2D$ (or $2+1$) NLSE. In this case, however, after some value is attained for the electric field, E, dissipation arrests this growth. This also explains why, despite LS are also observed in 1D [21], oscillations are not present in that case, since collapse does not occur in the 1D NLSE.

As one moves in parameter space away from the Hopf bifurcation, the LS oscillation amplitude grows and its frequency decreases. Eventually, the limit cycle touches the middle-branch LS in a saddle-loop bifurcation which leads to a regime of excitable dissipative structures [22, 19]. In the next two subsections we briefly explain the saddle-loop bifurcation and the excitable regime. For an extensive analysis of this scenario see, for instance, Ref. [1].

12.3.2 Saddle-loop bifurcation

A saddle-loop or homoclinic bifurcation is a global bifurcation in which a limit cycle becomes biasymptotic to a saddle point, or, in other terms, becomes the homoclinic orbit of the saddle, i.e., at criticality a trajectory leaving the saddle point through the unstable manifold returns to it through the stable manifold. Thus, at one side of this bifurcation one finds a detached limit cycle (stable or unstable), while at the other side the cycle does not exist any more, only its *ghost*, as the bifurcation creates an exit slit that makes the system dynamics to leave the region in phase space previously occupied by the cycle. Therefore, after the bifurcation the system dynamics jumps to another available attractor. In the present case this alternative attractor is the homogeneous solution.

The fact that the bifurcation is global, implies that it cannot be detected locally (a local eigenvalue passing through zero), but one can still resort to the Poincaré map technique to analyze it, and, interestingly, the main features of the bifurcation can be understood from the knowledge of the linear eigenvalues of the saddle [23].

The case studied here is the simplest: a saddle point with real eigenvalues, in a 2-dimensional phase space. Strictly speaking, in our case the saddle has an infinite number of eigenvalues, but only two eigenmodes take part in the dynamics close to the saddle [19].

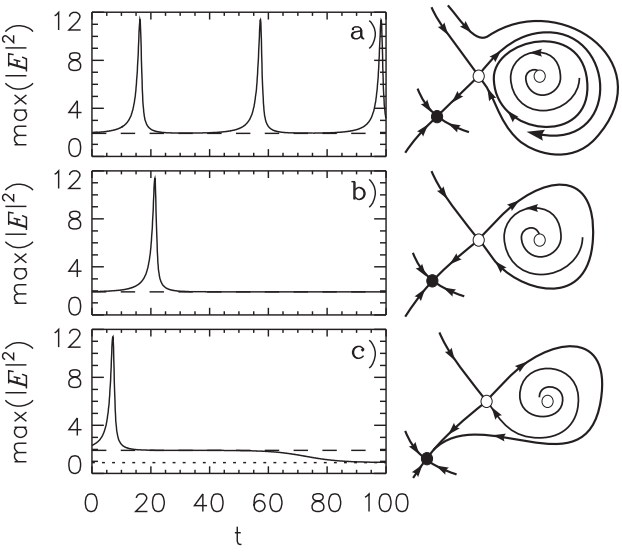

Fig. 12.2 Left: time evolution of the maximum of the LS plotted for three different values of the detuning: a) just below, b) at the saddle-loop bifurcation, and c) just above. Right: sketch of the phase space for each situation.

To identify such a transition one can study the period of the cycle close to this bifurcation, and to leading order it must be given by [24],

$$T \propto -\frac{1}{\lambda_u} \ln|\theta - \theta_c| \,, \tag{12.2}$$

where λ_u is the unstable eigenvalue of the saddle and θ_c the critical value of the detuning. Numerically the bifurcation point is characterized by the fact that approaching from the oscillatory side the period diverges to infinity, and also because past this bifurcation point the LS disappears and the system relaxes to the homogeneous solution as shown in Fig. 12.2.

A logarithmic-linear plot of the period versus the control parameter exhibits a linear slope according to the theoretical prediction (12.2), whit λ_u obtained from the linear stability analysis of the saddle [19].

12.3.3 Excitability

As in our case the saddle-loop bifurcation involves a fixed point (the homogeneous solution), on one side of the bifurcation, and an oscillation, on the other, the system is a candidate to exhibit excitability [25]. It must be stressed that excitable behavior is not guaranteed *per se* after a saddle-loop bifurcation, and, in particular one needs a fixed point attractor that is close enough to the saddle point that destroys the oscillation. The excitability threshold in this type of systems is the stable manifold of the saddle point, what implies that the observed behavior is formally Class I Excitability [25].

This excitability scenario was first shown in Ref. [22]. Fig. 12.3 shows the resulting trajectories after applying a localized perturbation in the direction of the unstable LS with three different amplitudes: one below the excitability threshold, and two above, one very close to threshold and another well above. For the one below threshold the perturbations decays exponentially to the homogeneous solution, while for the two above threshold a long excursion in phase space is performed before returning to the stable fixed point. The refractory period for the perturbation just above the excitability threshold is appreciably longer due to the effect of the saddle. After an initial localized excitation is applied, the peak grows to a large value until the losses stop it. Then it decays exponentially until it disappears. A remnant wave is emitted out of the center dissipating the remaining energy.

At this point it is worth noting that neglecting the spatial dependence Eq. (12.1) does not present any kind of excitability. The excitable behavior is an emergent property of the spatial dependence and it is strictly related to the dynamics of the 2D LS.

Finally, it is interesting to remark that the excitable region in parameter space is quite large and, potentially easy to observe experimentally. While this excitable behavior belongs to Class I (the period diverges to infinity when a perturbation hits the saddle), due to the logarithmic scaling law for the period (12.2), the parameter range over which the period increases dramatically is extremely narrow. Therefore, from an operational point of view, systems exhibiting this scenario might not be classified as Class I excitable, as the large period responses may be easily missed [26].

12.4 Interaction of two oscillating localized states

In the previous section we have reviewed the dynamics of a single LS. In this one we study the interaction between two oscillating LS, and how it affects their dynamics. Oscillating LS are an example of *non-punctual oscillators*, i.e. oscillators with an internal structure. The interaction between such oscillatory structures through the tails can not be, in general, reduced to a simple coupling term between oscillators, but it modifies the internal structure of the oscillators themselves, affecting the dynamics in a nontrivial way. The interplay between the coupling and the internal

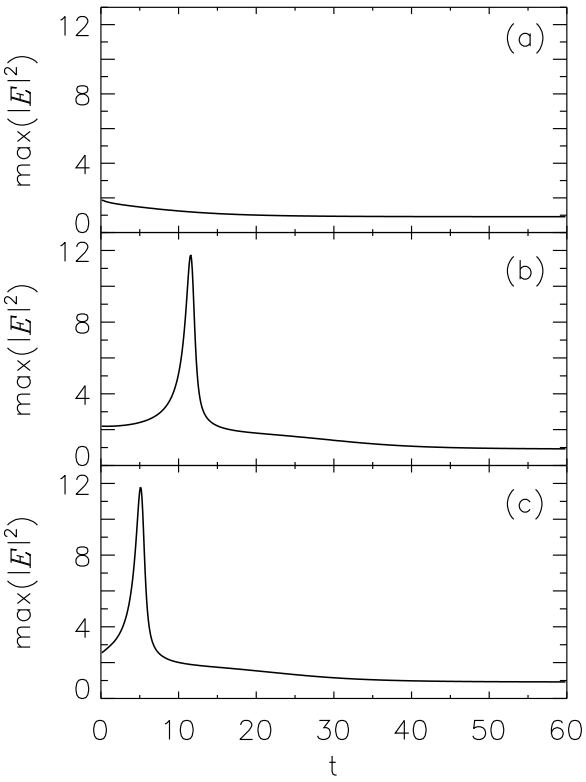

Fig. 12.3 Time evolution of the maximum intensity starting from the homogeneous solution plus a localized perturbation of the form of the unstable LS below (blue dashed line), just above (green solid line) and well above (red dotted line) threshold.

structure of non-punctual oscillators is a general phenomenon not well understood. This chapter aims to be an approach to the subject.

We will first describe in section 12.4.1 the dynamics of two coupled oscillating LS in the full system, and then in section 12.4.2 we will study how much of the observed dynamics can be explained by means of a simple model for two coupled oscillators, and which effects can or can not be attributed to the spatial extension of the oscillators.

12.4.1 Full system

Throughout this section we will set $I_s \sim 0.84$, and $\theta = 1.27$ corresponding to a region of oscillatory structures [22, 19]. This value of I_s is close to the modulational instability that occurs at $I_s = 1$, and because of this LS have large tails. As the

interaction between the structures is mediated by these tails, working in this region has the advantage that the interaction is strong and its effects are more evident.

Localized structures in this system have an intrinsic intensity profile with spatially oscillatory tails, and since the system is translationally invariant, the structures are free to move once created. When two stationary structures are placed close to each other, the presence of an adjacent structure sets only a discrete set of relative positions at which the structures can anchor, given by the intensity profile of the tails. Then if the structures are placed at arbitrary positions they will move until they sit at the zeros of the gradient of this intensity profile. This locking has been studied, both theoretically and experimentally, for stationary localized structures only [6, 7, 8].

Similarly to what happens with stationary LS, when two oscillatory localized structures are placed close to each other they move until they get locked by the tail interaction. For the selected parameters we observe three equilibrium distances that are $d_1 \sim 7.8, d_2 \sim 15.8$ and $d_3 \sim 19.9$. Beyond d_3 the interaction is so weak that the structures can be considered as independent. The movement of the structures from an arbitrary position towards the equilibrium distances is very slow compared with the oscillation period. Therefore we will restrict ourselves to study the behavior of the system when the structures are at the equilibrium distances, to avoid long transient times and complex effects introduced by the movement of the LS.

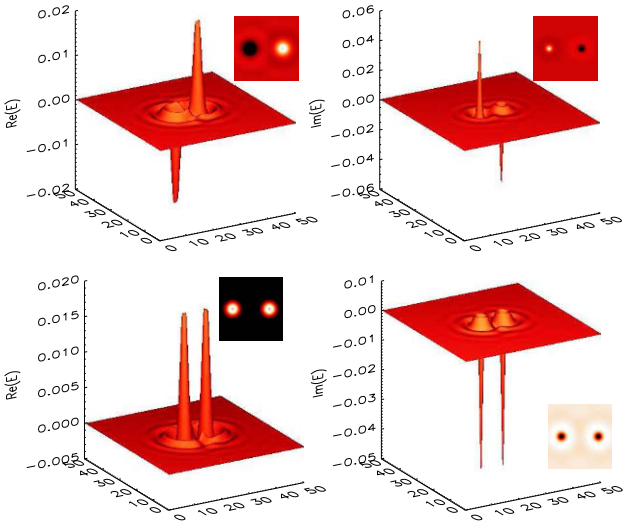

Fig. 12.4 Anti-phase (top) and in-phase (bottom) modes for $I_s = 0.86$ and $d = d_1 = 7.8$. These modes have been obtained from a full 2D linear stability analysis.

A single LS undergoes a Hopf bifurcation at $I_s = 0.8413$ and starts to oscillate. At the bifurcation point this solution has then two complex conjugate eigenvalues whose real part becomes positive with an imaginary part different from zero.

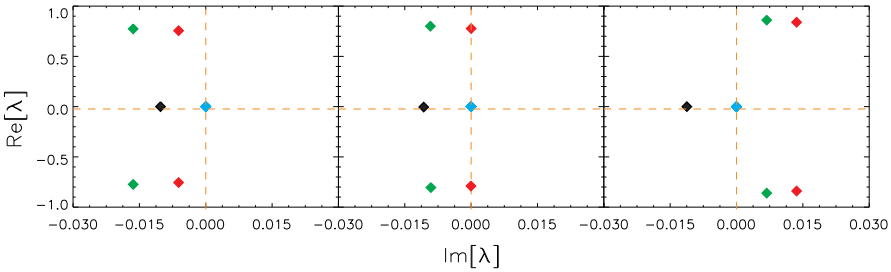

Fig. 12.5 Hopf bifurcation for two coupled LS at $d = d_1$. From left to right, Is=0.81,0.8266,0.83. Red and green dots are the eigenvalues corresponding to the anti-phase and in-phase modes respectively. The blue dots are three zero eigenvalues of the three Goldstone modes of the system of two LS, corresponding to global translations in the x and y directions, and to the rotation of the pair. The black dot is a damped mode associated with perturbations that modify the distance between the two LS.

If we now consider two very far apart (non interacting) structures the system has globally two degenerate pairs of Hopf unstable eigenvalues. Since in this case the structures are independent from each other, they become simultaneously unstable at $I_s = 0.8413$ and the LS can oscillate at any relative phase.

If the two LS are now placed closer together, at one of the equilibrium positions, the structures are no longer independent. Now the interaction breaks the degeneracy of the spectrum splitting the eigenvalues in two different pairs of complex conjugates: a pair corresponding to in-phase oscillations and other to anti-phase oscillations (Fig. 12.4). Since the eigenvalues of these modes are no longer degenerate, increasing the driving, one of these two pairs will cross the Hopf bifurcation first (see Fig. 12.5). Because of the splitting, the threshold of the mode that become first unstable is, generically, lower that the threshold of the single LS. Physically this is due to the fact that the coupling can transfers energy from one LS to the other, such that the collective oscillation can have a lower threshold that a single LS. Although the splitting takes place mainly in the direction of the real axis, the imaginary part is also slightly modified, so the two new cycles have different frequencies. This degeneracy breaking mechanism is crucial to understand the interaction of these LS.

For $d = d_3$ the interaction is very weak, and the degeneracy is merely broken. The real part of the eigenvalues corresponding to the in-phase and anti-phase oscillations become positive almost simultaneously, although the in-phase cycle appears first at $I_s = 0.8412$, very close to the threshold of an isolated LS. As a result, the in-phase solution is stable close to the bifurcation and the anti-phase solution is created just after and it is unstable. The stability is, however, interchanged for larger values of the input intensity in favor of the antiphase solution. This is illustrated in Fig. 12.6a, where the bifurcation diagram of the in-phase and anti-phase cycles is shown for the third equilibrium distance d_3.

For $d = d_2$ the difference between the two pairs of eigenvalues is still very small but, this time, the anti-phase mode crosses the Hopf bifurcation first. The changes in the threshold are still almost imperceptible. The anti-phase solution remains then

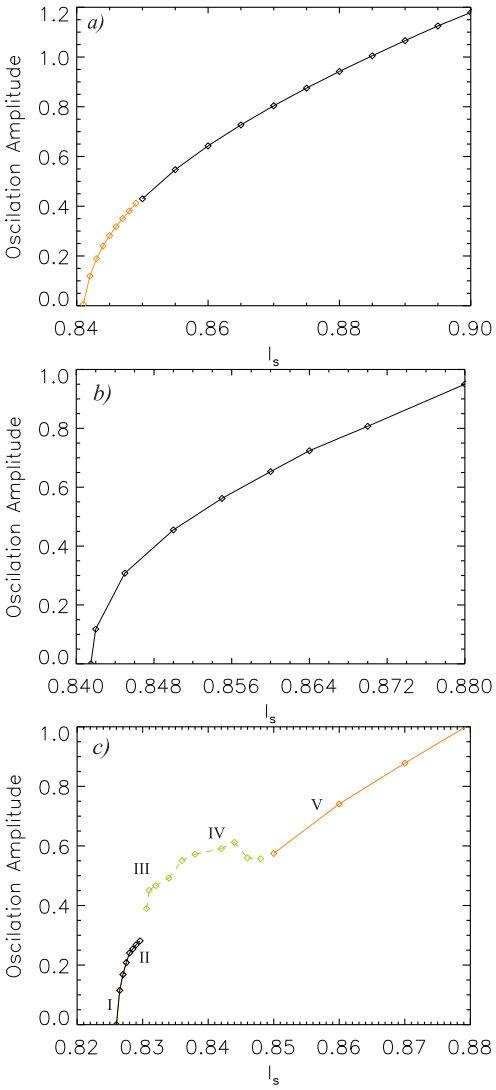

Fig. 12.6 Amplitude of the in-phase (orange), anti-phase (black) and mixed (green) oscillations as a function of I_s for the first three equilibrium distances: a) $d_3 = 19.9$, b) $d_2 = 15.8$, and c) $d_1 = 7.8$.

stable for all values of the input intensity (Fig. 12.6 b). In this case the inphase solution is always unstable.

Finally for $d = d_1$ the degeneration is completely broken, and the anti-phase mode crosses the Hopf bifurcation much before than the in-phase one, as shown in Fig. 12.5. For this the closest distance the interaction is quite strong and the situation is more complicated. First the stable anti-phase limit cycle is created at $I_s \simeq 0.8266$, much before that the threshold of an isolated LS. Initially, both structures have the

same oscillation amplitude. At $I_s \simeq 0.828$ there is a symmetry breaking bifurcation and the oscillation amplitude of the two structures becomes different, i.e. the two structures oscillate around the same mean value in anti-phase but with different amplitudes (regime II in Fig. 12.6c). The difference in the oscillation amplitude between the two structures grows gradually with I_s. An interesting effect due to the extended nature of the solutions is that in this region the pair of LS moves due to the asymmetry [27]. The centers of the two structures drift along the x axis in the direction of the structure with larger oscillation amplitude. For larger I_s the unstable in-phase limit cycle is created and it becomes stable at $I_s = 0.84$. In this case we observe also a third branch connecting the in-phase and anti-phase cycles corresponding to a mixed mode. Since the two cycles have a slightly different frequency, this mode presents a beating at the frequency difference of the in-phase and anti-phase modes.

This situation is illustrated in detail in Fig. 12.7. Each of the panels in the figure corresponds to one of the tags in Fig. 12.6c, showing a time trace of each dynamical regime. Fig. 12.7 I shows the anti-phase oscillations. Increasing I_s, we reach the regime where the anti-phase oscillations are asymmetric (Fig. 12.7 II). Further increasing I_s the anti-phase cycle become unstable and the amplitude of the oscillations is modulated by a slow frequency. Close to the anti-phase cycle the fast oscillations of this modulated cycle are almost in anti-phase (Fig. 12.7 III). Near the end of this branch the fast oscillations are almost in phase (Fig. 12.7 IV). Finally, the amplitude of the modulations decreases until we reach a the regime of in-phase oscillations (Fig. 12.7 V).

12.4.2 Simple model: two coupled Landau-Stuart oscillators

As the oscillating LS are extended oscillators it is interesting to wonder which part of the dynamics observed in the previous subsection can be attributed to the extended nature of the LS and which one simply to two coupled oscillators. To try to discern these to components in the dynamics we consider a simple model describing two interacting limit cycle oscillators close to a Hopf bifurcation, namely two coupled Landau-Stuart (L-S) equations. We give some hints on how to determine the effective parameters of these pair of equations from the full system, and describe the different dynamical regimes that arise from them.

We try to understand, then, the interaction of two oscillating LS in terms of a phase-amplitude reduction of two subsystems close to a Hopf bifurcation. In their classical paper Aronson *et al.* [28] analyze this situation. They arrive to a center manifold reduction for two limit cycles that allows to write the interaction in terms for the complex amplitudes A_1 and A_2 of two Landau-Stuart oscillators,

$$\begin{aligned} \dot{A_1} &= A_1[\mu + i\omega - (\gamma + i\alpha)|A_1|^2] + (\beta + i\delta)(A_2 - \kappa A_1) \\ \dot{A_2} &= A_2[\mu + i\omega - (\gamma + i\alpha)|A_2|^2] + (\beta + i\delta)(A_1 - \kappa A_2) \end{aligned} \tag{12.3}$$

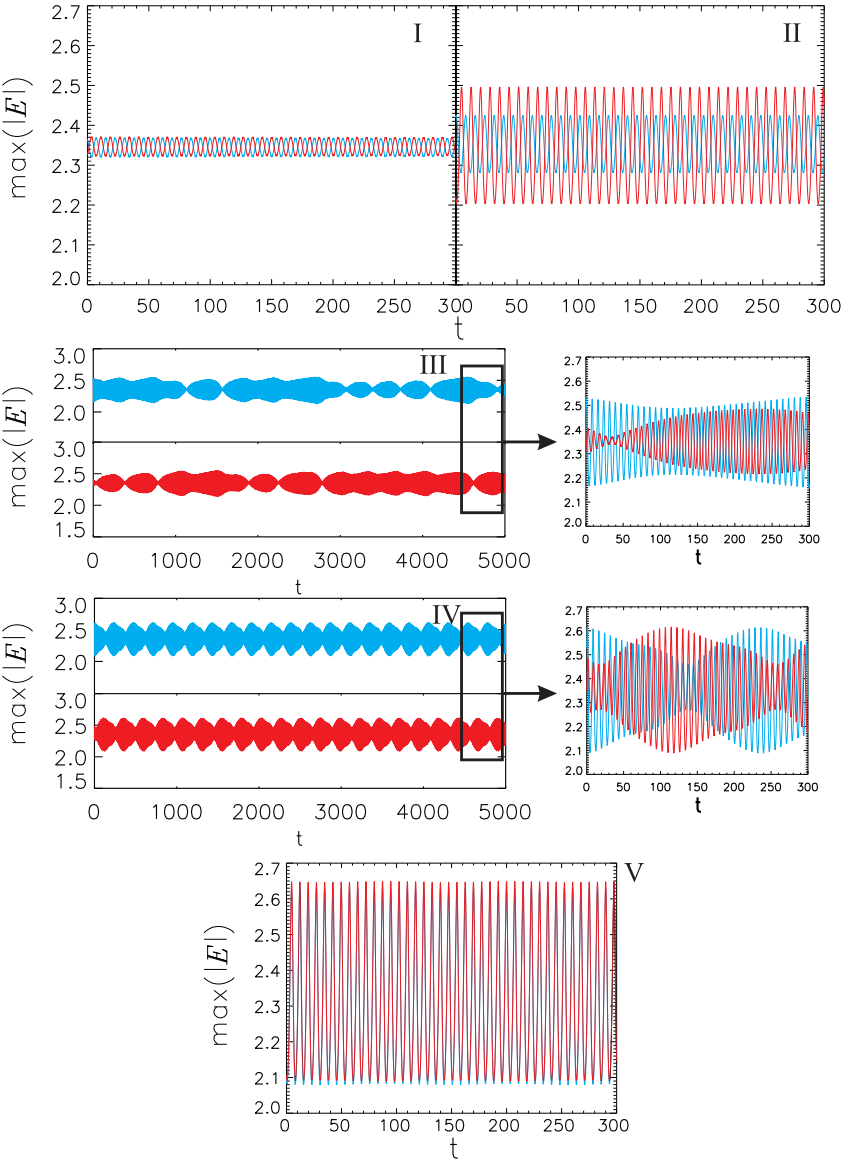

Fig. 12.7 Time traces of the maximum of the two LS for different values of I_s. Each panel corresponds to one of the tags of Fig. 12.6.

Here, for clarity, we have not rescaled the parameters of the oscillators and the only assumption we have done is that both oscillators are identical. With the presence of the parameter δ we consider the most general case of a nonscalar coupling (other authors also call it reactive, elastic or nondiagonal coupling). Physically, in a mechanical system, this couples momentum coordinates to position and/or viceversa. In optics this corresponds to the coupling associated to diffraction (in the paraxial approximation). Its most important consequence is that it couples amplitude with phase, breaking thus, the usual assumption that we can describe coupled oscillators only through their phases and neglecting amplitudes.

Another important ingredient that allows for a rich dynamical behavior is non-isochronicity, i.e., the nonlinear dependence of the frequency with the amplitude (also called shear or nonlinear frequency pulling in the literature) given by α. We note also that we have included, as in [28], the $\kappa \in [0,1]$ parameter, such that $\kappa = 1$ corresponds to the usual coupling (diffusive in the case that $\delta = 0$), while $\kappa = 0$ corresponds to direct coupling (no self-interaction term).

From these equations, using $A_{1,2} = R_{1,2}\exp(i\theta_{1,2})$, one can obtain the following equations in polar coordinates

$$\dot{R}_1 = R_1(\mu - \beta\kappa - \gamma R_1^2) + R_2(\beta\cos\psi - \delta\sin\psi) \tag{12.4}$$

$$\dot{R}_2 = R_2(\mu - \beta\kappa - \gamma R_2^2) + R_1(\beta\cos\psi + \delta\sin\psi) \tag{12.5}$$

$$\dot{\psi} = \alpha(R_1^2 - R_2^2) - \beta\sin\psi\left(\frac{R_1}{R_2} + \frac{R_2}{R_1}\right) + \delta\cos\psi\left(\frac{R_1}{R_2} - \frac{R_2}{R_1}\right) \tag{12.6}$$

where the phase difference $\psi = \theta_2 - \theta_1$ is the only relevant angular variable, due to the invariance symmetry under transformations with respect to the global phase exhibited by the evolution equations.

Let us first analyze the two symmetric solutions, with $R = R_1 = R_2$, the in-phase and the anti-phase solutions. As they are fixed point solutions, both of them satisfy

$$\mu - \beta\kappa - \gamma R^2 + \beta\cos\psi = 0 \tag{12.7}$$

or,

$$R^2 = [\mu + \beta(1-\kappa)]/\gamma \tag{12.8}$$

for the in-phase solution ($\psi = 0$), and

$$R^2 = [\mu - \beta(1+\kappa)]/\gamma \tag{12.9}$$

for the anti-phase one ($\psi = \pi$). As the amplitude (squared) for an uncoupled oscillator is $R_u^2 = \mu/\gamma$, we note that, for positive β (attractive coupling), except for the so-called diffusive coupling ($\kappa = 1$), the amplitude of the in-phase solution is *bigger* than the amplitude of an uncoupled oscillator. The opposite would happen for repulsive coupling $\beta < 0$. Similarly, for attractive coupling ($\beta > 0$) the amplitude of the anti-phase synchronized solution is *smaller* compared with the uncoupled oscillator (the opposite would happen for repulsive coupling).

12.4.2.1 Estimation of parameters I

From the previous results one gets a procedure to determine some effective parameters from the full model. Comparing the amplitudes of the in-phase and anti-phase symmetric solutions, and keeping all parameters fixed, from Eqs. (12.8) and (12.9) one gets

$$\begin{aligned} R_{inp}^2 - R_u^2 &= \beta(1-\kappa)/\gamma \\ R_u^2 - R_{antip}^2 &= \beta(1+\kappa)/\gamma \end{aligned} \tag{12.10}$$

where R_u is the amplitude of single uncoupled oscillator, and R_{inp} and R_{antip} are the amplitudes of the in-phase and anti-phase limit cycles respectively. As shown in Fig. 12.6, R_{inp} and R_{antip}, as well as R_u, can easily be calculated from the numerical integration of the full model (12.1). Then, κ and β/γ can be obtained from the system of two equations (12.10):

$$Q = \frac{R_{inp}^2 - R_u^2}{R_u^2 - R_{antip}^2} = \frac{1-\kappa}{1+\kappa}$$

$$\kappa = \frac{1-Q}{1+Q} \tag{12.11}$$

$$\frac{\beta\kappa}{\gamma} = R_u^2 - \frac{1}{2}(R_{inp}^2 + R_{antip}^2) \tag{12.12}$$

We note that measuring R_u, R_{inp} and R_{antip} for the same values of the parameters require working in a region of coexistence between in-phase and anti-phase oscillations. This is not necessarily possible and the stability of the two limit cycles must be first checked. Nevertheless in some cases it is possible to measure R_{inp} or R_{antip} even if one of these solutions is unstable. In order to do so, the growth rate of the unstable mode must be much slower that the frequency of the cycle, so that starting from an initial condition close to the unstable solution one can observe several oscillations where the radius does not change significantly.

We have also assumed here that κ, as well as β and δ are the same for the in-phase and anti-phase solutions. This is again not guaranteed, due to the spatial nature of the oscillators, and the coupling could depend explicitly on the shape of the solutions. In any case, for weak interaction (long distance between oscillators) this should be a reasonable first order approximation.

12.4.2.2 Estimation of parameters II: quenching experiments

In [29] Hynne and Sorensen reported a method to determine the coefficients of the cubic term of the Landau-Stuart normal form of a Hopf, namely γ and α. This is based on a so-called quenching experiment[1], in which one makes a perturbation of

[1] A theory of quenching is presented in [30]

a system sitting on a stable limit cycle to make it jump momentarily on the unstable fixed point (focus) in its center. One then measures quantitatively the return of the trajectory to the limit cycle attractor. The procedure goes as follows. One starts with a single, uncoupled, Landau-Stuart oscillator,

$$\dot{A} = A[\mu + i\omega - (\gamma + i\alpha)|A|^2], \tag{12.13}$$

or in polar representation

$$\dot{R} = R(\mu - \gamma R^2) \tag{12.14}$$

$$\dot{\theta} = \omega - \alpha R^2, \tag{12.15}$$

being the limit cycle defined by $R_u = \sqrt{\mu/\gamma}$ and the unstable focus at its center by $R = 0$. Then, one can determine the slope $s_{1/2}$ of the tangent to a time series of the radius at the half amplitude point $R = R_u/2$ (see Fig. 12.8) from a quenching experiment. Using Eq. (12.14),

$$s_{1/2} = \left.\frac{dR}{dt}\right|_{R=R_u/2} = \frac{\mu R_u}{2} - \frac{\gamma R_u^3}{8} = \frac{\gamma R_u^3}{2} - \frac{\gamma R_u^3}{8} = \frac{3}{8}\gamma R_u^3$$

and γ can be determined as,

$$\gamma = 8s_{1/2}/3R_u^3. \tag{12.16}$$

To determine the nonisochronicity α one has to analyze the dynamics of the phase θ. From Eq. (12.15) one obtain that

$$\alpha = \Delta\omega/R_u^2 \tag{12.17}$$

where $\Delta\omega$ is the difference between the frequency of *infinitesimally small oscillations* and the frequency of the stable limit cycle. The frequency of the small oscillations around the unstable fixed point is given by the imaginary part of the unstable eigenvalue of the focus, which can be determined exactly from a linear stability analysis. The frequency of the stable limit cycle is easily determined from a numerical simulation of the full system.

Finally, knowing how to determine γ, β can be obtained from (12.12), and μ can also be easily estimated from the amplitude of the limit cycle R_u. Thus, all the parameters of the system have been estimated, except for the reactive coupling coefficient δ, determined in the next section.

12.4.2.3 Estimation of δ

To obtain the reactive coupling coefficient δ one needs to study the relaxation of two coupled oscillators to a stable limit cycle after an asymmetric perturbation. In particular, it can be seen that the dynamics of the two oscillators close to the limit cycle depends directly on the value of δ [31]. Then, to determine this coefficient we

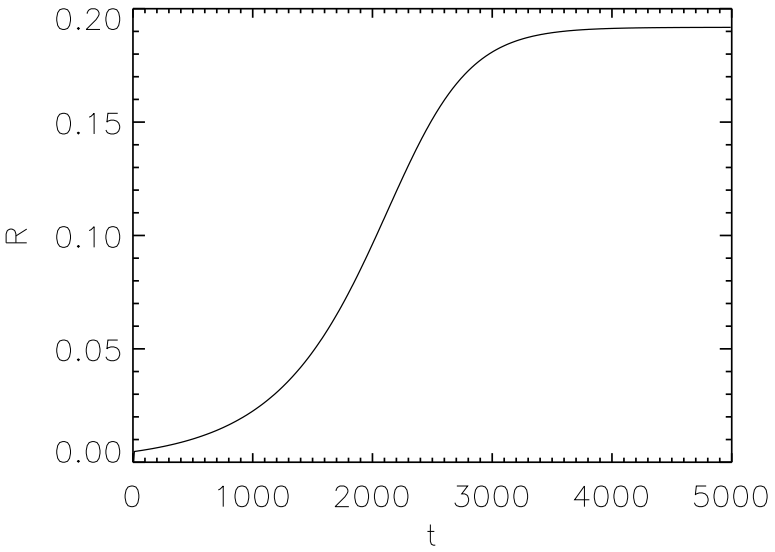

Fig. 12.8 Time trace of the maximum of a LS (R) in a quenching experiment starting from the unstable focus.

have performed systematically simulations of the simple model starting from the same asymmetric initial condition, and different values of δ. We then compare the results with a simulation of the full model where the two LS have been initialized with equivalent phases and radius than the two Landau-Stuart equations, and we choose the value of δ that better fits the dynamics of the full system.

Fig. 12.9 shows the evolution of the full and simple models for equivalent initial conditions and the best value of δ. There is a very good agreement between the dynamics of the two models, although this is the most difficult and less accurate estimation of all.

12.4.2.4 Results and dynamical regimes of the simple model

As a result of the procedures described above, we obtained the following parameters for the largest distance d_3:

For these parameters the dynamics of the two Landau-Stuart equations acceptably reproduce the dynamics observed for d_3 and, possibly for d_2. Fig. 12.10 shows the results of the stability analysis of the in-phase and anti-phase solutions of Eq. (12.3) for the parameter values given in Table 12.1. For small positive values of δ the in-phase solution is stable, while the anti-phase solution is unstable. The opposite situation occurs for small negative values of δ. In the previous Section we

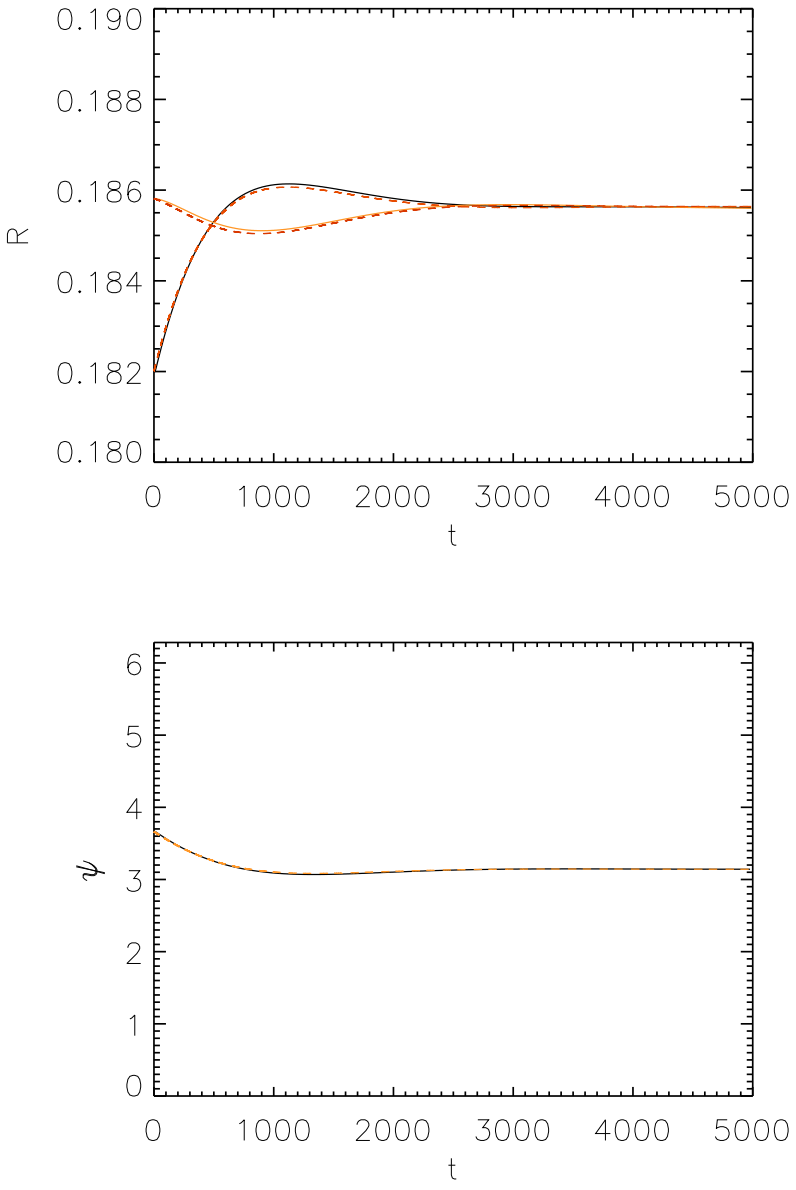

Fig. 12.9 Time evolution of the radius R of each oscillator, and their relative phase ψ, for the full system (solid lines) and the simple model of two coupled Landau-Stuart equations (dashed lines) after applying an asymmetric perturbation to the stable anti-phase limit cycle. For the right value of δ there is a very good agreement between the evolution of the two systems.

I_s	μ	κ	γ	α	β
0.843	0.0015843930	2.26433	0.04300	-0.26699925	2.97237×10^{-5}
0.845	0.0034164778	1.89287	0.04256	-0.28231057	3.51847×10^{-5}
0.847	0.0052667790	1.63081	0.04249	-0.27617558	3.93145×10^{-5}
0.849	0.0070653138	1.51109	0.04208	-0.27851949	4.09333×10^{-5}
$\delta = 9\times10^{-5}$					

Table 12.1 Estimated parameters for $d = d_3$.

estimated $\delta = 9\times10^{-5}$, which is in agreement with the fact that for $d = d_3$ we observe the in-phase solution to be stable close to the Hopf bifurcation while the anti-phase solution is unstable, although the simple model do not capture the interchange of stability observed in the full model for larger values of the input intensity. The estimation of δ is, however, not very accurate and since the value of δ is so small, the error bars would include both positive and negative values. Nevertheless, the fact that we find δ to be close to zero makes possible the fact that for $d = d_2$ we observe the opposite situation than for $d = d_3$, namely that the anti-phase solution is stable and the in-phase solution unstable, although we have not estimated the parameters for that distance.

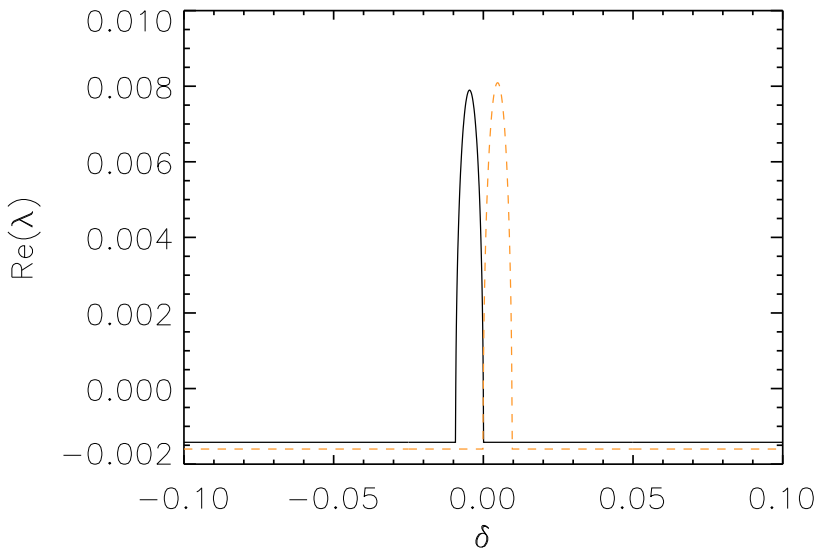

Fig. 12.10 Real part of the eigenvalues of the in-phase (solid line) and anti-phase (dashed line) limit cycles of the two coupled Landau-Stuart equations as a function of δ for the estimated parameters (Table 12.1).

In principle, this approach assumes that the only parameters that change from one distance to another are those associated with the coupling, i.e. α, β and κ, while those of an isolated oscillator remain the same. In the case of $d = d_1$, the interaction is so strong that we can not use the techniques explained above to estimated the parameters. We have then explored numerically different values of the parameters of the coupling, but we have not found any region where the simple model can exactly reproduce the dynamics of the full model for $d = d_1$. This seems to indicate that this approach is to simple for this case and that the spatial extension of the oscillators do play a role in the complex dynamics. Possibly, the interaction changes somehow the effective values of the parameters of the individual oscillators, or even more, these parameters may not even be constant at all. It is still possible, however, that for more remote effective parameter values, the system of two coupled Landau-Stuart Equation can reproduce, at least partially, the observed regimes, but this needs further investigation.

12.5 Interaction of excitable localized states: logical gates

In this section we explore the possibility of using excitable localized structures to perform logical operations. Computational properties of waves in chemical excitable media (e.g. the Belousov-Zhabotinsky reaction) have been used to solve mazes [32], to perform image computation [33], and also logic gates have been constructed from these (chemical) systems [34, 35, 36]. After all, excitability is a property exhibited by neurons and used by them to perform useful computations [37] in a different way than the more usual attractor neural networks [38, 39].

Optical computing, via photons instead of electrons, has long appealed researchers as a way of achieving ultrafast performance. Photons travel faster than electrons and do not radiate energy, even at fast frequencies. Despite the constant advances and miniaturization of electronic computers, optical computing remains a strongly studied subject. Probably the strategy to follow is not to seek to imitate electronic computers, but rather to try to fully utilize the Physics of these systems, e.g., their intrinsic parallelism.

Most of the systems studied in optical computing applications imply light propagation, for example optical correlators, already commercially used in optical processing applications [40]. Instead, with the goal of designing more compact optical schemes, localized structures have emerged as a potentially useful strategy for information storage, where a bit of information is represented by a LS. One can take this idea a step further and discuss the potential of LS, for carrying out computations, i.e., not just for information storage. In particular, logic gates can be designed using LS. We will show here how an AND and OR gates can be implemented using three excitable LS.

To make use of the excitable regime we use a set of addressing Gaussian beams that allow us to set precisely the distance between excitable spots and control the excitable threshold of each one [41]. Strictly speaking this Gaussian beam changes

slightly the scenario, but the underlying physics remains basically the same as described in section 12.3.3. So, to design a logical gate, we set three addressing beams at proper distances and intensities such that their interaction creates a dynamics whose response to two input perturbations is given by Table 12.2 reproducing an AND and an OR logical gates.

	Input 1	Input 2	Output
OR	0	0	0
	1	0	1
	0	1	1
	1	1	1
AND	0	0	0
	1	0	0
	0	1	0
	1	1	1

Table 12.2 Truth Table of AND and OR logic gates.

In particular we consider three excitable LS in a linear arrangement, with a separation d between them. Three permanent Gaussian localized beams are applied: I_{sh}^{I1} and I_{sh}^{I2} at each side for the input LS, and I_{sh}^{O} in the middle for the output LS. The Gaussian beams fix the spatial position of input and output LS. If there is an excitable excursion in the central localized structure the output is interpreted as a "1" and if there is no excitable response as a "0". At the input, superthreshold perturbations (i.e. causing an excitable excursion) correspond to a bit "1", while subthreshold (or the absence of) perturbations will be considered as a bit "0". Physically, the interaction is mediated by the tails of the structures and the remnant wave that radiate from the LS dissipating the energy to the surroundings during the excitable excursion.

Then, if the distance d between the input LS and the output is small enough, such that the excitable excursion of a single LS at the input is enough to excite an excursion at the output we will have an OR gate. To avoid that the output can excite the input LS I_{sh}^{I1} and I_{sh}^{I2} are smaller than I_{sh}^{O}, so that the excitable threshold of the input LS is too high to be excited by the excitable excursion of the output LS. If we simply make d larger so that the interaction of a single LS is not enough to excite the output, but the combined effect of the two input LS is, we have implemented an AND gate according to Table 12.2.

Fig. 12.11 shows the dynamics or an OR gate for a ("1", "0") input. Applying a similar perturbation to I_{sh}^{I2} [corresponding to ("0", "1")], the same result is obtained. Finally, if we simultaneously apply the same perturbation to both I_{sh}^{I1} and I_{sh}^{I2} [corresponding to ("1", "1")], a similar excitable excursion is obtained for the central (output) LS, as shown in Fig. 12.12.

Figs. 12.13 and 12.14 show the response of an AND gate to a ("1", "0") and a ("1", "1") inputs respectively.

With these two basic gates combined with a NOT gate, not explained here, it is possible to build the two universal logic gates, NAND and NOR, which are the

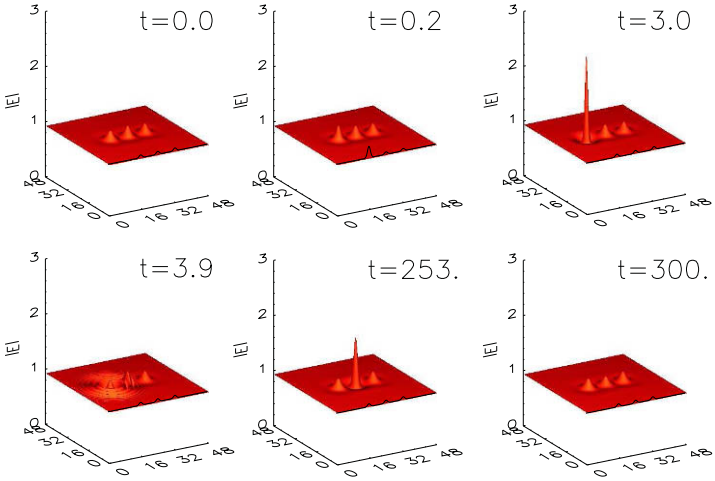

Fig. 12.11 Resonse of an OR logic gate to a ("1", "0") input.

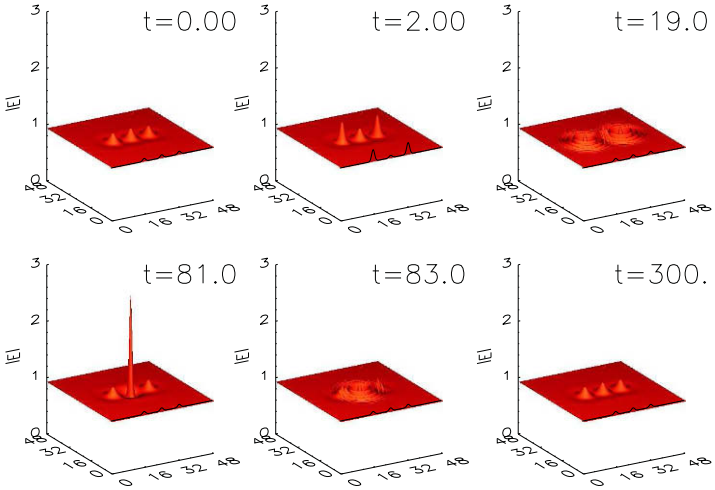

Fig. 12.12 The same as in Fig. 12.11 for a ("1", "1") input.

pillars of logic. In electronics, these gates are built from transistors, but they can be built by means of other technologies. We propose here using excitable LS. We have to note, however, that using excitability to perform computations may imply relatively long times inherent to the slow dynamics close to a fixed point. This drawback can be minimized by properly tuning the parameters of the system and optimizing the form of the perturbations. The aim of this work is just setting the basis of a new way to perform all-optical logical operations using localized states.

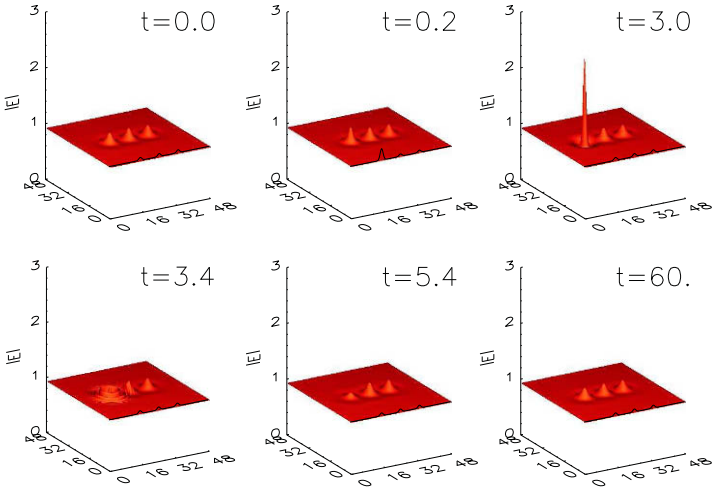

Fig. 12.13 Response of an AND logic gate to a (“1”, “0”)input.

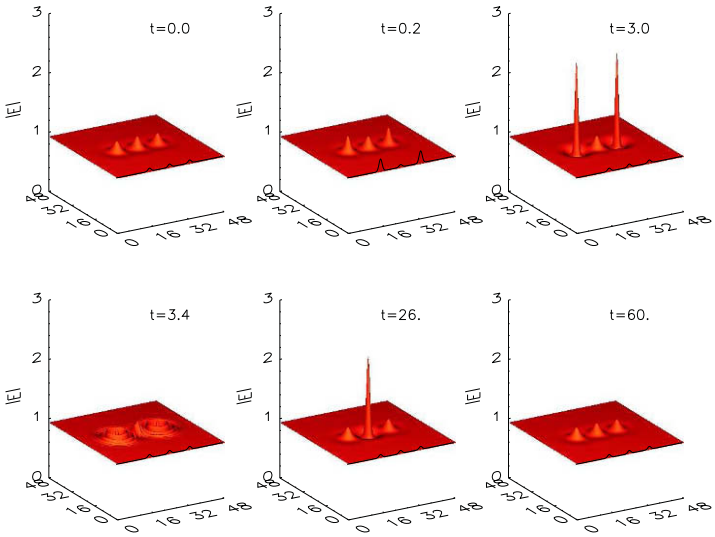

Fig. 12.14 The same as in Fig. 12.13 for a (“1”, “1”) input.

12.6 Summary

It is remarkable how such a simple model as (12.1) can show such a rich and surprising behavior through the dynamics of coherent structures. In particular, localized states show different emergent behavior that can not be explained in terms of the local dynamics of the model, but it is a self-organized phenomenon due to the spatial coupling provided by diffraction. In the first part, we have briefly reviewed two instabilities, namely a Hopf and a saddle-loop bifurcation, that signal the boundaries between three different dynamical regimes: stationary, oscillatory and excitable. An extensive analysis of this scenario can be found in [1].

Then, we have focused in the study of the interaction between two LS in the oscillatory regime. We have shown how the interaction breaks the degeneracy of the spectrum of two LS creating two limit cycles with slightly different frequencies. These two cycles bifurcate also for slightly different values of the control parameter and they correspond to in-phase and anti-phase oscillations. An important issue addressed in this section is the role of the internal structure of LS in the dynamics. For long distances between LS, i.e. weak interaction, we have shown that the dynamics can be reasonable explained by means of two simple coupled oscillators. We have given a simple model and described a method to estimated its parameters from the dynamics of the full system. For the closest distance, however, we observe a much more complex dynamics, and the simple model does not reproduce this behaviour, at least for the adjusted parameters. This seems to indicate that the internal degrees of freedom play a role in the dynamics and that interaction couples, for instance, the movement in the transverse plain with the oscillations.

Finally, in the last section, we have shown how coupling several LS in the excitable regime, one can perform logical operations. This opens the possibility to build new all-optical components to process information based on the use of LS.

References

1. P. Colet, D. Gomila, A. Jacobo, M.A. Matías, *Dissipative Solitons: From Optics to Biology and Medicine* (N. Akhmediev and A. Ankiewicz, eds.) , Springer-Verlag, 113-136 (2008).
2. F.T. Arecchi, S. Boccaletti, and P. Ramazza, Phys. Rep. **318** 1 (1999).
3. L.A. Lugiato, M. Brambilla, and A. Gatti, Adv. Atom. Mol. Opt. Phys. **40** 229 (1999).
4. W.J. Firth and C.O. Weiss, Opt. Photon. News **13** 55 (2002).
5. T. Ackemann, W.J. Firth, and G.-L. Oppo, Adv. Atom. Mol. Opt. Phys. **57** 323 (2009).
6. B. Schäpers, T. Ackemann and W. Lange, Phys. Rev. Lett. **85**, 748 (2000); J. Opt. Soc. Am. B **19**, 707 (2002).
7. P. L. Ramazza, E. Benkler, U. Bortolozzo, S. Boccaletti, S. Ducci, and F. T. Arecchi, Phys. Rev. E **65**, 066204 (2002).
8. P. L. Ramazza, U. Bortolozzo, and S. Boccaletti, Appl. Phys. B **81**, 921 (2005).
9. D. Michaelis, U. Peschel, and F. Lederer, Opt. Lett. **23** 1814 (1998).
10. W. J. Firth, G. K. Harkness, A. Lord, J. M. McSloy, D. Gomila, and P. Colet, J. Opt. Soc. Am. B **19**, 747 (2002).
11. L.A. Lugiato and R. Lefever, Phys. Rev. Lett. **58** 2209 (1987).

12. W.J. Firth, A. Lord, and A.J. Scroggie, Physica Scripta **67**, 12 (1996); W.J. Firth and A. Lord, J. Mod. Optic. **43**, 1071 (1996).
13. A. J. Scroggie, W. J. Firth, G. S. McDonald, M. Tlidi, R. Lefever, and L. A. Lugiato, Chaos, Solitons Fractals **4**, 1323 (1996).
14. D. Gomila and P. Colet, Phys. Rev. A **68**, 011801R (2003).
15. D. Gomila and P. Colet, Phys. Rev. E **76**, 016217 (2007).
16. P. D. Woods and A. R. Champneys, Physica D **129**, 147 (1999).
17. P. Coullet and C. Riera and C. Tresser, Phys. Rev. Lett. **84**, 3069 (2000).
18. J. M. McSloy, W. J. Firth, G. K. Harkness, and G. L. Oppo, Phys. Rev. E **66**, 046606 (2002).
19. D. Gomila, A. Jacobo, M. A. Matías and P. Colet, Phys. Rev. E **75** 026217 (2007).
20. D. V. Skryabin, J. Opt. Soc. Am. B **19**, 529 (2002).
21. D. Gomila, A.J. Scroggie, and W.J. Firth, Physica D **227**, 70 (2007).
22. D. Gomila, M. A. Matías and P. Colet, Phys. Rev. Lett. **94**, 063905 (2005).
23. P. Glendinning, Stability, Instability, and Chaos (Cambridge University Press, Cambridge, England, 1994).
24. P. Gaspard, J. Phys. Chem. **94**, 1 (1990).
25. E. M. Izhikevich, Int. J. Bifurcation Chaos Appl. Sci. Eng. **10**, 1171 (2000).
26. E. M. Izhikevich, Dynamical Systems in Neuroscience (MIT Press, Cambridge, MA, 2006).
27. A.J. Scroggie, D. Gomila, W.J. Firth, and G.-L. Oppo, Appl. Phys. B **81**, 963 (2005).
28. D.G. Aronson, G.B. Ermentrout, and N. Kopell, *Amplitude response of coupled oscillators*, Physica D **41**, 403-449 (1990).
29. F. Hynne and P.G. Sorensen, *Experimental determination of Ginzburg-Landau parameters for reaction-diffusion systems*, Phys. Rev. E **48**, 4106 (1993).
30. F. Hynne, P.G. Sorensen, and K. Nielsen, *Quenching of chemical oscillations: General theory*, J. Chem. Phys. **92**, 1747 (1990).
31. A. Pikovsky, M. Rosenblum, and J. Kurths, *Synchronization*, (Cambridge U.P.,2001).
32. O. Steinbock, A. Tóth, and K. Showalter, Science **267**, 868 (1995).
33. L. Kuhnert, K. I. Agladze, and V. I. Krinsky, Nature **337**,244 (1989).
34. A. Toth and K. Showalter, J. Chem. Phys. **103**, pp. 2058, (1995).
35. O. Steinbock, P. Kettunen, and K. Showalter, J. Phys. Chem. **100**, 18970 (1996).
36. J. Gorecka and J. Gorecki, J. Chem. Phys. **124**, 084101 (2006).
37. C. Koch, *Biophysics of Computation* (Oxford U.P., Oxford, 1999).
38. W. S. McCulloch and W. H. Pitts, Bull. Math. Biophys. **5**, 115 (1943).
39. D. J. Amit, *Modeling brain function* (Cambridge U.P., Cambridge, 1989).
40. E. J. Lerner, Laser Focus World **1**, 99 (2000).
41. A. Jacobo, D. Gomila, M.A. Matías, and P. Colet, Phys. Rev. A **78**, 053821 (2008).

Chapter 13
Lurching waves in thalamic neuronal networks

Jaime E. Cisternas, Thomas M. Wasylenko, and Ioannis G. Kevrekidis

Abstract Numerical bifurcation computations are used to characterize traveling waves for a family of models of thalamic neurons in a network. These models consist of two layers of neurons: one made up of excitatory neurons, and the other of inhibitory ones. The interplay of these two different couplings gives rise to the propagation of activity waves. This article contains some preliminary work on the characterization of the observed waves in a one-dimensional lattice and explores the effects of varying key parameters of the model. The stability of these solutions, as well as the presence of hysteresis and the coexistence of up to three different waves, are most naturally explained in terms of the theory of bifurcations of dynamical systems.

13.1 Introduction

One of the functions of the thalamus is the generation of rhythms that propagate to other regions of the brain during light sleep. This behavior has been also observed in slice preparations of thalamic neurons [18, 1, 12, 16], and in the computational models that have been constructed trying to explain the spatiotemporal behavior of such networks [9, 17, 4, 2, 7, 19, 6]. These minimal models consider two types of

Jaime E. Cisternas
Facultad de Ingeniería y Ciencias Aplicadas, Universidad de los Andes, Santiago, Chile,
e-mail: jecisternas@miuandes.cl

Thomas M. Wasylenko
Department of Chemical Engineering, Princeton University, Princeton, U.S.A. Current address: Department of Chemical Engineering, Massachusetts Institute of Technology, Cambridge, U.S.A.
e-mail: twasylen@mit.edu

Ioannis G. Kevrekidis
Department of Chemical Engineering and Program of Applied and Computational Mathematics, Princeton University, Princeton, U.S.A. e-mail: yannis@princeton.edu

O. Descalzi et al. (eds.), *Localized States in Physics: Solitons and Patterns*,
DOI 10.1007/978-3-642-16549-8_13,

cells: thalamocortical (TC) and reticularis (RE) neurons. In the following we will use the simplification found in the work of Terman et al. [19]: The TC cells are excitatory and project to other RE neurons in the neighborhood, while the RE cells are inhibitory and project to the TC cells located in a short range. The TC-RE pair exhibits the so-called post-inhibitory rebound (PIR), a burst of action potentials that propagate through the network. The mechanism of PIR is the following: the firing of a RE cell lowers the voltage of the neighboring TC cells, priming them to fire, and when the RE cell action potential ends, TC cells are released from inhibition and fire, exciting now other RE neurons in a larger neighborhood.

Rinzel et al. [17] considered a one-dimensional network based on these assumptions and found two basic types of propagating waves: "smooth" and "lurching" waves. The former travel across the lattice (modulo the lattice shift symmetry) in the same way a localized pulse propagates through homogeneous media: every neuron, in sequence, performs the same oscillation as the pulse passes through it. The latter are characterized by clusters of neurons that behave in a more or less synchronized way, as a result of the finite range of the couplings. The apparent time-delay between firing of neighboring clusters gives the propagation a 'saltatory' character. It was conjectured in [17] that the existence of two distinct waves is explained by the characteristics of the inter-neuron coupling as well as the interplay of two time scales. Even if most computational models of thalamic neurons have these two propagating waves, it's not currently possible to apply this classification to waves observed in slice preparations because of the limited spatial resolution of potential measurements.

Terman et al. [19] considered the 'full' network equations of the biophysical model used by Rinzel et al. without introducing simplifications. The authors used geometric methods and suitable limits to study the existence of smooth and lurching waves, arriving at explicit conditions that must be satisfied when a certain type of wave exists, and at formulas that give the speed of the wave in terms of neuronal parameters. Recent advances have been achieved using a simplified integrate-and-fire neuronal model made up of a continuous one-dimensional array of neurons [8, 5]. For this model and inside a certain parameter domain two types of smooth propagating pulses exist, which travel at different speeds. Outside this parameter domain, lurching pulses exist and are stable. In [6] a review of wave phenomena in purely cortical networks is presented, including stability analysis of fast, slow and saltatory pulses, assuming continuous space.

In this work, we explore the behavior of the two-layer model (presented in [19]) using bifurcation theory, but without giving up the discreteness of the neuronal network. Among other works that share the same spirit we should mention [3] and [8], which characterized transitions in neuronal networks using the language of bifurcations. A most helpful tool that we used in this work is the *return map* that represents the evolution of the state of the network during a specified time interval. For some one dimensional waves, it is possible to choose the duration of the interval so the state of the network looks undisturbed, modulo a spatial shift. For waves that don't have this invariance property, we used the *Poincaré map* that captures the evolution of the state of the network when the wave advances a specified number of lattice

sites. The properties of these maps, studied using extensive numerical computations, help to clarify the characterization of the behaviour of the neuronal network and the existence and stability of the propagating waves. As we will show, the full dynamics is far richer than the one extracted from simplified integrate-and-fire or continuous models.

In the next section we present briefly the model introduced in [19], and describe smooth and lurching waves. Section 3 introduces the return map and its fixed points. These fixed points represent the two types of propagating waves. Using continuation we construct branches of solutions, computing how a given solution changes when parameters of the model are varied. The problem of computing unstable solutions is addressed. The discussion in Section 4 contains an assessment of the relevance of the present study in light of the literature, as well as some open problems.

13.2 The model

As was explained in the introduction, several models of thalamic networks have been proposed, most of them based on two distinct populations of neurons. Here we based our work on the model proposed by Terman et al. [19], which exhibits smooth propagating pulses and other waves that propagate by "lurching" a certain number of sites in the lattice. This latter behavior is generated when a cluster of neurons fires at approximately the same time, and induces the delayed firing of another cluster in the direction of propagation. We will use the name 'lurcher' for this kind of pulse. In Ref. [19, Figs. 4 and 5] other propagation patterns were observed, such as trains of smooth pulses or lurchers and lurchers that leave a wake of periodic clustering as they propagate.

The model considers a one dimensional lattice, where each site consists of two neurons. The first cell is an excitatory thalamocortical (TC) neuron and its state is described by the variables v^{TC} (voltage) and h^{TC} (relative suppressive influence). The second cell at the site is an inhibitory reticular (RE) thalamic neuron and is described by the variables v^{RE} and h^{RE}.

For each lattice site $i = 1 \ldots N$, there are four differential equations describing the dynamics of the two neurons:

$$\frac{dv_i^{\mathrm{TC}}}{dt} = -g_L^{\mathrm{TC}}(v_i^{\mathrm{TC}} - e_L^{\mathrm{TC}}) - g_{\mathrm{Ca}}(m_\infty(v_i^{\mathrm{TC}}))^3 h_i^{\mathrm{TC}}(v_i^{\mathrm{TC}} - e_{\mathrm{Ca}}) - g_{\mathrm{TC}} s_\infty(v_i^{\mathrm{RE}})(v_i^{\mathrm{TC}} - e_{\mathrm{syn}}^{\mathrm{RE}}), \tag{13.1}$$

$$\frac{dh_i^{\mathrm{TC}}}{dt} = \varepsilon^{\mathrm{TC}} \frac{h_\infty(v_i^{\mathrm{TC}}) - h_i^{\mathrm{TC}}}{\tau_h(v_i^{\mathrm{TC}})}, \tag{13.2}$$

$$\frac{dv_i^{\mathrm{RE}}}{dt} = -g_L^{\mathrm{RE}}(v_i^{\mathrm{RE}} - e_L^{\mathrm{RE}}) - g_{\mathrm{Ca}}(m_\infty(v_i^{\mathrm{RE}}))^3 h_i^{\mathrm{RE}}(v_i^{\mathrm{RE}} - e_{\mathrm{Ca}}) - \frac{1}{2\omega+1}\left(\sum_{j=-\omega}^{\omega} g^{\mathrm{RE}} s_\infty(v_{i+j}^{\mathrm{TC}})\right)(v_i^{\mathrm{RE}} - e_{\mathrm{syn}}^{\mathrm{TC}}), \tag{13.3}$$

$$\frac{dh_i^{\mathrm{RE}}}{dt} = \varepsilon^{\mathrm{RE}} \frac{h_\infty(v_i^{\mathrm{RE}}) - h_i^{\mathrm{RE}}}{\tau_h(v_i^{\mathrm{RE}})}, \tag{13.4}$$

This set of ordinary differential equations can be represented for future reference by $\dot{x}_i = f_i(\{x_j\})$ or simply $\dot{x} = f(x)$ where $x \in \mathbb{R}^{4N}$.

Clearly the TC neuron receives signals only from the RE neuron at the same site, but the RE neuron receives input from the TC cells in the neighborhood. For this model we have considered a symmetric synaptic footprint that couples each RE neuron to the TC neuron at the same site, to its ω closest neighboring TC cells to the right (ω being a natural number), and to its ω closest neighboring TC cells to the left, resulting in a neighborhood of size $2\omega+1$ (see a schematic in Fig. 13.1).

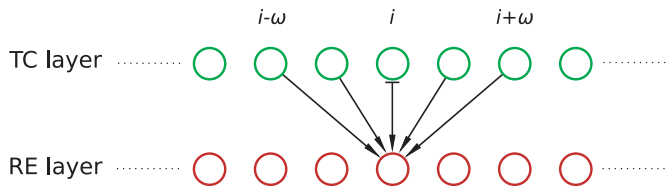

Fig. 13.1 Structure of the neuronal network. In this schematic figure $\omega = 2$ so each RE neuron receives input from the TC neuron at the same site and from the 4 neighboring TC neurons.

The behavior of a single neuron by itself (i.e. without coupling) and the PIR mechanism (postinhibitory rebound) are explained in full detail in Ref. [19]. If a cell receives inhibitory input during a certain time, and then it is released from inhibition, the cell may jump up to the active phase. This behavior can be described by the effect of inhibition on the nullclines in the (v,h) plane of a single cell.

Other functions that appear in equations (13.1–13.4), are bounded and have a sigmoidal shape:

$$
\begin{aligned}
m_\infty(v) &= \left[1+\exp\left(-\frac{v-v_{m,t}}{v_{m,s}}\right)\right]^{-1},\\
h_\infty(v) &= \left[1+\exp\left(-\frac{v-v_{h,t}}{v_{h,s}}\right)\right]^{-1},\\
s_\infty(v) &= \left[1+\exp\left(-\frac{v-v_{s,t}}{v_{s,s}}\right)\right]^{-1},\\
\tau_\infty(v) &= \tau_1+(\tau_2-\tau_1)\left[1+\exp\left(-\frac{v-v_{h,t}}{v_{h,s}}\right)\right]^{-1}.
\end{aligned}
$$

Values for the parameters in all the previous equations were extracted from [19] and are included in the next paragraph.

Instead of performing continuation with respect to one of the natural parameters of the system, we chose a homotopy using a new, nondimensional parameter s. When s varies, four of the natural parameters vary in a correlated way so that for $s=0$ we get a smooth wave ($\varepsilon^{\mathrm{TC}}=1, g^{\mathrm{TC}}=0.03$ ms^{-1}, $g^{\mathrm{RE}}=0.1$ ms^{-1}, $e_{\mathrm{Ca}}=120$ mV) while for $s=1$ we get a wave that propagates discontinuously, appearing to advance six sites and then remaining silent for a small time interval ($\varepsilon^{\mathrm{TC}}=3, g^{\mathrm{TC}}=0.01$ ms^{-1}, $g^{\mathrm{RE}}=0.3$ ms^{-1}, $e_{\mathrm{Ca}}=90$ mV). In this way the lurching wave apparently consists of clusters of siz neurons that behave in a (more or less) synchronized fashion (we analyze this solution in detail in the next section). To see how the transition occurs, we chose to do a one-parameter continuation along a straight line segment in 4-dimensional parameter space:

$$
\begin{aligned}
\varepsilon^{\mathrm{TC}} &= (1-s)+3s\,,\\
g^{\mathrm{TC}} &= 0.03(1-s)+0.01s\ \left[\mathrm{ms}^{-1}\right]\,,\\
g^{\mathrm{RE}} &= 0.1(1-s)+0.3s\ \left[\mathrm{ms}^{-1}\right]\,,\\
e_{\mathrm{Ca}} &= 120(1-s)+90s\ [\mathrm{mV}]\,.
\end{aligned}
$$

For the remaining natural parameters the following values were used: $g_L^{\mathrm{TC}}=0.01\,\mathrm{ms}^{-1}$, $e_L^{\mathrm{TC}}=-75$ mV, $e_{\mathrm{syn}}^{\mathrm{TC}}=0$ mV, $g_L^{\mathrm{RE}}=0.2$ ms^{-1}, $e_L^{\mathrm{RE}}=-80$ mV, $\varepsilon^{\mathrm{RE}}=2$, $e_{\mathrm{syn}}^{\mathrm{RE}}=-80$ mV, $g_{\mathrm{Ca}}=1$ ms^{-1}, $v_t=-20$ mV, $v_s=2$ mV, $v_{h,t}=-79$ mV, $v_{h,s}=5$ mV, $v_{m,t}=-65$ mV, $v_{m,s}=7.8$ mV, $v_{\tau,t}=-65$ mV, $v_{\tau,s}=4$ mV, $\tau_1=1$ ms, $\tau_2=80$ ms, $\omega=6$.

Varying the value of this new parameter s we were able to identify certain details of the transition and the existence of other intermediate states. Even if most of our findings were observed for the particular region of parameter space described by $s\in[0,1]$, we are confident that many features of the picture are ubiquitous across the parameter space of the model.

13.2.1 Smooth and Lurching waves

Using $s = 0.6$, and a localized initial perturbation in v^{TC} (over the homogeneous rest state), the behavior of the neurons will evolve towards a stationary state that has the appearance of a typical pulse-like wave (see Fig. 13.2(a)), invariant in some moving frame $\xi = x - ct$. But our 'space' is a discrete array of neurons, so the analogy may be slightly misleading. Fig. 13.2(b) shows the state of the neurons at a given time. Any two neurons exhibit the same trajectory in time modulo a delay. The curves $v^{\mathrm{TC}}(i,t)$ and $v^{\mathrm{TC}}(j,t+\tau_{ij})$ are the same for some time delay $\tau_{ij} = |i-j|/c$.

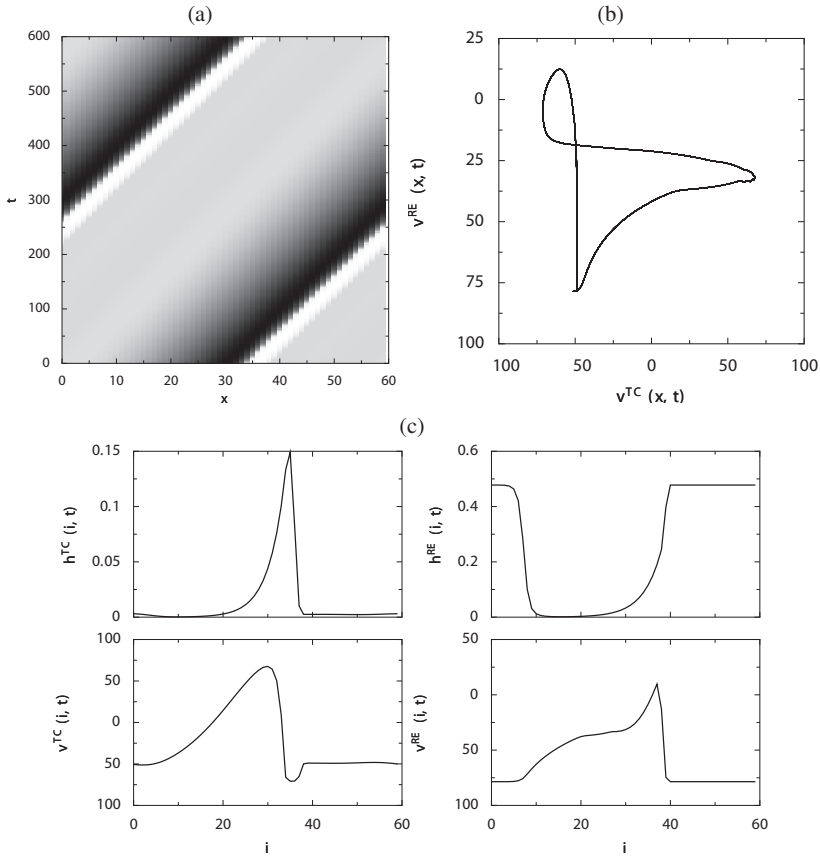

Fig. 13.2 (a) Space-time plot of the potential $v^{\mathrm{TC}}(x,t)$ corresponding to a smooth wave $s = 0.6$. Light shades of gray mean low values of voltage v^{TC}, and dark shades mean high values of v^{TC}. (b) Single-site phase plane for the network. The TC and RE cells located at every single site realize the same dynamics of respective TC and RE cells located at any other site, modulo a temporal delay. (c) Spatial profile of fields $v^{\mathrm{RE}}, v^{\mathrm{TC}}, h^{\mathrm{RE}}, h^{\mathrm{TC}}$ for the same wave.

Increasing the value of the parameter s up to 0.8, we can observe localized waves that advance in a saltatory way. Fig. 13.3(a) shows neurons that tend to synchronize and fire in clusters of six.

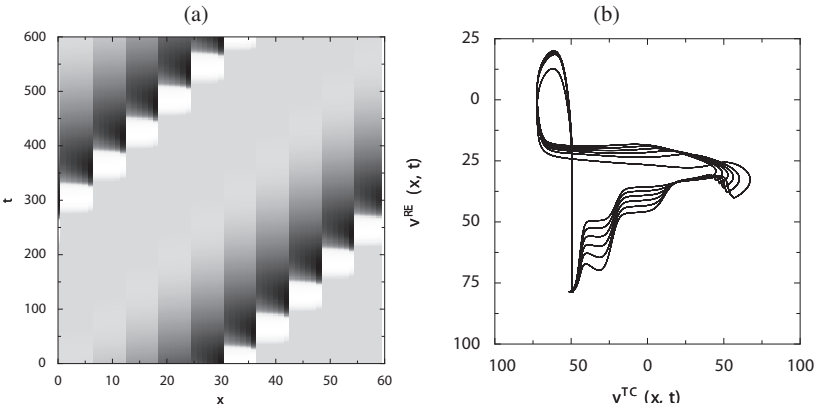

Fig. 13.3 (a) Space-time plot of the potential $v^{\mathrm{TC}}(x,t)$ for a 6-lurching wave $s = 0.8$. Light shades of gray mean low values of voltage v^{TC}, and dark shades mean high values of v^{TC}. (b) Single-site phase plane for cells located at, for instance $x = 1, 2, \ldots, 6$. Neurons, when the wave reaches them, leave the rest state (lowest point) and describe a complicated trajectory. Other neighboring neurons describe slightly different trajectories that depend on the specific location of the neuron within the cluster.

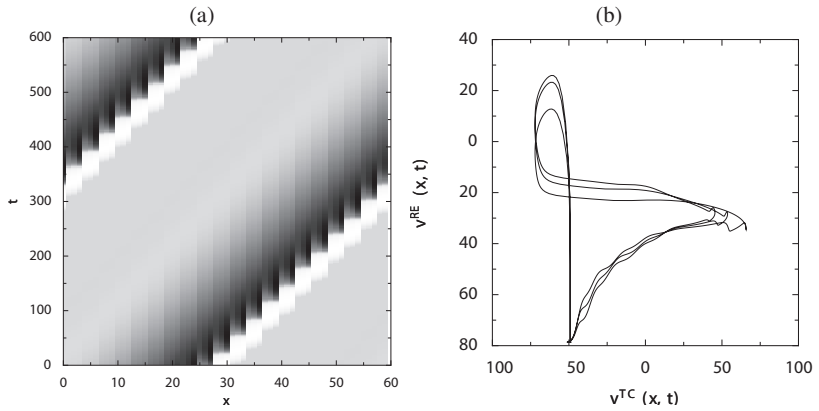

Fig. 13.4 (a) Space-time plot of the potential $v^{\mathrm{TC}}(x,t)$ for a 3-lurching wave $s = 0.76$. Light shades of gray mean low values of voltage v^{TC}, and dark shades mean high values of v^{TC}. (b) Single-site phase plane that shows how neurons describe trajectories that depend on the specific location of the neuron within the cluster.

Within each cluster neurons behave in a similar way, but the synchronization is not perfect, as can be appreciated in Fig. 13.3(b). Two neurons that occupy the same relative location in any two clusters, do behave in the same way modulo a time delay. The curves $v^{\mathrm{TC}}(i,t)$ and $v^{\mathrm{TC}}(i+6m,t+\tau_m)$ are the same for some time delay τ_m. Following Ref. [19] we call this type of a wave, for short, a six-lurcher.

Clusters of sizes 3 and 12 were also observed for other values of the parameters. Fig. 13.4 shows a three-lurcher found at $s = 0.76$. The fact that the observed cluster sizes were multiples of 3 seems to depend on the particular choice of $\omega = 6$ used in this work.

As previously mentioned, when initializing pulse simulations, we used a localized perturbation on the v^{TC} field over the rest state. This disturbance propagates in both directions, but temporarily changing the boundary conditions makes it possible to get rid of one of the traveling waves and keep only one pulse traveling to the right.

Using periodic boundary conditions and a large enough number of neurons ($N > 50$) the pulse advances invading the homogeneous rest state, which gets reestablished in its wake. For smaller rings ($N < 50$) the front of the pulse may start interacting with its tail, thus becoming unstable.

Other types of behavior that we found exhibit modifications from the basic smooth and lurching waves. For example at $s = 0.71$ (see Fig. 13.5(a,b)) there is a modulation in the propagation of the wave, yet a clear, perfectly defined n-cluster lurching is never established. For $s = 0.716$ (see Fig. 13.5(c,d)) there is another solution, that has the appearance of a "modulated" 3-lurcher. These two solutions are stable and live on invariant tori, as we will show below.

At this point a number of issues naturally arise: Can hysteresis between stable states be observed? What is the type of transitions, and what is their 'signature' on the linearization spectrum?

So far we have used two computational approaches: (a) direct time integration of the network ordinary differential equations (ODE's) as s-space is explored, and (b) Newton and pseudo-arclength methods to locate branches of fixed and periodic points of the return map.

13.3 Exploration of parameter space and continuation

13.3.1 Direct time integration

A more systematic picture of the different families of solutions the system possesses can be achieved by gradually varying the parameter s and letting the network evolve in time according to the differential equations (13.1–13.4). As shown in the previous section, varying s in the $[0,1]$ interval will produce a number of distinct behavior types.

We have used a FORTRAN 77 implementation of ODESSA [15], an integrator of stiff ODE's with sensitivity analysis.

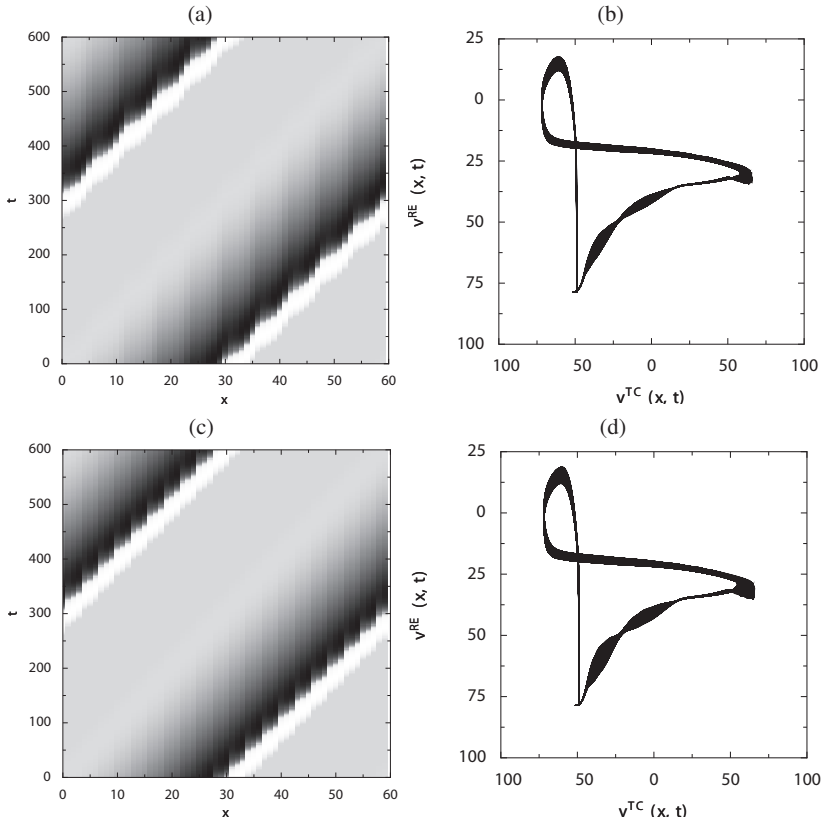

Fig. 13.5 Besides perfectly periodic solutions, the network exhibits behaviors that appear as spatio-temporal modulations of the lurchers: (a) Space-time plot for $s = 0.71$. (b) Single-site phase plane for $s = 0.71$ showing that no two neurons describe the same trajectory. (c) Space-time plot for $s = 0.716$. (d) Single-site phase plane for $s = 0.716$. These two solutions appear to be quasi-periodic. In figures (a) and (c) light shades of gray mean low values of voltage v^{TC}, and dark shades mean high values of v^{TC}.

The model ODE's were integrated in time starting with a localized perturbation over the uniform rest state; we then waited for a period of time long enough for the initial transients to be "washed out", giving us a well-defined traveling pulse. Computing the spatial averages of the four fields: $\langle v^{\mathrm{TC}} \rangle(t)$, $\langle h^{\mathrm{TC}} \rangle(t)$, $\langle v^{\mathrm{RE}} \rangle(t)$ and $\langle h^{\mathrm{RE}} \rangle(t)$, it was possible to find their temporal peaks. Repeating the process for a slightly different value of s (starting from the final state of the previous integration), and exploring s-space in both directions, we generated an extended picture of the waves and their ranges of stability. The mechanisms that explain the stability losses i.e. bifurcations, are going to be explained in the next section.

Using this simple approach we were able to outline a basic scenario for the stable solutions that exhibits hysteresis (see Fig. 13.6):

- Smooth waves exist for low values of s. These waves lose stability at $s \approx 0.702$ in what appears to be a Hopf bifurcation of traveling waves.
- 6-lurchers exist for high values of s. They will dissapear when s is decreased in what appears to be a saddle-node bifurcation at $s \approx 0.714$. For $s \approx 0.961$ the 6-lurcher becomes a stable 12-lurcher through a supercritical period doubling bifurcation.
- Stable 3-lurchers live in a parameter window defined between $s = 0.7154$ and $s = 0.7718$. At the lower limit there is a saddle-node bifurcation, and at the upper limit there is a period doubling that apparently is subcritical: the 6-lurcher created at that point is unstable.
- Associated to a Hopf bifurcation of the smooth wave (1-lurcher), a quasiperiodic solution (torus A in Fig. 13.6) arises and lives over an invariant torus. This non-simply-periodic solution is destroyed at $s = 0.7153$ by a global bifurcation.
- Another stable torus (torus B in Fig. 13.6) is observable between $s = 0.7011$ and $s = 0.718$. Its existence is most probably due to global (rather than local Hopf) bifurcations.

A better insight into the quasiperiodic solutions on the two tori A and B can be gained by looking at a Poincaré/return map. The map is defined in $(4N)$-dimensional space by selecting a codimension-1 hyperplane Σ defined by a scalar equation $p(x) = 0$ and recording the crossings of the trajectory $x(t)$ from one side to the other.

In other words the Poincaré map is defined:

$$P_d(x) \stackrel{\text{def}}{=} \Phi_{\tau(x)}(S_d(x)) \ : \ \Sigma \mapsto \Sigma \ ,$$

where S_d is a spatial shift of d sites to the left using periodic boundary conditions in the space dimensions, $\Phi_\tau(x^0)$ is the time evolution defined by $\dot{x} = f(x), x(0) = x^0$, and $\tau(x^0)$ is the minimal time that satisfies $\tau > 0, p(x)|_{x=\Phi_\tau(S_d(x^0))} = 0, (\nabla_x p, f)_{x=\Phi_\tau(S_d(x^0))} < 0$. Thus the map selects transverse crossings of Σ in only one direction.

In this work we used $p(x) = v_j^{\text{TC}} - p_0$ where j is some lattice index and p_0 a real value. Periodic solutions such as smooth waves and n-lurchers should appear in the P_n map as a return point $x^\star$ that repeats itself: $x^\star = P_n(x^\star) = P_n(P_n(x^\star)) = \cdots$ Poincaré maps of quasiperiodic solutions appear as closed curves, exactly as a transversal cut of a two-torus in 3-dimensions may look like. In Fig. 13.7 two such toroidal sections are shown, projected from $(4N-1)$ to 2-dimensional space. In each one the iterates of the Poincaré map seem to wander over the closed curve, eventually filling it.

13.3.2 Continuation using Newton method

In order to study in more detail the branches presented in Fig. 13.6 through dynamical systems concepts and tools, we use a return map that focuses on the change of

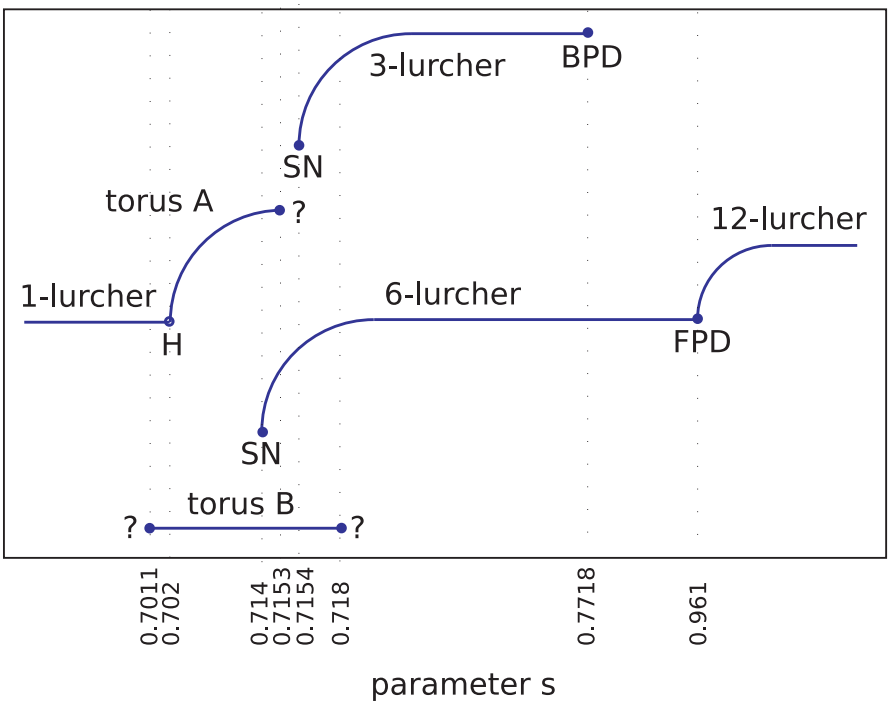

Fig. 13.6 Schematic depicting the stable solutions of the periodic network. The apparent location of the different events was meant to be qualitative only. The information represented in the figure was obtained by 'gently' varying the s parameter as the time integration is performed. Up to three stable solutions exist for some values of the parameters. The following symbols were used: H stands for Hopf bifurcation of limit cycles; SN for saddle-node bifurcation of limit cycles; FPD for forward (supercritical) period-doubling bifurcation of limit cycles; and BPD for backward (subcritical) period-doubling bifurcation of limit cycles. Here "?" indicates a tentative global bifurcation mechanism that deserves further investigation.

the entire network over one 'revolution'. For smooth waves and exact lurchers, the wave shape does not return to itself exactly; rather, it returns to a *shifted* version of itself —by an integer number d of sites, often $d = 1, 3, 6$ or 12— after an appropriate return time. The choice of d will depend on the particular wave that we are trying to find.

Thus we can implement a fixed-point algorithm to find traveling waves by searching for a state vector $x \in \mathbb{R}^{4N}$, that, after being shifted to the left d sites and evolved for a time interval τ following the differential equations (13.1–13.4), returns to the same state x. Now, we could represent a given wave by any instantaneous state. This multiplicity can be removed by defining a 'pinning condition' to test for this return, $p(x) = 0$. This equation quantifies the position of the pulse, the center of the pulse, or just some variable (for instance v^{RE}) of a given neuron minus a reference value. In general we can use some functional of the entire state of the network minus a

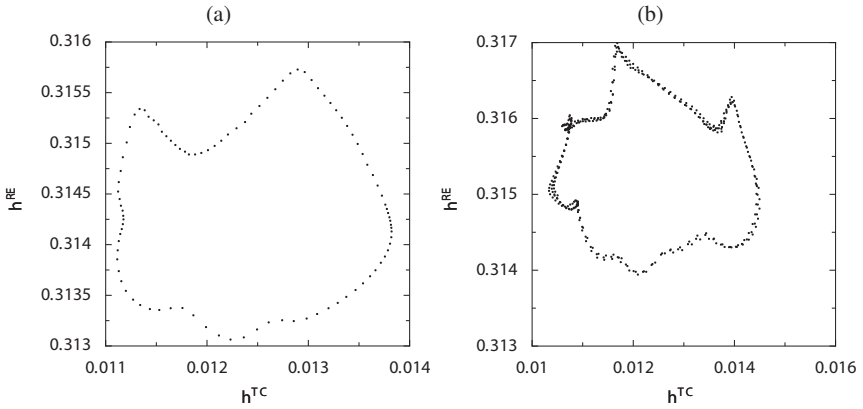

Fig. 13.7 Projections of the Poincaré maps of quasiperiodic solutions obtained for (a) $s = 0.71$, and (b) $s = 0.716$.

reference value. This pinning condition is an additional equation that helps locate the right period of the periodic solution (or the right speed of a traveling wave); the time the pulse takes to advance d sites.

Defining the set of equations that need to be set to zero:

$$F_{d,\tau}(x) \stackrel{\text{def}}{=} \Phi_\tau(S_d(x)) - x = 0\,. \tag{13.5}$$

Where Φ_τ symbolizes the result of forward integraton of $dx/dt = f(x)$ for a time interval τ. The operator S_d stands for a shift by d lattice points with periodic boundary conditions at the edges of the neuron lattice (the four fields v^{TC}, h^{TC}, v^{RE} and h^{RE} are shifted simultaneously). This operator can be represented by a $4N \times 4N$ matrix.

The integrator is also able to extract sensitivity analysis results with respect to variations in parameters and variations in the initial conditions. This last feature can be used to compute the Jacobian of the evolution map Φ_τ at each step:

$$J_{\tau,i,j} \stackrel{\text{def}}{=} \frac{\partial x_i(\tau)}{\partial x_j(0)}\,, \tag{13.6}$$

a matrix that is efficiently computed internally by ODESSA.

If the state x represents a stationary profile (modulo a shift) and a fixed point of $F_{d,\tau}(x)$, then $J_\tau S_d$ will have an eigenvalue $\mu = 1$ corresponding to the eigenvector $\dot{x}(\tau)$. This eigenvalue shows that any time-shift of the pulse $x(t+\tau)$ is also a fixed point of $F_{d,\tau}$. To remove this degeneracy of the map, we augment it with the pinning condition:

$$G(y) \stackrel{\text{def}}{=} \begin{pmatrix} F_{d,\tau}(x) \\ p(\Phi_\tau(S_d(x))) \end{pmatrix}, \tag{13.7}$$

that gives us $4N+1$ equations for the $4N+1$ unknowns $y \stackrel{\text{def}}{=} (x,\tau)^{\mathrm{T}} \in \mathbb{R}^{4N+1}$. The derivative of this map will be:

$$D \stackrel{\text{def}}{=} \frac{\partial G}{\partial y} = \begin{pmatrix} J_\tau S_d - \mathrm{Id} & f(\Phi_\tau(S_d(x))) \\ \nabla_x p(\Phi_\tau(S_d(x))) & 0 \end{pmatrix}. \tag{13.8}$$

In a Newton method for the (isolated) fixed point of this set of equations, the update Δy to an initial guess y_0 of the solution is given by:

$$\Delta y = y - y_0 = -D^{-1} G(y_0).$$

The algorithm was able to quantitatively characterize the loss of stability of the smooth wave when the parameter s crosses 0.702 from below, as well as the other local bifurcations of periodic orbits indicated in Fig. 13.6. To look at the smooth waves, we set $d = 1$ —for 3-,6- or 12-lurchers we would set $d = 3, 6$ and 12 respectively. Fig. 13.8 shows the eigenvalues of $J_\tau S_d$ (a $4N \times 4N$ matrix) in two different situations. The monodromy matrix $J_\tau S_d$ represents the combined action of shifting to the left and evolving in time small perturbations of periodic orbits. Its eigenvalues μ are the Floquet multipliers that characterize the growth or decay of these small perturbations and the stability of the periodic orbit (a similar analysis was developed in [13]). Fig. 13.8(a) shows the complex eigenvalues when $s \approx 0.7$. In addition to the expected $\mu = 1$ (which should not, and does not, move) we can see two bifurcating complex multipliers crossing the unit circle, implying the loss of the stability of the smooth wave under the time map Φ_τ. This Hopf bifurcation of the smooth wave was also found for an integrate-and-fire model in [8]. Note that the bifurcating eigenvalues are not integer roots of unity ($\mu^6 \neq 1$). The other three multipliers cross the unit circle for a slightly higher value of s.

The Newton method was also able to find fixed points corresponding to both 3-, 6- and 12-lurchers. It was, of course, easy to find good initial guesses when these lurchers were stable. For unstable solutions one needs an appropriate initial guess. Fig. 13.8(b) shows the spectrum of the stable 6-lurchers using the $d = 6$ map at $s = 0.71465$, right at the turning point as indicated in Fig. 13.6. Besides the trivial Floquet multiplier $\mu = 1$ there is another multiplier 1. For the period doubling bifurcations indicated in Fig. 13.6, for instance when following the 6-lurcher close to $s = 0.961$ with $d = 6$, there is a multiplier crossing the unit circle at $\mu = -1$.

Now, applying the return map with $d = 6$ and period τ two times, is just the same as applying the map with $d = 12$ and period 2τ, or more concisely $(J_\tau S_d)^2 = J_{2\tau} S_{2d}$, so the multipliers of these monodromy matrices must be related in the same way. When following the *bifurcated* 12-lurcher branch with the $d = 12$ map and decreasing s, what one sees is a multiplier approaching $\mu = 1$ from inside the unit circle, touching the unit circle, but then turning around and remaining inside as s keeps decreasing along the 6-lurcher branch. This positive multiplier obtained with the $d = 12$ map is the squared version of the -1 multiplier obtained with $d = 6$.

Clearly, there is a need to augment these observations and integrate them into a coherent and complete picture. This is work in progress.

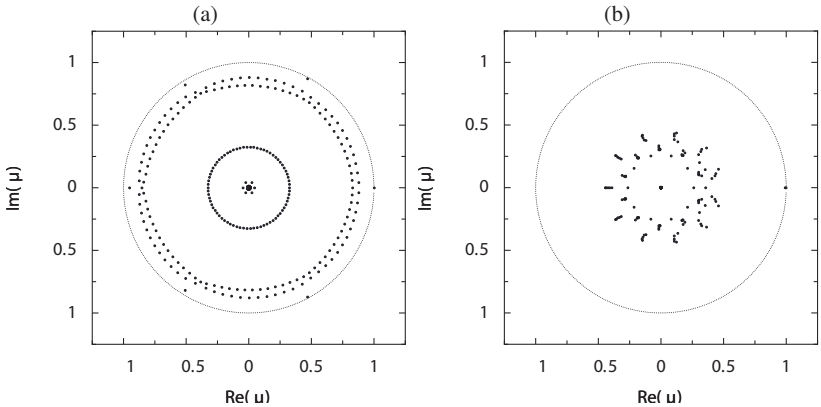

Fig. 13.8 Floquet multipliers of the linearized return map for periodic orbits. Both spectra include trivial multiplier $\mu = 1$. Multipliers crossing the unit circle give the signature of the bifurcation. (a) Spectrum of the smooth wave at $s = 0.6$. Two complex conjugated multipliers (in the righ-hand side of the complex plane) indicate a Hopf bifurcation of a limit cycle. Note that these bifurcating multipliers do not cross the circle at $\exp(\pm i\pi/3)$, and that the other three multipliers cross the unit circle at a later stage. (b) Spectrum of the 6-lurcher at $s \approx 0.71465$ close to the turning point. An isolated positive multiplier approaching $\mu = +1$ indicates a saddle-node bifurcation of a limit cycle.

13.3.3 Pseudo-arclength continuation

In a continuation context (see Ref. [11]), an additional 'arclength' parameter ξ can be introduced and the parameter s can be regarded as an unknown:

$$H(z) \stackrel{\text{def}}{=} \begin{pmatrix} F_{d,\tau}(x;s) \\ p(\Phi_\tau(S_d(x);s)) \\ \theta_x \hat{x}^{\mathrm{T}}(x-x_0) + \theta_\tau \hat{\tau}(\tau-\tau_0) + \theta_s \hat{s}(s-s_0) - (\xi-\xi_0) \end{pmatrix}, \qquad (13.9)$$

where $z \stackrel{\text{def}}{=} (x,\tau,s) \in \mathbb{R}^{4N+2}$. The positive weights θ_x, θ_τ and θ_s $(\theta_x + \theta_\tau + \theta_s = 1)$ define a metric in $(4N+2)$-dimensional space. The vector $\hat{x}$, and the scalars $\hat{\tau}$ and $\hat{s}$ are approximations to $dx/d\xi$, $d\tau/d\xi$ and $ds/d\xi$, which can be obtained in several ways. Here we used the estimate of the slope given by the last two points, (x_0,τ_0,s_0) and $(x_{-1},\tau_{-1},s_{-1})$ computed on the branch.

The solution of the linear system in the inner iterations of the Newton algorithm was found using a standard direct solver. We also used the Generalized Minimal Residual method (GMRES), that gives rise to the Newton-GMRES method (Ref. [10]). It has been succesfully used for time-steppers in Ref. [11]. This method focuses on the Krylov space generated by the linearization of the same operator G. In each iteration, it solves the linear system $D\Delta y = -G(y)$ using least squares estimation on this Krylov subspace.

It is also possible to compute a few leading eigenvalues of the monodromy matrix $J_\tau S_d$ and characterize the stability of the fixed points, using the Implicitly Restarted Arnoldi Method, that uses similar matrix-free ideas (see Ref. [14]).

Using judiciously small increments in the pseudo-arclength parameter ξ it is possible to follow unstable branches over wide parameter intervals, and elucidate the connection between different lurching solutions. We remark that all our computations are based on a time-stepper that performs forward integrations; this is the reason for the difficulty of following unstable solutions (see [20]).

13.4 Discussion

When confronted with a system of identical interconnected units like the neuronal network we studied in this article, it seems natural to consider simple geometries, for instance a ring, and build spatially continuous models of the system. Such an approach would capture a significant feature of the dynamics, namely the smooth waves, but might be unable to replicate the lurching waves that arise as an effect of the discreteness of the lattice.

The second idea would be to use the tools of the theory of dynamical systems that have proven to be extremely fruitful for systems of few degrees of freedom. But such a theory is built around the concept of the zero of a differential equation or the fixed point of a map. The zero state of the thalamocortical network is the rest state and thus uninteresting. In this article we have found propagating waves as fixed points of a return map compounded with a spatial shift. This idea applies both to smooth waves and lurching waves. The analyis of the map can be performed numerically using stiff solvers of ODE's and matrix-free linear algebra for the efficient solution of nonlinear systems of equations with many unknowns.

Using the map and its computational implementation, we have found that there is a rich scenario hiding behind the transition from smooth to lurching waves. We observe that the smooth waves become unstable in a supercritical Hopf bifurcation, while the lurching waves disappear (turn around) in saddle-node bifurcations. There exist other states whose appearance varies between smooth and lurching, all appearing (and overlapping) in a relatively narrow region of parameter space. The structure of these tori solutions found in numerical simulations and their connection with periodic solutions is going to be addressed in a separate article [20].

The method just described was not directly applicable to unstable branches. With systems of few degrees of freedom, stable and unstable solutions can be computed with similar ease given that traditional Newton method doesn't consider time in the sense of evolution, it just takes an algebraic system of equations and tries to solve it iteratively. The single shooting approach used here has problems in following branches with very large unstable Floquet multipliers; multiple shooting implementations may help the numerical continuation of such branches, otherwise very small increments in the pseudo-arclength parameter must be used.

With more extensive computations, possibly including multiple shooting formulations, numerical bifurcation theory may help elucidate the propagation of smooth and lurching waves in thalamic one-dimensional lattices.

Acknowledgments: J.C. wishes to acknowledge the financial support of Universidad de los Andes Grant (Project FAI ING-002-09). The work of I.G.K. was partially supported by the AFOSR and by the US DOE.

References

1. Bal, T., von Krosigk, M., McCormick, D.: Synaptic and membrane mechanisms underlying synchronized oscillations in the ferret lateral geniculate nucleus in vitro. J. Physiol. Lond. **483**, 641–663 (1995)
2. Bazhenov, M., Timofeev, I., Steriade, M., Stenowski, J.: Self-sustained rhythmic activity in the thalamic reticular nucleus mediated by depolarizing GABA-A receptor potentials. Nature Neurosci. **2**, 168–174 (1999)
3. Bressloff, P., Coombes, S.: A dynamical theory of spike train transitions in networks of integrate-and-fire oscillators. SIAM J. Appl. Math. **60**(3), 820–841 (2000)
4. Chen, Z., Ermentrout, B., Wang, X.J.: Wave propagation mediated by GABA-B synapse and rebound excitation in an inhibitory network. J. Comput. Neurosci. **5**, 53–69 (1998)
5. Coombes, S.: Dynamics of synaptically coupled integrate-and-fire-or-burst neurons. Phys. Rev. E **67**, 041,910 (2003)
6. Golomb, D.: Propagation of travelling pulses in cortical networks. In: N. Akhmediev, A. Ankiewicz (eds.) Dissipative Solitons: From Optics to Biology and Medicine, *Lect. Notes in Phys.*, vol. 751, pp. 403–430. Springer-Verlag, Berlin Heidelberg (2008)
7. Golomb, D., Ermentrout, G.: Continuous and lurching traveling pulses in neuronal networks with delay and spatially decaying connectivity. Proc. Natl. Acad. Sci. **96**, 13,480–13,485 (1999)
8. Golomb, D., Ermentrout, G.: Bistability in pulse propagation in networks of excitatory and inhibitory populations. Phys. Rev. Lett. **86**(18), 4179–4182 (2001)
9. Golomb, D., Wang, X.J., Rinzel, J.: Propagation of spindle waves in a thalamic slice model. J. Neurophysiol. **75**, 750–769 (1996)
10. Kelley, C.T.: Iterative Methods for Solving Linear and Nonlinear Equations. SIAM, Philadelphia (1995)
11. Kelley, C.T., Kevrekidis, I.G., Qiao, L.: Newton-Krylov solvers for time-steppers (2004). Available at `arXiv:math/0404374v1`
12. Kim, U., McCormick, D.: The functional influence of burst and tonic firing mode on synaptic interaction in the thalamus. J. Neurosci. **18**, 9500–9516 (1998)
13. Krishnan, J., Engelborghs, K., Bär, M., Lust, K., Roose, D., Kevrekidis, I.: A computer-assisted study of pulse dynamics in anisotropic media. Physica D **154**, 85–110 (2001)
14. Lehoucq, R., Sorensen, D., Yang, C.: ARPACK Users' Guide: Solution of Large-Scale Eigenvalue Problems with Implicitly Restarted Arnoldi Methods. SIAM Publications, Philadelphia (1998)
15. Leis, J., Kramer, M.: An ordinary differential equation solver with explicit simultaneous sensitivity analysis. ACM Trans. Math. Software **14**, 6167 (1988)
16. Pinault, D., Deschenes, M.: Anatomical evidence for a mechanism of lateral inhibition in the rat thalamus. Eur. J. Neurosci. **10**, 3462–3469 (1998)
17. Rinzel, J., Terman, D., Wang, X.J., Ermentrout, B.: Propagating activity patterns in large-scale inhibitory neuronal networks. Science **279**, 1351–1355 (1998)

18. Steriade, M., McCormick, D., Sejnowski, T.: Thalamocortical oscillations in the sleeping and aroused brain. Science **262**, 679–685 (1993)
19. Terman, D., Ermentrout, G., Yew, A.: Propagating activity patterns in thalamic neuronal networks. SIAM J. Appl. Math. **61**, 1578–1604 (2001)
20. Wasylenko, T., Cisternas, J., Kevrekidis, I.: Bifurcations of smooth and lurching waves in thalamic neuronal networks (2010). In preparation

Index

O. Descalzi et al. (eds.), *Localized States in Physics: Solitons and Patterns*,
DOI 10.1007/978-3-642-16549-8,